DATA-DRIVEN RISK ASSESSMENT OF BRIDGES SUBJECT TO CORROSION AND SCOUR

A Dissertation
Presented to
The Academic Faculty

by

Yijian Zhang

In Partial Fulfillment
of the Requirements for the Degree
Doctor of Philosophy in the
School of Civil and Environmental Engineering

Georgia Institute of Technology
May 2021

DATA-DRIVEN RISK ASSESSMENT OF BRIDGES SUBJECT TO CORROSION AND SCOUR

Approved by:

Dr. Iris Tien, Advisor
School of Civil and Environmental Engineering
Georgia Institute of Technology

Dr. Donald W. White
School of Civil and Environmental Engineering
Georgia Institute of Technology

Dr. Reginald DesRoches
Department of Civil and Environmental Engineering
Rice University

Dr. Ting Zhu
The George W. Woodruff School of Mechanical Engineering
Georgia Institute of Technology

Dr. Yang Wang
School of Civil and Environmental Engineering
Georgia Institute of Technology

Date Approved: [April 27th, 2021]

ACKNOWLEDGEMENTS

First of all, I would like to express my profound gratitude to my advisor, Dr. Iris Tien, who has granted me the opportunity to work in her research group at Georgia Tech. Without her supportive guidance, diligent attitude, professional mentorship, and constant encouragement, I would not have accomplished my research throughout my graduate career.

I would also like to extend my warm gratitude to one of my thesis committees, Dr. Reginald DesRoches, who has offered me generous support, professional advice, and research opportunity, especially at the beginning of my Ph.D. study. I sincerely appreciate the time Dr. Iris Tien and Dr. Reginald DesRoches have spent on me through the weekly research meeting, which gave me clear guidance and insight into my research.

I would also like to thank other thesis committees, Dr. Wang Yang, Dr. Donald W. White, and Dr. Ting Zhu, for their supports on my Ph.D. thesis. Their coursework equips me with useful technical tools and knowledge for my research.

I would also like to thank my colleagues and friends for their friendships and supports. Special thanks to Dr. Chuang-Sheng (Walter) Yang for his helpful advice about the Ph.D. study.

Finally, I am deeply thankful to my mother, Xiaofang Tang, and my father, Jianhua Zhang. They have given me unconditional support and encouragement throughout my life.

This project was partially funded by the INSPIRE University Transportation Center (UTC). Financial support for INSPIRE UTC projects is provided by the U.S. Department of Transportation, Office of the Assistant Secretary for Research and Technology

(USDOT/OSTR) under Grant No. 69A3551747126 through INSPIRE University Transportation Center at Missouri University of Science and Technology, all of which are gratefully acknowledged.

TABLE OF CONTENTS

LIST OF TABLES

LIST OF FIGURES

SUMMARY

Aging of bridge structural components due to natural degradation events, such as corrosion and scour, creates safety issues in the structural system and can lead to possible bridge failures. Collecting and analyzing inspection data provide a way to monitor and assess the safety condition of bridges. This dissertation presents new methods for data-driven risk assessment of bridges subject to corrosion and scour. The research focuses on utilizing collected inspection data to evaluate the structural conditions of the bridges through novel modeling approaches for structural risk analysis, including bridge fragility assessments.

In light of the contents described above, the thesis covers three main topics throughout the dissertation: the impact of corrosion on bridge structures' seismic performance, the impact of foundation scour on the structural performance of bridges/foundation piles, and the ability to simulate other degradation mechanisms on structures. Each main topic consists of two subtopics to further explore the details of the research findings, and a total of six subtopics are investigated in the study.

The road map of the dissertation starts with an introduction in Chapter 1. Chapter 1 presents an overview of the entire study, and it also briefly discusses the structure of the dissertation. Chapter 2 delves into the research motivation and background of all six subtopics. As such, thorough literature reviews and potential research topics are presented. The next three chapters will describe the work accomplished within each topic. Chapter 3 covers details regarding the investigation of the impacts of corrosion on the seismic performance of bridges. The two subtopics covered relate to: (1) exploration of failure

modes of aging structural columns considering the impacts of measured corrosion, and (2) a new methodology to update fragility assessment through Bayesian inference to reduce the computational cost for bridge risk assessment applied to the assessment of corroded bridges. Chapter 4 investigates the influence of scour on the structural performance of bridges and foundation piles. The two subtopics covered include: (3) methodologies to assess structural reliability accounting for physical phenomena after scour events, including the impacts of soil stress history, scour hole dimensions, and layered soils effects; and (4) investigation of the influence of measured non-uniform scour on bridge responses. Chapter 5 presents the last topic covered in this dissertation: the study of other degrading mechanisms, including: (5) fragility assessment of bridges utilizing both scour and corrosion inspection data, and (6) methodology to increase the numerical robustness and accuracy of analyzing frame elements with a softening material constitutive behavior such as in analyzing the impact of short lap splices on the seismic performance of bridge columns. Lastly, Chapter 6 summarizes all six subtopics' research contributions and descriptions of the importance of this study. It also gives a brief introduction of the ongoing work related to the dynamic buckling of the foundation pile in the presence of the scour and recommended topics for future study.

The six subtopic areas provide an increased understanding of the performance of bridges subject to corrosion and scour and provide a robust framework to assess the safety condition of bridges based on collected inspection data. In determining the safety of bridges across a transportation network, the framework allows accurate identification of the most vulnerable bridges and supports decisions to reduce bridges' vulnerability across the network.

CHAPTER 1. INTRODUCTION

Aging of bridge structural components due to natural degradation events, such as corrosion and scour, creates safety issues in the structural system and can lead to possible bridge failures. Collecting and analyzing inspection data provide a way to monitor and assess the safety condition of bridges. This thesis presents new methods for data-driven risk assessment of bridges subject to corrosion and scour. The research focuses on utilizing collected inspection data to evaluate the bridges' structural conditions through fragility assessments. This study adopts the general research procedure shown in Figure 1, with primary focuses on Step 2 and Step 3. Data acquisition is the first step of this procedure. Note that collected data is relevant to informing structural states due to degrading mechanisms, for example, mass loss of column reinforcement due to the impact of corrosion or scour depth indicating level of foundation scour. However, data acquisition is not the main focus of this study; it is assumed to be known and the objective is to create methodologies to utilize this data to update assessments of bridge risk. Damage mapping indicates the change of mechanical properties due to a specific degrading mechanism. This change of mechanical properties can then be implemented in updated structural analyses, for example in the use of finite element models. Finally, to capture the particular degrading mechanism's impact, risk assessment is conducted through updating fragility curves.

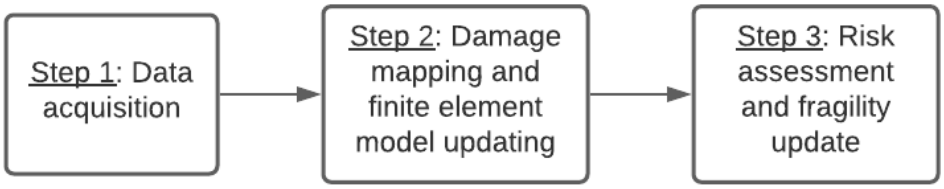

Figure 1. General research procedure

The dissertation's contributions can be summarized into three main areas shown in Figure 2 with six individual subtopics. The three research areas include independent investigations of the impact of corrosion on highway bridges, the impact of foundation scour on bridges and foundation piles, and other degradation mechanisms, such as the combined effect of corrosion on scoured bridges and the numerical modeling of bridges with short lap splices.

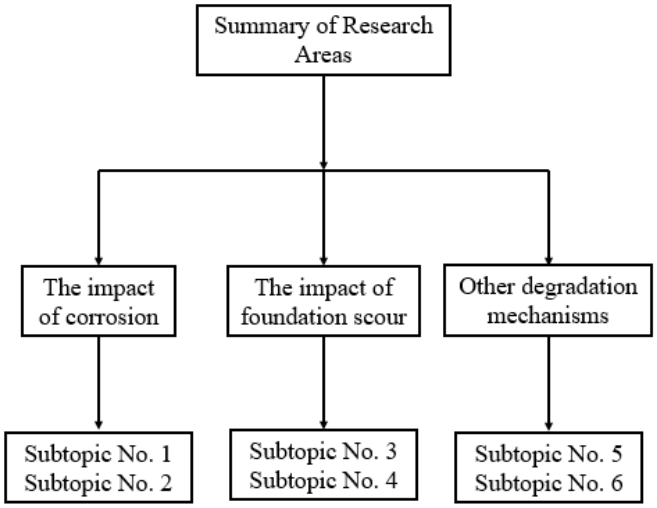

Figure 2. Flowchart of research contributions

Within each main research area, two individual subtopics are investigated in the study. The following list presents the title of each subtopic. As noted, the advancements in each subtopic focus on work related to the second and third steps shown in Figure 1.

1. Exploration of failure modes of aging structural columns considering the impacts of measured corrosion
2. Methodology to update fragility assessment through Bayesian inference to reduce the computational cost for bridge risk assessment
3. Methodologies to assess the structural reliability accounting for physical phenomena after scour events, including the impacts of soil stress history, scour hole dimensions, and layered soils effects
4. Investigation of the influence of measured non-uniform scour on bridge responses
5. Fragility assessment of bridges utilizing both scour and corrosion inspection data
6. Methodology to increase the numerical robustness and accuracy of analyzing frame elements with a softening material constitutive behavior

Chapter 2 presents detailed literature reviews and an introduction to each of the six research topics aforementioned. Chapters 3, 4, and 5 provide comprehensive analysis results and discussion for each of the main research topics shown in Figure 2. Finally, Chapter 6 summarizes the research findings and future work for this study.

CHAPTER 2. BACKGROUND AND MOTIVATION

2.1 Introduction

The following six sections will present an overview of each subtopic's background and motivation, as shown in Figure 2 (Chapter 1). Detailed investigations of each subtopic can be found in Chapters 3, 4, and 5, accordingly.

2.1.1 Subtopic No. 1: Exploration offailure modes of aging structural columns considering corrosion impacts of measured corrosion

The first research topic explores the impact of corrosion on bridge seismic performance with low-ductility columns, including shear-critical columns and columns with short lap splices. For highway bridges in California built pre-1970s, transverse reinforcement of #4 stirrups at 12-inch spacing regardless of its dimensions or longitudinal reinforcement is a typical reinforcement detailing for bridge columns (Ramanathan, 2012). Meanwhile, it is also common for bridge columns to have short lap splices of 20-24 times the longitudinal bar diameter above the footing (Mangalathu, 2017; Soleimani, 2017). These low-ductility columns are often associated with brittle and catastrophic failure modes and pose a difficult problem for structural engineers to predict their responses. Figure 3 shows field observations of shear failure and pull-out failure of bridge columns in the 1971 San Fernando earthquake.

(a) (b)

Figure 3. Bridge column with (a) shear failure and (b) pull-out failure in 1971 San Fernando earthquake (Veletzos et al., 2006)

Meanwhile, corrosion poses another critical issue for aging bridges, presenting high costs for retrofitting (Padgett, 2007) and severe safety issues under seismic loadings (Ghosh and Padgett, 2010; Choe et al., 2009). Previous studies have investigated the influence of pitting corrosion on the mechanical properties of corroded steel bars (Almusallam, 2001; Du et al., 2005; Apostolopoulos et al., 2006). Du et al. (2005) have studied the effect of corrosion damage on residual capacity and corroded bars' ductility to account for the impact of pitting corrosion on the constitutive behavior of reinforcement in tension. An investigation of spatial variability in corrosion patterns of corroded bars using 3D optical measurements has been conducted by Kashani et al. (2013). They have found that the geometrical properties of corroded bars can be modeled using a lognormal distribution.

However, few previous studies quantify corrosion's impact across different column failure modes based on the literature. Therefore, one of the main goals for this research is to create a methodology to assess and quantify corroded and low-ductility columns' performance. The study explores the effect of varying levels of measured corrosion on bridge performance to facilitate engineering design and analysis.

2.1.2 *Subtopic No. 2: Methodology to update fragility assessment through Bayesian inference to reduce the computational cost for bridge risk assessment*

Fragility functions provide a way to quantify structural risks under varying loading intensities. Equation (1) represents the conditional probability of a structure exceeding a specific damage state DS given a realization y of intensity measure IM.

$$Fragility = Pr[DS|IM = y] \quad (1)$$

Analytical fragility curves can be obtained through running nonlinear time history analyses (Choi et al., 2004; Nielson and DesRoches, 2007; Padgett, 2007; Zhang et al., 2019a; Ramanathan et al., 2012) or through incremental dynamic analysis with nonlinear finite-element models (Luco and Cornell, 1998; Vamvastikos and Cornell, 2002; Mackie and Stojadinovic, 2005; Zhang and Huo, 2009). Fragility curves obtained from nonlinear time history analyses have been found to be more reliable (Shinozuka et al., 2000) due to the ability to account for various sources of uncertainty. However, several limitations arise in running nonlinear time history analyses to obtain analytical fragility curves. These include the high computational cost of the process, both in building the model and performing the calculations. In particular, getting stable fragility assessments requires the performing of a sufficient number of dynamic analyses. The cost further increases to perform dynamic analyses for high fidelity finite-element models with high nonlinearity. Besides, building the finite-element model itself for large and complex structural systems can be time-consuming. This research presents a methodology to address these limitations by reducing the computational costs to obtain analytical fragility curves for structural risk assessment. The method utilizes Bayesian updating to efficiently and accurately generate

analytical fragility curves by minimizing the number of nonlinear analyses required or performing component-level analyses with reduced complexity.

Bayesian techniques have been adopted to obtain fragility curves in several previous studies. Singhal and Kiremidjian (1998) utilize building damage data on reinforced concrete buildings with fragility curves to arrive at more robust fragility assessments. Li et al. (2013) incorporate hybrid simulation with Bayesian updating techniques to improve the accuracy of the fragility function. Der Kiureghian (2002) takes advantage of Bayesian methods to assess the fragility of electrical substation equipment based on field observations after an earthquake. Koutsourelakis (2010) combines Bayesian methods with Markov Chain Monte Carlo (MCMC) to evaluate structural vulnerability using fragility surfaces. Gardoni et al. (2002) develop a methodology to establish probabilistic capacity models of structural components and a Bayesian updating approach based on observational data. Choe et al. (2007) and Zhong et al. (2008) have developed fragility estimates for reinforced concrete columns and bridges through a Bayesian methodology following Gardoni et al.'s work. Koutsourelakis (2010) combines Bayesian methods with Markov Chain Monte Carlo (MCMC) techniques to assess structural vulnerability using fragility surfaces. Li et al. (2013) incorporate hybrid simulation with Bayesian updating techniques to improve the accuracy of the fragility function. Baker (2015) proposes a framework for obtaining efficient analytical fragility functions through multiple stripe analysis procedures. Noh et al. (2017) use conjugate Bayesian models to develop vulnerability functions combined with mortality rate data for treating the uncertainties in the earthquake.

However, among these studies, none have been found to investigate the use of Bayesian updating techniques and conjugate Bayesian inference to reduce the computational cost required to create and update analytical fragility curves with a minimal number of structural analyses. Compared to previous works, this research proposes a method using updating rules from conjugate Bayesian inference to efficiently and accurately estimate fragility curves based on inspection data. It provides a way to utilize collected bridge inspection data to update the fragility assessment of bridges efficiently.

2.1.3 Subtopic No. 3: Methodologies to assess the structural reliabilityaccounting for physical phenomena after scour events, including the impacts of soil stress history, scour hole dimensions, and layered soils effects

Over time, the material is carried away from the bed and banks for water-crossing bridge structures due to flowing water's erosive action, leading to scour conditions for these bridges' foundation systems. Researchers have shown that 60% of bridge failures in the U.S. are related to scour at the bridge foundation (Wardhana and Hadipriono, 2003; Lagasse et al., 2007). Therefore, it is essential to have a way to model soil-structure interaction that accurately captures bridge performance considering scour phenomenon. Traditional modeling of soil-structure interaction involves the simple removal of soil springs without considering the changes of stress states and corresponding properties of the remaining soil due to scour (Alipour and shafei, 2012; Banerjee and Prasad 2013; Wang et al., 2014).

Previous studies have investigated the influence of soil stress history on the lateral response of piles in sand and soft clay (Lin et al., 2010; Lin et al., 2014). Others have

studied piles' lateral behavior in layered soil deposits (Davisson and Gill, 1963; Georgiadis, 1983; Gazetas et al., 1984). However, there have been no studies on the effect of soil stress history on layered soils' properties. Moreover, the seismic performance of bridges subject to scour, including the impact of soil stress history of layered soils, is unstudied. This research develops a methodology to account for the influence of layered deposits and soil stress history in evaluating the seismic performance of bridges susceptible to scour. It provides an approach that can accurately assess the vulnerability of bridges located in layered soil deposits based on measured scour data.

In addition to soil stress history, the effect of scour-hole dimensions on the vulnerability of scoured bridges is also commonly neglected in bridge design and analysis. Figure 4(a) shows a scour hole's geometry with scour depth, scour width, and slope angle. Lin et al. (2014, 2016) have investigated the effect of scour-hole dimensions on the lateral behavior of a single pile for cohesionless and cohesive materials through the use of an imaginary equivalent wedge failure model shown in Figure 4(b). To evaluate the effect of scour-hole dimensions on the pile's axial response, Lin (2017) has proposed a closed-form solution of additional vertical stress due to scour-hole geometry through integrating Boussinesq's analytical solution. Zhang et al. (2016) have proposed a methodology to compute lateral resistance of soil numerically considering both scour-hole geometry and possible changes of stress due to scour effect in soft clay with the aid of integration of Mindlin's elastic solutions. However, this methodology only applies to cohesive material, and the study does not investigate how scour-hole geometry and stress history impact the vertical resistance of the soil. This research provides a framework to account for the combined effect of soil stress history and scour-hole geometry for both cohesive and cohesionless soils. The

framework is implemented by modifying the parameters for ultimate soil resistance. The modified parameters can then be used for the nonlinear backbone curves of the corresponding soil springs constituting the soil-structural interaction.

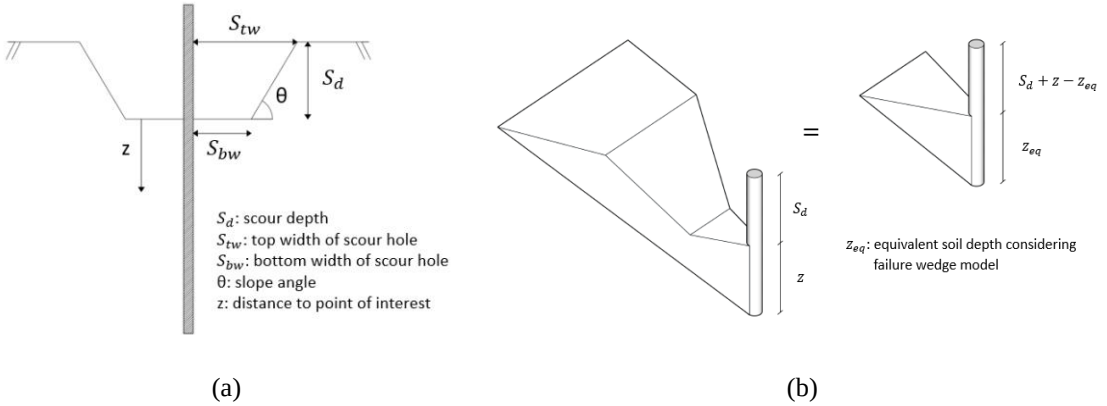

Figure 4. (a) Geometry of scour hole and (b) a wedge failure model considering scour-hole dimensions and equivalent wedge model without scour-hole dimensions

2.1.4 Subtopic No. 4: Investigation of the influence of measured non-uniform scour on bridge responses

While uniform flood-induced scour followed by an earthquake has been investigated in the existing literature (Alipour and Shafei, 2012; Banerjee and Prasad 2013; Wang et al., 2014), the effect of non-uniformity in scour depth for multiple columns has received limited attention. Numerous researchers have shown that pile numbers, arrangements, and spacing affect scour depth (Chang et al., 2013; Castiblanco, 2016). Moreover, the studies indicate that bridge piers experience non-uniform scour depth at the foundations in failure scenarios (Khan and Amanat, 2015; Song et al., 2015; Tubaldi et al., 2018). In particular, within a multiple-pier bent, the upstream pier usually experiences a greater extent of scour, indicated by increased scour depth, than the downstream pier does

because the upstream pier reduces the flow velocity. Some of the soils are transported from the upstream pier and deposited in the downstream pier (Khan and Amanat, 2015).

A recent paper published by Fioklou and Alipour (2019) has discussed the multi-hazard performance of a bridge considering non-uniformity in scour depth. In particular, Fioklou and Alipour (2019) investigate the dynamic characteristics and seismic performance of a selected bridge type under the effect of non-uniform soil erosion with the upstream and downstream pier foundations experiencing notably different scour depths. However, for bridges consisting of multiple column bents, piers under different bents could experience a different soil erosion level due to non-uniform water velocity and other factors. No literature has investigated the effect of non-uniformity in scour depths for pier foundations under separate column bents. Moreover, non-uniformity in scour depths could impact the bridge performance differently depending on the loading types (e.g., earthquake event versus flooding event). This research investigates the effect of non-uniformity in scour depths on bridge performance.

2.1.5 Subtopic No. 5: Fragility assessment of bridges utilizing both scour and corrosion inspection data

Multiple forms of aging and deterioration mechanisms take place and impact the bridge system's functionality during the life cycle of reinforced concrete highway bridges (Zhang et al., 2019b). In particular, deteriorating mechanisms may include the result of environmental stressors such as corrosion attacks and flood-induced erosion of the soil near the foundation of bridge piles resulting in scour.

The majority of the literature has focused on the individual effect of these deterioration mechanisms on highway bridges' seismic performance. For example, Choe et al. (2009) investigate the reduction of reinforced concrete bridge columns' capacity due to corrosion. Ghosh and Padgett (2012) evaluate corrosion's impact on bridge fragility considering multiple component deterioration and exposure conditions. On the other hand, Banerjee and Prasad (2013) assess the seismic performance of bridges located in seismically-active and flood-prone regions in the presence of flood-induced scour. Wang et al. (2014) investigate the impact of local scour on seismic fragility of various California bridge types.

However, as corrosion and scour effects are prevalent across bridges, the impacts could act simultaneously on highway bridges' seismic performance, particularly in marine environments. Previous research has not assessed the combined effects of corrosion and bridge scour on bridge seismic fragility. This research investigates bridge risk utilizing corrosion and scour inspection data, evaluating the potentially increased vulnerability of these structures, including any combined effects.

2.1.6 Subtopic No. 6: Methodology to increase the numerical robustness and accuracy of analyzing frame elements with a softening material constitutive behavior

For structures built pre-1970s, it was common for reinforced concrete columns to consist of widely spaced transverse reinforcement and short lap splices at the base of the column with a lap length of 20 to 24 times the longitudinal bar diameter (Chail et al., 1991; Sun and Priestley, 1993; Melek and Wallace, 2004). These structures are more likely to exhibit poor seismic performance (Zhang et al., 2019a). To be able to evaluate these structures under varying conditions, it is essential to have a numerical modeling approach

to simulate the nonlinear behavior of columns with short lap splices that results in accurate assessments of performance (Zhang and Tien, 2020).

Several previous numerical models have been proposed to investigate the nonlinear response of columns with short lap splices (Reyes and Pincheira, 1999; Cho and Pincheira, 2006; Tariverdilo et al., 2009). Cho and Pincheira (2006) develop an analytical modeling approach using nonlinear rotational springs at the element end to simulate the degradation of stiffness and strength with increasing deformation amplitude. This modeling approach utilizes a concentrated plasticity model, which exhibits low computational cost. Still, it requires the analyst to obtain parameters used to define the moment-rotation relationship through experimental tests. Tariverdilo et al. (2009) develop a model capable of capturing the degrading response due to bar slip in the lap splice based on the configuration and yield stress of the longitudinal reinforcement and the spacing and amount of transverse reinforcement through a distributed plasticity modeling approach. The model exhibits a good correlation with results from experimental tests. However, Tariverdilo et al.'s model uses force-based beam-column elements, consisting of fiber discretization with a softening stress-strain relation at the material level to model the degrading mechanism due to bar slip, so the loss of objectivity due to strain localization has become a critical issue from a numerical accuracy standpoint.

Tariverdilo et al.'s model suggests using two Gauss-Lobatto integration points within the lap-spliced element to model short lap splices' response regardless of the splice's length. Numerically, the selection of two integration points is ambiguous because the appropriate use of the number of integration points in the lapped region could change as the lapped region's physical length changes from a test specimen to a full-scale structural

column. As a result, the assumption of using two integration points in the lapped region can give rise to inaccurate predictions of the nonlinear response of a real structural column with a short lap splice at the base. Previous studies (Coleman and Spacone, 2001; Addessi and Ciampi, 2007; Scott and Hamutcuoglu, 2008) have investigated the issue of loss of objectivity in the force-based beam-column element and found that the number of integration points used dictates the numerical accuracy of the model when it comes to softening constitutive behavior in the material. Coleman and Spacone (2001) present a regularization approach to handle strain localization for softening concrete response in compression.

However, no studies have investigated reinforced concrete columns' softening response with short lap splice if a stress-strain approach is adopted. This research proposes a methodology to regularize force-based beam-column elements for reinforced concrete columns with short lap splices at the column base. The process of regularization is based on the use of a constant energy criterion, which imposes an extra constraint in the material level to stabilize the element response, resulting in more accurate and robust analysis results.

CHAPTER 3. CORROSION IMPACT ON SEISMIC PERFORMANCE OF BRIDGES

3.1 Introduction

This chapter entails the impact of corrosion on bridges' seismic performance, and the primary focus for this study will be on the corroded bridge column. As shown in Figure 2 and Chapter 2, subtopics 1 and 2 will be presented in this chapter. The first subtopic explores failure modes of aging structural columns considering the impacts of measured corrosion based on our publication Zhang et al. (2019a). The second subtopic is the methodology to update fragility assessment through Bayesian inference to reduce the computational cost for bridge risk assessment.

3.2 Subtopic No. 1

3.2.1 Shear-critical columns considering corrosion effect

Both experimental research and post-earthquake data have shown that columns with widely spaced transverse reinforcement have a higher probability of failing in shear, leading to collapse of the system (Elwood, 2004). Widely spaced transverse reinforcement is a characteristic of many bridges built prior to the 1970s before the importance of transverse reinforcement was understood. In this section, a numerical model is established and used to assess bridge behavior. A calibrated shear spring element is adopted to capture shear degradation (LeBorgne, 2012) for simulation in OpenSees (McKenna et al., 1997). More specifically, the shear spring element can monitor forces and deformation in the

beam-column element. Shear degradation is triggered by reaching either a limiting lateral force or a limiting plastic-hinge rotation capacity (LeBorgne and Ghannoum, 2013).

Figure 5 presents the numerical model with a double-curvature bridge column. Since the bridge column's boundary conditions are fixed at both the top and bottom in this selected bridge type, the inflection point approximately occurs at the bridge column's mid-span. A middle node is added to capture the displacement demand at the mid-span. Two force-based beam-column elements are in series with a zero-length shear spring element and a bond-slip element used to account for the strain penetration effect. The bond slip typically occurs along a portion of anchorage length (Zhao and Sritharan, 2007). Each force-based beam-column element possesses four gauss integration points, which allows the model to capture the spread of plasticity along the column and fiber section consisting of uniaxial constitutive models for steel and concrete. A shear spring is added at the bottom end of the column to account for the effect of shear degradation in the case of shear failure mode. As the shear spring element is designed for a column with a rectangular cross section, the column's width and depth are taken as $0.89D$ adopted from ACI provisions (2011) and Liu et al. (2015), where D is the column diameter.

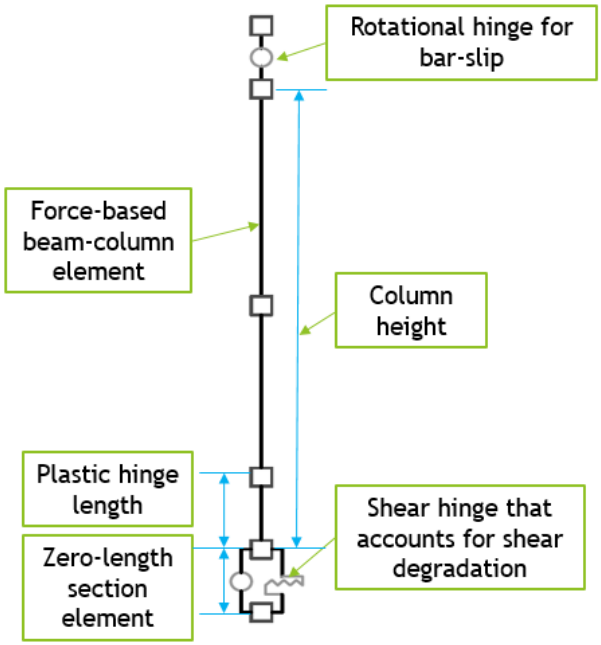

Figure 5. The numerical model for shear-critical column

Force-displacement curves from the model are compared to those from experimental tests of circular shear-critical columns conducted by Ghee (1985) To verify the numerical model's accuracy. Experimental data on corroded shear-critical columns are not available, so results are compared with the pristine column. The two specimens for comparison have a diameter of 400 mm and a height of 600 mm. Longitudinal reinforcement consists of 20 steel bars with a diameter of 16 mm, and transverse reinforcement consists of steel bars with a diameter of 6 mm at 60 mm and 80 mm spacing for the two specimens. Figure 6 shows both experimental and numerical results from static cyclic tests for each specimen.

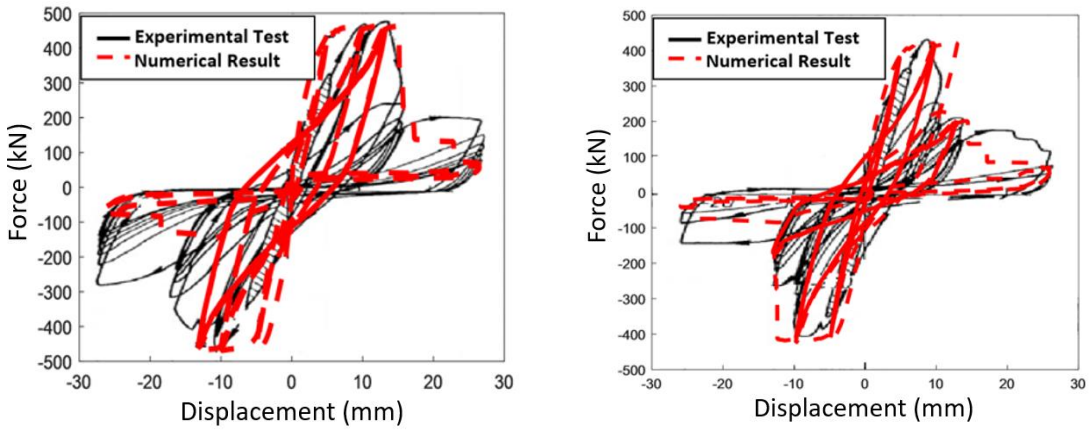

Figure 6. Force-displacement curves for specimens with (a) 60 mm and (b) 80 mm transverse reinforcement spacing from experimental tests (Ghee, 1985) and numerical models developed in this study

The solid line and dashed line represent experimental results and numerical results, respectively. From Figure 6, the numerical model can capture the force-displacement envelope, including the point where the specimen begins to lose its load-carrying resistance due to shear failure. Table 1 shows the percentage differences in the peak force and displacement corresponding with a 20% strength drop between the numerical and experimental results.

Table 1. Comparison between experimental tests and numerical model results for shear-critical column

	60 mm Transverse Spacing Specimen		**80 mm Transverse Spacing Specimen**	
	Peak Force (kN)	Displ. at 20% Strength Drop (mm)	Peak Force (kN)	Displ. at 20% Strength Drop (mm)
Experimental Test	462	15.1	468	10.1
Numerical Model	469	13.8	450	9.3
% Difference	1.6%	8.6%	3.8%	7.9%

From Table 1, the percentage differences for both specimens between the experimental and numerical results are less than 5% and 10% for the peak force and displacement corresponding with a 20% strength drop, respectively.

Previous studies have investigated the effect of pitting corrosion on the mechanical properties of corroded steel bars (Almusallam, 2001; Du et al., 2005; Apostolopoulos et al., 2006). The effects of corrosion damage on residual capacity and the ductility of corroded bars are adopted in this study as in Du et al. (2005) to account for the effect of pitting corrosion on the constitutive behavior of reinforcement in tension. Kashani et al. (2013) have conducted 3D optical measurements of corroded bars to investigate spatial variability in corrosion patterns and found that corroded bars' geometrical properties can be modeled using a lognormal distribution. This study uses the lognormal distribution's mean values to account for pitting corrosion's impact on corroded bars' geometric properties. In other words, the influence of corrosion is accounted for in terms of the averaged response of the stress-strain behavior and the averaged reduced cross section of steel with uniform mass loss (Kashani et al., 2015; Kashani et al., 2016).

To account for corrosion in the shear-critical column, both the strength limit curve and unloading stiffness are modified in the shear spring element. First, the strength limit curve is constructed following Equation (2) provided in ASCE 41 (2007). The curve is then modified by considering the average reductions in diameter of reinforcement and yield strength as shown in Equations (3) and (4).

$$V_n = k\frac{A_v f_y d_b}{s} + \lambda k\left(\frac{6\sqrt{f_c'}}{\frac{M}{VD}}\sqrt{1+\frac{N_u}{6\sqrt{f_c'}A_g}}\right)0.8A_g \qquad (2)$$

$$d_{b\_cor} = \frac{d_b}{10}\sqrt{100 - \psi} \tag{3}$$

$$f_{y\_cor} = f_y(1 - \beta\psi) \tag{4}$$

V_n is the lateral shear strength of the column and A_v is an area of transverse reinforcement. d_{b_cor} and d_b are the corroded and pristine diameter of either longitudinal or transverse steel bar, respectively, while f_{y_cor} and f_y are corroded and pristine yield strength of steel bar, respectively. s is spacing of transverse reinforcement, N_u is axial compression force, $\frac{M}{VD}$ is the largest ratio of a moment to shear times the effective depth, A_g is the gross cross-sectional area of the column, and f_c' is the compressive strength of concrete. λ and k are adjustment factors for displacement ductility at shear failure and lightweight concrete, respectively, and are taken to be unity in this study. $\psi/100$ is the mass loss ratio, and β is the pitting coefficient that accounts for the influence of corrosion. Substituting Equations (3) and (4) into Equation (2) and rearranging terms results in the modified strength limit as shown in Equation (5)

$$V_{n\_cor} = C_v k\frac{A_v f_y d_b}{s} + \lambda k\left(\frac{6\sqrt{f_c'}}{\frac{M}{VD}}\sqrt{1 + \frac{N_u}{6\sqrt{f_c'}A_g}}\right)0.8A_g \tag{5a}$$

$$C_v = 10(100 - \psi)^{\frac{3}{2}}(1 - \beta\psi) \tag{5b}$$

where C_v is the reduction factor that accounts for the corrosion effect. The strength limit curve is one of the thresholds that trigger shear degradation.

Next, the unloading stiffness is modified due to corrosion. Total displacement (Δ_{total}) of the system consists of contributions from the shear spring (Δ_s) and flexural element (Δ_f). As the shear spring and flexural element are connected in series, the total unloading stiffness (K_{deg}^t) is given in Equation (6) (Elwood, 2004).

$$K_{deg}^{t} = \left(\frac{1}{K_{deg}} + \frac{1}{K_{unload}}\right)^{-1} \quad (6)$$

K_{deg} is unloading stiffness of the shear spring and K_{unload} is unloading stiffness of the flexural element. Corrosion of reinforcement affects the shear spring's unloading stiffness, and therefore, on the total unloading stiffness. The unloading stiffness of the shear spring is a function of the maximum shear strength and the residual deformation (Δ_r) (LeBorgne, 2012), with residual deformation, computed based on the difference in shear deformation from the shear failure point to the point of zero shear force along the backbone as shown in Equation (7a). The residual drift ratio can be determined by clear column span (L) as in Equation (7b).

$$\Delta_r = -\frac{|V_n|}{K_{deg}} \quad (7a)$$

$$\frac{\Delta_r}{L} = -\frac{|V_n|}{K_{deg}L} \quad (7b)$$

The relation between the residual drift ratio and the column's multiple geometric and mechanical parameters is based on a stepwise regression shown in Equation (8).

$$\frac{\Delta_r}{L} = -0.16 - 15.4\rho_t - 0.009\frac{l_d}{d_b} + 0.7\frac{A_{cc}}{A_g} + 0.58\frac{f_y A_s}{f_c' A_g} \geq 0.02 \quad (8)$$

ρ_t is transverse reinforcement ratio, l_d is development length of longitudinal bars, A_{cc} is the gross confined area bounded by transverse reinforcement in the column section, and A_s is the total area of longitudinal reinforcement bars. To account for corrosion, Equations (7) and (8) is modified to

$$\frac{\Delta_{r\_cor}}{L} = -\frac{|V_{n\_cor}|}{K_{deg}^{cor} L} \tag{9}$$

$$\frac{\Delta_{r\_cor}}{L} = -0.16 - 15.4 C_t \rho_t - 0.009 C_b \frac{l_d}{d_b} + 0.7 C_{cc} \frac{A_{cc}}{A_g} \tag{10}$$

$$+ 0.58 C_y \frac{f_y A_s}{f_c' A_g} \geq 0.02$$

where C_t, C_b, C_{cc}, and C_y are reduction factors for transverse reinforcement ratio, development ratio ($\frac{l_d}{d_b}$), confinement ratio ($\frac{A_{cc}}{A_g}$), and longitudinal steel distribution in column section ($\frac{f_y A_s}{f_c' A_g}$), respectively. Each of these corrosion reduction factors can be expressed in terms of mass loss (ψ) and pitting corrosion coefficient (β) as

$$C_t = 1 - \frac{\psi}{100} \tag{11a}$$

$$C_b = \frac{10}{\sqrt{100 - \psi}} \tag{11b}$$

$$C_{cc} = 1 \tag{11c}$$

$$C_y = 1 - \beta \psi \tag{11d}$$

Note that Equation (11c) is a unit under the assumption that corrosion has a minimal effect on the confinement ratio. From Equations (9) and (10), the corroded unloading stiffness of the shear spring (K_{deg}^{cor}) is expressed as shown in Equation (12).

$$K_{deg}^{cor} \tag{12}$$

$$= -\frac{\left| C_v k \frac{A_v f_y d_b}{s} + \lambda k \left(\frac{6\sqrt{f_c'}}{\frac{M}{VD}} \sqrt{1 + \frac{N_u}{6\sqrt{f_c'} A_g}} \right) 0.8 A_g \right|}{\left(-0.16 - 15.4 C_t \rho_t - 0.009 C_b \frac{l_d}{d_b} + 0.7 C_{cc} \frac{A_{cc}}{A_g} + 0.58 C_y \frac{f_y A_s}{f_c' A_g} \right) L}$$

Assuming corrosion has a minimal effect on the unloading stiffness of the flexural element, the updated total unloading stiffness for a shear-critical column ($K_{deg}^{t\_cor}$) is

$$K_{deg}^{t\_cor} = \left(\frac{1}{K_{deg}^{cor}} + \frac{1}{K_{unload}}\right)^{-1} \tag{13}$$

The shear spring is triggered by reaching either the strength limit or plastic hinge rotation capacity. The force-displacement relation, shown in Figure 7, is for the scenario where the strength limit is the governing factor. This scenario represents either a pure shear failure in which shear degradation is triggered before yielding of longitudinal reinforcement takes place, or shear-flexure failure in which the column fails in shear with a certain level of flexural deformation. Corrosion also impacts the column's total unloading stiffness due to the residual drift change in the shear spring backbone curve.

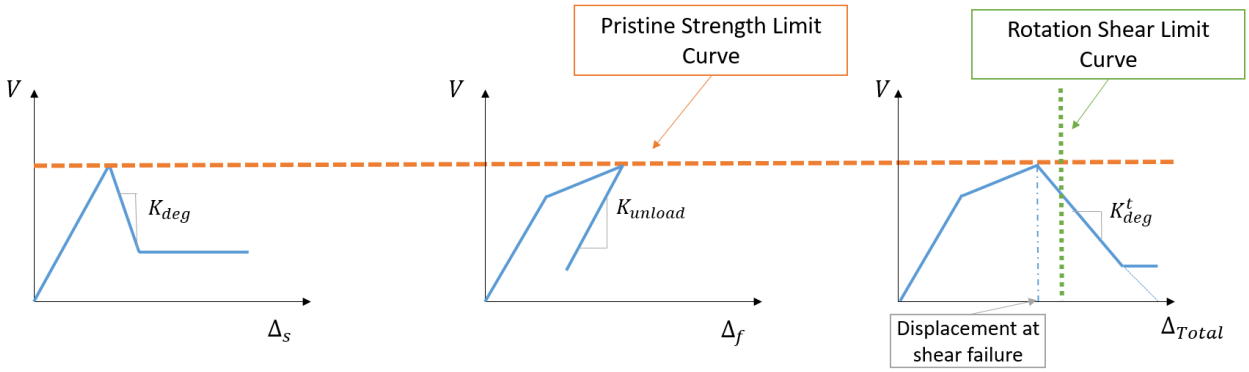

Figure 7. Force-displacement relation and effect of corrosion with shear spring controlled by strength limit curve

Another scenario is when shear degradation is triggered when the plastic hinge region's rotation reaches its limit. Physically, this typically represents shear-flexure failure. This study assumes that corrosion has no impact on the rotational capacity across the plastic

hinge at shear failure. Rotational capacity (θ_f) is computed based on Equation (14) obtained from a stepwise regression as in Leborgne (2012).

$$\theta_f = 0.027 - 0.033\frac{N_u}{A_g f_c^{'}} - 0.01\frac{s}{d} \geq 0.006 \quad (14)$$

s is transverse reinforcement spacing, and d is column depth.

The implementation of corrosion on the risk assessment of a bridge with a shear-critical column is presented in section 1.1.3. This is performed through seismic fragility assessment of a sample bridge consisting of a corroded shear-critical column. Results quantify the impact of corrosion on this failure mode in terms of increasing the probabilities of exceeding defined damage states.

3.2.2 Columns with short lap splice considering corrosion effect

Many aging bridges with lap-sliced columns, including those with pre-1970s designs, include short starter bars and widely spaced transverse reinforcement in the bottom of the column. This study combines findings from several previous studies to model the behavior of lap-spliced columns. The mechanism transferring the tensile stress in the splice relies on the concrete tensile stress capacity. The concrete acts as an intermediate material that transfers forces between two adjacent bars (Priestley et al. 1996). This stress-transferring mechanism causes radially outward pressures on the concrete, leading to splitting cracks along the bars. Cracking the concrete in tension causes softening initiation due to the degrading behavior of lap-spliced reinforcement (Wight and MacGregor, 2009). In addition to inadequate lap-spliced length, light transverse reinforcement in the lap-spliced region reduces the column's ductility once the cover concrete has spalled.

To quantify the lap-spliced constitutive behavior, this work adopts the relations found in Priestley et al. (1996) to obtain the value of maximum stress and residual stress in the splice. Equations (15) and (16) show maximum force and stress developed in the lap-spliced region, respectively.

$$T_b = A_b f_s = F_t p l_{sp} \tag{15}$$

$$f_s = \frac{F_t p l_{sp}}{A_b} \tag{16}$$

T_b and f_s are force and stress developed in the lap-spliced bar, respectively, A_b is the cross-sectional area of the longitudinal bar, F_t is the tensile strength of concrete, l_{sp} is the length of the lap splice, and p is the perimeter of the cylindrical block, which is determined through Equation (17) with an upper limit for widely spaced spliced bars.

$$p = \frac{s}{2} + 2(d_b + c) \leq 2\sqrt{2(c + d_b)} \tag{17}$$

s is the average distance between lap-spliced bars, and c is the length of concrete cover. Once degradation has initiated, residual stress f_r is computed based on Equation (18) as proposed by Wight and MacGregor (2009).

$$f_r = \frac{\mu A_h f_s}{n A_b} \frac{l_{sp}}{S} \tag{18}$$

μ is a frictional factor, which is taken as 1.4, A_h is the cross-sectional area of transverse reinforcement, and n is the number of spliced bars. This study obtains strain at both peak stress and residual stress by Tariverdio et al. (2009), which assumes that displacement corresponding to maximum stress is 1 mm, and displacement corresponding to slip occurrence is 10 mm. Equation (19) shows the calculation of strain at peak stress.

$$\varepsilon_s = \frac{f_s}{E_s} + \frac{\Delta_{BarSlip}}{l_{ss}} \quad (19)$$

E_s is the elastic modulus of steel bar, $\Delta_{BarSlip}$ at peak stress is taken as 1 mm, and l_{ss} is the length in which displacement due to slip occurs. Figure 8(a) shows the material constitutive behavior of lap-spliced bar (Tariverdio et al., 2009).

Figure 8(b) shows the numerical beam-column model used to capture lap-spliced failure in this study. Similar to the model for a shear-critical column, the numerical model consists of two bond-slip elements located at the top and bottom of the column and a middle node to account for the inflection point at the column mid-span. However, unlike the shear-critical model with two beam-column elements, this model consists of an additional beam-column element at the column's bottom. The length of the bottom element is set to be equivalent to the length of the lap splice. Uniaxial fibers used in the bottom element constitute confined and unconfined concrete fibers and steel fibers with the lap-splice stress-strain model shown in Figure 8(a), which can account for degradation triggered by lap-splice failure.

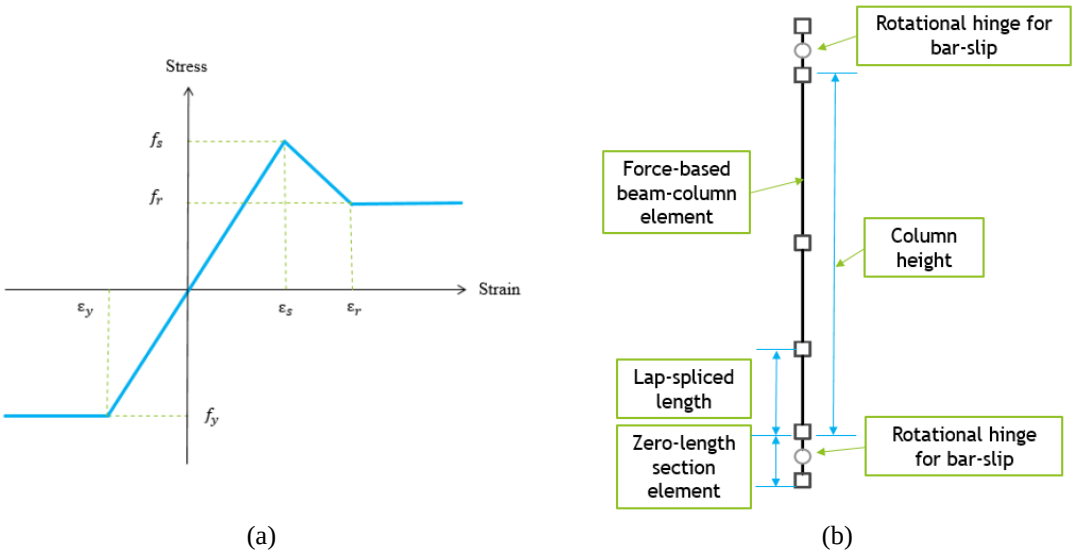

(a) (b)

Figure 8. (a) Constitutive material model of the lap-spliced bar (Tariverdio et al., 2009) and (b) numerical model for lap-spliced column

Results from the model are compared with outcomes from two experimental column tests to verify the numerical model of the lap-spliced column. Experimental data on corroded lap-spliced columns are not available, so results are compared with pristine columns. The first test specimen for comparison is from static cyclic tests conducted by Sun and Priestley (1993). The column has a rectangular cross section with a width of 730 mm and a height of 3.66 m. The lap splice length is 381 mm with longitudinal and transverse reinforcement ratios of 2.55% and 0.184%, respectively. The lap-spliced length is 20 times the diameter of the longitudinal bar. Numerical static cyclic test results (dashed line) compared to experimental results (solid line) from this specimen are shown in Figure 9(a). The numerical model can predict degradation in load-carrying capacity and capture the failure mode of the bond slip of lapped reinforcement.

The second test specimen is from tests conducted by Chail et al. (1991). The column is circular with a diameter of 610 mm and a clear height of 3.66 m. Longitudinal and transverse reinforcement ratios are 2.53% and 0.174%, respectively. The lap-spliced length is 381 mm, which is 20 times the diameter of the longitudinal bar. Numerical compared to experimental static cyclic test results for this specimen are shown in Figure 9(b). Comparing the numerical and experimental results, the numerical model can capture the load-carrying capacity degradation as demand increases.

Table 2 shows the percentage differences between the numerical and experimental results regarding peak force and displacement corresponding with a 20% strength drop. Most of the percentage differences are below 10%, except for the second specimen's displacement quantity with around a 16% difference. This discrepancy could be caused by measurement error during the experimental test or modeling error in terms of accuracy of

the fiber uniaxial behavior and damage parameters accounting for pinching behavior. However, with the other results, the numerical model is able to capture the force-displacement envelope of the lap-splice column with sufficient accuracy.

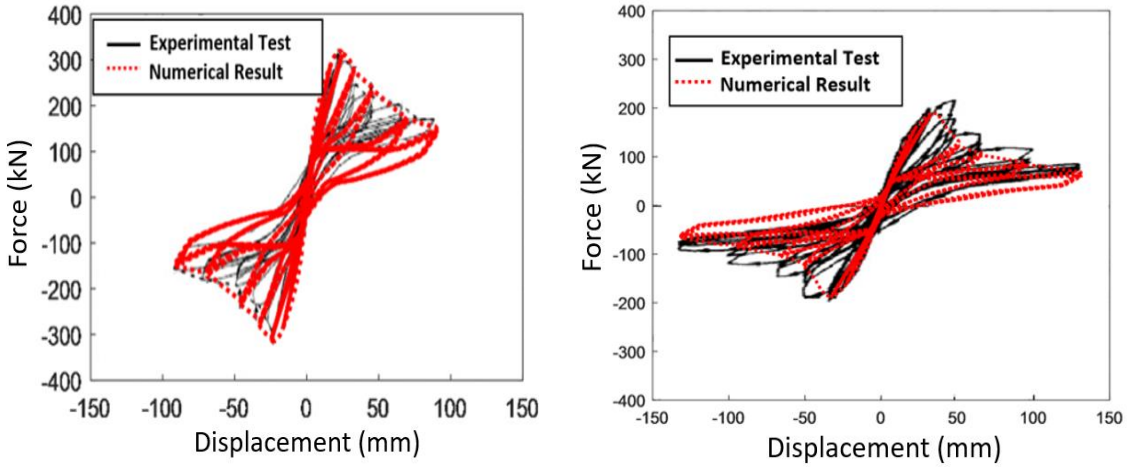

(a) (b)

Figure 9. Static cyclic curves comparing experimental test results from (a) Sun and Priestley (1993) and (b) Chail et al. (1991) with numerical results from this study

Table 2. Comparison between experimental tests and numerical model results for lap-spliced column

	Specimen 1		**Specimen 2**	
	Peak Force (kN)	Displ. at 20% Strength Drop (mm)	Peak Force (kN)	Displ. at 20% Strength Drop (mm)
Experimental Test	300	37.0	218	59.7
Numerical Model	318	39.0	198	50.1
% Difference	6.0%	5.4%	9.2%	16.2%

3.2.3 Seismic fragility assessment

Before integrating the numerical models into a full bridge to perform fragility assessment, there are several steps to select the column type for the analysis, starting with

the column's material and geometric information, influencing the failure mode. Figure 10 shows the flowchart for choosing the column type.

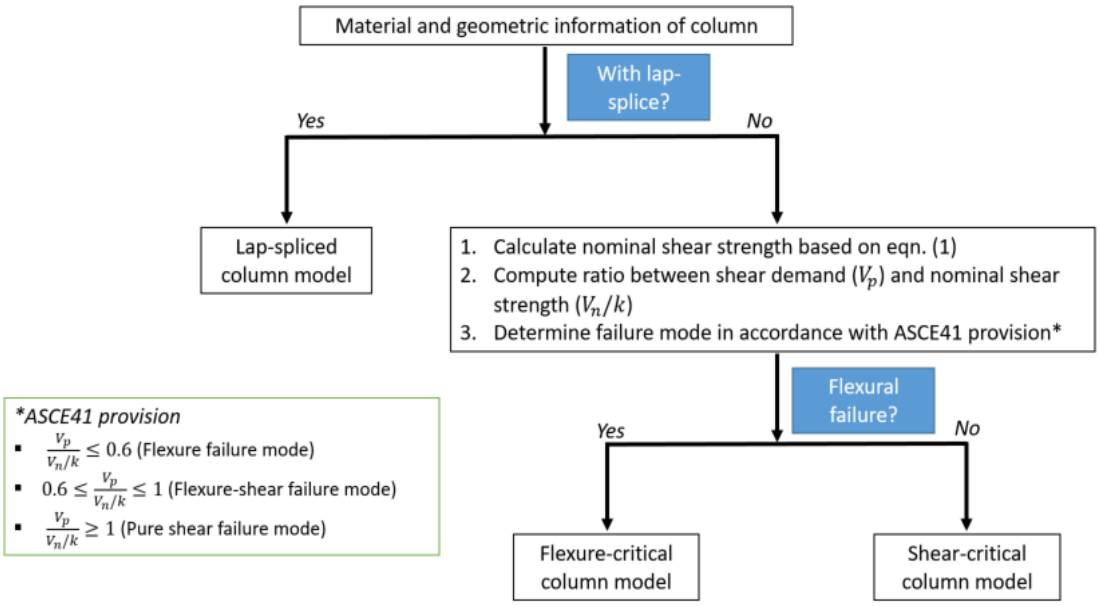

Figure 10. Flowchart for selecting an appropriate numerical model for bridge column

Note that the lap-spliced model presented in this work can predict the structural response of a column with both short lap splice (20-24 times d_b) and long lap splice. In other words, the lap-spliced column model is able to capture both pull-out failure and flexural failure. The shear-critical column model, shown in Figure 10, is able to capture both pure shear and flexure-shear failure modes.

A full bridge is studied to assess the impact of corrosion on fragility. The sample multi-continuous concrete single frame box girder bridge is shown in Figure 11. This bridge type is typically used for longer spans and constitutes, for example, the bulk of the highway bridge inventory in California (Ramanathan, 2012). Table 3 summarizes the geometric parameters' median and dispersion values describing this bridge class built before 1971. These values and the corresponding distributions are used for the generation of fragility

curves in this study. Values used for column diameter are 1.2 m, 1.5 m, and 1.8 m, and transverse spacing is 305 mm on center irrespective of the column size or reinforcement.

Table 3. Median values of geometric parameters used for fragility assessment

Geometric Parameters	Distribution Type	Median	Standard Deviation
Span length (L)	Lognormal	36.6 m	0.27 m
Deck width (Dw)	Lognormal	10.5 m	0.16 m
Column height (H)	Lognormal	6.8 m	0.12 m
Total depth of super-structure (h)	Lognormal	1.46 m	0.27 m
Longitudinal reinforcement ratio	Uniform	1.9 %	0.08 %

A finite-element model of this bridge is built in OpenSees. The column is modeled with fiber sections for the sub-structure, consisting of the appropriate uniaxial constitutive models for concrete and steel. This element type enables us to capture the spread of plasticity along the column. Uncertainty in material parameters includes the compressive strength of concrete and yield strength of Grade 60 reinforcement. The concrete compressive strength is modeled using a normal distribution with a mean of 5000 psi and a standard deviation of 627 psi (Choi, 2002). Yield strength is modeled as lognormally distributed with a median of 4.21 ksi and coefficient of variation 0.08 (Ellingwood and Hwang, 1985). The super-structure is modeled using equivalent elastic beam-column elements under the assumption that elements remain linear elastic during a seismic event. For the foundation system, translational and rotational springs are used to model pile-supported footings, including a pile cap and piles underneath, with foundation springs consisting of zero-length elements at the columns' base. Uncertainty in the bridge system's damping is modeled using a normal distribution with a mean of 0.045 and a standard

deviation of 0.0125 (Nielson, 2005; Padgett, 2007). Further details on the modeling of bridge components can be found in Ramanathan (2012).

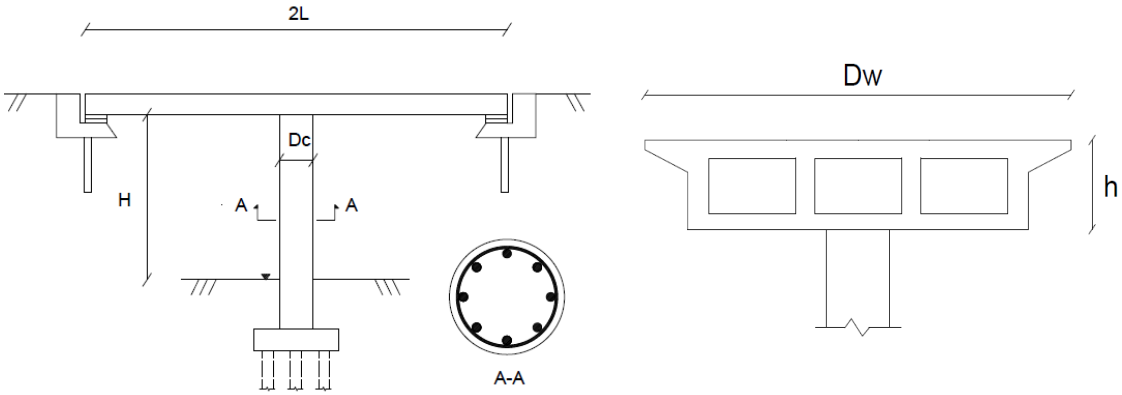

Figure 11. (a) Longitudinal view and (b) transverse view of sample bridge

This study utilizes a suite of ground motions selected from the NGA-2 database (Chiou et al., 2008) for the fragility assessment. The selected ground motion suite consists of 320 ground motions developed to match California's hazard characteristics. The first 160 motions' median response is similar to that of the full 320-motion set; therefore, the first 160 ground motions are included in the analysis. The response spectra of the ground motions in the two horizontal directions are shown in Figure 12.

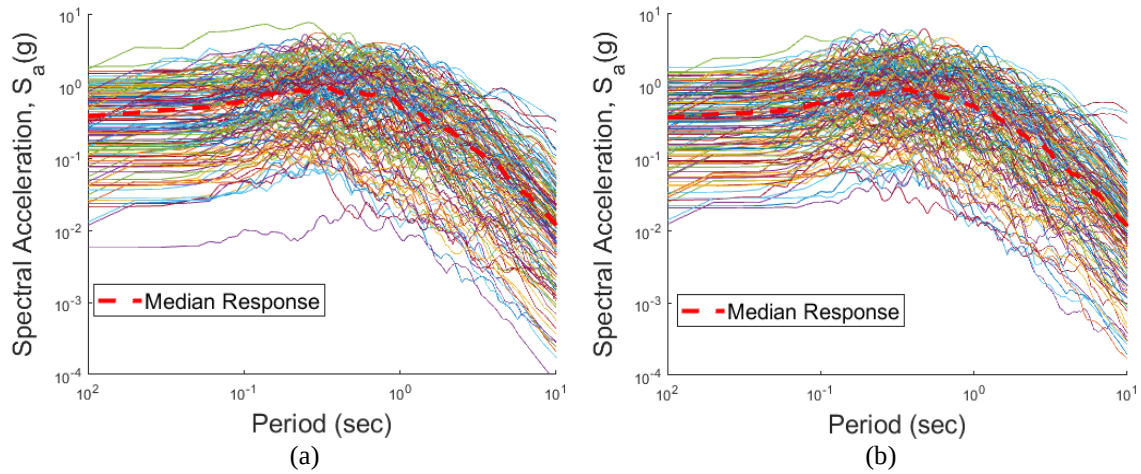

Figure 12. Response spectra for the selected ground motions in (a) horizontal component one and (b) horizontal component two

To assess risk, analytical fragility curves are computed by running a series of nonlinear time history analyses (Shinozuka et al., 2000). This approach is chosen to account for the multiple sources of uncertainty present in the problem, including bridge geometries, material properties, and loading characteristics. In particular, the uncertainties considered in the analysis include the bridge geometry parameters shown in Table 3, as well as uncertainties in the top flange thickness, longitudinal reinforcement ratio, transverse reinforcement ratio, height of the abutment backwall, translational and rotational stiffness of foundation, concrete compressive strength, yield strength of reinforcing steel, the gap between the girder and the shear key, the gap between the deck and the abutment backwall, multiplication factor for deck mass, damping ratio, ground motions, and direction. Several previous studies have adopted this methodology for fragility assessment (Choi et al., 2004; Nielson & DesRoches, 2007a, 2007b; Padgett, 2007; Pan et al., 2010; Ramanathan et al., 2012). However, these studies have not explicitly considered corrosion in shear-critical and lap-spliced columns to quantify this deterioration's effect on predicted bridge performance.

Risk is quantified based on calculated fragilities, where fragility is defined as in Equation (24), interpreted as the probability of exceeding a particular damage state given a specific ground motion intensity.

$$P_f = P[DS|IM = y] \tag{24}$$

P_f is the probability of exceedance, DS is damage state, IM is intensity measure of ground motion, and y is a realization of intensity measure. Equation (24) can also be expressed as a function of parameters of capacity and demand variables assuming both follow lognormal distributions as shown in Equation (25).

$$P_f = \Phi\left(\frac{\ln S_d/S_c}{\sqrt{\xi_d^2 + \xi_c^2}}\right) \quad (25)$$

S_d and S_c are the median parameters for the demand and capacity distributions, respectively, ξ_d and ξ_c are the lognormal standard deviation of the demand and capacity distributions, respectively, and $\Phi(\cdot)$ is the standard normal cumulative distribution function. The engineering demand parameter used for the fragility analysis is the displacement at the bridge column's mid-span.

Damage is discretized into four damage states, as shown in Table 4. A description of each damage state for shear-critical and lap-spliced columns is provided in terms of displacement ductility. As the damage state increases, the column undergoes more damage until it reaches a near collapse state (DS-4). Figure 13 and Figure 14 show fragility curves for the shear-critical and lap-spliced column, respectively. Fragility is a function of ground motion intensity as indicated by peak ground acceleration (PGA). Results provide probabilities of exceeding each damage state for columns with varying corrosion levels measured by percentage mass loss of reinforcement.

Table 4. Description of column damage states

Damage State	*Description*	*Shear-critical*	*Lap-spliced*
DS-1	Slight	Initial cracking	Initial cracking
DS-2	Moderate	Onset of diagonal cracking	Significant cracking
DS-3	Extensive	Significant diagonal cracking	Initial spalling
DS-4	Complete	Shear failure	Complete spalling/lap-splice failure

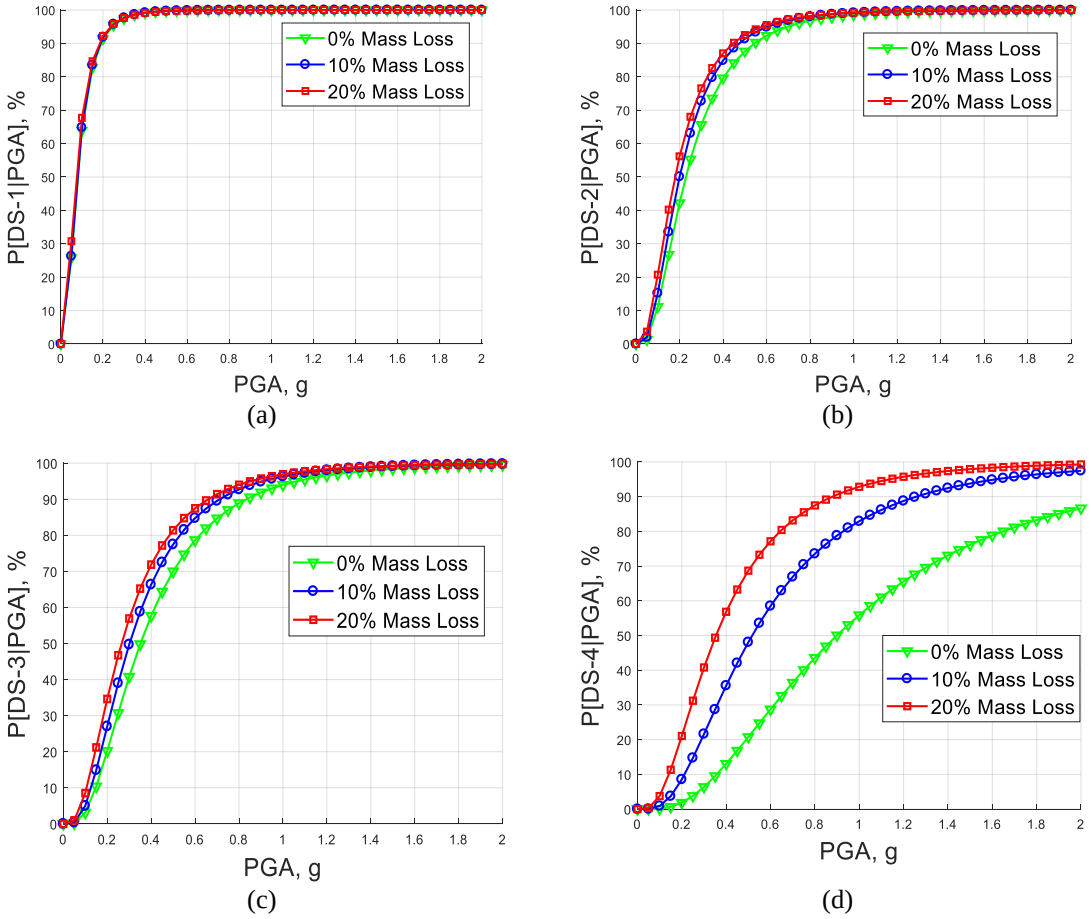

Figure 13. Fragility curves for probabilities of exceeding (a) DS-1, (b) DS-2, (c) DS-3, and (D) DS-4 for the shear-critical column with varying levels of corrosion

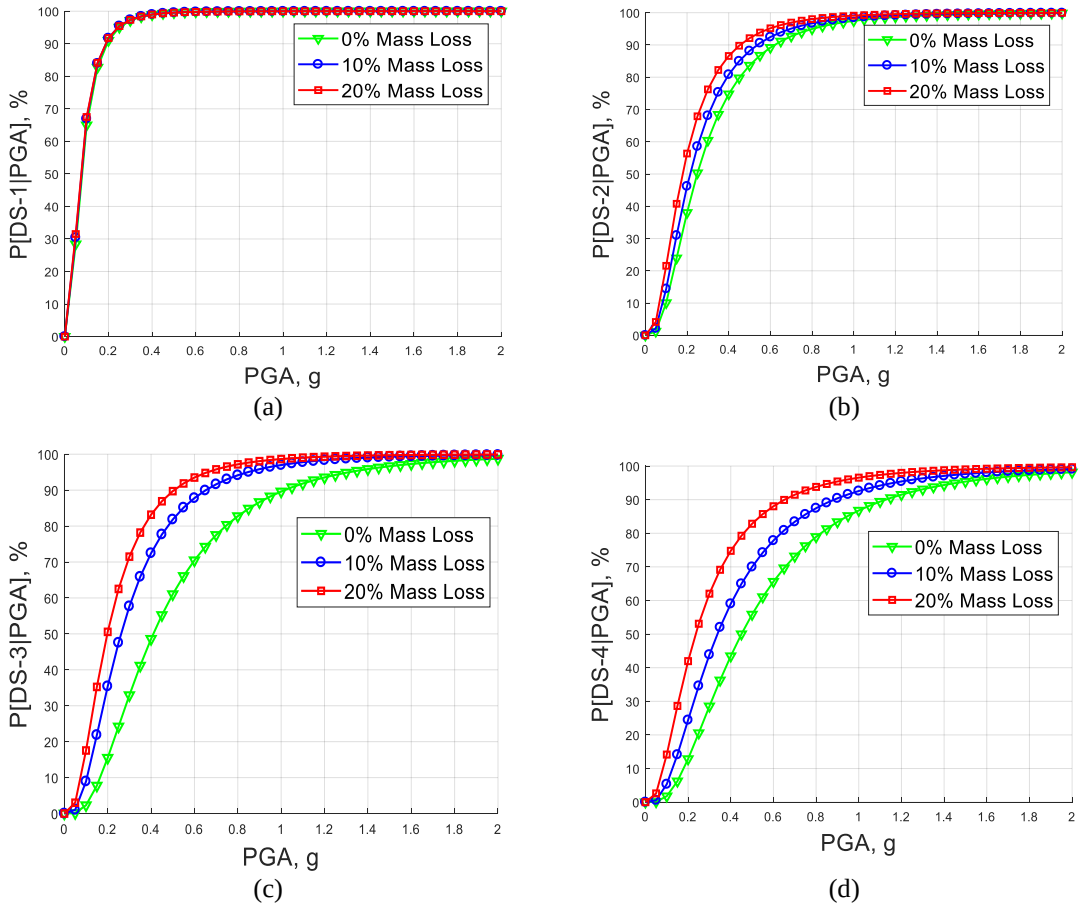

Figure 14. Fragility curves for probabilities of exceeding (a) DS-1, (b) DS-2, (c) DS-3, and (D) DS-4 for the column with short lap splice and varying levels of corrosion

From Figure 13 and Figure 14, corrosion has a minimal effect on both failure modes' initial damage state. As damage accumulates, however, the influence of corrosion increases, with larger increases in the probabilities of exceeding undesired damage states compared to the non-corroded state. This is mainly seen in DS-4 (near collapse state) for shear-critical bridges. To better assess corrosion's influence, Figure 15 shows the difference in probability of exceeding DS-4 for each column type. The comparison is between the pristine state and the 10% mass loss and 20% mass loss corroded cases. This enables quantification of the increase in risk from corroded columns. From Figure 15, 20% mass loss increases the failure probabilities of a shear-critical column and lap-spliced

column by up to 49% and 34%, respectively. This indicates the importance of considering corrosion in assessing structural risk. At higher PGA values, the effect of increasing corrosion is less pronounced. This is because, under high-intensity loadings, structures are more likely to fail regardless of the structure's condition. Instead, there is uncertainty about the structure's performance in the intermediate loading intensities, and corrosion has a more significant effect.

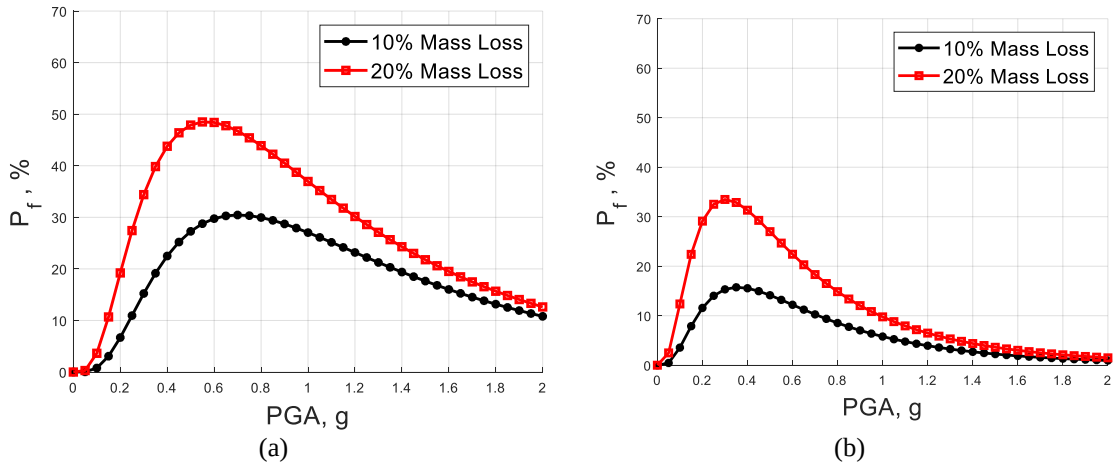

Figure 15. The difference in failure probability for DS-4 between the pristine state and varying corrosion levels for (a) shear-critical column and (b) lap-spliced column

Figure 16 shows the fragility curves for DS-4 for a shear-critical column and lap-spliced column to compare corrosion's effect across failure modes. Besides, the authors have previously investigated the fragility of flexure-critical columns for the same bridge type. These results are also provided in Figure 16 for comparison. The reader is referred to Zhang et al. (2018) for more details on the flexure-critical analysis. Figure 16 shows that lap-spliced columns are the most vulnerable at 10% mass loss, followed by shear-critical then flexure-critical columns. At 20% mass loss, lap-spliced columns remain the most vulnerable among the three. However, the difference between the three modes is less pronounced. At relatively low corrosion levels, the effect of corrosion on the shear-

critical column is more extensive than for flexure-critical because the shear-critical case experiences additional damage due to shear degradation. In comparison, at higher corrosion levels, the effect of further damage due to shear degradation becomes relatively less significant compared with the pure corrosion effect on the geometric and material properties of reinforcement, leading to changes in column performance. Thus, flexure-critical columns' failure probability becomes close to that of shear-critical columns at the higher corrosion level.

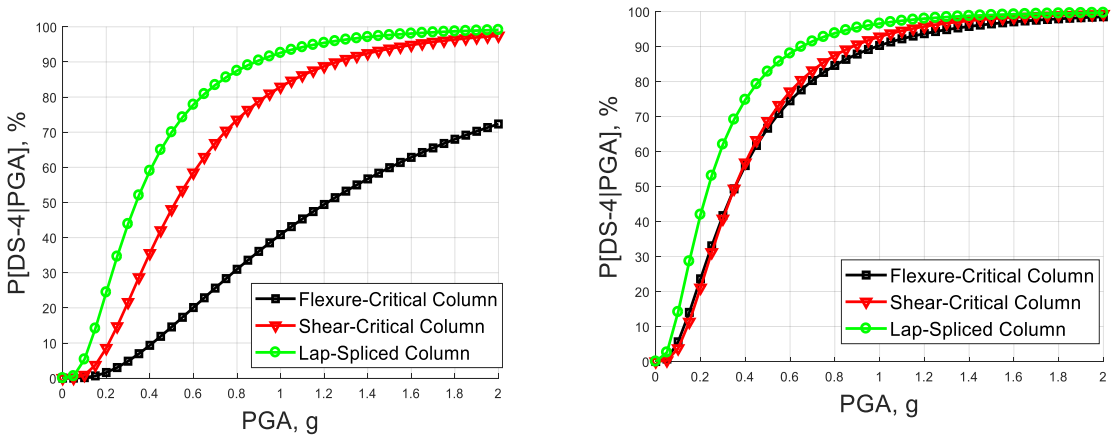

Figure 16. Fragility curves for DS-4 considering different failure modes with corrosion levels of (a) 10% mass loss and (b) 20% mass loss

3.2.4 Conclusions

This study presents a methodology to account for corrosion's effect on low-ductility columns' predicted performance, such as shear-critical columns and columns with short lap splices. Corrosion's effects include reducing the amount of longitudinal and transverse

reinforcement and weakening the bond strength between steel and concrete through corrosion-induced cracking.

For shear-critical columns, corrosion decreases the shear capacity with reduced contribution from the transverse reinforcement. With the reduced shear strength limit, the column undergoes early shear degradation, eventually leading to brittle shear failure. For columns with short lap splice, corrosion causes volumetric expansion of reinforcement, generating tensile stress on the surrounding concrete. Consequently, cracking of concrete cover leads to bond deterioration and loss of the force transferring mechanism between the concrete and reinforcement in the lapped region. This reduces the column load-carrying capacity, leading to pull-out failure.

With these effects accounted for, corrosion's impact on bridges' predicted performance with shear-critical and short lap-spliced columns is analyzed. This is done through conducting analytical fragility assessments. Results quantify the increases in probabilities of the bridge exceeding given damage states with increasing levels of corrosion. The results show corrosion having a larger effect for more severe damage states and at intermediate loading intensities. Twenty percent mass loss of column reinforcement increases the probability of exceeding the complete damage state by up to 49% and 34% for a shear-critical and lap-spliced column, respectively. Moreover, columns with short lap splice are more vulnerable to collapse under the same corrosion attack level than shear-critical columns.

3.3 Subtopic No. 2

3.3.1 Introduction to Bayesian updating and fragility function

In this subtopic, a novel method based on Bayesian updating is proposed to generate analytical fragility curves efficiently. The proposed process takes advantage of updating rules in conjugate Bayesian inference to estimate fragility curves combined with observational data. Equation (26) computes the posterior distribution of parameters $\boldsymbol{\theta}$ given new information ($\boldsymbol{X}$) obtained from collected experimental or numerical data (Ang and Tang, 1975).

$$f''(\boldsymbol{\theta}|\boldsymbol{X}) = kL(\boldsymbol{X}|\boldsymbol{\theta})f'(\boldsymbol{\theta}) \tag{26}$$

k is a normalizing factor, $L(\boldsymbol{X}|\boldsymbol{\theta})$ the likelihood function, $f'(\boldsymbol{\theta})$ the prior distribution of parameter vector $\boldsymbol{\theta}$, and $f''(\boldsymbol{\theta}|\boldsymbol{X})$ the posterior distribution of parameter vector $\boldsymbol{\theta}$ given new information.

In the proposed method, updating rules from conjugate Bayesian inference efficiently and accurately estimate fragility curves based on observational data with an analytically tractable posterior distribution. This is done by directly updating the fragility parameters with limited observational data rather than conducting the full set of analyses as typically required. The method is applied to assess the fragility of bridge structures in particular. With the idea of facilitating efficient and accurate fragility curve updating based on structural inspection data, the proposed method is applied to update the fragility of a bridge column under varying levels of measured corrosion. Corrosion is a common inspection parameter of interest, particularly for reinforced concrete bridges (Jacinto, 2011). The idea is to be able to generate and update analytical fragility curves based on new inspection information without needing to re-run the full set of analyses. The proposed

method is evaluated both in terms of computational efficiency and accuracy of the resulting calculated fragilities. The current work puts emphasis on utilizing inspection data obtained from the field (e.g., mass loss due to corrosion) and simplified numerical data from a reduced finite-element model (e.g., displacement ductility from column response analyses) to efficiently and accurately update the fragility assessment. Results show two main advancements of the proposed method: 1) reduction in the number of structural analyses required to obtain stable fragility results, and 2) the ability to use reduced component-level analyses to update estimates of full structural performance.

In Equation (1), the fragility is expressed explicitly as the probability of exceeding some damage state (DS) for a specific intensity measure (IM). The fragility function can also be defined as the probability of the demand, in this case, seismic demand (S_d), exceeding the structural capacity (S_c) at a given intensity measure as shown in Equation (27).

$$Fragility = Pr[S_d \geq S_c|IM] = \Pr\left[\frac{S_d}{S_c} \geq 1\middle|IM\right] \tag{27}$$

When both the demand and capacity distributions follow lognormal distributions, the fragility function has a closed-form solution. In this study, a classical lognormal fragility function is adopted due to its simple parametric form (Shinozuka et al., 2000; Ellingwood, 2001; Nielson, 2005; Ghosh and Jamie, 2010; Li et al., 2013). While simulation-based approaches exist to assess seismic fragilities, the focus here is on generating analytical fragility curves. The probability of structural failure P_f indicating the probability of the demand exceeding the capacity for a structural component is represented using parameters of the lognormal distributions of structural demand and capacity as shown in Equation (28a). The reader is referred to Hwang et al. (2001) and Melchers (2001) for

more details on this solution's derivation. Alternatively, the fragility function can be expressed for the ground motion intensity (e.g., peak ground acceleration or spectral acceleration) shown in Equation (28b) (Koutsourelakis 2010).

$$P_f = \Phi\left(\frac{\ln(\frac{S_d}{S_c})}{\sqrt{\xi_d^2 + \xi_c^2}}\right) \tag{28a}$$

$$P_f = F(IM;\ \lambda, \xi) = \frac{1}{2} + \frac{1}{2}\text{erf}[\frac{\ln(IM) - \lambda}{\xi\sqrt{2}}] \tag{28b}$$

$\Phi(\cdot)$ is the cumulative distribution function of the standard normal distribution; S_d and S_c are the median parameters of the demand and capacity distributions, respectively; and ξ_d and ξ_c are the lognormal standard deviation parameters of the demand and capacity distributions, respectively. erfis an error function, ξ is dispersion which is equal to $\sqrt{\xi_d^2 + \xi_c^2}$, and λ is the natural logarithm of the median ground motion intensity corresponding to unity of $\frac{S_d}{S_c}$. In the context of estimating the median demand from the probabilistic seismic demand models (PSDMs) using linear regression, Equation (29) shows the estimate of the median of the demand distribution of the m^{th} structural component by a power model (Cornell et al., 2002).

$$S_{D,m} = a_m IM^{b_m} \tag{29a}$$

$$\ln(S_{D,m}) = \ln(a_m) + b_m \ln(IM) \tag{29b}$$

$\ln(a_m)$ and b_m are the coefficients of the linear regression for the m^{th} component. Together with Equation (29), the fragility function, shown in Equation (28), can be expressed as presented in Equation (30) (Nielson, 2005).

$$P_f = \Phi\left(\frac{ln(IM) - \lambda_m}{\xi_m}\right) \tag{30a}$$

$$\lambda_m = \frac{\ln(S_{c,m}) - \ln(a_m)}{b_m} \tag{30b}$$

$$\xi_m = \frac{\sqrt{\xi_d^2 + \xi_c^2}}{b_m} \tag{30c}$$

λ_m is the lognormal mean for the m^{th} component and ξ_m its dispersion value.

3.3.2 Derivation of updating rules using conjugate Bayesian inference

To obtain an updated analytical fragility curve, the general idea is to update the original curve with new information through Bayesian inference, as shown in Equation (26). Within a Bayesian framework, both the original data and parameters that describe the distribution of the original data are treated as random variables. The original fragility data follows a lognormal distribution defined by its mean (λ'_m) and variance (ξ'^2_m). It is assumed that the mean (λ'_m) of the original fragility function is unknown, while the variance (ξ'^2_m) is known. This assumption holds within the study context where the original fragility function is known, and the objective is to update the estimated fragilities based on new information efficiently.

The following is the derivation of the updating rules. Let $\boldsymbol{Y}$ represent the original lognormal fragility data. y_j represent independent sample points $1 \dots n$ from the original fragility curve as shown in Equation (31).

$$y_j \sim LN(\lambda'_m, \xi'^2_m), \quad j = 1 \dots n \tag{31a}$$

$$\ln(y_j) \sim N(\lambda'_m, \xi'^2_m), \quad j = 1 \dots n \tag{31b}$$

From Equation (26), the unknown parameter ($\boldsymbol{\theta}$) is chosen to be the unknown mean of the lognormal distribution (λ'_m). This is assumed to follow a normal distribution (Li et

al., 2013). Note that other distributions may also be appropriate, but the performance of various prior distributions is out of the scope of this study. The mean and standard deviation of the distribution are determined from the normal prior distribution of λ'_m under a specified order of ground intensity measures. This process is discussed in more detail in the following section. Equation (32) shows the normal prior distribution of the mean (λ'_m).

$$\lambda'_m \sim N(\mu',\ \sigma'^{\,2}) \tag{32}$$

μ' is the mean of the normal distribution of the parameter (λ'_m) and $\sigma'^{\,2}$ its variance. From Equation (26), one can show that the posterior distribution of the unknown parameter given observational data is proportional to the product of the likelihood and prior distribution, as shown in Equation (33).

$$f\left(\lambda'_m \middle| \ln(\breve{y})\right) \propto L(\ln(\breve{y})|\lambda'_m) f(\lambda'_m) \tag{33}$$

$f\left(\lambda'_m \middle| \ln(\breve{y})\right)$ is the posterior distribution for λ'_m conditioned on observational data, $f(\lambda'_m)$ is the prior distribution of λ'_m which is assumed to be normally distributed, and $L(\ln(\breve{y})|\lambda'_m)$ is the likelihood function conditioned on n observational data points, which can be represented by the product of probability density functions (PDFs) of the lognormal distribution evaluated at each new observational data point. $\ln(\breve{y})$ is new information (i.e., displacement ductility of the column). Observational data (i.e., an observed mean of displacement ductility) can then be computed by combining the new information, $\ln(\breve{y})$, and the regression analysis is shown in Equation (29) and Equation (30). Substituting the expression for the lognormal PDF into Equation (33) results in Equation (34).

$$f\left(\lambda'_m \middle| \ln(\breve{y})\right) \propto \exp\left(-\frac{1}{2}\frac{\sum_{i=1}^{n}(\ln(\breve{y}_i) - \lambda'_m)^2}{\xi'^{\,2}_m}\right) \exp\left(-\frac{1}{2}\frac{(\lambda'_m - \mu')^2}{\sigma'^{\,2}}\right) \tag{34}$$

Next, by introducing a new variable n_o, one can substitute $\xi_m'^2$ in Equation (34) with the expression in Equation (35) to obtain the result in Equation (36).

$$\sigma'^2 = \frac{\xi_m'^2}{n_o} \tag{35}$$

$$f\left(\lambda_m' \middle| \ln(\breve{y})\right) \propto \exp\left(-\frac{1}{2}\frac{\sum_{i=1}^{n}(\ln(\breve{y}_i) - \lambda_m')^2}{\xi_m'^2}\right)\exp\left(-\frac{1}{2}\frac{(\lambda_m' - \mu')^2}{\frac{\xi_m'^2}{n_o}}\right) \tag{36}$$

n_o represents the effective number of observations in the prior distribution (Lunn et al., 2012). Intuitively, n_o captures information about the standard deviation of the prior distribution, as the magnitude of n_o is inversely proportional to the prior standard deviation. The expression on the right-hand side of Equation (36) can be further simplified to Equation (37) by expanding terms and ignoring terms that do not depend on $\ln(\lambda_m')$.

$$f\left(\lambda_m' \middle| \ln(\breve{y})\right) \propto \exp\left(-\frac{1}{\frac{2\xi_m'^2}{n+n_o}}\left(\lambda_m' - \frac{n\overline{\ln(\breve{y})} + n_o\mu'}{n+n_o}\right)^2\right) \tag{37}$$

$\overline{\ln(\breve{y})}$ is the mean value of $\ln(\breve{y}_i)$. The resulting updating rules for the posterior distribution parameters are as shown in Equation (38).

$$\mu'' = \frac{n\overline{\ln(\breve{y})} + n_o\mu'}{n+n_o} \tag{38a}$$

$$\sigma''^2 = \frac{\xi_m'^2}{n + n_o} \tag{38b}$$

μ'' and σ''^2 represent the mean and variance of the posterior distribution, respectively. Finally, the posterior-predictive distribution data ($\widehat{\boldsymbol{Y}}$) can be computed based on Equation (39), assuming future data ($\widehat{\boldsymbol{Y}}$) is conditionally independent given λ_m'.

$$f(\ln(\hat{y}) \mid \ln(\breve{y})) = \int f(\ln(\hat{y}), \lambda_m' \mid \ln(\breve{y}))d\lambda_m' \tag{39a}$$

$$f(\ln(\hat{y}) \mid \ln(\breve{y})) = \int f(\ln(\hat{y}) \mid \lambda'_m) \times f(\lambda'_m \mid \ln(\breve{y}))d\lambda'_m \tag{39b}$$

With the recognition of the first and second terms on the right-hand side of Equation (39b) to be the likelihood estimator and posterior distribution, respectively, further simplification of Equation (39) leads to to the sum of the two independent normal distributions as shown in Equation (40) and parameters of the predictive-posterior distribution in Equation (41).

$$f(\ln(\hat{y}) \mid \ln(\breve{y})) = \mathrm{N}(\mu'', \xi_m'^2 + \sigma''^2) \tag{40}$$

$$\lambda''_m = \mu'' \tag{41a}$$

$$\xi_m''^2 = \xi_m'^2 + \sigma''^2 \tag{41b}$$

In Equation (41), λ''_m and $\xi_m''^2$ represent the mean and variance of the posterior-predictive distribution, respectively. In other words, these also refer to the mean and variance of the updated fragility function for the m^{th} component.

3.3.3 Determination of parameters of the prior distribution and observational data for Bayesian updating

Determining the parameters of the distribution of λ'_m requires a series of λ'_m sample points based on the loading intensity measure's specified orders, e.g., peak ground acceleration (PGA) for ground motion intensity in the assessment of seismic fragility. In the context of the probabilistic seismic demand model (PSDM), each new λ'_m is generated according to Equation (28a) and Equation (28b) by adding one numerical data point of displacement ductility at a time for the linear regression analysis. In general, for PSDM, the ground motion intensity measures are generated randomly. This renders results with high randomness and influences the accuracy of the results. For example, if PGA values

are ordered by increasing PGA, it overestimates the fragility; if data points are ordered by decreasing PGA, it underestimates the fragility. Therefore, in this study, the ground intensity measures are ordered such that the numerical data points start at the mean PGA value and oscillate around the mean with increasing deviation from the mean. This decreases the randomness in the outcome and results in a more robust method. While not all prior studies of fragility functions use ordered ground motions, for consistency in comparison in the results in this study, the ordered ground motion approach is used in both the proposed and existing methods. Figure 17 shows the PGA values for a set of 160 ground motions sequenced, such that it follows the order as mentioned above.

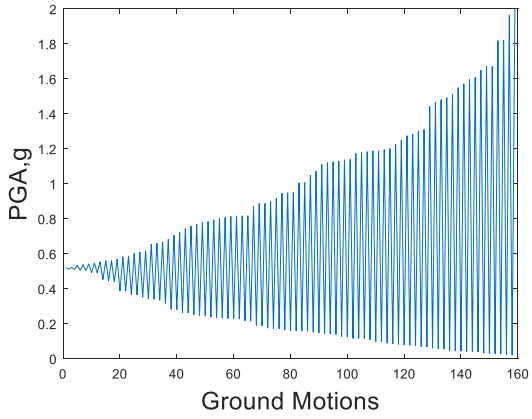

Figure 17. A sequence of PGA values

The method of obtaining the series of λ'_m points for both the prior distribution and the observational data for Bayesian updating are the same. Once the prior distribution of λ'_m is specified, the mean and standard deviation of the prior distribution can be determined. Similarly, once assembly of the observational data is generated from the new information $\ln(\check{y})$, the updating rules as derived in the previous section can be applied to obtain the posterior distribution of λ'_m.

The final step is to calculate the total sample variance (σ_t) of the predictive mean (λ_m'') of the fragility function by combining the posterior-predictive variance and the standard deviation of the mean of observational data used for Bayesian updating by the square root of the sum of the squares (SRSS). The upper and lower bounds of the predictive mean (λ_m'') are then computed accordingly. Rather than rendering a single value, the lower bound and upper bound of the posterior-predictive mean provide a range of possible values and corresponding confidence in the results. The bounds can be interpreted as capturing the epistemic uncertainty, with the confidence bounds becoming narrower as the number of observational data points increases.

The overall method proceeds as follows: The first step is to obtain the original lognormal distribution with mean and variance λ_m' and $\xi_m'^2$, respectively. The mean of the original lognormal distribution is assumed to follow a normal distribution with the mean and standard deviation of λ_m' computed based on the prior distribution as described in the previous section. Once the prior distribution is found, the updating rules (Equations 38a and 38b) for normal conjugate pairs are applied to compute the posterior parameters. The posterior-predictive distribution parameters are then calculated by summing the two independent normal distributions as shown from Equation (39) to Equation (41). The final confidence bounds on the result are then computed by SRSS. The flowchart, shown in Figure 18, summarizes the procedures to obtain the updated fragility function's final parameters.

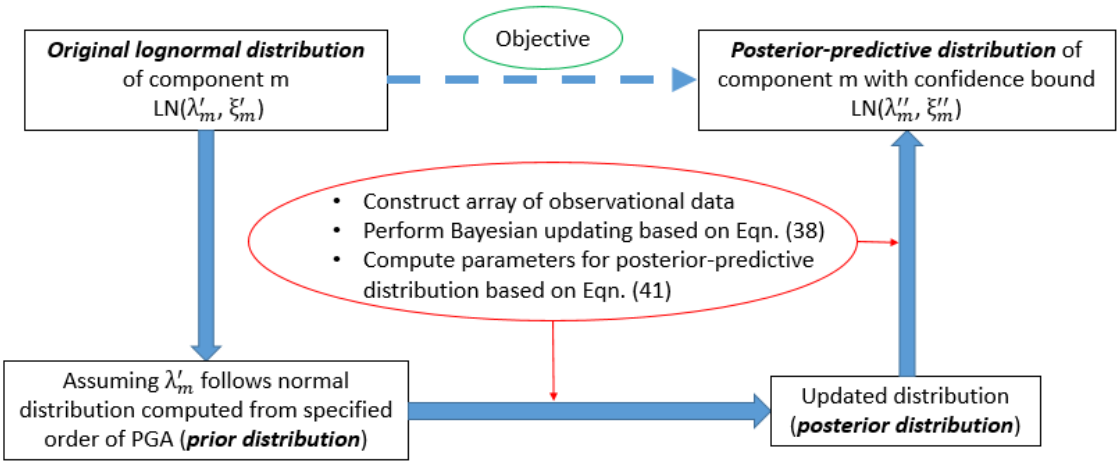

Figure 18. Flowchart of the procedures to obtain the final parameters of the updated fragility function

3.3.4 Corrosion effect and bridge description

To demonstrate and evaluate the proposed method to efficiently update fragility curves, the proposed framework has been applied to a sample bridge structure where the objective is to update the component fragility of the bridge column given observational data considering corrosion's effect.

Multiple studies have shown the significant influence on steel's mechanical properties due to the effect of pitting corrosion (Almusallam, 2001; Du et al., 2005; Apostolopoulos et al., 2006). Du et al. (2005) have investigated the effects of pitting corrosion on steel bars' ductility and residual capacity. Kashani et al. (2013) use 3D optical measurements of corroded bars to evaluate corrosion patterns' spatial variability. They have shown that the geometrical properties of corroded bars can be treated as a lognormal distribution. Meanwhile, several studies (Kashani et al., 2015; Kashani et al., 2016; Zhang et al., 2019) have adopted the findings mentioned above to account for the influence of pitting corrosion

on the geometric properties of corroded steel bars with the mean values of a lognormal distribution. The corrosion effect on reinforcement in reinforced concrete bridge structures is represented by applying the average reductions in diameter of the reinforcement and yield strength shown in Equations (42) and (43), respectively.

$$d_{b\_cor} = \frac{d_b}{10}\sqrt{100 - \psi} \tag{42}$$

$$f_{y\_cor} = f_y(1 - \beta\psi) \tag{43}$$

d_{b_cor} and d_b are the corroded and pristine diameter of longitudinal bars, respectively; f_{y_cor} and f_y are corroded and pristine yield strength of steel bar, respectively. $\psi/100$ is mass loss ratio measuring the level of corrosion; and β is pitting coefficient. Meanwhile, corrosion on concrete cracking is modeled based on modified compression field theory (Vecchio and Collins, 1986) shown in Equation (44),

$$f_{cr} = \frac{f_c}{1 + K\frac{\varepsilon_1}{\varepsilon_{co}}} \tag{44}$$

f_{cr} and f_c are reduced concrete strength due to cracking and pristine compressive concrete strength, respectively; K is coefficient related to bar roughness and diameter with the value of 0.1 (Cape, 1999); and $\varepsilon_{co}$and ε_1 are the strain of the peak concrete compressive strength and smeared tensile strain in the cracked concrete with right angles to the compression direction. There is a reduction of strength and stiffness of the concrete constitutive behavior in compression due to transverse tensile strain. This theory has been applied to corroded reinforced concrete beams to capture the effect of cracked concrete cover (Coronelli and Gambarova, 2004). Besides, a theoretical relation between mass loss of longitudinal reinforcement and crack width has been adopted in this study, derivation details of which can be found in Molina et al. (1993) and Shang et al. (2011).

The sample bridge is a typical multi-continuous concrete box girder bridge (Ramanathan, 2012), with longitudinal and transverse views shown in Figure 11. In addition to ground motion uncertainties, this study has accounted for the uncertainties in the selected bridge's geometric and material properties (Ramanathan, 2012; Zhang et al., 2019). Table 5 summarizes the geometric parameters' median and dispersion values with lognormal distributions as indicated in Figure 11 based on an extensive review of bridge plans. Table 6 summarizes the distributions of key mechanical and material properties of the bridges. The sample bridge consists of two spans and a single-column bent with an integral type connection. The bridge employs a circular column supported on a pile cap with a group of piles underneath it. The column consists of #11 longitudinal rebars and #4 stirrups with 75mm spacing on center. The bridge girders are cast-in-place prestressed concrete boxes with 0.04 for depth-to-span ratios, and the bridge deck is seated on the elastomeric bearing pad at the abutments, which consist of a 1.8m tall backwall and Class 70 piles with a spacing of 2m on center.

The bridge's 3-D numerical model is built in the finite-element software OpenSees (McKenna, 1997). The models are developed by sampling across the parameters listed in Table 1 through Latin Hypercube Sampling (LHS) (McKay et al., 1979). For the sub-structure, the column is modeled using a single force-based element with fiber discretization. The foundation consists of calibrated rotational and translational springs. For the superstructure, the bridge deck is modeled using equivalent elastic beam-column elements under the assumption that the bridge deck remains linearly elastic during seismic events. For the highway bridges' fragility assessment, the study mainly focuses on the damage that occurred in the bridge column with displacement ductility as the engineering

demand parameter. The damage states used to quantify the damage levels are shown in Table 7 with flexural dominant failure mode. A suite of ground motions is selected from the NGA-2 database (Chiou et al., 2008), consisting of 160 motions matching California's hazard characteristics for which this bridge type is common. The ground motions' response spectra in the two horizontal directions are shown in Figure 12 in the previous section.

Table 5. Median and dispersion values of geometric parameters of the sample bridges

Geometric Parameters	Distribution Type	Median	Standard Deviation
L	Lognormal	36.6 m	0.27 m
Dw	Lognormal	10.5 m	0.16 m
H	Lognormal	6.8 m	0.12 m
h	Lognormal	1.46 m	0.27 m

Table 6. Details of the distribution of mechanical/material parameters of the sample bridges

Mechanical Parameters	Distribution Type	Distribution Parameter 1	Distribution Parameter 2
Concrete compressive strength (MPa)	Normal	34.5 (mean)	4.3 (standard deviation)
Yield strength of steel (MPa)	Lognormal	29.0 (median)	2.3 (logarithm standard deviation)
Shear modulus of the elastomeric bearing pad (MPa)	Uniform	551.6 (lower bound)	1723.7 (upper bound)
Coefficient of friction of the elastomeric bearing pad	Lognormal	0.0 (median)	0.10 (logarithm standard deviation)
Longitudinal reinforced ratio of column (%)	Uniform	1.0 (lower bound)	3.5 (upper bound)
Transverse reinforced ratio of column (%)	Uniform	0.4 (lower bound)	1.7 (upper bound)

Table 7. Description of damage states

Flexure-Critical Column	*Description*	*Damage Level*
DS-1	Significant Cracking	Slight
DS-2	Initial Spalling	Moderate
DS-3	Core Exposure	Extensive
DS-4	20% Strength Degradation	Complete

As the goal of this work is to update the original fragility curve with new observational or inspection data to obtain the new fragility function with reduced computational cost, it is assumed that from prior analyses, the original fragility function is known. The original fragility curve need not be obtained from running nonlinear time history analyses on a full structural finite-element model, but can also be from the literature, expertise, or empirical data. The updating is done by taking limited observational data to calculate fragilities using the derived Bayesian updating rules, rather than having to run the full set of nonlinear time history analyses with a sufficient number of ground motions to obtain stable fragility function parameters.

In this case, new data is taken as observations of the response under corrosion conditions in the column. Therefore, the original fragility function refers to the fragility curve with a pristine bridge column, and the updated fragility function provides the fragility with a corroded bridge column. To assess the differences in accuracy and computation time between using different types of data and analyses to perform the updating, the following section presents results from using two types of observational data to update the fragility function. The first type of data refers to the displacement ductility of the bridge column under seismic loadings from analyzing the full bridge response, i.e., using the full structural finite-element model; the second type of data refers to the displacement ductility of the bridge column under seismic loadings considering the single column only. The resulting

performance of the proposed approach in terms of accuracy and computational cost are compared with existing methods for both types of observational information.

3.3.5 Bayesian updating of fragility curves considering bridge response

The results in this section use observational data computed from the bridge column's displacement ductility based on nonlinear time history analyses considering the entire bridge's response. As is typical for fragility assessments, the full structural finite-element model is required. However, the number of dynamic analyses required using the proposed compared to existing method to obtain stable fragility results differs. To show the impact of corrosion on structural performance, Figure 19(a) shows the prior and posterior distributions of the unknown parameter λ'_m with 25 observational data points. Figure 19(b) shows the original and updated fragility curves for the collapse damage state using these 25 observational data points. The original fragility curve represents fragility for the pristine bridge column; the updated fragility curve represents fragility with a corroded column with a 20% mass loss of reinforcement. Mass loss of reinforcement is used as a measure of corrosion as a readily obtainable structural inspection parameter (Jacinto, 2011).

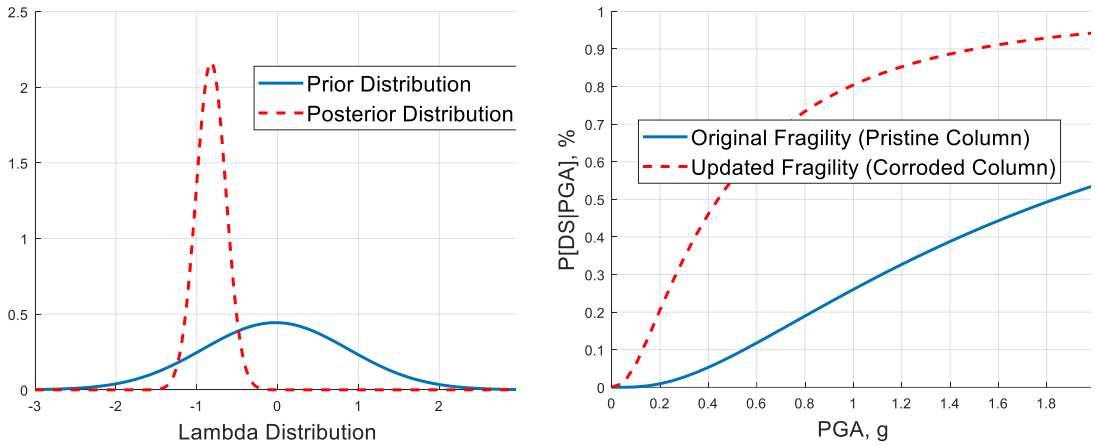

Figure 19. (a) Prior distribution compared to posterior distribution for λ'_m and (b) original fragility curve (pristine column) for collapse damage state compared to updated fragility curve (corrosion with 20% mass loss of reinforcement) using 25 observational data points

To assess the accuracy of the proposed approach, Figures 20 and 21 show the fragility results across the four damage states from using the proposed approach compared with the exact result. The exact result is taken as the fragility function generated by running nonlinear time history analyses over the full set of 160 ground motions. The updated fragility curves for each damage state are shown, including 95% confidence bounds from the proposed approach computed using 25 and 50 observational data points, compared to the exact fragility curve.

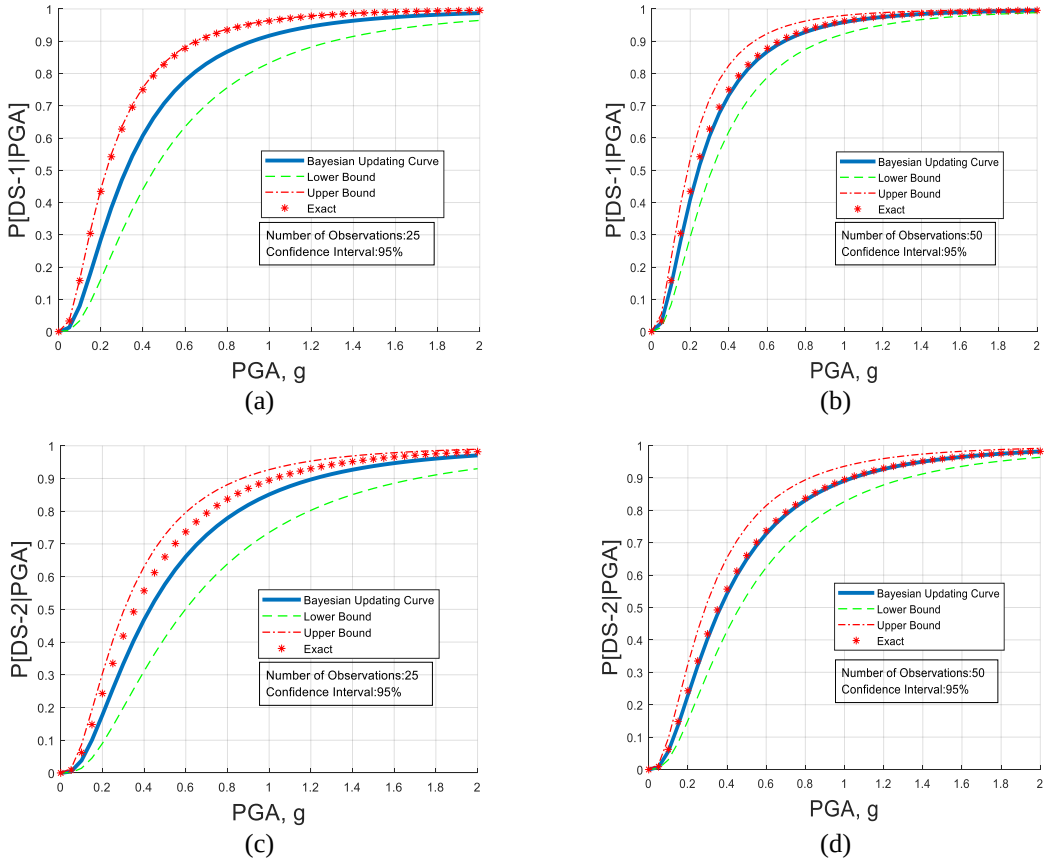

Figure 20. Bayesian updated fragility curve compared to exact fragility curve considering 25 observational data points (left) and 50 observational data points (right) for (a) & (b) DS-1 and (c) & (d) DS-2

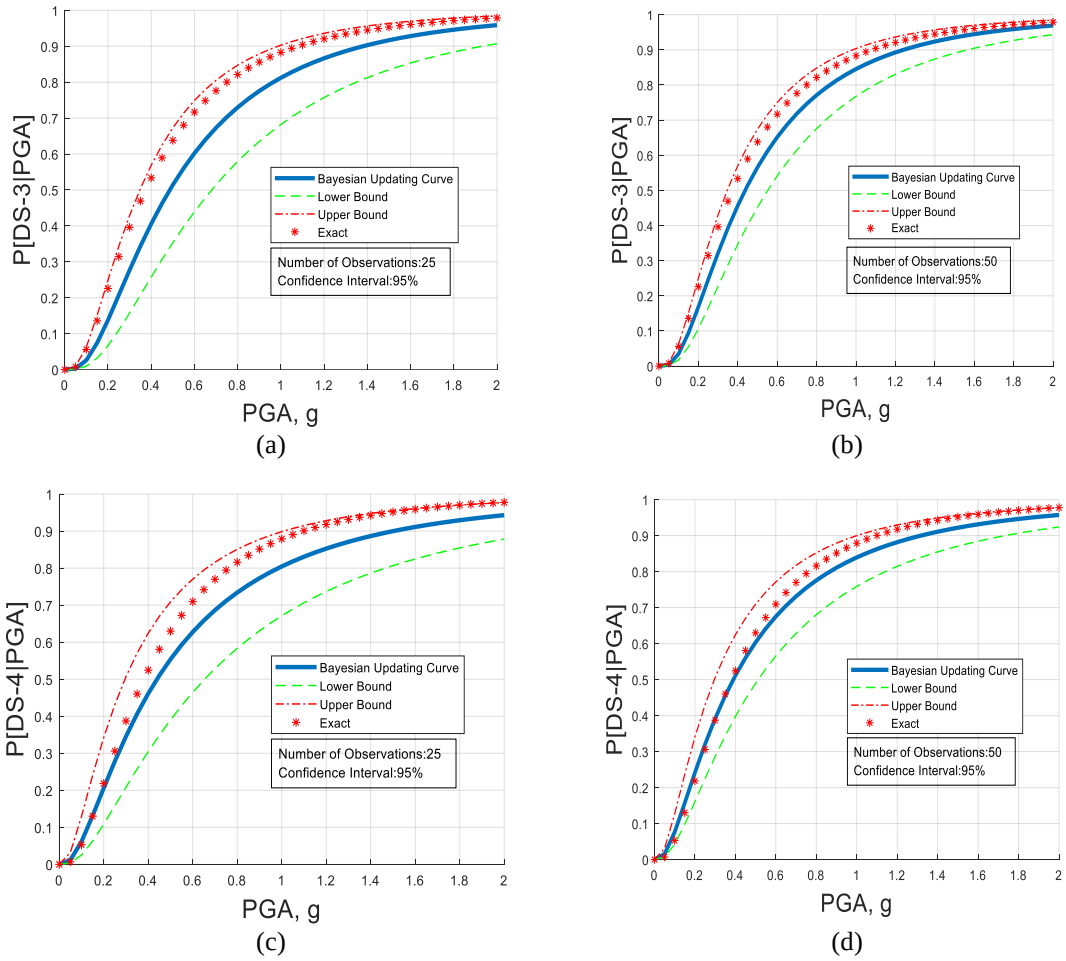

Figure 21. Bayesian updated fragility curve compared to exact fragility curve considering 25 observational data points (left) and 50 observational data points (right) for (a) & (b) DS-3 and (c) & (d) DS-4

In Figures 20 and 21, the narrowing of the confidence bounds in using 50 compared to 25 observational data points is observed. As expected, more accurate results using the Bayesian updating approach are obtained as the number of observational data points increases. The maximum failure probability differences between the results from the Bayesian updating approach using 25 and 50 observational data points and the exact result are 16% and 2% for DS-1, 9% and 2% for DS-2, 12% and 8% for DS-3, and 9% and 4% for DS-4, respectively. The exact result lies within the 95% confidence bounds in both cases and for all damage states.

To further quantify the proposed method's performance, and assess differences in achieving convergence between the proposed and existing approaches, comparison of the performance as the number of observations increases is also investigated. Figure 22(a) and 22(c) show the evolution of the lognormal mean and variance as the number of observations increases for both approaches. Note that the existing approach employs the standard method of moments to estimate the fragility parameters, and that the ordered set of ground motions is used to limit the influence of randomness in loading intensities on the variability of the results for the existing method. Figures 22(b) and 22(d) show the lognormal mean and variance errors from the exact values as the number of observations increases for the two approaches.

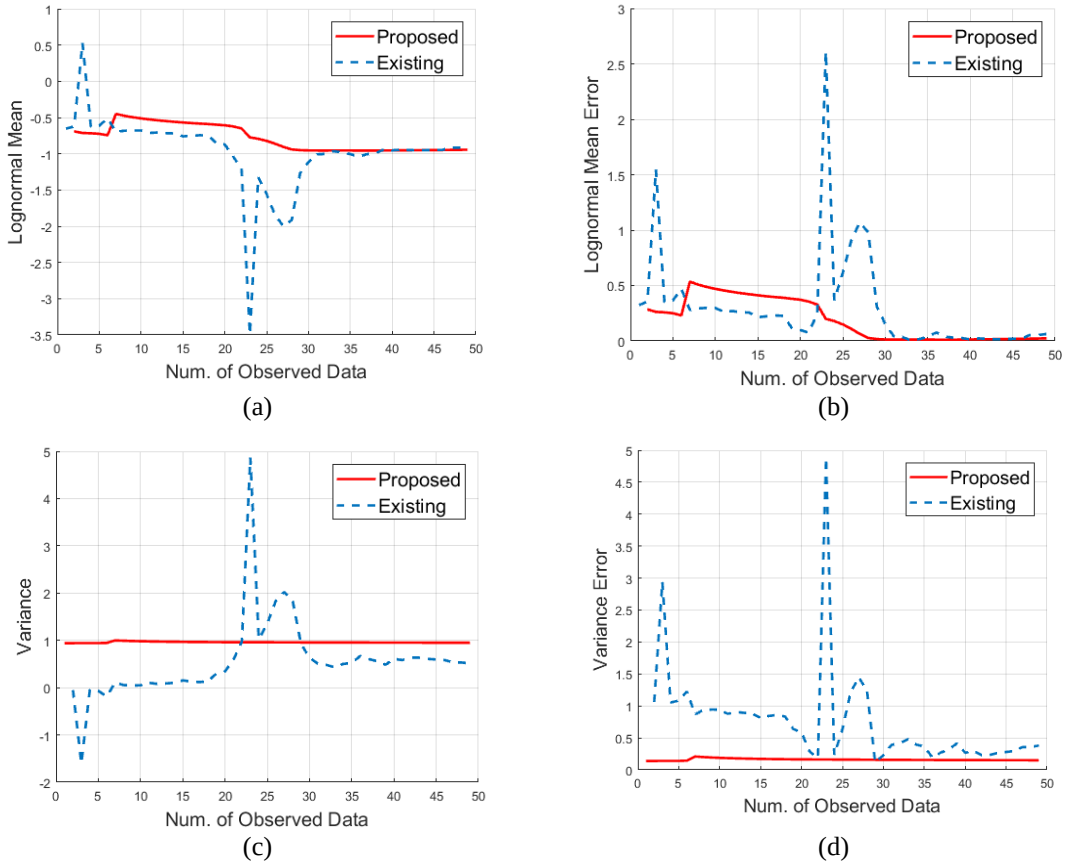

Figure 22. Evolution of (a) lognormal mean and (c) variance & error of (b) lognormal mean and (d) variance between the exact value and results from Bayesian updating approach and existing approach for DS-4 under 20% mass loss

Figure 22 shows that the lognormal mean converges faster and more smoothly using the proposed Bayesian updating method compared with the existing approach. In the existing approach, the parameters for the fragility function are generated directly based on PSDMs. The Bayesian updating approach evaluates the lognormal parameters by updating rules and calculating the mean as in Equation (38a), resulting in smoother estimates of the parameters. The lognormal mean's maximum error is 50% for the proposed compared with 260% for the existing approach. The proposed approach reduces error significantly with only 25 observational data points, whereas the existing approach requires 32 or more observational data points to reach a relatively stable lognormal mean.

Figure 23 investigates the accuracy of the two approaches, showing the errors in terms of the root mean square error (RMSE) for the fragility curves over the full range of PGA values as well as the maximum differences in probabilities of exceeding each damage state for the proposed compared to existingapproaches. Error and probability difference calculations are made compared with the results from the full set of 160 analyses. The left-hand side of Figure 23 shows RMSE, and on the right-hand side, the maximum difference in failure probability for probabilities of exceeding damage states DS-1 through DS-4. The plots for the existing approach begin at seven data points because the first six data points generate a negative slope in the PSDM (i.e., a negative b_m value in Equation (29b)), which consequently leads to a negative lognormal variance from Equation (30c).

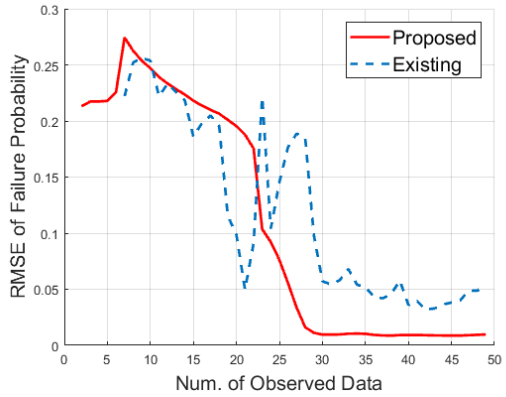
Proposed
Existing
RMSE of Failure Probability
Num. of Observed Data

(a)

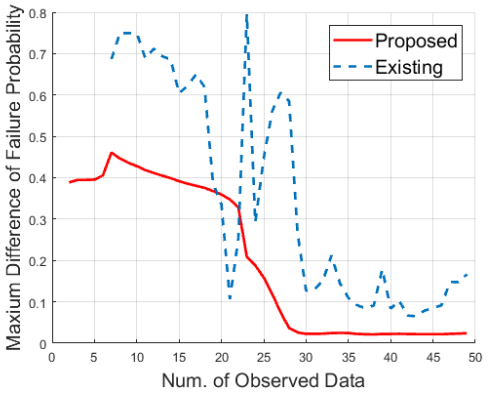
Proposed
Existing
Maxium Difference of Failure Probability
Num. of Observed Data

(b)

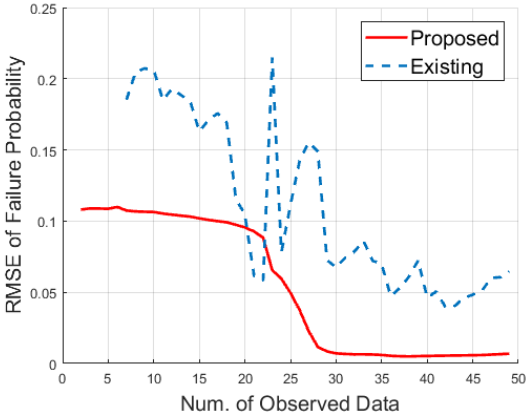
Proposed
Existing
RMSE of Failure Probability
Num. of Observed Data

(c)

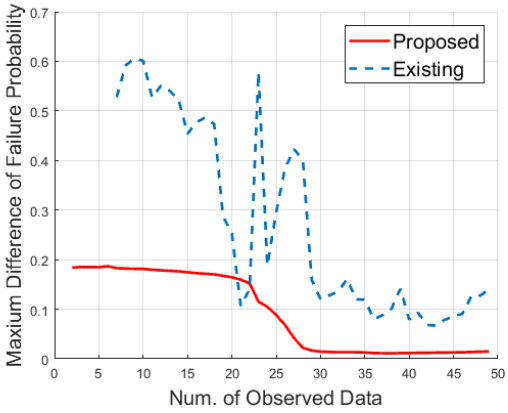
Proposed
Existing
Maxium Difference of Failure Probability
Num. of Observed Data

(d)

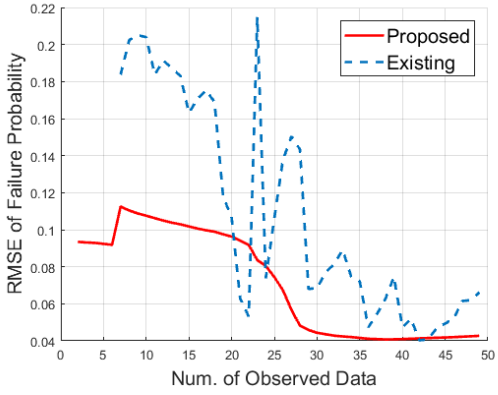
Proposed
Existing
RMSE of Failure Probability
Num. of Observed Data

(e)

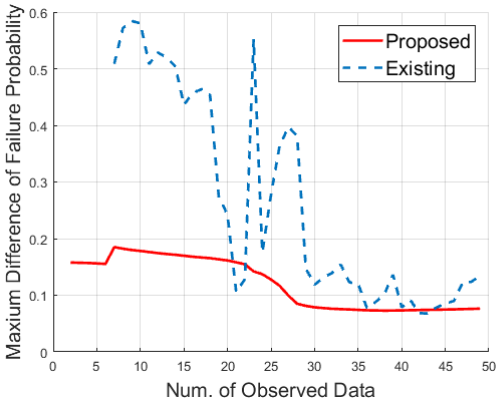
Proposed
Existing
Maxium Difference of Failure Probability
Num. of Observed Data

(f)

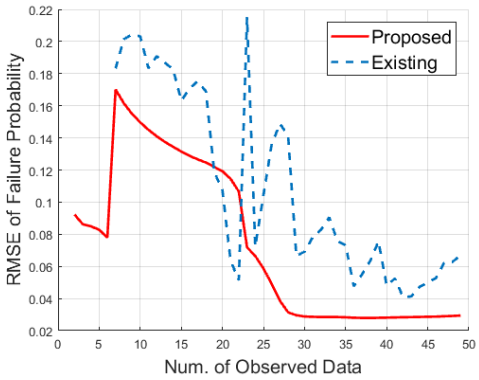

(g)

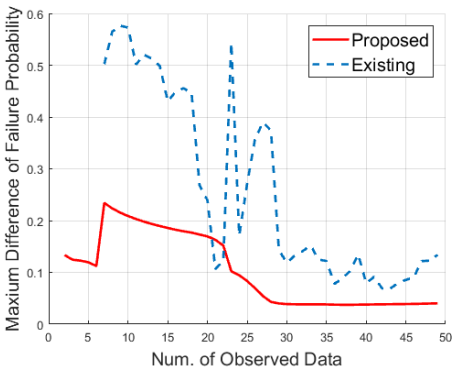

(h)

Figure 23. RMSE and maximum difference of failure probability for (a) & (b) DS-1, (c) & (d) DS-2, (e) & (f) DS-3, and (g) & (h) DS-4 for the proposed compared to existing appraoches

Figure 23 shows that the proposed Bayesian updating approach leads to a smoother result with faster convergence and lower error than the existing approach. In all cases, the proposed approach converges to a lower RMSE and lower maximum probability difference than existing methods, indicating increased accuracy of the proposed approach. To facilitate comparison between the two approaches, a threshold of 6% and 10% are chosen for RMSE and maximum probability difference, respectively, based on the convergence values of the results. The proposed approach achieves faster convergence to these accuracy threshold values and more stable results. For example, looking at the most extreme damage state DS-4, the proposed approach requires only 25 observational data points to reduce RMSE and the maximum difference in failure probability to below 6% and 10%, respectively. In addition, once a minimal RMSE and maximum probability difference level is achieved, the outcome remains stable using the proposed approach. In comparison, it requires more than 50 observational data points for existing methods to reach the minimum RMSE and probability difference thresholds. The instability of results using the existing approach is also seen as the RMSE and probability difference values are observed to increase.. These trends in accuracy, convergence, and stability are observed for the other

damage states as well. Table 8 summarizes the number of analyses required to reduce RMSE and maximum difference to below the 6% and 10% theresholds, respectively, as well as the minimum RMSE and probability difference achieved, for each damage state.

Table 8. Comparison of computational cost and accuracy between the proposed and existing approaches

Num. of Analyses Required	RMSE ≤ 6%		Max. Prob. Diff. (≤ 10%)		Min. RMSE (%) with 50 Observ. Data		Min. Max. Prob. Diff. (%) with 50 Observ. Data	
	Proposed	Existing	Proposed	Existing	Proposed	Existing	Proposed	Existing
DS-1	26	61	26	80	0.87	3.20	2.12	6.51
DS-2	25	65	25	79	0.50	3.96	1.11	6.71
DS-3	26	65	26	79	4.07	4.02	7.29	6.77
DS-4	25	65	23	79	2.78	4.07	3.74	6.85

From Table 8, for all damage states, the existing approaches require an average of 64 and 79 analyses for the RMSE and maximum probability difference to reduce below 6% and 10%, respectively. Comparatively, it takes an average of 25 analyses for the proposed approach to do so. The average computational time saved to obtain updated fragility functions for each damage state is more than 60%, with a savings of 61% to achieve RMSE under 6%, and a savings of 68% to achieve maximum probability difference under 10%. In addition, the proposed approach achieves more accurate results across all damage states, measured in terms of both RMSE and maximum probability difference. On the other hand, except for DS-3, the proposed approach yield better results in terms of the values of the minimum RMSE and maximum probability different for other damage states across 50 observational data points. The results show that the proposed approach can achieve accurate and stable updated fragility assessments with fewer data points and significantly reduce computational cost compared to existing methods.

3.3.6 Bayesian updating of fragility curves considering column response

Results in the previous section show the reduction in number of analyses possible using the proposed method. However, a full structural finite-element model is required. This section investigates the further reduction of computational cost by using information from a reduced complexity finite-element model. Instead of performing nonlinear time history analyses at the full-bridge level, this section considers data from nonlinear time history analyses performed on the column level only. The goal is to investigate the ability to use component-level analyses to update estimates of full structural performance. If possible, the time to obtain the updated fragility functions can be further reduced through decreasing the degrees of freedom and complexity of the structural model and analyses. For the case of the bridge structure, the column behavior often dictates the bridge behavior. Therefore, the reduced finite-element model is taken to be one of the column only. The following results show the use of the proposed Bayesian updating approach based on the outcomes of nonlinear analyses of the single column to obtain updated fragility curves considering the effect of measured corrosion.

As structural analyses of the column only are significantly less computationally intensive compared to the full bridge structure, 51 nonlinear time history analyses are performed on the bridge column, transformed to 50 observational data points. The computational requirements for conducting these analyses are provided at the end of this section. The procedures, shown in Figure 18, are then applied to the single-column responses to obtain a corroded bridge column's updated fragility curves. It is noted that the prior distribution for this data type is also computed based on single-column analyses rather than the full-bridge response. To show how the proposed method performs as the expected

performance of the structure varies, e.g., with varying levels of corrosion, Figure 24 shows the resulting fragility curves considering 10% mass loss of reinforcement (left-hand plots) and 20% mass loss (right-hand plots) for each of the four damage states. The results from the proposed method including 95% confidence bounds are shown compared to the exact value obtained from running the full set of 160 nonlinear time history analyses on the full bridge finite-element model.

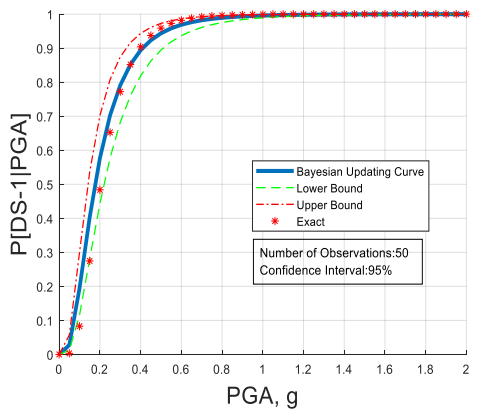

(a)

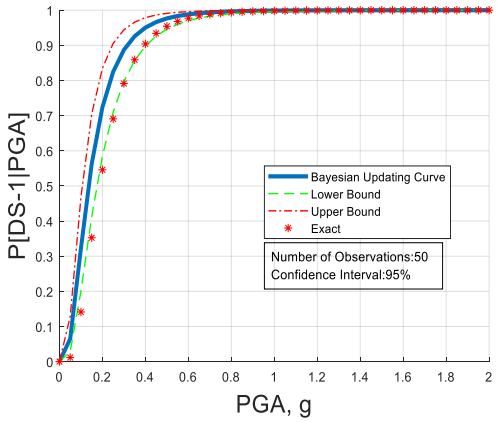

(b)

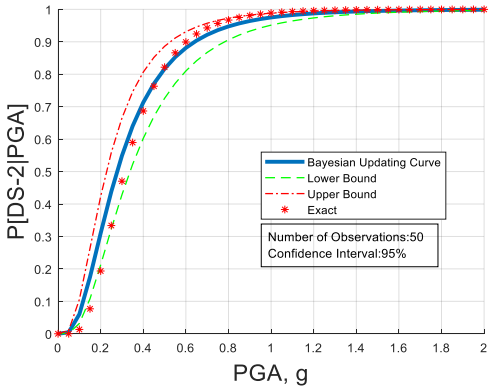

(c)

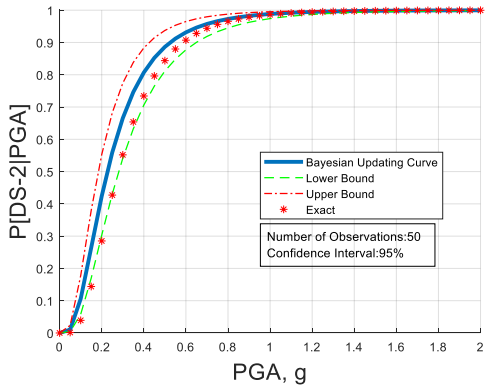

(d)

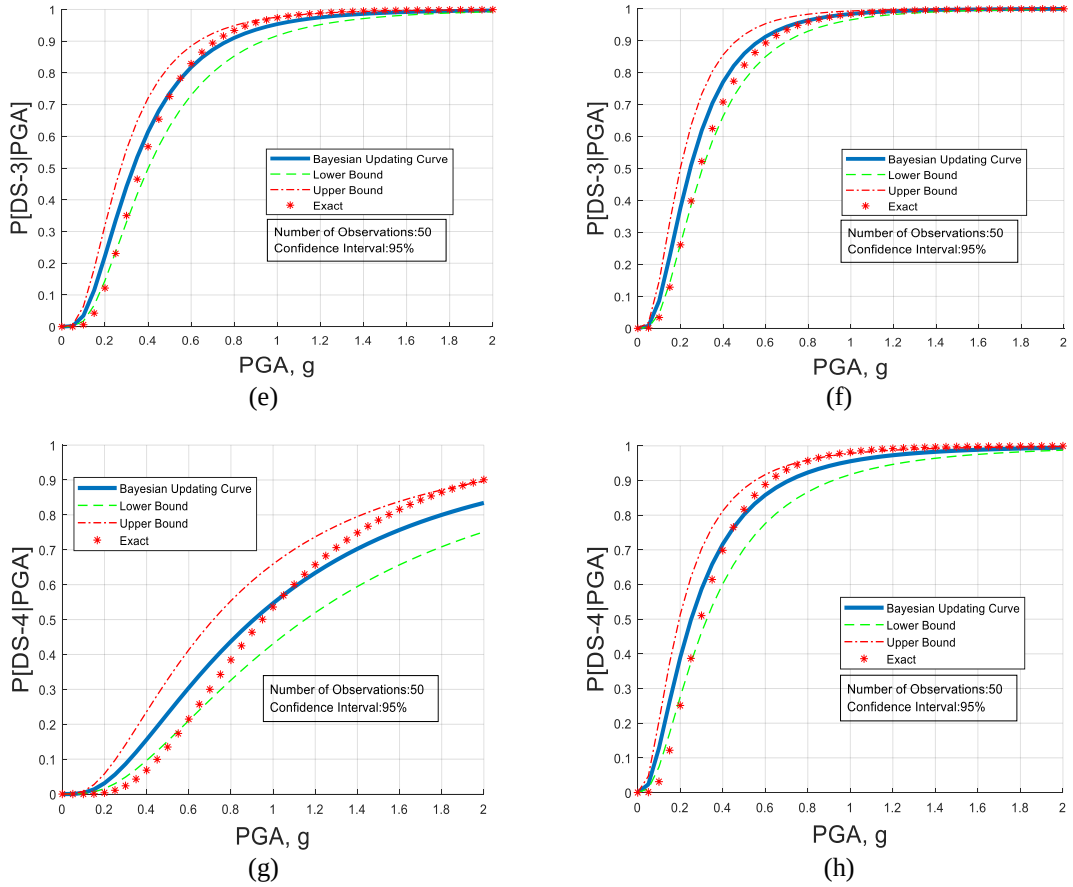

Figure 24. Bayesian updated fragility curve compared to exact fragility curve considering 10% mass loss of reinforcement (left) and 20% mass loss (right) for (a) & (b) DS-1, (c) & (d) DS-2, (e) & (f) DS-3, and (g) & (h) DS-4

Figure 24 shows that the Bayesian updating approach can predict the fragility parameters and accurately update the fragility functions based on the the limited data obtained from the reduced finite-element model of the displacement ductility between the pristine and corroded columns. The exact value lies within the 95% confidence bounds in all cases except for DS-4 at low PGA values. In Figure 23, as expected, there is a certain level of difference between the Bayesian updated result and the exact result due to the simplification of the dataset. The observational data is generated from a single-column time history analysis and does not include constraints from the super-structure that may affect the column's response. However, the error is small compared to the time saved to obtain

the fragility function. This is due to not needing to build the full-bridge model and faster runtimes for each analysis with a reduced complexity structural model. Table 8 summarizes the computational cost of running nonlinear time history analyses for the full-bridge model compared to a single-column model for the exact, existing, and proposed approaches. As shown in Figure 23 and Table 8, the number of analyses required to obtain stable fragilities varies somewhat across the damage states. Where applicable, the average number of analyses required for the four damage states is shown. All analyses are conducted on a computer with 16.0 GB RAM and i7-3770 processor.

From Table 9, considering only the single-column model combined with the proposed Bayesian updating approach reduces the computation cost significantly, with more than an order of magnitude savings from existing methods.. Comparing with each method, the computation time needed to obtain a stable updated fragility curve for the corroded states is reduced by 98.7%, 96.8%, and 91.4% compared to the exact, existing, and proposed approaches considering the full-bridge, respectively. In addition to the analysis time, the savings in computational effort to build just a single-column model compared to the full finite-element bridge model is significant. Combining the reduced observational data type with the proposed Bayesian updating approach achieves updated fragility assessments with sufficient accuracy in failure probabilityin failure probability from the target fragility function for all damage states across hazard intensities.

Table 9. Comparison of computational cost between using observational data from the full-bridge and single-column models

	Exact (Full Bridge)	Existing (Full Bridge)	Proposed (Full Bridge)	Proposed (Single Column)
Average Time Per Analysis (min.)	14	14	14	0.6
Num. of Analyses Required	160	79*	25*	50
Total Computation Time (min.)	2240	948	350	30
% Reduction Compared with Single Column	98.7%	96.8%	91.4%	-

* The average number of analyses required for four damage states.

3.3.7 Conclusions

Dynamic analysis large and complex finite element models is typically accompanied by high computational costs, especially for high-fidelity structural finite element models. Running probabilistic analyses with a series of nonlinear dynamic analyses for problems considering a range of uncertainties requires even more computational effort to obtain stable results, including to construct fragility functions assessing structural risk. This section presents a methodology to obtain updated analytical fragility curves through a Bayesian approach that is able to achieve accurate and stable results with significantly decreased computational cost. The method is applied to assess the fragilities of bridges considering the effect of corrosion. The methodology utilizes two types of observational data to reduce time and obtain the desired fragility function.

Using the proposed updating rules in the context of conjugate Bayesian inference, the proposed method decreases the time to obtain stable fragility functions by reducing the number of nonlinear time history analyses required. The proposed approach shows faster

convergence and results in more stable estimates of the fragility function parameters. Compared to existing methods, the proposed approach reduces computational cost by 61% to achieve RMSE under 6%, and by 68% to achieve maximum probability difference under 10%. It is proposed to reduce computation time even further by performing nonlinear analyses at component level rather than for the full structure. Doing so reduces the computational cost by as much as 96.8% compared to existing approaches. The 95% confidence interval fragility estimates capture the exact fragility values across almost all damage states and loading intensities. While the proposed approach is demonstrated to updating the fragility function based on numerical structural response information considering the effect of measured corrosion levels, the proposed approach provides a framework that enables updating fragility curves by combining data from experimental testing, hybrid simulation, or other observational types of data.

CHAPTER 4. SCOUR IMPACT ON STRUCTURAL PERFORMANCE OF BRIDGES AND FOUNDATION PILES

4.1 Introduction

Besides corrosions, the effect of scour on bridge foundation is another core topic investigated in this thesis. According to a study done by Wardhana and Hadipriono (2003), 60% of bridge failures in the U.S. are related to bridge scour. As such, bridge scour has become an essential topic investigated by several researchers in the past. This chapter presents a detailed study regarding the impact of scour on the seismic performance of highway bridges. The first subtopic (Subtopic No. 3) discusses the methodologies to assess the structural reliability by accounting for physical phenomena after scour events, including the impacts of soil stress history, scour hole dimensions, and layered soils effects. The first part of subtopic No.3 emphasizes the impact of layered soil's stress history on bridge seismic performance under scour conditions, and the main content of this part is based on our publication Zhang and Tien (2020b). On the other hand, the second part of Subtopic No. 3 presents the combined effect of stress history and scour-hole dimensions in homogenous soils on the laterally and vertically loaded piles. The second subtopic (Subtopic No. 4) focuses on the influence of measured non-uniform scour on bridge responses.

4.2 Subtopic No. 3 (Part 1)

4.2.1 Background and related work

In the past decade, researchers have studied the seismic performance of bridges in the presence of scour (Alipour and Shafei, 2012; Banerjee and Prasad, 2013; Wang et al., 2014; Fioklou and Alipour, 2019). However, these studies employ traditional scour modeling with the simple removal of soil springs without considering the stress states' changes and related properties of the remaining soil due to scour. Meanwhile, other studies have investigated the influence of soil stress history on laterally loaded single piles in sand and soft clay (Lin et al., 2010, 2014). These studies show that neglecting the stress history effect can lead to unconservative responses of scoured piles. However, most of the previous studies regarding the impact of stress history still focus on a homogeneous soil type. At the same time, it is common for bridges to be located at sites with layered soil deposits (Yamada and Takemiya, 1981; Soneji and Jangid, 2007; Aygun, 2009). Modeling profiles consisting of layers of multiple soil types as a homogeneous material neglects the layered soil effects. Researchers have investigated the lateral (Davisson and Gill, 1963; Georgiadis, 1983; Gazetas et al., 1984; Zhang et al., 2015) and the vertical (Cairo and Conte, 2006; Huang et al., 2011; Wang et al., 2012) behaviors of piles in layered soil deposits. However, these studies do not account for the impact of stress history in layered soils, and most do not focus on addressing vulnerability assessment of full-bridge structures. In summary, there have been no previous studies on the effect of soil stress history on the properties of layered soils. Besides, evaluating the seismic performance of bridges subject to scour, including soil stress history of layered soils, is unstudied. This study proposes a methodology to account for the influence of layered deposits and soil stress history in

evaluating the performance of bridges susceptible to scour. The method includes the ability to analyze profiles that consist of both sandy and clayey soils. This study is the first to account for the stress history effects of layered soils. The main contributions present the new equivalent stress history and layered effects (ESHaLE) approach and results showing the importance of taking such an approach in the vulnerability assessment of scoured bridges. Using the proposed methodology enables the vulnerability of bridges located in layered soil deposits susceptible to scour to be more accurately and comprehensively assessed.

The next section introduces background information regarding the effect of soil stress history on a single homogeneous soil deposit. Second, the behavior of layered soils due to multiple heterogeneous deposits. The following section describes the proposed ESHaLE methodology for combining the effects of soil stress history and layered soils for the modeling and analysis of bridges susceptible to scour. The next section applies the methods to an example bridge and soil profile. Using ESHaLE compared to unmodified soil models in the vulnerability assessment of a scoured bridge under seismic loading is shown. Finally, concluding remarks and a summary of findings are provided.

4.2.2 Stress history of soils

The deposition of soils can be viewed as a loading process, while scour can be considered an unloading process as the surrounding soils are removed. Due to the unloading process, the remaining soil after scour experiences different stress states, leading to changes in the soil properties. In particular, the soils change from normally consolidated to overconsolidated states (Brown and Castelli, 2010), represented by an overconsolidation

ratio (OCR) between the previous maximum stress and present stress. The OCR increases as scour depth increases, leading to changes in the soil properties. Detailed information regarding calculating the changes in the soil properties due to the effect of stress history in sandy (Lin et al., 2010) and clayey (Lin et al., 2014) soils is provided in the appendix.

Soils are traditionally modeled using springs in three directions: p-y springs model lateral soil behavior, t-z springs model vertical soil behavior, skin friction between the pile and soil, and q-z springs model behavior at the pile tip. For cohesionless soils (e.g., sand), including the effect of soil stress history due to scour reduces the relative density, unit weight, and modulus of subgrade reaction and increases the friction angle and OCR of the remaining soil (Lin et al., 2010). Reese et al. (1974) propose a p-y relation for sand, with the ultimate resistance for wedge failure near the ground surface (P_{st}) and flow failure well below the ground surface (P_{sd}) computed based on Equation (46) and Equation (47), respectively.

$$P_{st} = \gamma' z \left\{ \frac{K_o z \tan(\phi') \sin(\beta)}{\tan(\beta - \phi') \cos(\alpha)} + \frac{\tan(\beta)}{\tan(\beta - \phi')} [B + z \tan(\beta) \tan(\alpha)] + K_o z \tan(\beta) [\tan(\phi') \sin(\beta) - \tan(\alpha)] - K_a B \right\} \quad (46)$$

$$P_{sd} = K_a B \gamma' z [\tan^8(\beta) - 1] + K_o B \gamma' z \tan(\phi') \tan^4(\beta) \quad (47)$$

γ' is the effective unit weight of sand, z is the distance between mudline and point of interest, β is passive failure angle, α is angle defining the shape of the failure wedge, K_a is the minimum coefficient of active earth pressure, K_o is the coefficient of lateral earth pressure at rest, B is the diameter of the pile, and ϕ' is friction angle. This study adopts the p-y relation shown in Equation (48) for sand from the American Petroleum Institute (API, 2011) in combination with Equation (46) and Equation (47) to compute the ultimate lateral

resistance of the sand. P_{ult_sand} in Equation (48) is computed based on the minimum value between P_{st} and P_{sd} depending on the depth of interest obtained from Equation (46) and Equation (47), respectively.

$$P = AP_{ult\_sand} \tanh\left[\frac{kH}{AP_{ult\_sand}} y\right] \quad (48)$$

P is lateral soil resistance at any depth H, A is a modification factor that accounts for static or cyclic loading (0.9 in this case), P_{ult} is ultimate bearing capacity at depth H, y is lateral deflection, and k is the initial modulus of subgrade reaction. The effect of the soil stress history is accounted for by updating the relative density and coefficient of lateral earth pressure of the remaining sand after scour due to the change from normally consolidated to overconsolidated soil. The change of relative density is caused by the changes of the void ratio and overburden stress, which leads to the change of additional properties of sand, including unit weight, modulus of subgrade reaction, and friction angle.

For t-z relations, the ultimate unit shaft resistance of sand (T_{ult_sand}) is computed as in Equation (49) (Tuma and Reese, 1974), where $\sigma_v{}'$ is effective vertical stress at a point of interest.

$$T_{ult\_sand} = 0.7\tan(\phi')\sigma_v{}' \quad (49)$$

The ultimate end bearing resistance (Q_{ult_sand}) of sand is computed based on Meyerhof (1976) with Equation (50).

$$Q_{ult\_sand} = N_q\sigma_v{}' \quad (50)$$

N_q is a dimensionless bearing capacity factor. The t-z relation for sand is adopted based on Mosher (1984), which uses a hyperbolic representation of the t-z curve as shown in Equation (51).

$$T = \frac{z}{\frac{1}{E_f} + \frac{1}{T_{ult\_sand}}(z)} \tag{51}$$

E_f is the value of the initial modulus, z is the movement of the pile segment, and T is total shear transfer. The q-z curve's backbone for sand is approximated using Vijayvergiya's relation (1977) shown in Equation (52).

$$Q = (\frac{z}{z_c})^{\frac{1}{3}} * Q_{ult\_sand} \qquad (z \leq z_c) \tag{52a}$$

$$Q = Q_{ult\_sand} \qquad (z > z_c) \tag{52b}$$

Q is pile tip resistance and z_c is movement required to mobilize Q_{ult_sand} (6.35mm for sand).

The change of remaining properties of sand due to stress history can also affect the vertical behavior of sand (i.e., T_{ult_sand} and Q_{ult_sand}) and these changes are also considered in this study. More details regarding capturing the stress history of sand can be found in Lin et al. (2010).

For cohesive soils (e.g., soft clay), the ultimate soil resistance (P_{ult_sand}) is computed as in Equation (53) (Matlock, 1970).

$$P_{ult\_clay} = \min\left\{\left(3 + \frac{\gamma'}{C_u}\mathrm{z} + \frac{J}{B}\mathrm{z}\right)C_u B, 9C_u B\right\} \tag{53}$$

C_u is the undrained shear strength of clay, and J is set as a constant with a value of 0.5. The p-y relation for soft clay is adopted from Matlock (1970). P_{ult_clay} of stiff clay without free water can also be computed based on Equation (53) (Welch and Reese, 1972; Reese and Welch, 1975). Stiff clay without free water indicates a stiff clay layer located above the water table. As the OCR and scour depth change, including the soil stress history, also influences the effective unit weight and undrained shear strength of soft clay. While the

effective unit weight difference is insignificant, the undrained shear strength is significantly reduced when soil stress history is considered (Lin et al., 2014). The ultimate unit shaft resistance of clay is computed according to Equation (54) (Tomlison, 1992).

$$T_{ult\_clay} = \alpha C_u \tag{54}$$

α is an adhesion factor for piles in clay, computed by Equation (55).

$$\alpha = 0.5\psi^{-0.5} \qquad (\psi \leq 1.0) \tag{55a}$$

$$\alpha = 0.5\psi^{-0.25} \qquad (\psi > 1.0) \tag{55a}$$

ψ is the ratio between undrained shear strength of the soil (C_u) and effective overburden pressure (σ_v') at the point of interest. Note that the value of α should not exceed 1.0. The t-z relation for clay is adopted from Reese and O'Neill (1987). The computation of point-bearing capacity (Q_{ult_clay}) of clay is based on Terzaghi's bearing capacity theory (Terzaghi, 1943). Due to the characteristics of cohesive soils and piles, the relation can be simplified to Equation (56), where A_p is the cross-sectional area of the pile.

$$Q_{ult\_clay} = 9A_pC_u \tag{56}$$

The q-z relation for clay is adopted based on Reese and O'Neill (1987). The change of the vertical response of clay accounting for soil stress history effects is also considered in this study, manifested through the decrease in undrained shear strength (C_u). The change in undrained shear strength after scour is quantified and established based on critical state soil mechanics and expressed as a function of the OCR (Lin et al., 2014).

4.2.3 The behavior of layered soils

To account for layered soils' behavior, previous studies have calculated "equivalent" soil depths, for example, using conservation of strength to obtain the p-y behavior for layered soil deposits (Georgiadis, 1983). As p-y curves only apply to homogeneous soil deposits, the p-y curve for a profile with successive layers of different soil types is determined using a series of equivalent depth calculations. For example, the equivalent depth of a second soil layer is found by first calculating the force (F_1) acting at the layer interface as shown in Equation (57).

$$F_1 = \int_0^{D_1} P_{ult1} dH \tag{57}$$

P_{ult1} is the ultimate soil resistance of the first layer and D_1 is the thickness of the first layer. The equivalent depth (X_{py2}) of the first soil layer that includes the characteristics of the soil deposit from the second layer is then obtained by solving Equation (58).

$$F_1 = \int_0^{X_{py2}} P_{ult2} dH \tag{58}$$

P_{ult2} is the ultimate soil resistance of the second layer. The same procedure is applied to obtain the equivalent depth for the second layer, including the soil deposit of the third layer and so on through the layers in the soil profile. This approach has been verified experimentally (Georgiadis et al., 1999) for a single pile loaded laterally and vertically in layered soils. The effect of layered soils in the vertical direction is considered for both sands and clays through evaluating the value of effective vertical stress. The theoretical basis is that the effective vertical stress is a function of effective unit weight, which changes

from layer to layer, and composite action is required to maintain the continuity of strength in the vertical direction. For sands, the ultimate axial resistances of sand (T_{ult_sand} and Q_{ult_sand}) are a function of effective vertical stress as indicated in Equation (49) and Equation (50). For clays, the ultimate unit shaft resistance (T_{ult_clay}), as shown in Equation (54), is a function of both undrained shear strength (C_u) and alpha (α), where the value of alpha is a function of effective vertical stress (σ_v'). Meanwhile, the ultimate end bearing resistance (Q_{ult_clay}) of clay is assumed to be only a function of undrained shear strength (C_u) as shown in Equation (56). In this study, the authors take an equivalent depth approach to model the behavior of layered soils. However, in addition to conservation of strength, conservation of mass is utilized to account for soil stress history in layered soils. The proposed approach is described in detail in the following section.

4.2.4 Proposed equivalent stress history and layered effects (ESHaLE) methodology

The scour process removes soils, unloading and reducing the effective vertical stress acting on the remaining soil. Figure 25 shows the consolidation curve of clay under scour conditions considering the soil stress history. The subscripts int and sc represent parameters before and after scour, respectively. σ_v' is effective vertical stress, e is the void ratio of soil, C_c is compression index, and C_r is recompression index. The soil stress history leads to a change in effective vertical stress, which leads to a change in void ratio.

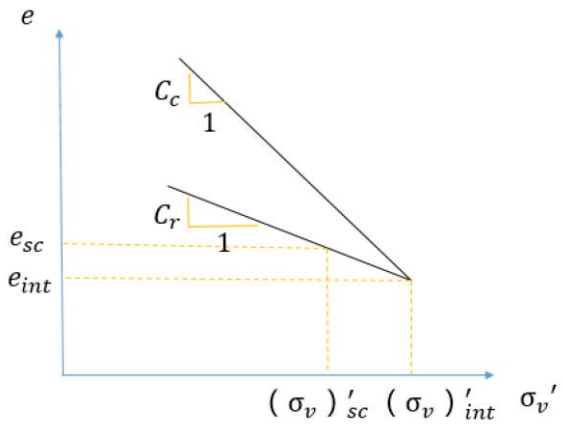

Figure 25. Consolidation curve of clay under scour conditions

Sand will exhibit similar consolidation behavior except for changing the value on the x-axis from σ_v' to the mean effective stress P', where P' is used to quantify the change of effective pressure. P' can also be represented in terms of effective vertical stress as shown in Equation (59), where σ_h' is effective horizontal stress.

$$P' = \frac{\sigma_v' + 2\sigma_h'}{3} \tag{59a}$$

$$P' = \left(\frac{1 + 2K_o}{3}\right)\sigma_v' \tag{59b}$$

The objective is to find an equivalent scour depth and equivalent layer depths that account for soil parameters' changes due to stress history effects. The difference in effective vertical stress is obtained based on conservation of mass as follows. Consider first a soil profile with two layers. The stress history effect in the lower layer is accounted for with the partial or full removal of the upper layer. The mass loss quantifies the change in effective vertical stress due to removing the soil as if it only consists of soil material from the lower layer. This holds for general scour conditions, which neglects the effect of scour

hole dimensions in the case of local scour conditions. An "equivalent" scour depth is then found, which is computed based on mass conservation.

In general, for a layered soil deposit with layer i and $i+1$ as shown in Figure 26, let D_i be the depth of layer i and S_d the scour depth. z_{pi} is the distance between the initial mudline and point of interest, and z_{sc} the distance between the new mudline after scour and point of interest. Each point of interest corresponds with a soil spring for which the parameters must be updated. The objective is to find an equivalent depth of layer i in terms of the layer $i+1$ soil material (D_{i_e}), an equivalent scour depth (S_{d_e}), and equivalent distances z_{sc_e} and z_{pi_e}.

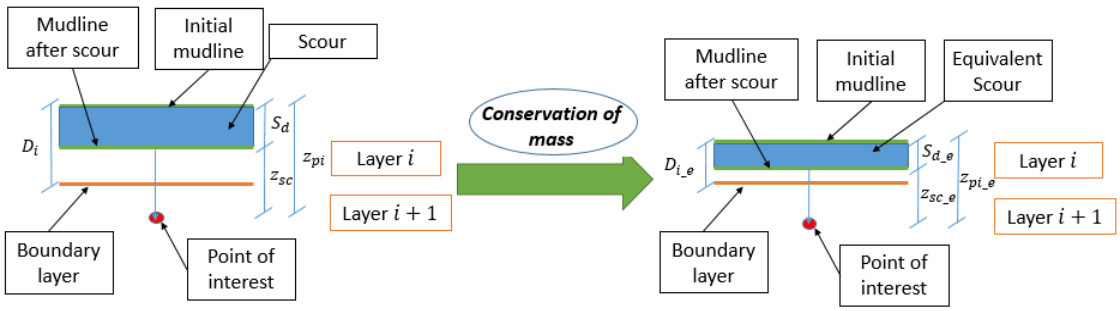

Figure 26. Finding equivalent layer depth and scour depth for layered soils accounting for stress history effects based on conservation of mass

The equivalent scour depth and layer depth for a layer i are calculated based on conservation of mass as shown in Equation (60a) and Equation (60b), using the ratio of effective unit weights between adjacent layers. Next, z_{sc_e} and z_{pi_e} are computed based on the geometric relations shown in Figure 26 combined with the relations established in Equation (60a) and Equation (60b). The expressions for the equivalent distances are derived in terms of effective unit weights, scour depth, and layer depth, as shown in Equation (60c) and Equation (60d).

$$S_{d\_e} = \frac{\gamma_i'}{\gamma_{i+1}'} S_d \tag{60a}$$

$$D_{i\_e} = \frac{\gamma_i'}{\gamma_{i+1}'} D_i \tag{60b}$$

$$z_{sc\_e} = z_{sc} + \left(\frac{\gamma_i'}{\gamma_{i+1}'} - 1\right)(D_i - S_d) \tag{60c}$$

$$z_{pi\_e} = z_{sc_e} + S_{d\_e} \tag{60d}$$

γ_i' is the effective unit weight of layer i and γ_{i+1}' is the effective unit weight of layer $i+1$. Once the equivalent depths and distances are found, the values of S_{d_e} and z_{sc_e} can be used to compute the updated soil properties, including the effect of soil stress history as if the soil consists of a homogeneous layer with the detailed procedures presented in the appendix (Figures 70 and 71). Note that Equation (60) is only applicable for the scenario indicated in Figure 26, where the point of interest is located within the second layer and scour occurs within the first layer. To generalize to other scenarios, new expressions for S_{d_e} and z_{sc_e} need to be determined. The following sections present a comprehensive set of these expressions for soil with two and three layers and varying scour depths. With this proposed methodology, the effect of stress history can be accounted for in any soil layer of interest.

4.2.5 An overall approach to account for stress history effects in layered soils

The goal is to obtain modified p-y, t-z, and q-z relations given scour depth and the soil profile considering both the stress history and layered soil effects. The stress history effect is applied to the soil model first to obtain updated soil properties after scour. Next,

the equivalent depths due to the layered effect are calculated based on the soil layer's updated properties. This sequence is chosen such that the equivalent depth can be calculated based on the most up-to-date soil properties, including the stress history effects, enabling more realistic and accurate results. Finally, the p-y, t-z, and q-z parameters (i.e., ultimate soil resistance) are determined based on the combined updated soil properties and equivalent depths. Figure 27 shows the overall procedure of the proposed methodology.

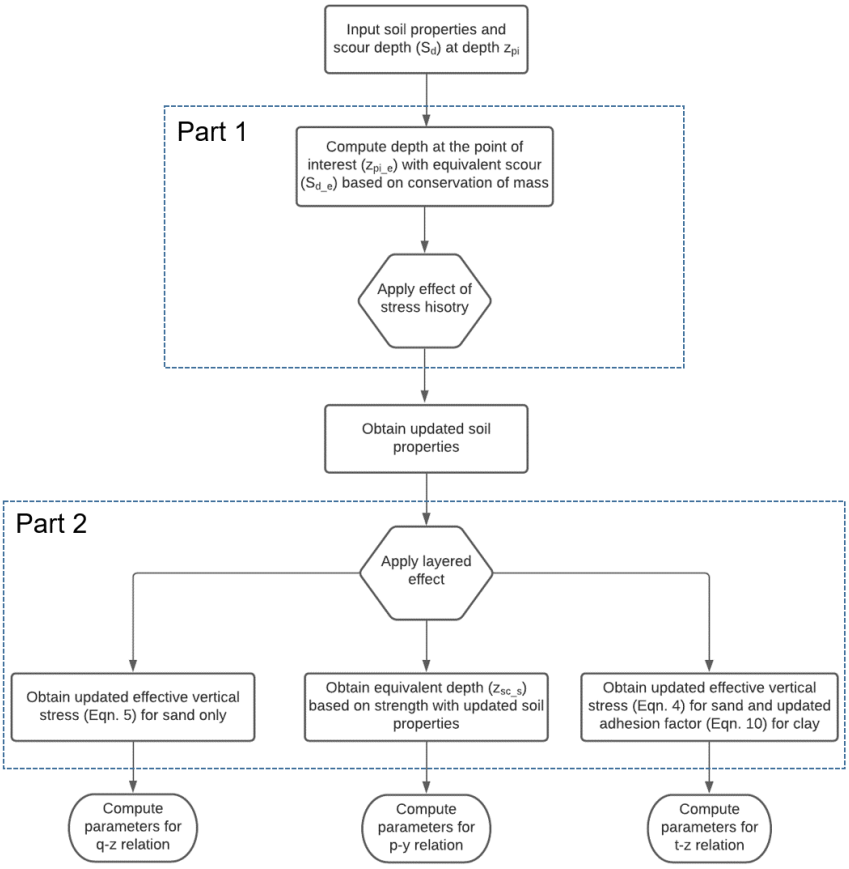

Figure 27. A proposed approach to account for soil stress history and layered effects in layered soil profiles

4.2.6 Parameters for soils with multiple layers

To accurately model the soil springs after scour, including the effect of soil stress history for layered soils, the soil parameters at varying points of interest below the mudline must be calculated. Each point of interest, an example of which is shown in Figure 26, corresponds with a specific soil spring location. The derived expressions for the parameters for different points of interest below the mudline are now provided. The first case considered is a soil deposit with two layers. Figure 28 shows the four scenarios for this case, with varying scour depths S_d and locations of points of interest below the mudline. D_i is the initial soil layer depth, z_{pi} the distance between the initial mudline and point of interest, and z_{sc} the distance between the new mudline after scour and point of interest.

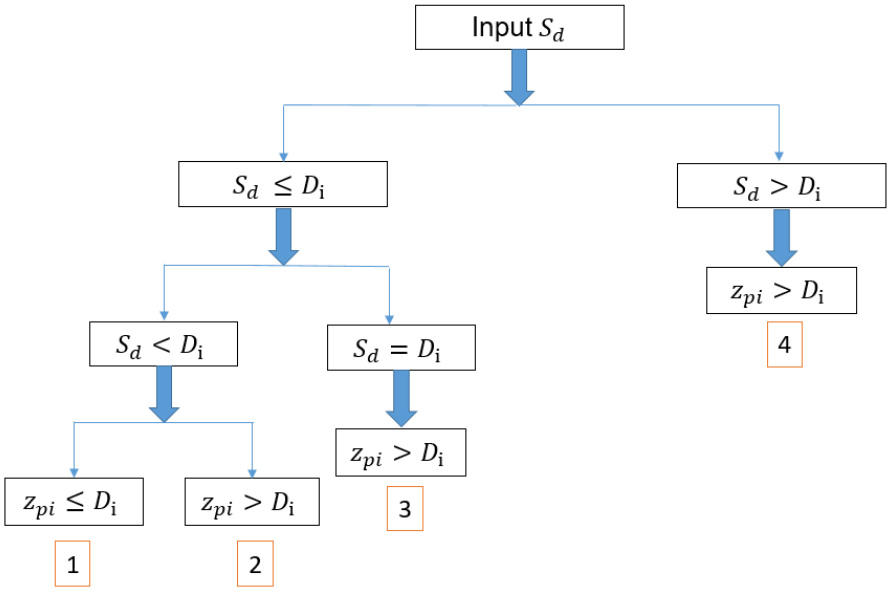

Figure 28. Four scenarios for varying scour depths and points of interest below the mudline for two-layered soil deposits

Table 10. Equivalent quantities for soil deposits with two layers

Scenario	S_{d_e}	z_{sc_e}	z_{sc_s}	X_{pyk}
1	S_d	z_{sc}	z_{sc}	-
2	$\frac{\gamma_i'}{\gamma_{i+1}'} S_d$	$z_{sc} + \left(\frac{\gamma_i'}{\gamma_{i+1}'} - 1\right)(D_i - S_d)$	$z_{sc} + X_{py2} + S_d - D_i$	$\int_0^{D_i - S_d} P_{ult\_py\_i} dH = \int_0^{X_{py2}} P_{ult\_py\_i+1} dH$
3	$\frac{\gamma_i'}{\gamma_{i+1}'} S_d$	z_{sc}	z_{sc}	-
4	$\left(\frac{\gamma_i'}{\gamma_{i+1}'} - 1\right) D_i + S_d$	z_{sc}	z_{sc}	-

For each scenario shown in Figure 28, modified values of S_d and z_{sc} need to be computed to account for the combined soil stress history and layered soil effects. The symbolic expression for each term as derived based on the proposed methodology is shown in Table 10. Two equivalent depths are calculated: z_{sc_e} is the equivalent value calculated based on conservation of mass, which is used to determine the updated soil properties due to the effect of soil stress history; and z_{sc_s} is the equivalent value calculated based on conservation of strength, which is used to determine the ultimate soil resistance. In the calculation of z_{sc_s}, an additional term X_{pyk} is needed. X_{pyk} is a value of equivalent depth that accounts for the layered effect in the lateral direction, with the subscript k representing the term for the kth scenario. The value of X_{pyk} is computed by numerical integration of the equation shown in the rightmost column of Table 10. $P_{ult\_py\_i}$ is the ultimate soil resistance of layer i in the lateral direction.

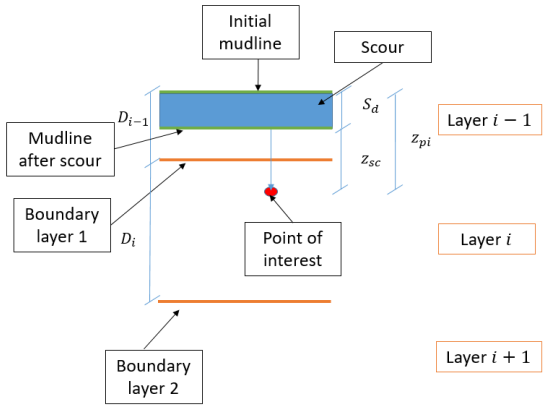

Figure 29. Scoured soil deposit with three layers and point of interest below the mudline

The next case considered is a soil deposit with three layers. Instead of four separate scenarios as for a two-layered deposit, there are now a total of nine scenarios. Figure 29 shows a point of interest among layers $i-1$, i, and $i+1$, where the scour occurs only partially in layer $i-1$. D_{i-1} is the depth of layer $i-1$. The scour scenario extends into the second layer and is also addressed in the derived equivalent quantities given in Table 11. Figure 30 shows the nine scenarios corresponding to the varying scour depths and points of interest for three-layered soil deposits. The equivalent quantities derived for each of the nine scenarios shown in Figure 30 are given in Table 11.

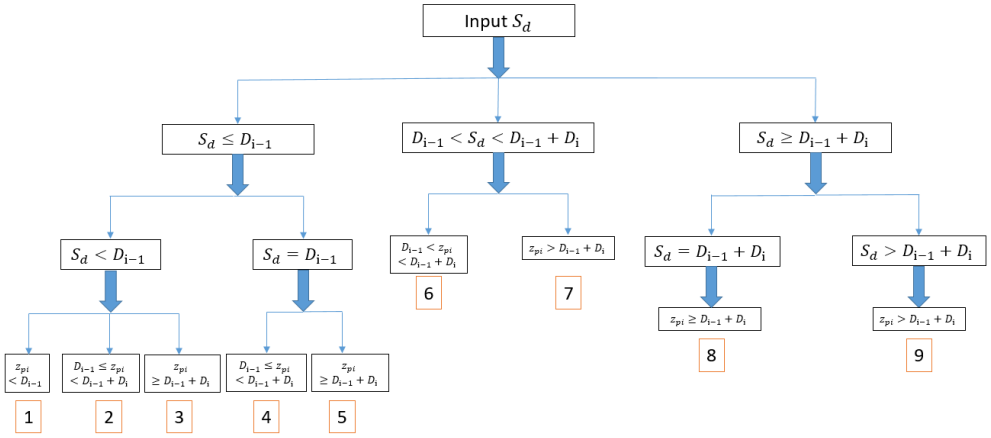

Figure 30. Nine scenarios for varying scour depths and points of interest below the mudline for three-layered soil deposits

Table 11. Equivalent quantities for soil deposits with three layers

Scenario	S_{d_e}	z_{sc_e}	z_{sc_s}	X_{pyk}
1	S_d	z_{sc}	z_{sc}	-
2	$\frac{\gamma'_{i-1}}{\gamma'_i} S_d$	$z_{sc} + \left(\frac{\gamma'_{i-1}}{\gamma'_i} - 1\right)(D_{i-1} - S_d)$	$z_{sc} + X_{py2} + S_d - D_{i-1}$	$\int_0^{D_{i-1}-S_d} P_{ult\_py\_i-1} dH = \int_0^{X_{py2}} P_{ult\_py\_i} dH$
3	$\frac{\gamma'_{i-1}}{\gamma'_{i+1}} S_d$	$z_{sc} + \left(\frac{\gamma'_{i-1}}{\gamma'_{i+1}} - 1\right)(D_{i-1} - S_d) + \left(\frac{\gamma'_i}{\gamma'_{i+1}} - 1\right) D_i$	$z_{sc} + X_{py3} + S_d - D_{i-1} - D_i$	$\int_0^{D_i+X_{py2}} P_{ult\_py\_i} dH = \int_0^{X_{py3}} P_{ult\_py\_i+1} dH$
4	$\frac{\gamma'_{i-1}}{\gamma'_i} S_d$	z_{sc}	z_{sc}	-
5	$\frac{\gamma'_{i-1}}{\gamma'_{i+1}} S_d$	$z_{sc} + \left(\frac{\gamma'_i}{\gamma'_{i+1}} - 1\right) D_i$	$z_{sc} + X_{py5} + S_d - D_i$	$\int_0^{D_i} P_{ult\_py\_i} dH = \int_0^{X_{py5}} P_{ult\_py\_i+1} dH$
6	$\left(\frac{\gamma'_{i-1}}{\gamma'_i} - 1\right) D_{i-1} + S_d$	z_{sc}	z_{sc}	-
7	$\left(\frac{\gamma'_{i-1}}{\gamma'_{i+1}} - \frac{\gamma'_i}{\gamma'_{i+1}}\right) D_{i-1} + \frac{\gamma'_i}{\gamma'_{i+1}} S_d$	$z_{sc} + \left(\frac{\gamma'_i}{\gamma'_{i+1}} - 1\right)(D_{i-1} + D_i - S_d)$	$z_{sc} + X_{py7} + S_d - D_{i-1} - D_i$	$\int_0^{D_{i-1}+D_i-S_d} P_{ult\_py\_i} dH = \int_0^{X_{py7}} P_{ult\_py\_i+1} dH$
8	$\frac{\gamma'_{i-1}}{\gamma'_{i+1}} D_{i-1} + \frac{\gamma'_i}{\gamma'_{i+1}} D_i$	z_{sc}	z_{sc}	-
9	$\left(\frac{\gamma'_{i-1}}{\gamma'_{i+1}} - 1\right) D_{i-1} + \left(\frac{\gamma'_i}{\gamma'_{i+1}} - 1\right) D_i + S_d$	z_{sc}	z_{sc}	-

For soil deposits with more than three layers, the number of scenarios will increase further, but a similar methodology can be applied to derive the equivalent quantities. The derived expressions presented in Table 10 and Table 11 and the analysis procedure shown in Figure 27 comprise the proposed ESHaLE approach.

4.2.7 Example soil profile and single pile test

An example soil profile is chosen from the literature (Aygun, 2009) to illustrate the proposed methodology's results. To obtain a realistic soil profile for bridge foundations, fifty blueprints of existing South Carolina bridges were analyzed (Aygun, 2009). The profile chosen for this study is shown in Figure 31 and is typical of low lands stratigraphy. The soil profile consists of three layers, with each layer's properties specified based on typical soil conditions (Yang et al., 2008). The concrete pile for the bridge is assumed to be 18m in length with a 2m circular diameter, shown in Figure 31.

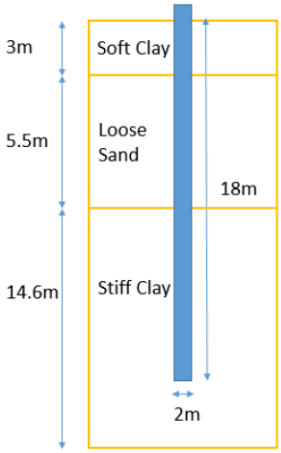

Figure 31. Representative soil profile and pile geometry

For this soil profile, the results from three models are shown to compare the outcomes from varying modeling approaches to evaluate the soil's ultimate resistance. The first model represents the basic approach with the simple removal of soil springs due to scour without modification. This model is referred to as "UMD" in the rest of this study, representing an *unmodified* soil model. The second model includes only the effect of layered soils, modeled using equivalent depth calculations. This model is referred to as "LEO" in the rest of this study, representing a model that accounts for the *layered effect*

only. The third model is the proposed *ESHaLE* model that includes both the soil stress history and layered soil effects. The comparison is conducted first between the UMD and ESHaLE models and next between the LEO and ESHaLE models.

Figure 32 shows the resulting ultimate lateral resistance of soil, comparing the UMD and ESHaLE models in 1m intervals along the depth of the pile with scour depths (S_d) ranging from 1m to 9m. Although 9m of scour is large relative to the structural dimensions, it is included for illustrative purposes to account for the extreme condition and the scenario such that the first two soil layers have been removed due to scour. At each scour depth, the solid line indicates the result from using the ESHaLE model; the dashed line indicates the result using the UMD model. Figure 32(a) compares the values of the ultimate lateral resistance of soil (P_{ult}) along the length of the pile as soil depth increases from the UMD and ESHaLE models. Figure 32(b) shows the percentage difference between the two models. The two boundary layers in the profile are also indicated.

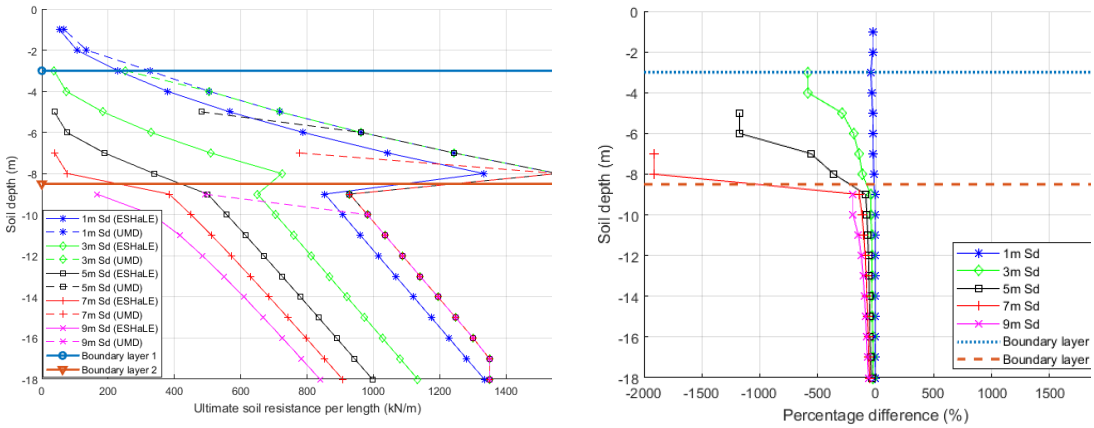

(a) (b)

Figure 32. (a) Comparison of ultimate lateral resistance (P_{ult}) between proposed ESHaLE and UMD models at varying scour depths and (b) percentage difference between the two models

In Figure 32, the UMD resistance curve is the same across scour depths except for the first point for each level of scour because, in the unmodified model, an increase in scour depth does not affect the soil behavior. The varying initial points are because the first point's resistance is assumed to be half of the next point. For the initial point, when scour depth is 1m, the difference between the ESHaLE and UMD models is relatively small. However, as scour depth increases, the maximum percentage difference increases significantly, up to 2000% in the sand layer for a scour depth of 7m.

Figure 33 shows the comparison of ultimate unit shaft resistance (T_{ult}) between the UMD and proposed ESHaLE models. Similar to the lateral behavior shown in Figure 32, the ultimate unit shaft resistance using the UMD model follows the same line regardless of the scour level except for the first point. At the first point, the differences between using the UMD and ESHaLE models can still be significant, with a maximum reduction of up to 700% in ultimate unit shaft resistance, occurring in the sand layer with 7m scour depth. Figure 33 shows that the ESHaLE model results in smaller soil resistance values along the pile's depth for all scour levels. This is because accounting for the layered soil effect in the proposed approach results in smaller equivalent depths than the physical depths used in the UMD model.

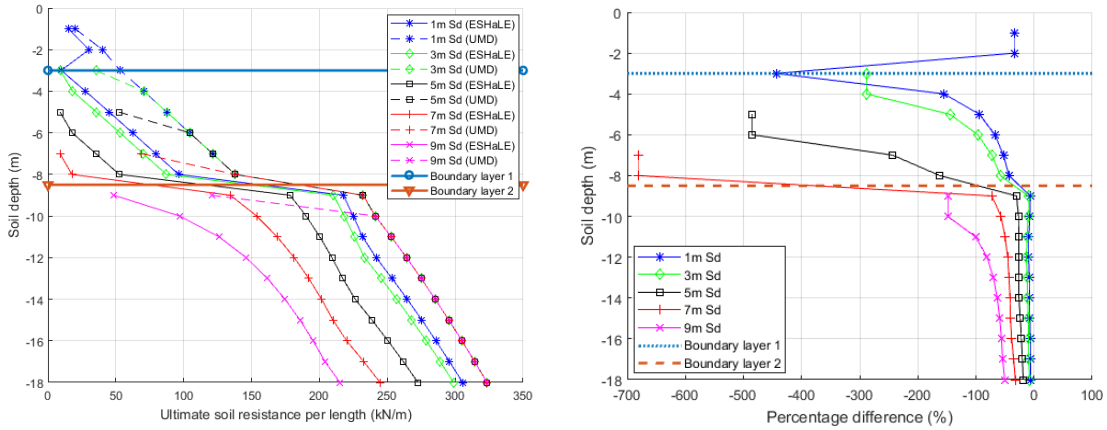

(a) (b)

Figure 33. (a) Comparison of ultimate vertical resistance (T_{ult}) between proposed ESHaLE and UMD models at varying scour depths and (b) percentage difference between the two models

The unmodified (UMD) model is usually adopted in practice, accounting for the effect of scour by simply removing the soil springs in the scoured area without considering any additional effects. Alternative existing models account for the layered effect only (LEO). A comparison between the LEO model and the proposed ESHaLE model – which accounts for stress history in addition to layered soil effects – has also been conducted. Figure 34(a) compares the calculated ultimate lateral resistance of soil (P_{ult}) along the depth of the pile that is obtained from using the LEO (dashed line) and proposed ESHaLE (solid line) models as scour depth increases. Figure 34(b) gives the percentage difference between the two models.

Several interesting points can be observed from Figure 34. First, there is a reduction of ultimate resistance for both LEO and ESHaLE models at the second interface for 1m and 3m scour depths due to the layered effect from the first two layers. Second, when the scour depth is larger than 5m, the stress history effect dominates. This is observed because clay's soil stress history reduces its ultimate lateral resistance while sand's stress history increases its resistance. In comparison, when the scour depth is less than 5m, the layered

effect is more pronounced, as is observed from the result from the third layer. Third, the importance of accounting for the stress history effect and not only the layered effect is observed, with a maximum percentage difference in the soil ultimate lateral resistance between the LEO and ESHaLE models of around 50%.

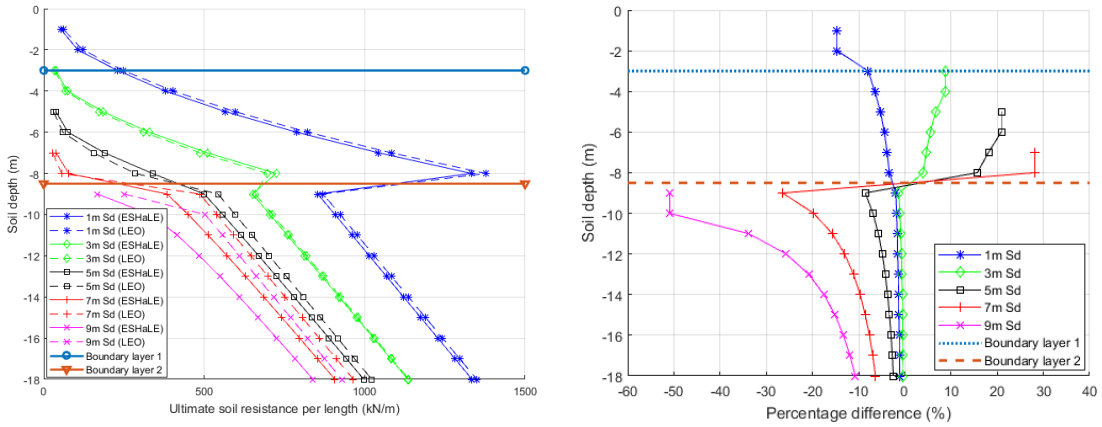

(a) (b)

Figure 34. (a) Comparison of ultimate lateral resistance (P_{ult}) between proposed ESHaLE and LEO models at varying scour depths and (b) percentage difference between the two models

Figure 35 shows the ultimate unit shaft resistance of soil (T_{ult}) between the LEO and ESHaLE models. Figure 35(a) shows that the stress history effect reduces the vertical resistance of clay because the unloading process associated with scour reduces the value of the undrained shear strength, which is proportional to T_{ult} of clay. In comparison, the stress history effect increases the vertical resistance of sand because both friction angle and unit weight increase in the presence of scour. Moreover, there is a reduction at the first boundary for both models due to loose sand yielding a smaller ultimate lateral resistance even after accounting for the contribution to the first layer's strength. Figure 35(b) shows the importance of accounting for stress history effects in addition to layered soil effects, as the maximum percentage difference between the LEO and ESHaLE models is close to 38%, occurring in the clay layer with a scour depth of 9m.

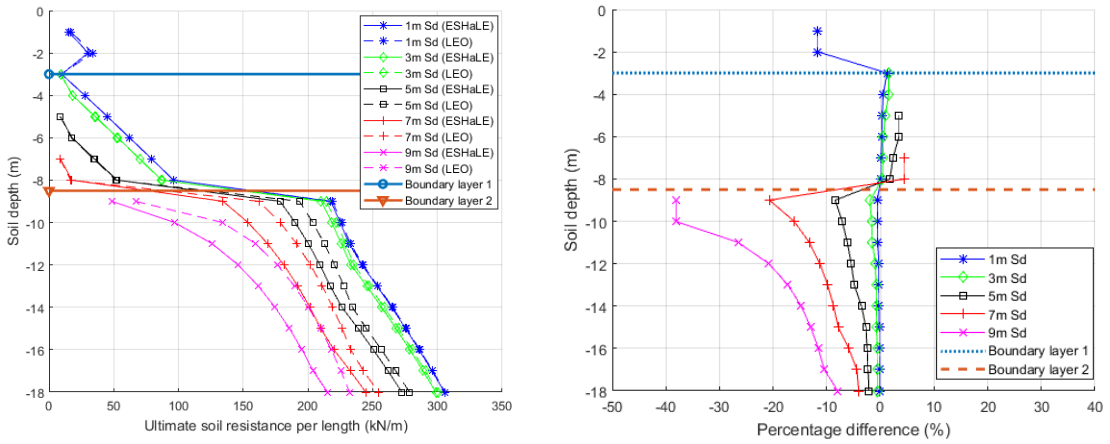

(a) (b)

Figure 35. (a) Comparison of ultimate vertical resistance (T_{ult}) between proposed ESHaLE and LEO models at varying scour depths and (b) percentage difference between the two models

Figure 36(a) presents a comparison among all three models in terms of ultimate bearing capacity (Q_{ult}) at varying scour depths. Figure 36(b) shows the percentage difference between the ESHaLE and LEO models and the baseline UMD model results. For this soil profile, the bearing resistance is provided by stiff clay only. Figure 36 shows the UMD and LEO models give a constant bearing resistance regardless of scour level. In comparison, the ESHaLE model results in a decreased calculated bearing resistance as scour depth increases. This is because the stress history effect reduces the undrained shear strength of the clay. The next section presents results regarding a single pile test with lateral and vertical loadings applied separately at the top of the pile considering the ESHaLE, LEO, and UMD soil models.

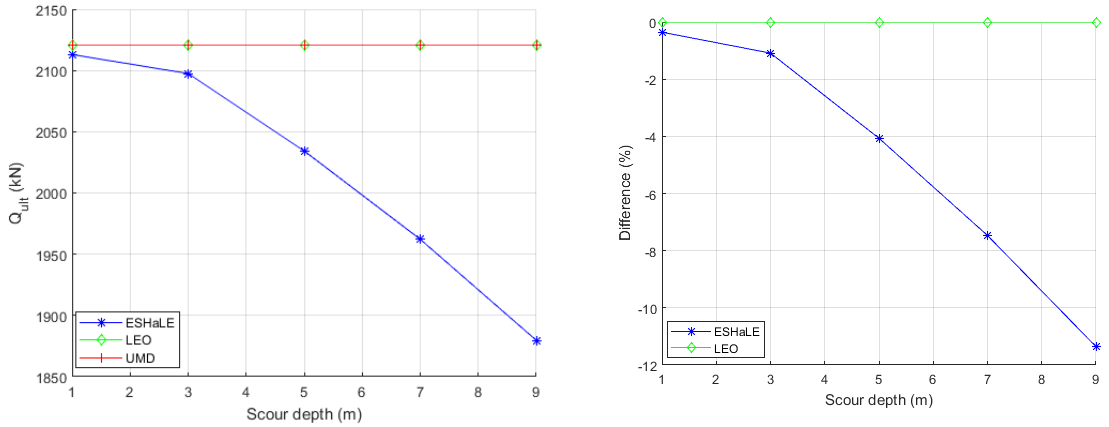

(a) (b)

Figure 36. (a) Comparison of ultimate bearing resistance (Q_{ult}) between proposed ESHaLE, LEO, and UMD models at varying scour depths and (b) percentage difference between the three models

4.2.8 Verification and single pile test

Verification of the proposed method with numerical and experimental results is now provided. An extensive review of the literature has shown that experimental data regarding scour effects on piles' structural performance is scarce. At the same time, numerical models that capture the impact of stress history in layered soils under scour conditions are also lacking in the literature. Therefore, the authors verify the proposed ESHaLE framework by parts, as indicated in Figure 27. Part 1 verifies the effect of stress history in homogeneous soils under scour using both experimental tests and numerical models. Part 2 verifies the layered effect using experimental results. Details regarding the verification of each part are now shown.

Comparing results from the ESHaLE model with results from experimental tests and numerical models in homogeneous soils considering scour provides verification of the stress history effects captured in ESHaLE. As only a homogeneous soil is presented, S_d =

S_{d_e} and $z_{pi} = z_{pi\_e}$, verifying the accuracy of the ESHaLE model within only an individual soil layer, but considering both stress history and scour effects. Verification is provided for both sand and soft clay. For the analysis in a sand foundation, for an initial condition, results from ESHaLE are compared with experimental field pile tests without scour as a baseline. Table 12 shows the uniformly-graded fine sand's soil properties from Mustang Island, Texas (Cox et al., 1974). As shown in Figure 37(a), the laterally loaded pile has a length, outer diameter, and thickness of 21.3m, 0.61m, and 0.0095m, respectively. The effect of scour is analyzed by comparing results from the ESHaLE model with those from a numerical model obtained using LPILE Plus 5.0 from Lin et al. (2010), considering a scour depth of 3m and the effect of stress history. The ESHaLE model is implemented in the finite element platform OpenSees (McKenna, 1997). Figure 37(b) presents the results for verification. Compared with the pre-scoured condition, 3m scour depth increases the lateral pile deflection at the ground line due to soil removal. The results from the ESHaLE model and numerical model from Lin et al. (2010) are close, with the discrepancy mainly due to the different selection of p-y relations between the two models. Lin et al. (2010) adopt the p-y relation from Reese et al. (1974), whereas the current study uses the p-y relation from API shown in Equation (48) available in OpenSees. The resulting difference between the two models is small, with an average difference of 8.0%.

Table 12. Properties of sand (Cox et al., 1974)

Critical friction angle (°)	Effective unit weight (kN/m^3)	Relative density (%)	Maximum void ratio	Minimum void ratio	Specific gravity
28.5	10.4	70 (depth ≤ 3m) 90 (depth ≥ 3m)	1.0	0.598	2.65

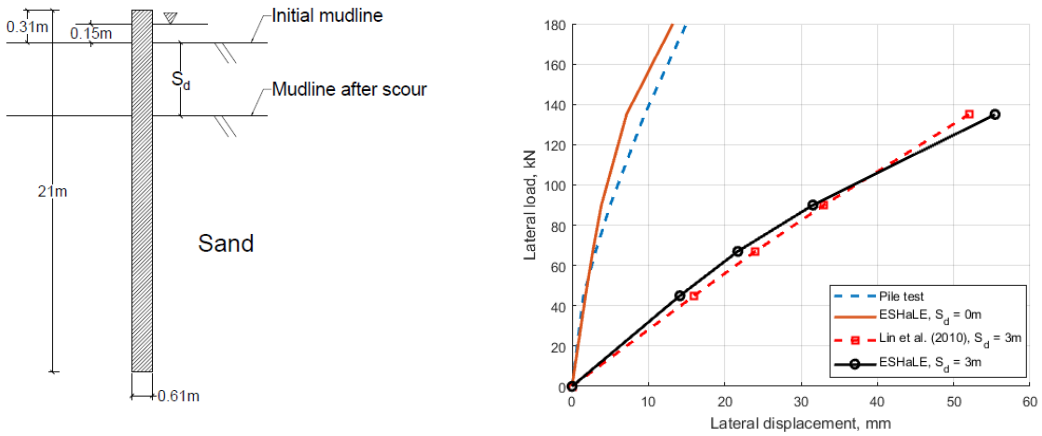

(a) (b)

Figure 37. (a) Laterally loaded pile in uniform fine sand and (b) deflection at ground line versus laterally applied load for measured data and numerical models with the effect of stress history under scour

Next, a similar verification process is performed for a single pile embedded in a clay foundation. The soil is soft clay near Lake Austin, Texas, with a pile test conducted by Matlock (1970) for baseline pre-scour conditions. The soil properties are listed in Table 13, and the undrained shear strength along the depth of the soil is shown in Figure 38 (Reese and Van Impe, 2001). Figure 39(a) shows the geometry of the laterally loaded pile in clay. Figure 39(b) shows the pile-head deflection versus laterally applied load for ESHaLE results compared to experimental and numerical results. The numerical result from Lin et al. (2014) is obtained using LPILE 5.0 considering the effect of stress history and scour. The value of scour depth (S_d) used for comparison is $10B$, where B is the diameter of the pile. The difference between the results from ESHaLE and the numerical model from Lin et al. (2014) is small due to the use of the same p-y relation (Matlock, 1970) and methodology to account for the effect of stress history, with an average difference of 2.3%.

Table 13. Properties of soft clay

Effective unit weight ($\mathbf{kN/m^3}$)	Water content (%)	Compression index	Swelling index	Strain at half of maximum stress	Effective friction angel (°)
10	44.5	0.38	0.076	0.012	20

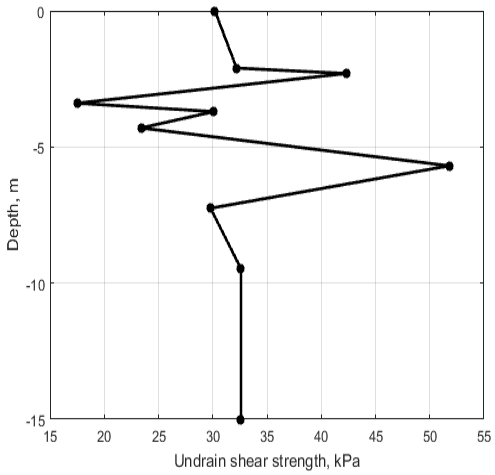

Figure 38. Distribution of undrained shear strength of soft clay measured by Reese and Van Impe (2001)

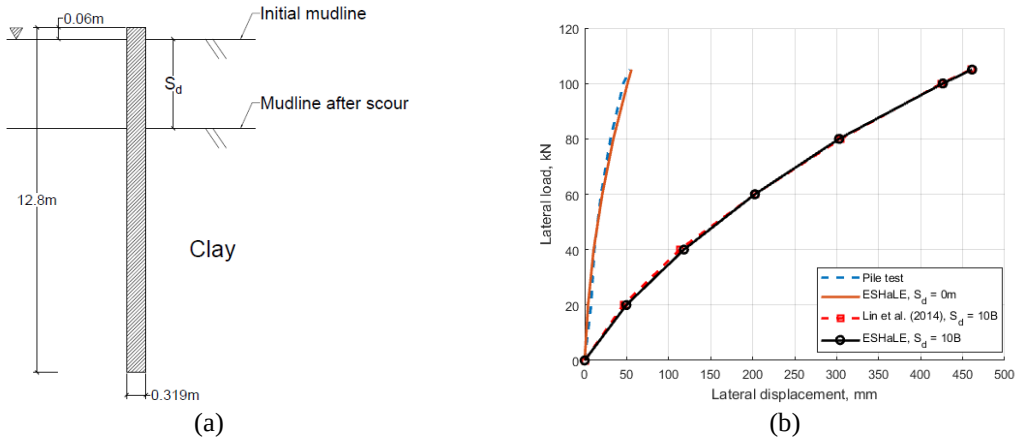

Figure 39. (a) Laterally loaded pile in soft clay and (b) pile-head deflection versus laterally applied load for measured data and numerical models with the effect of stress history under scour

The first part of the verification verifies the ability of ESHaLE to capture scour and stress history effects. The second part of the verification focuses on the proposed approach's ability to capture layered soil effects. Results from the ESHaLE model are compared with results from experimental tests for a single pile loaded laterally and vertically in layered soils under no scour conditions (S_d = 0) as shown in Figure 40(a) (Georgiadis et al., 1999). Note that the LEO model is equivalent to the ESHaLE model when considering responses in layered soils with no scour. Further verification between the ESHaLE and LEO models is conducted for single pile test results that follow. For the experimental test, the full-scale pile has a total length of 42.0m with a 3m diameter from ground level to a depth of 3.0m and 1.5m below this depth. The pile test is subjected to an axial load and subsequently to a lateral load using hydraulic jacks. The soil profile is derived from a geotechnical site investigation. Figure 40 shows the details regarding the pile geometry, design soil profile, and the ESHaLE model's verification with experimental results in terms of the lateral and vertical displacements versus applied loads. The results show close agreement between the results from the ESHaLE model and those from the pile test, especially in the lateral direction, where the displacement differences range from 0.2mm to 2.2mm, with an average percent difference of 7.1%. For the vertical direction, the larger difference between the numerical and experimental results, with displacement differences ranging from 0.2mm to 2.4mm and an average percent difference of 27.1%, is mainly due to the lack of information regarding the modeling of the q-z behavior of the bottom soil layer. The bottom layer consists of interbedded dense sand and stiff clay, but the finite element platform OpenSees only allows modeling of q-z relations with homogenous soil types. The authors have found that the ultimate end-bearing capacity and

the choice of q-z relation used at the base of the pile to simulate soil-structure interaction will impact the overall results. Note that the verification results in this section are comparable to the verification of previous numerical models with experimental test results, where, for example, in Georgiadis et al. (1999), displacement differences range from 0.0mm to 3.0mm with an average percent difference of 6.0% for lateral loads. Displacement differences range from 0.0mm to 7.5mm, with an average percent difference of 19.9% for vertical loads.

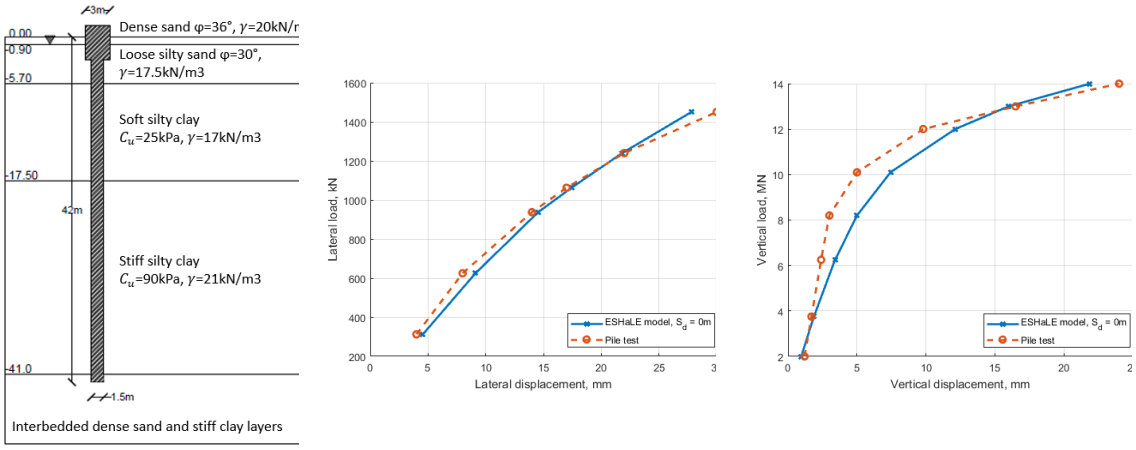

(a) (b) (c)

Figure 40. (a) Setup of pile test and soil profile (Georgiadis et al., 1999), (b) lateral load versus pile head lateral displacement, and (c) axial load versus pile settlement for ESHaLE model compared with experimental pile test in layered soil

The proposed ESHaLE model is now implemented and compared to prior models through investigating the lateral and vertical responses from the ESHaLE, LEO, and UMD models for a single pile test in the soil profile shown in Figure 31. Note that the proposed ESHaLE model results would be identical to those from the LEO model under zero scour conditions. The results, shown in this section, also explore the structural performance across scour depths of a laterally- and vertically-loaded pile in layered soil considering the different soil models under static loading. Figure 41(a) presents the geometry, applied loads, and composition of the layered soil used in this example. The pile has a diameter of

2m, embedded length of 18m, and pile head length of 1m, and it is modeled as a beam on a nonlinear Winkler foundation using OpenSees. The pile consists of 19 displacement-based beam-column elements with discretized length of 1m between nodes, and the constitutive material is assumed to be linear elastic for simplicity. Figure 41(b) shows the modeling of the soil-structure interaction. The soil springs, consisting of p-y, t-z, and q-z springs, are modeled using zero-length elements with uniaxial material assigned in lateral and vertical directions separately. This analysis considers applying a lateral load (P_h) of 1000 kN and a vertical load (P_v) of 2000 kN in the positive x-direction and negative z-direction, respectively.

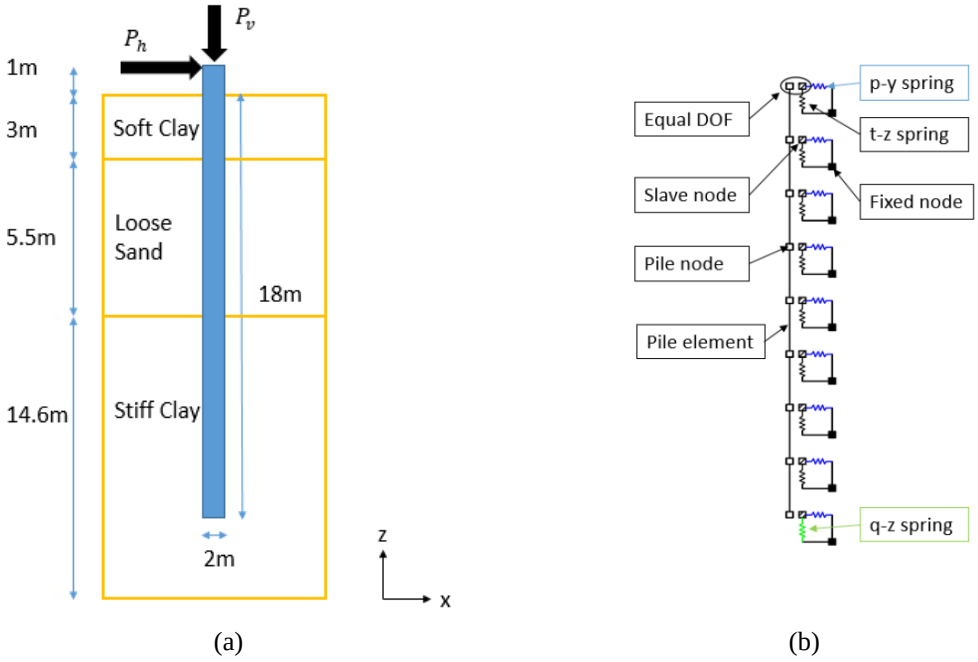

(a) (b)

Figure 41. (a) Schematics of single pile and (b) modeling of the soil-structure interaction with lateral and vertical loadings applied separately in layered soil

Figure 42(a) shows results for the displacement along the pile under a laterally applied load (P_h) with varying scour depths of 0m, 1m, and 3m. The main observations are as follows. First, the ESHaLE and LEO models' lateral responses converge at 0m scour

depth as no scour event has occurred. A minimal difference between the ESHaLE and LEO models is observed at 1m scour depth, which indicates the impact of stress history on piles' lateral behavior is limited for small scour depths in terms of pile deflection. As scour level increases, the difference between the ESHaLE and LEO increases, indicating the effect of stress history on the response. Second, the UMD soil model gives unreliable deflection results because the UMD model assumes no change has been made to soil parameters (i.e., P_{ult}, T_{ult}, and Q_{ult}) in the presence of scour and neglects the influence of the layered soil effect. The difference, i.e., error, between the UMD and the other two models increases as the scour level increases. Figures 42(b) and 42(c) present the corresponding shear and moment diagrams along the pile in response to the laterally applied load.

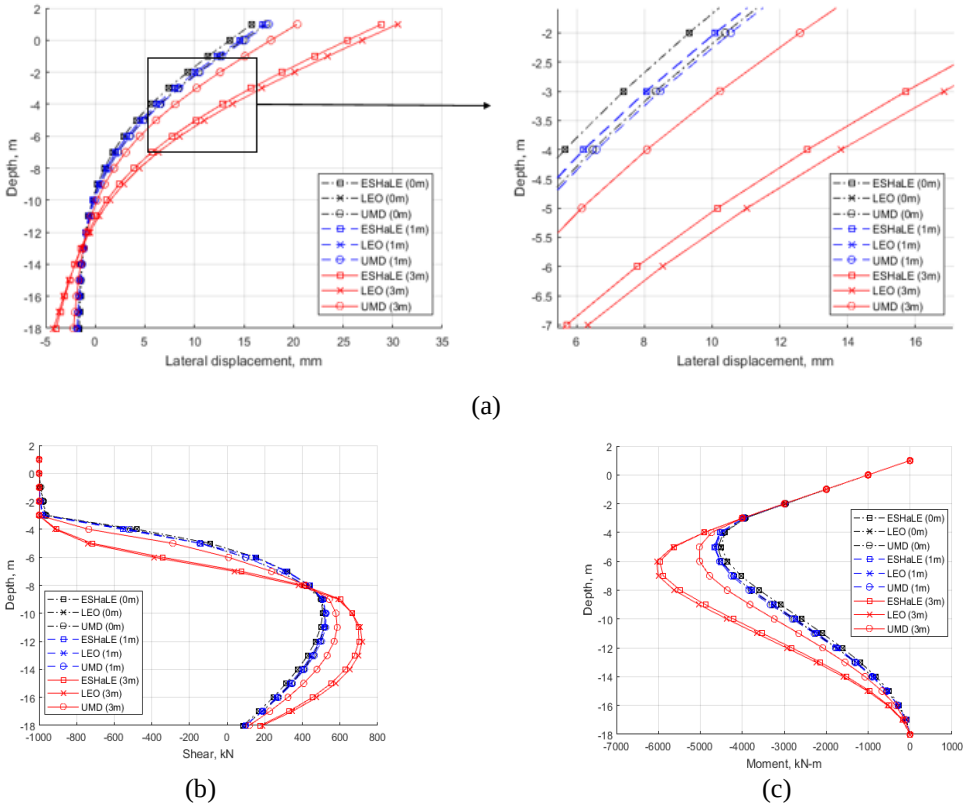

Figure 42. (a) Lateral displacement, (b) shear, and (c) moment diagrams along a single pile considering three soil models and varying scour depths under the laterally applied load

To examine the pile's vertical performance considering varying scour depths and different soil models, Figure 43(a) shows the maximum axial displacement of the pile after applying a vertical load of 2000 kN at the pile head considering varying scour depths. Consistent with previous soil responses, the pile with the ESHaLE model exhibits the highest axial displacement with a maximum increase of more than 110% at a scour depth of 9m compared to the UMD model's response shown in Figure 43(b). Unlike the response from the laterally-loaded pile, the impact of stress history is significant in terms of the axial response, with a maximum increase of 30% between the ESHaLE and LEO models at a scour depth of 9m. The difference is mainly attributed to the reduction of end-bearing capacity with the inclusion of stress history in ESHaLE, as shown in Figure 36. In Figures 39 and 40, as expected, the difference between the ESHaLE and previously verified LEO model is minimal at minimum scour depths. Finally, while results are shown here for single pile foundations, the ESHaLE model will also work for pile groups with the note that the ESHaLE model is only valid under the assumption of a general scour scenario. For cases where local scour effects are of interest, the scour hole geometry will impact single piles and pile groups differently. Future research can incorporate the ESHaLE model and the influence of scour hole geometry in layered soils for both single piles and pile groups.

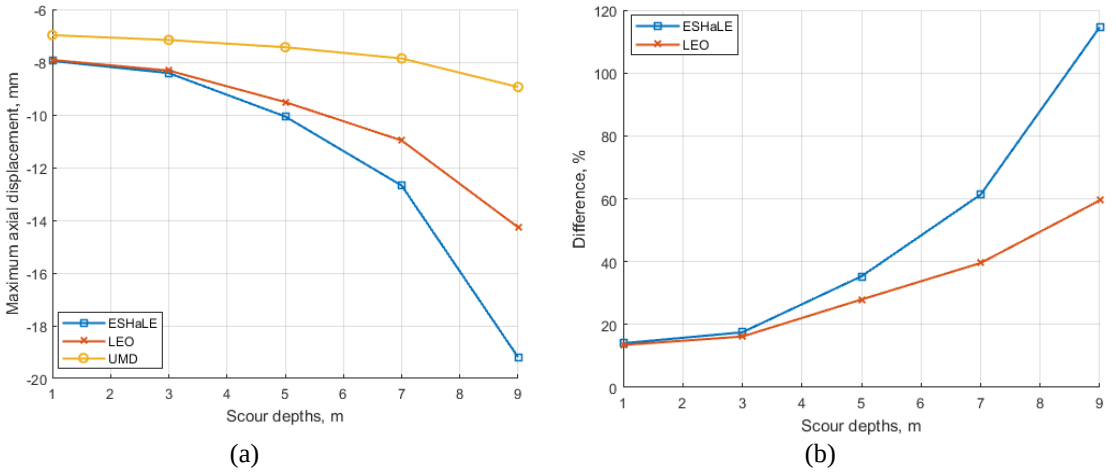

(a) (b)

Figure 43. (a) Comparison of maximum axial displacement of the single pile between ESHaLE, LEO, and UMD models at varying scour depths and (b) percentage difference between the three models

The next section shows how the differences in calculated soil properties (i.e., the varying ultimate soil resistance values shown in this section) from using the ESHaLE compared to layered effect only and unmodified soil models impact the vulnerability of full-bridge structures under scour conditions. The impact is investigated considering the dynamic response of a bridge analyzed using varying soil models.

4.2.9 Bridge geometry and modeling details

The bridge studied is of a common single-bent concrete box-girder type with an integral pier (Mackie and Stojadinovic, 2003). The bridge type is selected for illustrative purposes, and previous research (Wang et al., 2014) having also used this bridge type for the study of scour phenomenon. The bridge has a span length of 36.6m and a 2m wide circular column diameter with a height of 10m. The deck's cross-section is a 4-cell box girder with reinforced concrete construction with a total width of 11m and depth of 2m. A Type I pile shaft foundation is used, and the length of the embedded pile shaft is assumed

to be 1.75 times the length of the column above grade. Figure 44 shows the longitudinal and transverse views of the selected bridge type. The corresponding dimensions of the bridge are shown in Table 14. Further bridge details can be found in Mackie and Stojadinovic (2003). The soil profile for the bridge evaluation is as shown in Section 3.3. The profile consists of three soil layers of soft clay, loose sand, and stiff clay from top to bottom.

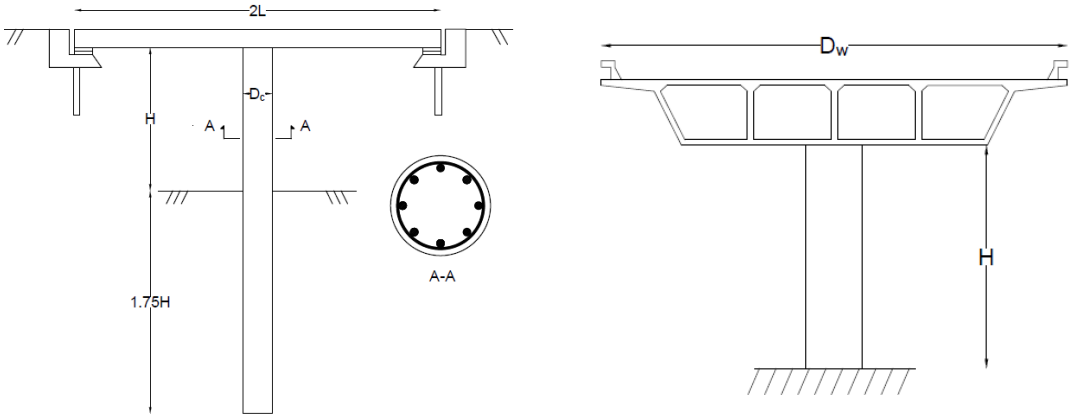

Figure 44. (a) Longitudinal view of the single-frame box-girder concrete bridge and (b) transverse view

Table 14. Geometric parameters of the selected bridge

	Span Length (L), m	Column height (H), m	Column diameter (D_c), m	Deck width (D_w), m
Single-bent box-girder bridge	36.6	10.0	2.0	11

A finite-element model of the bridge is built in the software OpenSees. For the substructure, the bridge column is modeled using a single force-based element with fiber discretization in the cross-section. Four integration points along the column are used to capture the flexural response. The "Concrete02" material model is used for the concrete's

uniaxial constitutive behavior. The column's confinement effect is captured through special treatment of the concrete fiber's stress-strain behavior (Mander et al., 1988). The "Steel01" material model is used for the uniaxial reinforcement material with linear hardening behavior. The pile foundation is implemented using multiple force-based elements with two integrations points (He et al., 2016), consisting of the same fiber discretization as in the column section.

For the superstructure, the deck is modeled using linear elastic beam-column elements. The abutment modeling adopts the SDC 2004 abutment model (Mackie and Stojadinovic, 2006), and it is assumed to be a seat-type abutment with an initial gap of about 150mm (Priestley et al., 1996). The abutment model consists of longitudinal, transverse, and vertical nonlinear abutment responses. In particular, the longitudinal system response considers the responses of the elastomeric bearing, gap, abutment pile, backfill material, and impact between the deck and abutment backwall. The transverse response considers system responses of the elastomeric bearing, wing walls, abutment piles, and backfill material. The abutment model's vertical response is assumed to be affected only by the bearing pad's vertical stiffness. Two bearing pad springs with 50mm depth (Mackie and Stojadinovic, 2003) have also been added to the bridge models. The elastomeric bearing modeling uses nonlinear springs with perfectly-plastic behavior, and yield displacement of the bearings is assumed to be at 150% of the shear strain.

The modeling of soil-structure interaction (SSI), as shown in Figure 41(b), is implemented using the dynamic p-y method to explicitly account for SSI effects while maintaining an acceptable computing time for probabilistic analyses (Wang et al., 2014). The nonlinear p-y and q-z behaviors are conceptualized as consisting of elastic, plastic, and

gap components in series; the nonlinear t-z behavior is conceptualized as consisting of elastic and plastic components in series. Further details regarding this method can be found in Boulanger et al. (1999). The foundation pile is modeled as a beam on a nonlinear Winkler foundation. Lateral SSI is captured by a p-y spring, while vertical axial friction and tip bearing capacity are captured by t-z and q-z springs, respectively. This study assumes stiff clay and soft clay share the same p-y relation due to the limited set of p-y relations implemented in OpenSees, and the fact that the p-y relation for stiff clay without free water does not soften after reaching peak stress (Welch and Reese, 1972). Note that the proposed ESHaLE framework will be valid regardless of the modeled behavior of the soil p-y relation. In specifying the soil spring properties, the three varying soil models (ESHaLE, LEO, and UMD) are implemented in OpenSees to capture differences in the soil response.

4.2.10 Seismic response of bridge with layered soils

To assess the bridge response in detail, this section presents the bridge's seismic response under a particular ground motion shown in Figure 45. Fragility assessment of the bridge under a suite of ground motions is presented in the following section. The ground motion is selected from the PEER database (Baker et al., 2011) with two horizontal components and one vertical component, as shown in Figure 45. The ground motion name is Loma Prieta, with a magnitude of 6.93 and shear wave velocity in the top 30m of 489 m/s. The seismic analysis is implemented through a uniform input across the soil depth (Shang et al., 2018). Five scour levels are considered for this section: scour depths of 1m, 3m, 5m, 7m, and 9m. Nonlinear response history analyses are run, and the performance of critical bridge elements is evaluated. The critical responses include the column's vertical

displacement, the curvature distribution of the bridge column, and the transverse and longitudinal deck displacements.

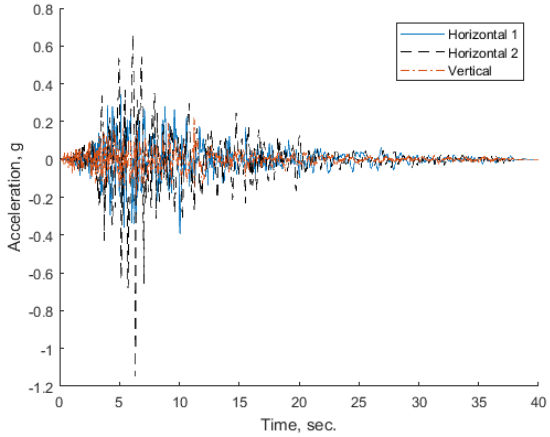

Figure 45. Three components of the selected ground motion

Excessive vertical displacement of the column could lead to the bridge deck's local failure due to concrete crushing in the compression region. Figure 45 presents the column's maximum vertical displacement at each scour depth using the three soil models. Figure 45 shows that when the scour depth is less than 3m, the LEO model exhibits slightly larger vertical displacements among the three soil models because sand's stress history effect becomes the governing factor, increasing the vertical resistance. However, the trend changes at higher scour depths. From Figure 45(b), looking over the full time history, there is an increase of 16% and 10% in calculated vertical displacement between the ESHaLE versus UMD and LEO versus UMD models, respectively. These values indicate underestimating the vertical displacement response if analyses do not properly account for both the stress history and layered soil effects.

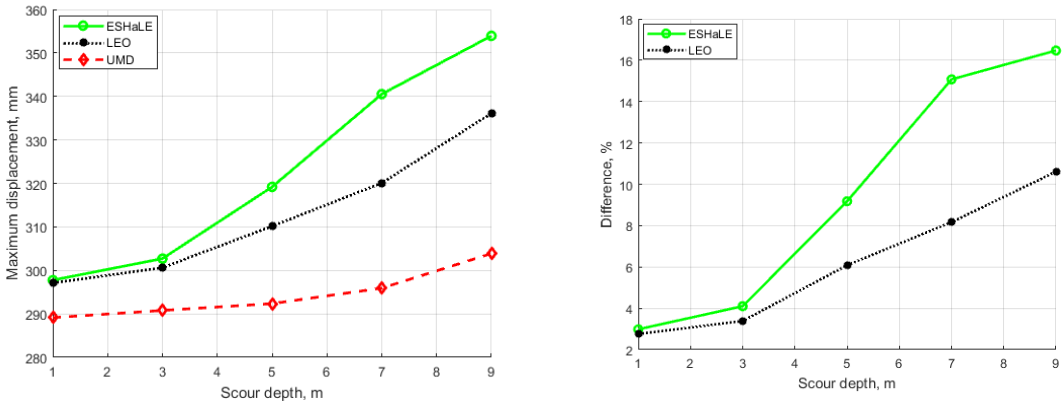

(a) (b)

Figure 45 (a) Maximum vertical displacement of the column for varying scour depths considering three soil models and (b) percentage differences between ESHaLE versus UMD models and LEO versus UMD models

Figure 46 presents the maximum curvature distribution along the column and pile for the five different scour levels. The curvature distribution, shown in Figure 46, accounts for both the transverse and longitudinal directions through their geometric mean. Excessive curvature demand could lead to flexural failure of the column. The results in Figure 46 lead to several observations. First, the maximum curvature distribution of the ESHaLE model and LEO models are close to each other regardless of changes in scour depth, implying that the stress history effect has a limited influence on the lateral behavior of the vertical element. Second, due to the layered effect, the maximum curvature distributions of the ESHaLE and LEO models begin to deviate from the UMD model from a scour depth of 3m onward. The maximum curvature distribution changes by decreasing the relative curvature at the top of the column and the portion below the mudline level for the ESHaLE and LEO models compared with the UMD model. This is because of the redistribution of forces along the pile since the change of soil stiffness influences the structural member's deformation. Third, the largest maximum curvature demand always occurs in the UMD model due to the stiffer soil model without accounting for the layered soil effects. Fourth,

the magnitude of the maximum curvature distribution for all three cases decreases as scour depth increases due to the lengthening of the structural period and reduction of seismic force attracted. In addition to the maximum curvature distributions, Figure 47 presents hysteresis loops at the top of the bridge column where maximum curvature occurs considering the three different models. Figure 47 shows both transverse and longitudinal moment-curvature responses of the column. The results are consistent with those from Figure 46, showing inelastic behaviors and the largest curvature value in the UMD model.

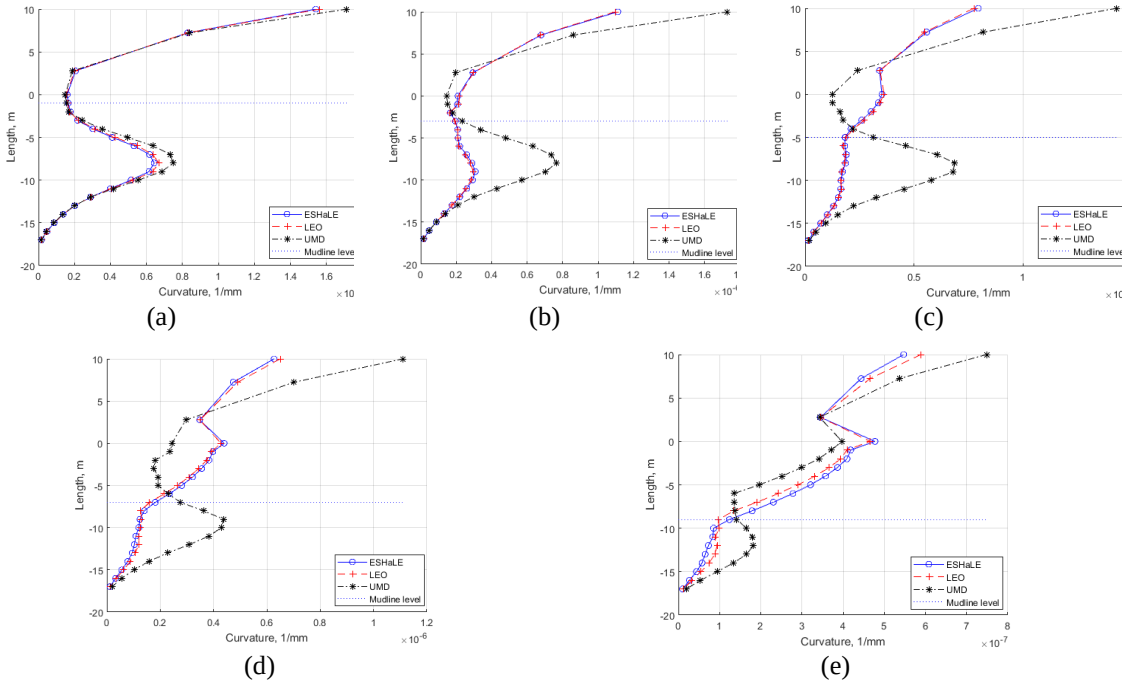

Figure 46. Curvature envelope along column and foundation pile using the three soil models considering (a) 1m, (b) 3m, (c) 5m, (d) 7m, and (e) 9m scour depths

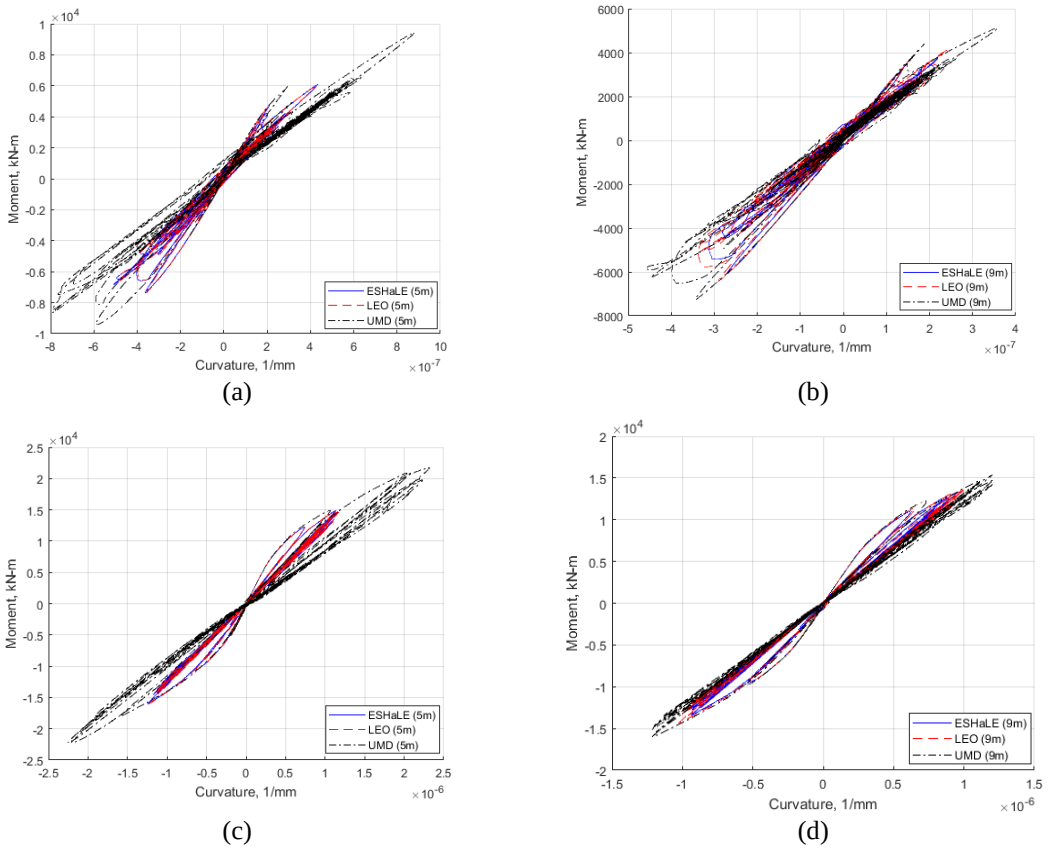

Figure 47. Moment-curvature responses of the column in (a) & (b) transverse and (c) & (d) longitudinal directions for scour levels of (a) & (c) 5m and (b) & (d) 9m

Finally, the horizontal displacement of the deck is also evaluated. Excessive displacement of the deck at the seat abutments could lead to unseating of the bridge deck. For brevity, the time-history responses of the bridge deck for only two levels of scour of 5m and 9m are shown in the transverse (Figures 48(a) and 48(b)) and longitudinal (Figures 48(c) and 48(d)) directions, respectively. From Figure 48, one observes that first, there is only a small difference in terms of maximum displacement exhibited among the three soil models, especially in the longitudinal direction. Second, the lower scour level (i.e., 5m) leads to a higher displacement demand than the higher scour level (i.e., 9m) in the transverse direction. This is due to the increasing structural period with scour depth, decreasing the attraction of seismic force at higher scour levels. Third, a residual

displacement is observed from the deck's time-history response in the transverse direction, with the UMD model resulting in a higher residual displacement than the other two models. The authors have found that the difference of residual displacement among the three models is due to several factors, including characteristics of the ground motion, soil modeling, and scour level after investigating the bridge deck's residual displacement considering multiple ground motions. The next section provides an assessment of the three soil models considering multiple ground motions using fragility analyses.

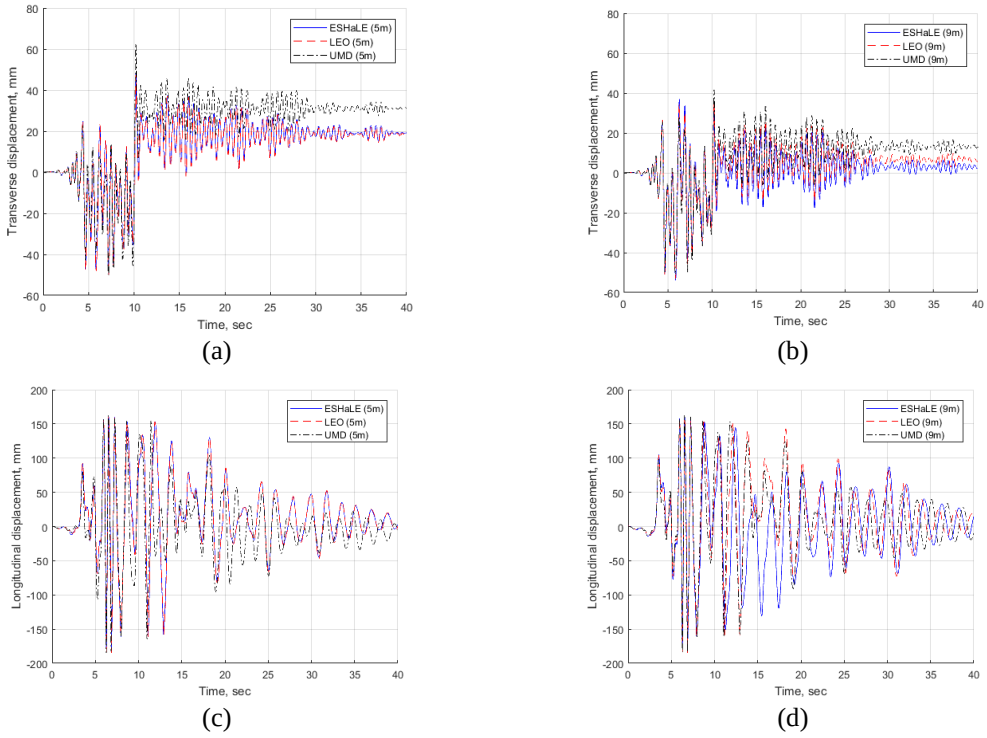

Figure 48. Time history response of deck (a) & (b) transverse and (c) & (d) longitudinal displacement for scour levels of 5m and 9m

4.2.11 Fragility assessment of bridges with layered soils

A total of 59 ground motions with two horizontal components and one vertical component are considered for fragility assessment. The ground motion suite is chosen from the PEER database (Baker et al., 2011), and the spectral accelerations for all three components are shown in Figure 49. Note that the current study only focuses on uncertainty in ground motions with the assumption that the same uncertainties exist between the proposed and existing models because the goal of the study is to present a new soil model (ESHaLE) that is capable of capturing the impact of stress history of the layered soil in both lateral and vertical directions. The uncertainties associated with the soil profile, e.g., layer thickness, soil composition, etc., as well as uncertainties in the soil properties will influence the bridge fragility assessment. However, these analyses, including the effects of uncertainties, are outside the scope of the current study and would be an interesting topic for future studies on bridge performance.

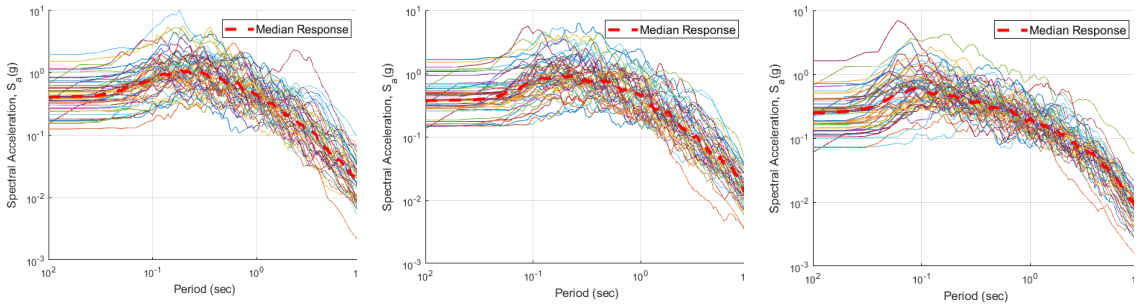

Figure 49. Spectral accelerations of ground motion suite for (a) horizontal component one, (b) horizontal component two, and (c) vertical component

Here, analytical fragility curves are computed by running a series of nonlinear time history analyses on deterministic bridges. Several previous studies have adopted this methodology for fragility assessment (Choi et al., 2004; Nielson and DesRoches, 2007a,

2007b; Padgett, 2007; Zhang et al., 2019a). The uncertainty considered in this fragility assessment is in a variation of ground motions. The column fragility is expressed as the probability of exceeding some damage state for a specific intensity measure. This probability of failure P_f can be expressed as a function of parameters of the capacity and demand variables assuming both follow a lognormal distribution as shown in Equation (61).

$$P_f = \Phi\left(\frac{\ln S_d/S_c}{\sqrt{\xi_d^2 + \xi_c^2}}\right) \tag{61}$$

$\Phi(\cdot)$ is the standard normal cumulative distribution function. S_d and S_c are the median parameters for the demand and capacity distributions, respectively, and ξ_d and ξ_c are the lognormal standard deviation of the demand and capacity distributions, respectively.

Following the previous section's findings, the engineering demand parameters are selected to be the column's vertical displacement and curvature ductility. As the ESHaLE model results in a reduced curvature demand compared with the UMD model, as shown in Figure 46, column curvature is expected to yield a decreased curvature demand compared with the UMD model. The stress history of layered soils has a less significant impact on the curvature demand due to a large portion of bridge lateral stiffness contributed from the abutments. In terms of lateral bridge performance, a curvature ductility (μ_ϕ) value of 12 is selected to be a threshold value to describe the column's flexural failure due to buckling of the longitudinal reinforcement in post-1990s bridge designs (Ramanathan et al., 2012). Note that the bridge column's shear failure is not considered in this study as it is less likely to occur for this bridge type where the column and pile shaft share the same cross section. Increasing the unbraced length due to scour leads to a larger shear span to depth ratio,

which could increase flexural cracking and reduce shear strength (Sezen and Moehle, 2004). However, the reduction of seismic demand due to scour for this bridge type (Zhang et al., 2019b) decreases the probability of shear failure.

In terms of the performance of the bridge deck, bridge deck deflection limits are considered. AASHTO (2012) defines a serviceability limit of L/800 for the bridge deck deflection. Assuming the bridge deflection limit goes beyond the serviceability limit, this study uses L/250 as the fragility assessment threshold. This value is selected based on previous studies of bridge inspections (Roeder et al., 2002). In that study, the largest deflection measured among inspected bridges after applying HS20-44 standard truck loading was a critical deflection of L/264 in the center span as experienced by the US-50 bypass bridge. As such, a similar value is used as a benchmark to evaluate the bridge deck deflection under a larger loading. Note that other limit states can also be chosen. For example, the bridge deck can be modeled with nonlinear elements to capture the bridge deck's nonlinear behavior and an instance of material failure (i.e., crushing of concrete or buckling of reinforcement). Such limit states can be defined, and the proposed ESHaLE method can be applied for analysis without loss of generality.

Fragility curves for column lateral performance are shown in Figure 50 for 1m, 3m, 5m, 7m, and 9m scour depths. Based on the results, the failure probabilities obtained from all three models are consistent with the results presented previously. The results show the following: first, as scour levels increase, the probabilities of exceeding the collapse damage state for all three models decrease. This is because, for this bridge type, the removal of soil springs due to scour lengthens the fundamental period of the bridge, reducing the seismic demand (e.g., the curvature ductility demand) and acting as base isolation in the presence

of a more flexible foundation system. This phenomenon is also observed in Wang et al. (2014). The decrease in failure probability can also be due to the characteristics of the selected bridge type. In contrast to having a relatively flexible connection (i.e., elastomeric bearing) between the bridge deck and column, the integral connection enables the superstructure and substructure to act as a whole and restrains the column from displacing excessively under scour conditions. A different soil type could also influence the bridge response by providing different stiffness in the presence of scour. Second, the results show that the UMD model yields the highest failure probabilities among the three models across all scour levels. This is because the UMD model produces stiffer soil springs since it is accompanied by a higher value of lateral resistance, as shown in Figure 46, attracting a greater seismic demand. Third, by comparing the fragility curves between the ESHaLE and LEO models, the impact of stress history is more influential at low scour levels (e.g., 1m) with a slightly higher failure probability from the LEO model because the low scour level is accompanied by the attraction of a higher seismic force. The impact of the stress history of layered soils on lateral bridge performance is minimal at higher scour levels.

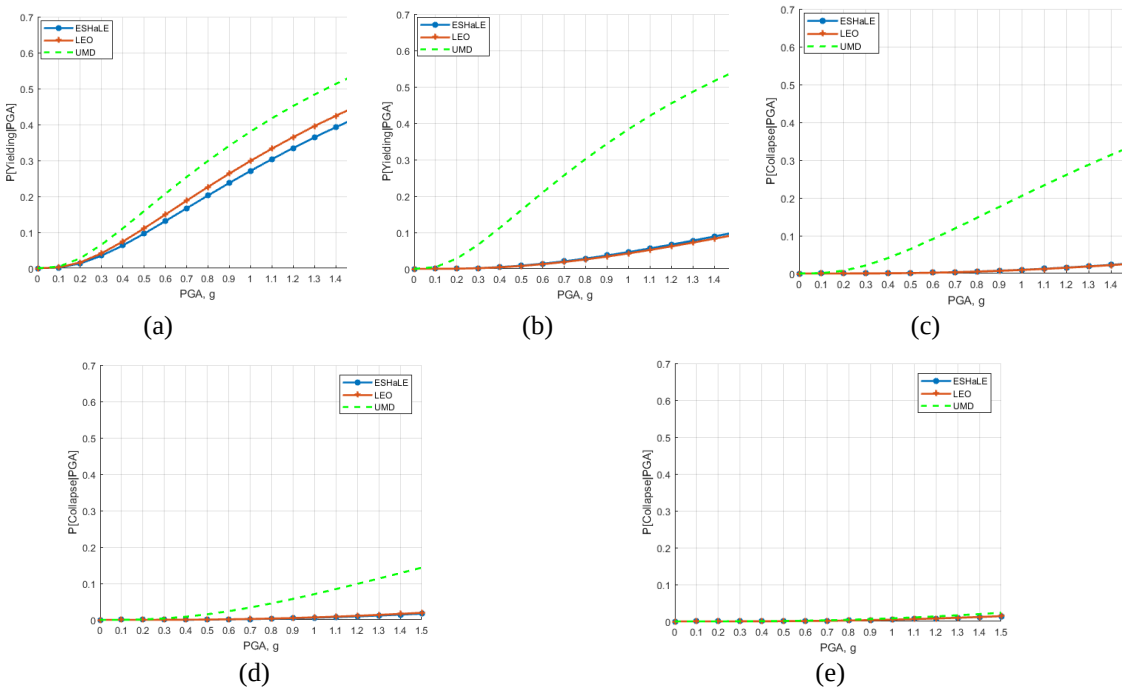

Figure 50. Probability of exceeding flexural failure of bridge column using the three soil models for (a) 1m, (b) 3m, (c) 5m, (d) 7m, and (e) 9m scour levels

Figure 51 presents the demand distribution of bridge deck deflections as a function of peak ground acceleration (PGA) for 1m, 3m, 5m, 7m, and 9m sour levels after performing 59 nonlinear time history analyses for each scour depth. Figure 52 summarizes the mean values from Figure 51 and shows that the proposed model exhibits the highest deflection among the three models. There is a maximum increase of 16% and 8% for the ESHaLE versus UMD models and the LEO versus UMD models, respectively. The ESHaLE model results in a larger increase in the mean value of the deck deflection because as scour depth increases, the contribution of side friction reduces due to the removal of t-z springs, which in turn increases the contribution of the tip resistance. As a result, based on Figure 36, the ESHaLE model has lower resistance at larger scour depths than the other models.

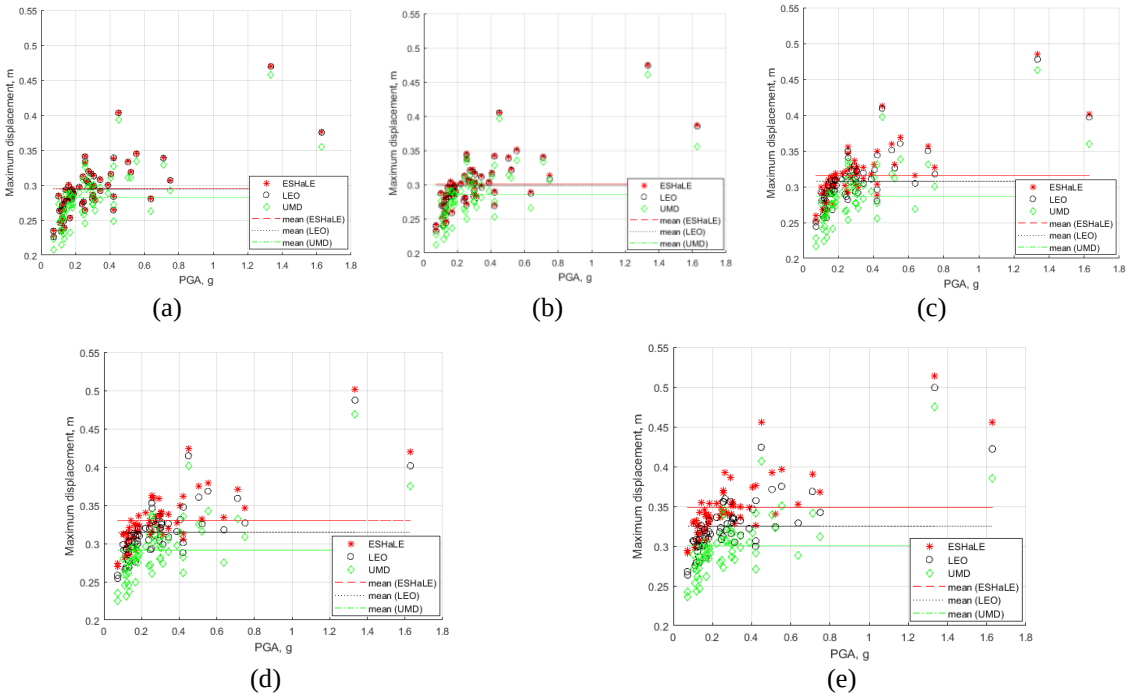

Figure 51. Maximum vertical displacement of bridge deck versus PGA for (a) 1m, (b) 3m, (c) 5m, (d) 7m, and (e) 9m scour depths

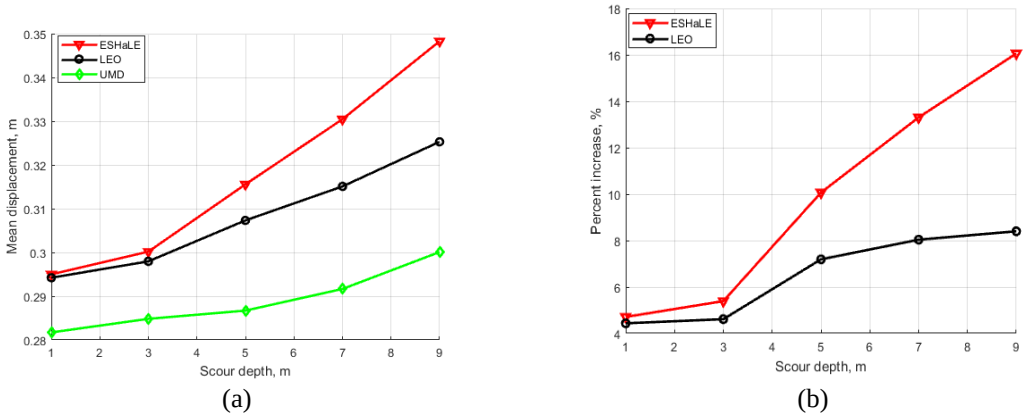

Figure 52. (a) Mean deflections of bridge deck versus scour depth and (b) percent increase between the ESHaLE and UMD and LEO and UMD models

Fragility curves for vertical displacement of the column are presented in Figure 53 for 1m, 3m, 5m, 7m, and 9m scour depths. The fragility assessment results are consistent with the component-level column vertical displacement responses presented in Figure 45. When the scour depth is less than 5m, the LEO model results in a higher probability of

exceedance as the sand layer's stress history effect increases the soil's vertical resistance. However, when the scour depth is 5m or larger, the ESHaLE model yields a higher probability of exceedance. Figure 54 presents the probability differences among the three soil models based on the results shown in Figure 53. Figure 54(a) gives the probability difference between the ESHaLE and LEO models, with a maximum probability difference of around 25% at 9m scour depth. Figure 54(b) gives the probability difference between the ESHaLE and UMD models, with a maximum probability difference of around 46% at 9m scour depth. Both Figures 54(a) and 54(b) show that the impact of including the stress history effect in bridge vulnerability assessment is magnified and becomes more critical as scour depth increases.

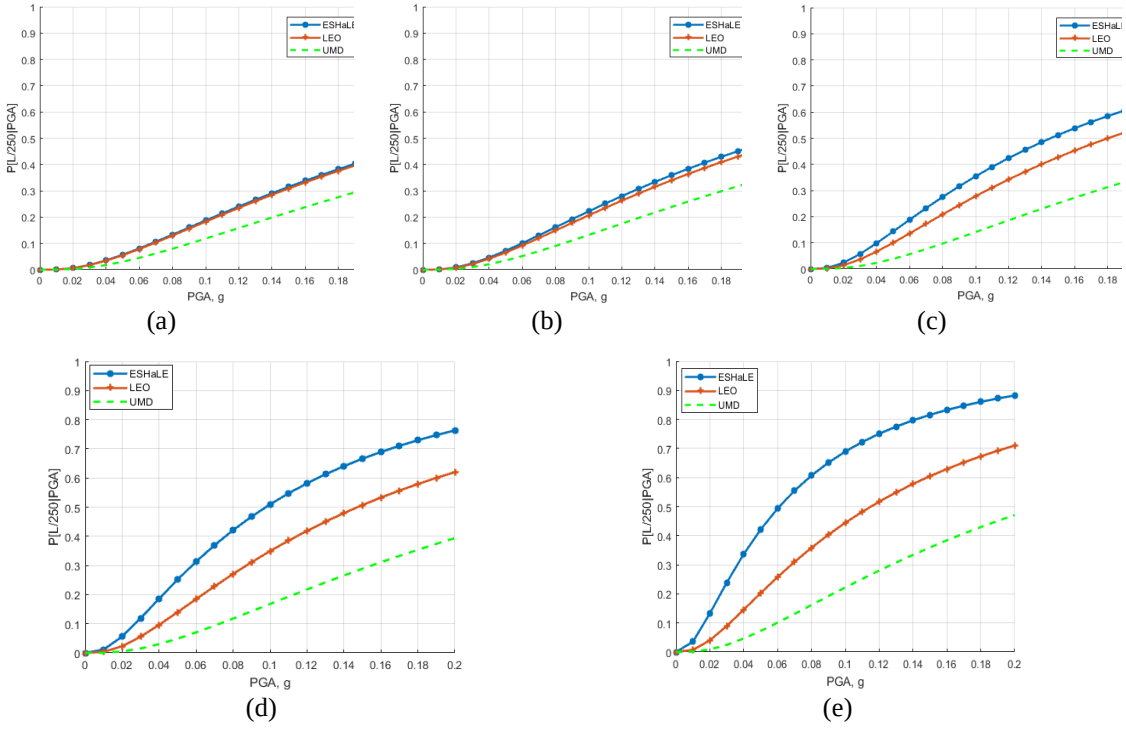

Figure 53. Probability of exceeding L/250 deflection of bridge deck using the three soil models for (a) 1m, (b) 3m, (c) 5m, (d) 7m, and (e) 9m scour levels

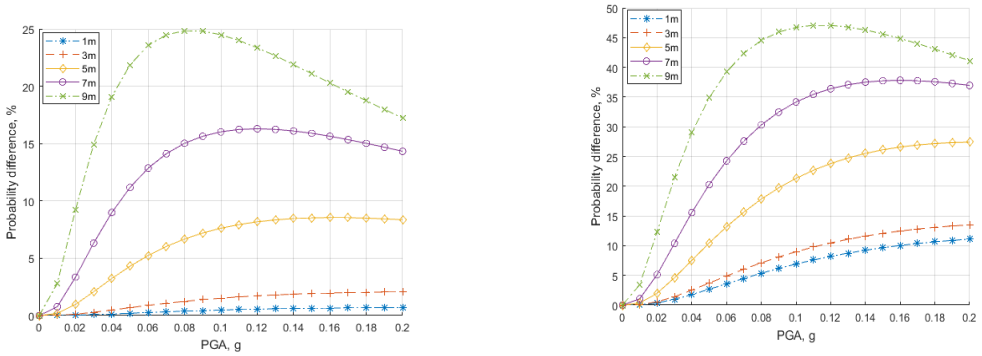

Figure 54. Probability differences between ESHaLE model and (a) LEO model and (b) UMD model in terms of probability of exceeding L/250 deflection threshold

4.2.12 Conclusions

This study proposes a new methodology called the equivalent stress history and layered effects (ESHaLE) approach to account for stress history in soil profiles with multiple layers, including sandy and clayey soils. The theoretical basis of the ESHaLE model consists of two main aspects. First, the impact of stress history on soils' behavior is captured based on mass conservation, assuming a general scour scenario. Second, to accommodate layered soils' unique characteristics, the layered effect is also included in the ESHaLE model based on conservation of strength for the lateral response and continuity of effective vertical stress for the vertical response. The conservation of mass and the conservation of strength are used to find equivalent layers and corresponding equivalent layer depths, scour depths, and soil properties for vulnerability assessment of scoured bridges. The methodology is verified through comparison with both existing models and experimental tests. ESHaLE is evaluated on an example soil profile and implemented on a laterally and vertically loaded pile for static analysis and a full-bridge structure for dynamic analysis to

assess seismic vulnerability under scour conditions. Three soil models are compared: the proposed ESHaLE model that can capture both the stress history and layered soil effects, the LEO model that includes the layered effect only, and the UMD model representing the unmodified soil model and ignores both the layered and stress history effects. The main findings based on the results from the single pile test and the seismic vulnerability analyses of the bridge considering the three soil models are as follows:

- The laterally and vertically loaded pile results show that the impact of stress history on the pile's lateral response increases as scour level increases. For the vertically loaded pile, using the proposed ESHaLE model results in the largest value of axial displacement among the three models with a maximum rise of 35% compared to the LEO model due to stress history effects on the structural response.
- From the results from a selected ground motion, an increase of up to 10% and 16% in column vertical displacement is observed using the proposed ESHaLE model compared with the LEO and UMD models, respectively. Importantly, as scour depth increases, vertical column displacements obtained from using the ESHaLE model are amplified compared to the values from the LEO or UMD models.
- From the fragility assessments for the flexural failure of the bridge column, the failure probabilities obtained from implementing the proposed ESHaLE model compared with the LEO model show the impact of stress history is more significant at low scour levels due to the attraction of higher seismic force in comparison with results for higher scour levels.

- From the fragility curves, using the ESHaLE soil model results in a 25% and 46% higher probability that the deflection of the deck will exceed an L/250 threshold in comparison with the LEO and UMD models, respectively. The increase in estimated exceedance probability increases as scour depth increases.
- Taken together, these findings show the importance of implementing a modeling approach as proposed with ESHaLE that includes the effect of soil stress history to assess the vulnerability of scoured bridges in layered soils.

4.3 Subtopic No. 3 (Part 2)

4.3.1 Background and related work

For studies regarding the impact of soil stress history, Lin et al. (2010, 2014a) investigate the effect of stress history on lateral behavior of piles under scour conditions in sand and soft clay, respectively. Liang et al. (2015) perform a buckling analysis of bridge piles in the presence of scour, considering the impact of stress history in soft clay. Zhang and Tien (2020) present a methodology to account for the impact of stress history in layered soils in the risk assessment of scoured bridges. For studies regarding the impact of scour-hole dimensions, Lin et al. (2014b, 2016) propose a simplified method to account for the effect of scour-hole geometries on laterally loaded piles through an equivalent wedge failure model in sand and soft clay, respectively. Later, Lin (2017) studies the loss of pile axial capacities in the presence of scour considering scour-hole dimensions based on Boussinesq's theory. Zhang et al. (2016) and Liang et al. (2018) investigate the combined

effect of soil stress history and scour-hole geometries on the lateral performance of piles in clay.

Among the literature above, a comprehensive approach to account for the combined effect of stress history and scour-hole dimensions for both clay and sand on the behavior of foundation piles is lacking. In particular, existing studies focus on the impact of the soil effect on the lateral performance of piles while ignoring the impact on the axial performance (i.e., settlement) of the piles in the presence of scour. This study presents a methodology to combine the effects of soil stress history and scour-hole dimensions to more comprehensively model soil-structure interaction in both sand and clay. The combined effect is captured through updating the parameters of the nonlinear soil springs (e.g., p-y, t-z, and q-z springs) in both the lateral and vertical directions. For the first time, comprehensive verification of the proposed generalized approach for modeling laterally and axially loaded piles in sand and clay subject to scour is provided.

The rest of the study is structured as follows. The next section introduces background on the effects of soil stress history and scour-hole dimensions for both sand and clay. The proposed methodology that combines these two soil effects is then presented. Derivations of the relationships updating the soil parameters in the presence of scour are provided. The following section provides validations/verifications and multiple analyses of laterally and axially loaded piles with and without considering soil effects in sand and clay. The proposed method is validated through comparing the pile deflection response using the proposed approach with measured results from field tests and is verified with existing numerical models considering either individual or combined soil effects under scour scenarios. Analyses show the impacts of including soil effects in estimated pile

responses. The last part of this section demonstrates the ability of the proposed method to capture the combined soil effect with load-settlement curves in the presence of scour, showing the importance of including these soil effects in the estimation of structural responses under scour.

To conduct nonlinear time history analyses and explicitly account for soil-structure interaction within tractable computing times, a dynamic beam on a nonlinear Winkler foundation or dynamic p-y method is adopted (Boulanger et al., 1999; Wang et al., 2014). The soil-structure interaction is modeled via three nonlinear springs (i.e., p-y, t-z, and q-z springs) to simulate lateral, frictional, and bearing responses shown in Figure 41(b) in the previous subtoptic. The nonlinear interaction between the soil and structure consists of elastic, plastic, and gap components in series (Boulanger et al., 1999). The nonlinear backbone curves and corresponding ultimate resistances for sand and clay implemented in this study are based on the literature, as shown in Table 15.

Table 15. Nonlinear backbone curves for sand and clay

Soil parameters	Sand	Clay
p-y curve	A.P.I. (2000)	Matlock (1970)
Ultimate lateral resistance (P_{ult})	Reese et al. (1974)	Matlock (1970)
t-z curve	Mosher (1984)	Reese and O'Neill (1987)
Ultimate unit shaft resistance (T_{ult})	Tuma and Reese (1974)	Tomlison (1992)
q-z curve	Vijayvergiya (1977)	Reese and O'Neill (1987)
Ultimate bearing resistance (Q_{ult})	Meyerhof (1976)	Terzaghi (1943)

4.3.2 Effect of stress history

The deposition of soils can be considered as a loading process, while the removal of soil due to scour can be considered as an unloading process. As a result, the remaining soil experiences a new stress state, quantified by the increase of the overconsolidation ratio (OCR) or ratio between the previous maximum stress and present stress. Lin et al. (2010, 2014b) have investigated the effect of soil stress history on the soil properties of cohesionless soils and cohesive soils. For cohesionless soils (i.e., sand), soil parameters such as friction angle, effective unit weight, and modulus of subgrade reaction can be modified due to the change of stress state after scour events. For cohesive soils (i.e., soft clay), undrained shear strain and effective unit weight are influenced by the effect of stress history before and after scour events through the OCR and scour depth. Further details on soil property changes due to stress history effects in cohesionless and cohesive materials are shown in Figures 70 and 71 in the appendix, respectively. These studies focus on the influence of stress history on a single pile in the lateral direction while the influence in the axial direction is neglected. In comparison, Zhang and Tien (2020) have investigated the influence of stress history of layered soils on single piles in the axial direction through accounting for the change of parameters of unit shaft and bearing resistance due to the change of stress state after scour events. Both lateral and axial effects are considered in this study.

4.3.3 Effect of scour-hole dimensions

One of the common practices in modeling scour is to neglect the effect of the shape and geometry of a scour hole. However, the scour-hole dimensions influence the behavior of piles in both the lateral and vertical directions. Lin et al. (2014a, 2015) have investigated the effect of scour-hole dimensions on lateral behavior of a single pile for cohesionless and cohesive materials using an equivalent wedge failure model shown in Figure 4(b). This simplified method accounts for the change of lateral soil resistance by considering the weight of the soil wedge above the failure plane and its interactions with the structure and soil. On the other hand, for the effect of scour-hole dimensions on the axial response of the pile, Lin (2017) has proposed a closed-form solution for the additional vertical stress due to scour-hole geometry by integrating Boussinesq's analytical solution. Lin (2017) applies the approach to sands but not to clays as the undrained shear strength of clay is irrelevant to the stress change. Further details on the effect of scour-hole dimensions in cohesionless and cohesive materials are shown in Figures 72 and 73 in the appendix, respectively. In this study, the effect of scour-hole dimensions on the axial response with clayey soil is considered by modifying a dimensionless factor (α), which is a function of effective overburden pressure and directly relates to the skin friction capacity of cohesive soils. This approach is described further in the proposed methodology section. The parameters defining the scour-hole dimensions are shown in Figure 4(a) with scour depth, scour width, and slope angle. For a typical bridge, scour level (S_d) can range from 0.5m to 15m, but most observed scour depths (i.e., up to 41%) range from 0.5m and 5.0m (Lin et al., 2014c); scour width (S_{tw}) has been approximated as twice the scour depth (Richardson and Davis,

2001); the value of slope angle (θ) depends on the bed material and is approximately equal to the angle of repose of the surrounding soils (Richardson and Davis, 2001).

Zhang et al. (2016) have proposed a methodology to compute lateral resistance of soil numerically considering both scour-hole geometry and possible changes of stress due to scour in soft clay with the aid of integration of Mindlin's elastic solutions. However, this methodology only applies to cohesive material, and the study does not investigate how scour-hole geometry and stress history impact the vertical resistance of the soil.

4.3.4 Proposed methodology

This study proposes a generalized approach to account for the effects of soil stress history and scour-hole geometry for both cohesive and cohesionless soils. In addition, the framework considers impacts on soil resistance in both lateral and vertical directions. In the proposed model, for given soil properties and scour-hole geometry, the effect of scour-hole geometry is first captured through computing an equivalent depth based on an equivalent wedge model at a point of interest. Next, the mechanical properties at the point of interest after scour events are updated as it undergoes a new stress state. With the equivalent depth and updated soil property values, the key parameters (i.e., P_{ult} indicating ultimate lateral resistance and Q_{ult} indicating ultimate end bearing resistance) for the p-y curve and q-z curves are obtained. Simultaneously, the total vertical effective stress which includes soils above as well as the additional stress induced by the overburden pressure due to scour-hole geometry is computed by integrating Boussinesq's point load solution. With the values of total vertical effective stress and soil properties at the point of interest, the soil ultimate unit shaft resistance (T_{ult}) is obtained for the t-z backbone curve. Figure

3 presents a flowchart that summarizes the steps to obtain the key soil parameters (i.e., P_{ult}, Q_{ult}, and T_{ult}) in modeling the soil-structure interaction under scour. Note that the process shown in Figure 55 applies to both cohesive and cohesionless materials with corresponding nonlinear backbone relationships.

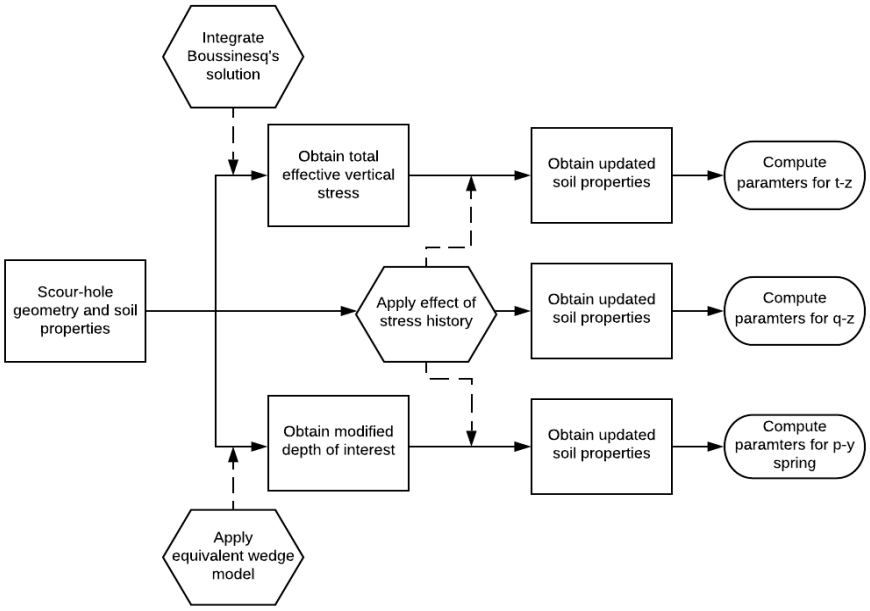

Figure 55. Flowchart of the process to compute parameters of soil resistance

Specifics for calculating the soil resistance parameters now follow. For cohesionless soils (e.g., sand), calculating ultimate soil lateral resistance (P_{ult}) begins with considering a wedge-type failure near the surface (P_{st}) and plane strain failure well below the ground surface (P_{sd}) as shown in Equation (62a) and Equation (62b) (Reese et al., 1974). In all equations that follow, the variables with subscripts sh and shd indicate that they are affected by the effect of the soil stress history and scour-hole dimensions, respectively.

$$P_{st} = \gamma'_{sh} z_{shd} \left\{ \frac{K_{o(sh)} z_{shd} \tan(\phi'_{sh}) \sin(\beta)}{\tan(\beta - \phi'_{sh}) \cos(\alpha)} \right.$$

$$+ \frac{\tan(\beta)}{\tan(\beta - \phi'_{sh})} [B + z_{shd} \tan(\beta) \tan(\alpha)] \quad (62a)$$

$$\left. + K_{o(sh)} z_{shd} \tan(\beta) [\tan(\phi'_{sh}) \sin(\beta) - \tan(\alpha)] - K_a D \right\}$$

$$P_{sd} = K_a B \gamma'_{sh} z_{shd} [\tan^8(\beta) - 1] + K_{o(sh)} B \gamma'_{sh} z_{shd} \tan(\phi'_{sh}) \tan^4(\beta) \quad (62b)$$

z_{shd} is the distance between the ground surface and point of interest, and it is an equivalent depth determined based on the failure-wedge model; γ'_{sh} is effective unit weight; β is passive failure angle; α is angle defining the shape of the failure wedge; K_a is the minimum coefficient of active earth pressure; D is the diameter of the pile; K_o is the coefficient of lateral earth pressure at rest; ϕ'_{sh} is friction angle. Ultimate skin friction resistance (T_{ult}) is a function of effective total vertical stress ($\sigma_{va(shd)}{}'$) as shown in Equation (63) (Tuma and Reese, 1974)

$$T_{ult} = K_o \tan(\phi'_{sh}) \sigma_{va(shd)}{}' \quad (63)$$

where $\sigma_{va(shd)}{}'$ is computed as in Equation (64) (Lin, 2017).

$$\sigma'_{va(shd)} = \gamma' z \left\{ 1 + \tan(\theta) \left[\frac{\frac{S_d}{\tan(\theta)} + S_{bw}}{\sqrt{\left(\frac{S_d}{\tan(\theta)} + S_{bw}\right)^2 + z^2}} - \frac{S_{bw}}{\sqrt{{S_{bw}}^2 + z^2}} \right] \right\} \quad (64)$$

The parameters S_d, S_{bw} and θ are as defined in Figure 4(a). Equation (65) presents an equation for computing the ultimate end bearing resistance (Meyerhof, 1976).

$$Q_{ult} = N_{q(sh)} \sigma_v{}' \quad (65)$$

$N_{q(sh)}$ is bearing capacity factor, which is a function of ϕ'_{sh} and $K_{o(sh)}$; $\sigma_v{}'$ is effective vertical stress, and it is assumed to be invariant of depth and scour-hole dimensions as it is usually located well below the mudline level.

Calculating the soil parameters for cohesive soils (e.g., clay) follows a similar approach as for sand but with different nonlinear backbone curves and corresponding equations for the ultimate resistance parameters. The procedure starts with determining the equivalent depth (z_{shd}) based on the failure-wedge model, which accounts for the effect of scour-hole geometry. Ultimate lateral resistance is then computed based on the smaller of the two values shown in Equation (66) (Matlock, 1970).

$$P_{ult} = \min\left\{\left(3 + \frac{\gamma'_{sh}}{C_{u(sh)}} z_{shd} + \frac{J}{B} z_{shd}\right) C_{u(sh)} B,\ 9C_{u(sh)} D\right\} \tag{66}$$

$C_{u(sh)}$ is the undrained shear strength of soft clay, and J is a constant with a value set to be 0.5. The ultimate skin friction resistance of clay is determined according to Equation (67) (Tomlison, 1992).

$$T_{ult} = \alpha_{sh\&shd} C_{u(sh)} \tag{67}$$

$\alpha_{sh\&shd}$ is a dimensionless factor with the constraint of being not greater than 1, and it is affected by both soil stress history and scour-hole geometry through parameter $\boldsymbol{\psi}$ based on A.P.I. (2000) as shown in Equations (68a) and (68b)

$$\alpha_{sh\&shd} = 0.5\boldsymbol{\psi}^{-0.5}, \quad \boldsymbol{\psi} \leq \mathbf{1} \tag{68a}$$

$$\alpha_{sh\&shd} = 0.5\boldsymbol{\psi}^{-0.25}, \quad \boldsymbol{\psi} > 1 \tag{68b}$$

where

$$\boldsymbol{\psi} = \frac{C_{u(sh)}}{\sigma'_{va(shd)}} \tag{68c}$$

Thus, the skin friction resistance of clay (T_{ult}) is influenced by both soil stress history and scour-hole dimensions. Finally, the end-bearing resistance (Q_{ult}) of clay is based on Terzaghi's bearing capacity theory (Terzaghi, 1943), with the relation simplified to Equation (69) due to the characteristics of cohesive soils and piles. A_p is the cross-sectional area of the pile.

$$Q_{ult} = 9A_p C_{u(sh)} \tag{69}$$

Tables 16, 17, and 18 summarize the methodologies to compute ultimate resistance for cohesionless and cohesive soils for P_{ult}, T_{ult}, and Q_{ult}, respectively.

Table 16. Methodologies to obtain P_{ult}

P_{ult}	**Sand**	**Clay**
Soil stress history	OCR approach (Equation 62 and Figure 70)	OCR approach (Equation 66 and Figure 71)
Scour-hole dimensions	Equivalent depth approach with failure-wedge model (Equations 62 and Figure 72)	Equivalent depth approach with failure-wedge model (Equation 66 and Figure 73)

Table 17. Methodologies to obtain T_{ult}

T_{ult}	**Sand**	**Clay**
Soil stress history	OCR approach (Equation 63 and Figure 70)	OCR approach (Equation 67 and Figure 71)
Scour-hole dimensions	Analytical solution approach with Boussinesq's solution (Equations 63 and 64)	Analytical solution approach with Boussinesq's solution (Equations 64, 67, and 68)

Table 18. Methodologies to obtain Q_{ult}

Q_{ult}	Sand	Clay
Soil stress history	OCR approach (Equation 65 and Figure 70)	OCR approach (Equation 69 and Figure 71)
Scour-hole dimensions	-*	-*

Note -*: Scour-hole dimensions do not influence end-bearing capacity due to the depth in this study

The novelty of the proposed approach is to combine all soil effects in the updating of soil parameters due to scour, for both cohesive and cohesionless soils and in both lateral and vertical directions. Results provided in later sections show the importance of including these combined effects of soil stress history and scour-hole dimensions in the assessment of scoured bridges. The following section presents comparisons between the proposed model and other soil models and experimental tests for verification and validation in terms of multiple response parameters for a selected single-pile structure.

4.3.5 *Analaysis of the proposed methodology*

The proposed framework is implemented in the open-source finite element platform OpenSees (Mckenna, 1997), with the soil-structure interaction modeled as shown in Figure 41(b). The validation and verification focuses on the response of laterally and axially loaded piles in sand and clay. Table 19 gives the details in terms of analysis type, soil type, field tests, and numerical models found from the existing literature. The numerical result from the proposed model is first validated with experimental field test data for both lateral and axial responses without considering scour events. This validation acts as a benchmark to ensure the proposed model yields reliable results before considering the scour

phenomenon. Next, after an extensive literature review, as experimental tests of laterally and axially loaded piles in the presence of scour are scarce, the authors use existing numerical results to verify the proposed framework considering scour. The numerical models for sand are selected from Lin et al. (2010, 2014b), which account for the effects of stress history and scour-hole dimensions, respectively, in the presence of scour. Lin et al. (2014a, 2015) focus on effects of stress history and scour-hole dimensions, respectively, for a laterally loaded pile in clay. The numerical response considering the combined effect of stress history and scour-hole dimensions from Zhang et al. (2016) is also compared with the proposed model for verification. Note that numerical results for axially loaded piles considering scour do not exist in the literature and are unavailable for comparison, as shown with a dash in Table 19.

Table 19. Summary of validation of the proposed framework

Analysis Type	***Soil Type***	***Field Tests Without Scour***	***Numerical Models With Scour***
Laterally Loaded Piles	Sand	Cox et al., 1974	Lin et al., 2010, 2014b
	Clay	Reese and Van Impe, 2001	Lin et al., 2014a, 2015 & Zhang et al., 2016
Axially Loaded Piles	Sand	Briaud et al., 1989	-
	Clay	O'Neill et al., 1982	-

4.3.6 *Laterally loaded piles under scour conditions*

The laterally loaded pile field test in sand is performed in a modified soil profile from Mustang Island, Texas (Cox et al., 1974), reported to be uniform-graded fine sand. The properties of the sand are listed in Table 20. The geometries of the pile and the applied load (P_h) are shown in Figure 56(a). The moment of inertia and elastic modulus of the pile

is 8.1×10^{-4} m^4 and 2.0×10^8 kN/m^2, respectively. Figure 56(b) shows the ground line deflection versus laterally applied load at the pile head without considering scour. The displacement curves for the measured data and values obtained from the proposed model track closely, with a maximum displacement difference of 1.58mm. The difference can be attributed to the estimation of the soil parameters and empirical equations used in the numerical modeling such as the p-y relation.

Table 20. Sand properties in Mustang Island (Cox et al., 1974)

Critical friction angle (°)	Effective unit weight (kN/m^3)	Relative density (%)	Maximum void ratio	Minimum void ratio	Specific gravity
28.5	10.4	70 (depth < 3m) 90 (depth ≥ 3m)	1.0	0.598	2.65

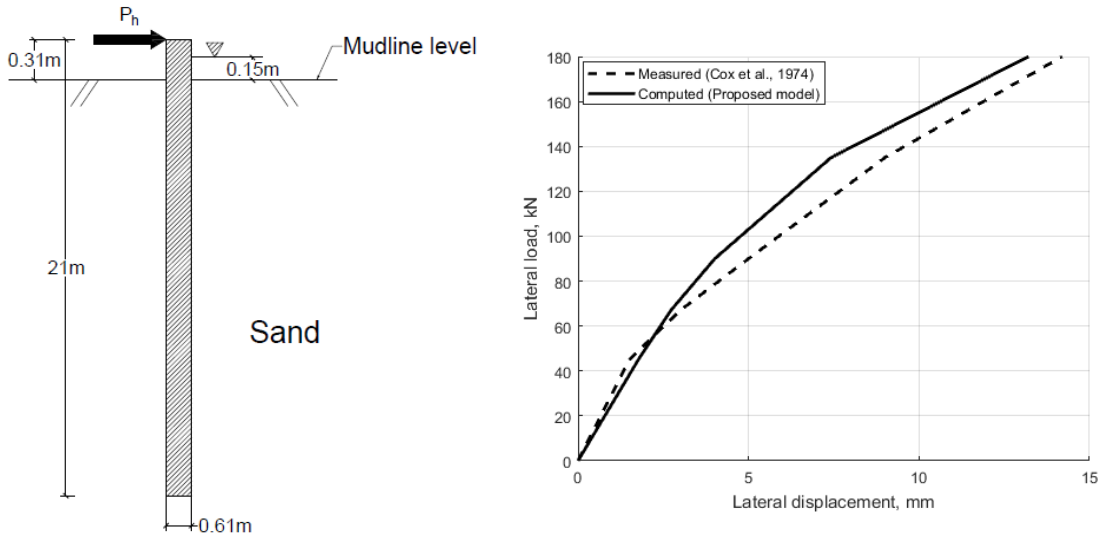

(a) (b)

Figure 56. (a) Laterally loaded pile in the sand and (b) deflection at the ground line versus laterally applied load for measured data and computed result without considering scour

For scour scenarios, due to the scarcity of existing experimental data, the authors choose to verify the proposed model with results from existing numerical models. Figure

57 presents a comparison of the proposed approach with the results from Lin et al. (2010) for 3m scour depth (S_d) and 39º slope angle (θ). As opposed to Lin et al. (2010)'s model, which only considers the effect of stress history in sand, the proposed model is capable of capturing the impact from scour-hole dimensions. The results for the proposed model shown in Figure 57 consist of three different values of bottom scour width (S_w): 0, D and ∞. D is the diameter of the pile with a value of 0.61m. Scour width of ∞ is equivalent to neglecting scour-hole dimensions. From Figure 57, as the scour width increases, the magnitude of the lateral deflection also increases as the impact from the scour-hole dimensions decreases. The case of bottom scour width equal to ∞ for the proposed model is closest to the Lin et al. (2010), which neglects the effect of scour-hole dimensions and only accounts for the effect of stress history in sand. The discrepancy between Lin et al. (2010)'s model and the proposed model with the infinite value of scour width is mainly due to the use of different p-y relations in the lateral soil spring.

For comparison, Figure 58 provides the results from Lin et al. (2014b), which only considers the effect of scour-hole dimensions, with those from the proposed model for a scour depth of $3\times D$, bottom scour width of 0, and slope angle of 39º. The proposed approach includes both scour-hole dimension and soil stress history effects. The stress history effect slightly reduces the effective unit weight, relative density, and modulus of subgrade reaction of the remaining sand. However, the unloading process with scour increases the friction angle and over-consolidation ratio, which has a greater impact on the lateral resistance of sand resulting in increased soil lateral resistance. Therefore, a reduced lateral deflection is expected with the inclusion of stress history effects. The results in

Figure 58 show this with the proposed model yielding smaller lateral deflections at the ground level due to its ability to include the effect of stress history.

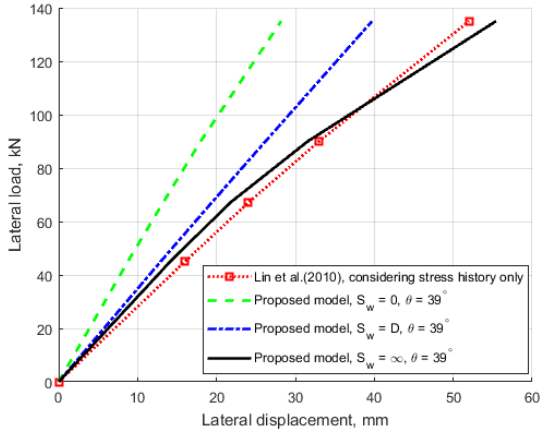

Figure 57. Comparison between numerical models of deflection at the ground line versus laterally applied load with scour depth of 3m in sand

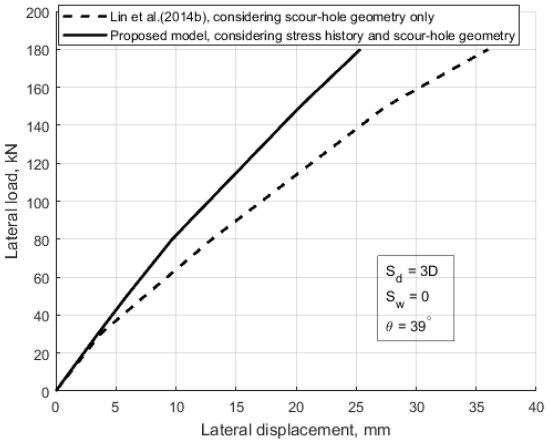

Figure 58. Comparison between numerical models of deflection at the ground line versus laterally applied load with scour depth of 3×D, scour width of 0 and slope angle of 39º in sand

To investigate the impact of including soil effects in the analysis of laterally loaded piles in sand, Figure 59 shows a comparison of estimated pile deflection versus laterally applied load, with and without considering the combined soil effect under varying scour conditions. The combined soil effect is indicated with an abbreviation of "s.e.". Several

observations can be made based on the results shown in Figure 59. First, an increase in scour depth increases the flexibility of the pile in sand with a larger scour depth leading to larger values of pile lateral deflection. Second, the combined soil effect increases the lateral soil resistance, reducing the deflection in comparison with not considering soil effects for a given value of applied load and scour depth. Third, the impact of the combined soil effect increases as scour depth increases, as observed by the increasing difference between the solid line and dashed line as scour depth increases. In summary, not considering soil effects could lead to an overly conservative design in terms of the lateral response of a pile in sand.

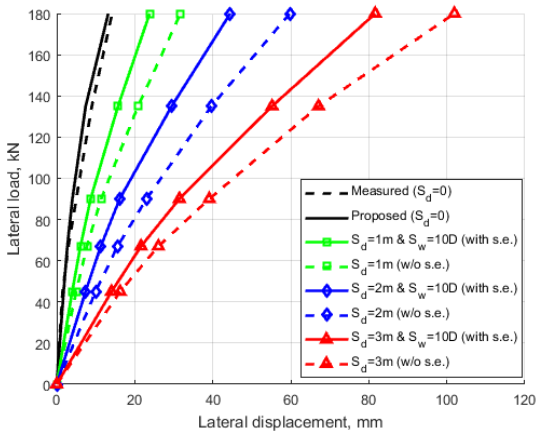

Figure 59. Comparison of deflection at the ground line versus laterally applied load with and without considering combined soil effect under varying scour conditions in sand

The field tests for laterally loaded piles in clay are in a soft clay profile near Austin, Texas. The soil properties are summarized in Table 21 and categorized as fat clay based on the Unified Soil Classification System. The swelling index is estimated empirically as 1/5 of the compression index (Kulhawy and Mayne, 1990). The distribution of undrained shear strength was measured by Reese and Van Impe (2001) with values plotted in Figure 38. The parameters of the pile are obtained from Reese and Van Impe (2001) with a length of 12.8m, an outer diameter of 0.319m, a thickness of 0.0127m, a moment of inertia of 1.44

$\times 10^{-4}$ m^4, and elastic modulus of 218 GPa. Figure 60(a) shows the geometry of the pile, and Figure 60(b) gives a comparison between the proposed model result and experimental data in terms of pile head deflection versus laterally applied load without considering scour. The two results follow a close trend, with an average percentage difference of 14%. While no scour is considered in the experimental test, the comparison provides a benchmark for further study of the proposed model under scour conditions.

Table 21. Properties of soft clay near Lake Austin, Texas

Effective unit weight (kN/m^3)	Water content (%)	Compression index	Swelling index	Strain at half of maximum stress	Effective friction angel (°)
10	44.5	0.38	0.076	0.012	20

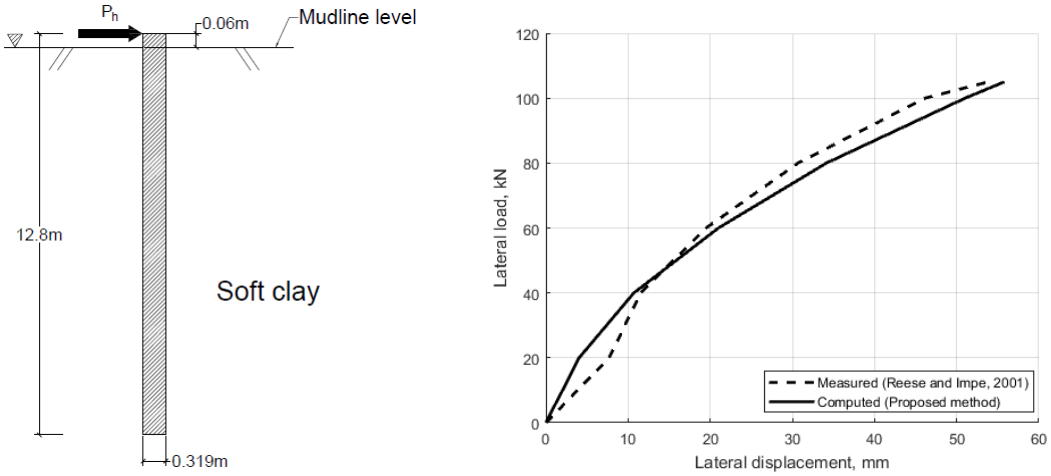

(a) (b)

Figure 60. (a) Laterally loaded pile in soft clay and (b) deflection at the pile head versus laterally applied load for measured data and computed result without considering scour

Figure 61 presents a comparison of the pile head deflection versus laterally applied load between Lin et al. (2014a)'s model and results from the proposed model with scour depth of $10\times D$, where D is 0.319 m, which is also the diameter of the pile. Results for the proposed model for a slope angle of 40° and bottom scour width of 0, $5\times D$, and ∞ are

shown. The scour width of ∞ indicates the impact of scour-hole dimensions is neglected. As a result, the result from Lin et al. (2014a) that captures only the effect of stress history yields the same result as the proposed model for scour width of ∞. Note that both the proposed model and Lin et al. (2014a) adopt the same p-y curve (Matlock, 1970). In comparison, for the other curves, the proposed model considers both the effects of stress history and scour-hole dimensions. From Figure 61, the effect of scour-hole dimensions increases the lateral resistance of clay, leading to an increase in pile head deflection as the bottom scour width increases from 0 to ∞.

Figure 62 presents a comparison of deflection between three different numerical models under scour depth of $6\times D$, scour width of 0m, and slope angle of 40°. The numerical result from Lin et al. (2015) captures only the impact of scour-hole dimensions. In comparison, both numerical results from Zhang et al. (2016) and the proposed model are able to account for the combined effect of stress history and scour-hole dimensions in clay. As shown in Figure 62, the soil stress history reduces the lateral resistance of clay, increasing the pile head deflection. The Zhang et al. (2016) and proposed models track closely with the proposed model yielding a slightly more conservative result. The increase in pile head displacement estimated in clay when the combined stress history and scour-hole dimensions effects are considered differs from the effect observed in sand.

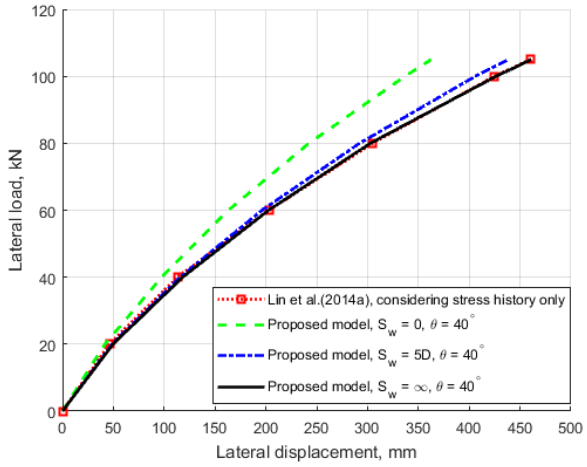

Figure 61. Comparison between numerical models of pile head deflection versus laterally applied load with scour depth of 10×D in soft clay

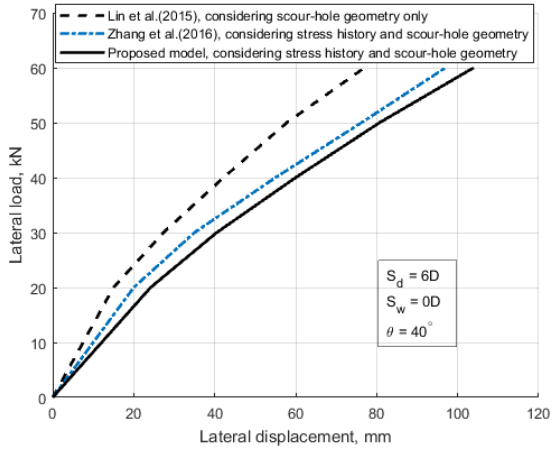

Figure 62. Comparison between numerical models of deflection at the pile head versus laterally applied load with scour depth of 6×D, scour width of zero and slope angle of 40º in soft clay

Figure 63 investigates the soil effect as a function of scour depth, showing the estimated deflection versus laterally applied load with and without considering the combined soil effect under varying scour conditions in soft clay. The observations made from Figure 63 are as follows. First, as scour depth increases, the lateral load resistance of the clay decreases, leading to larger deflection values. Second, accounting for the combined

soil effect leads to increased estimated pile head deflections. However, unlike the results shown in Figure 59 for sand, the combined soil effect in clay does not appear to be amplified as scour depth increases. This is because unlike in sand, there are counteracting effects in clay. The influence of stress history in clay is counteracted by the influence of scour-hole dimensions as scour depth increases. Third, as including soil effects leads to larger estimated deflections, the impact of stress history is the dominating factor in clay in comparison with the impact of scour-hole dimensions across varying scour depths. This phenomenon is observed from the differences in estimated pile head deflection values between the dashed and solid lines in Figure 63.

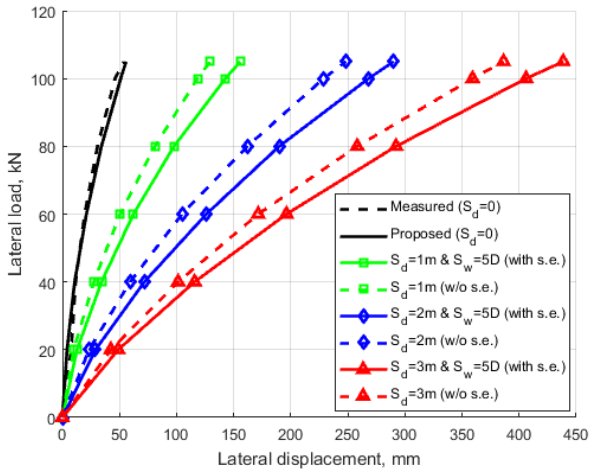

Figure 63. Comparison of deflection at the pile head versus laterally applied load with and without considering combined soil effect under varying scour conditions in soft clay

4.3.7 Axially loaded piles under scour conditions

This section examines the pile axial behavior. The goal is to illustrate that the proposed method is capable of predicting the settlement of axially loaded piles under scour conditions considering the combined soil effect. The field test of axially loaded piles in sand is reported by Briaud et al. (1989). The soil is made of a hydraulic fill with clean sand with a shear modulus of 38.3 MPa, friction angle of 35°, and dry unit weight of 15.7 kN/m^3. As shown in Figure 64(a), the closed-end steel pile with a diameter of 273mm and a wall thickness of 9.3mm is driven to a depth of 9.15m below the mudline in the sand. The steel pile has a Young's modulus of 2.1×10^5 MPa.

From Castelli and Maugeri (2002), a linearly increasing unit skin shaft capacity ranging from 0 at the mudline level up to 45 kPa at the pile base should be used for the numerical model. The analysis of the axially loaded pile is performed in OpenSees, with the load-settlement response plotted in Figure 64(b). The measured experimental data along with computed numerical data from Castelli and Maugeri (2002) and the proposed model without considering scour are shown. The proposed model tracks both the experimental and previous numerical results closely, with an average percentage difference of 17.2% and 11.6% compared with the experimental data and numerical data from Castelli and Maugeri (2002), respectively. The validation shown in Figure 64(b) serves as a benchmark for further study of the pile response under scour conditions.

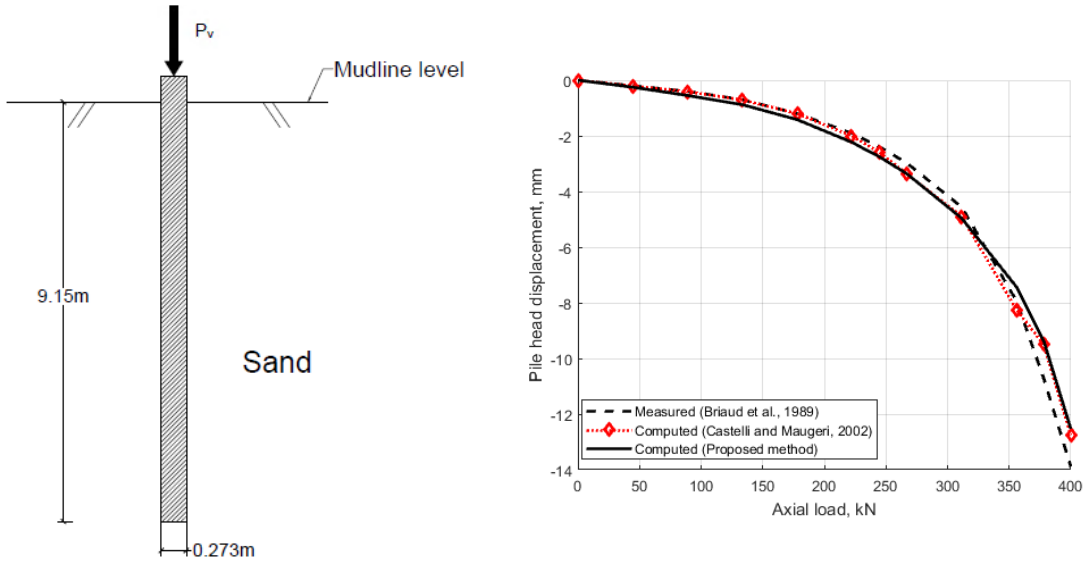

Figure 64. (a) Axially loaded pile in the sand and (b) settlement at the pile head versus axially applied load for measured data and computed results without considering scour

Before computing the response of the axially loaded pile under scour conditions with the proposed method, several assumptions need to be addressed. The slope angle and relative density are taken as 35° and 55%, respectively, for medium dense sand, and the critical friction angle is taken to be 28.5°. The effective unit weight of sand is back-calculated based on the value of the dry unit weight of 15.7 kN/m^3 and assumed specific gravity of 2.65, which gives a value of 9.78 kN/m^3. Figure 65 gives the load-settlement curves for varying scour depths and two different values of bottom scour width with and without considering the combined soil effect. Scour depths vary from 2×D to 6×D with the value of D equal to 0.273 m. Figure 65(a) and Figure 65(b) give results for a bottom scour width of 0 and 15×D, respectively. From Figure 65, as scour depth increases, the ability of the soil to resist a vertical load decreases, leading to increased pile head settlements. Comparing Figure 65(a) and Figure 65(b), the scour width has a significant impact on the vertical behavior of the pile. As the bottom scour width increases, considering the combined soil effect leads to a significant increase in the settlement expected under an axial

load. This is because by increasing the scour width, the vertical load-carrying capacity is reduced in the sand as the scour-hole geometry provides additional vertical stress as shown in Equation (64), which in turn decreases the vertical resistance in the sand. Figure 66 further investigates the impact of scour width, showing load-settlement curves for a scour depth of $4\times D$ and varying scour width ranges from 0 to ∞. Scour width values of 0 and ∞ provide an upper and lower bound, respectively, for a given scour depth, which is consistent with the previous observation regarding the role of scour-hole dimensions in the lateral response shown in Figure 61. A scour width of ∞ implies the effect of scour-hole dimensions is neglected. Comparing it with the results without considering the soil effect shows that the impact of stress history weakens the vertical response of the pile in sand, differing from the lateral behavior in sand, which is more greatly affected by the friction angle. This is because the reduction of effective unit weight during the stress history loading and unloading process plays an important role in determining the vertical resistance of the sand. Table 22 summarizes the impact of stress history, showing that including the effect of stress history in sand increases estimated pile settlement by up to 34.1% at $4\times D$ scour depth and 311.5 kN axial load. Therefore, neglecting to include the impact of stress history in the analysis could lead to an unconservative design. While in this case, the load-settlement curve not considering soil effects is close to that considering stress history and scour-hole geometry with scour width of $10\times D$, one cannot rely on these coincidental outcomes, and varying levels of scour depth, scour width, etc., would result in varying settlement curves. Therefore, it is critical to be able to quantitatively include the impacts of stress history and scour-hole dimensions in the analysis of piles subject to scour as presented in this study to accurately estimate pile behavior under varying conditions.

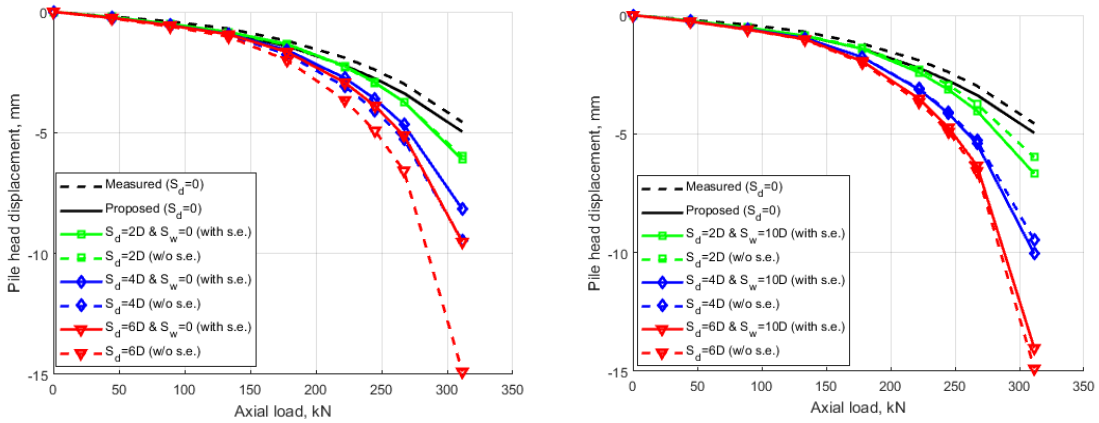

(a) (b)

Figure 65. Load-settlement curves at the pile head with varying scour depths and the values of (a) zero and (b) 15×D for bottom scour width in sand

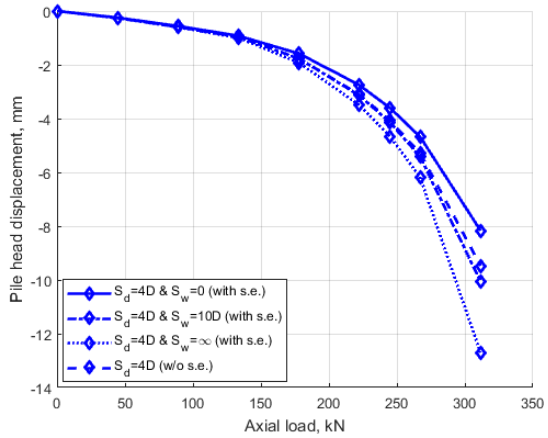

Figure 66. Load-settlement curves at the pile head with 4×D scour depth and varying bottom scour width in sand

Table 22. Summary of settlement values considering 4×D scour depth with and without including the effect of stress history in sand

Axial load (kN)	44.5	89	133.5	178	222	245	267	311.5
Settlement without soil effect (mm)	0.26	0.59	0.97	1.76	3.09	4.08	5.29	9.47
Settlement with $S_w = \infty$ (mm)	0.26	0.60	1.00	1.93	3.49	4.67	6.17	12.70
Percentage increase due to the effect of stress history	0.0%	1.3%	2.7%	9.3%	12.7%	14.4%	16.8%	34.1%

The second axially loaded pile test is reported by O'Neill et al. (1982) in stiff overconsolidated clay. The closed-end steel pile with an external radius of 0.137m and thickness of 9.3mm is driven in stiff clay with an embedded length of 13.1m as shown in Figure 67(a). According to the back analysis by Catelli and Maugeri (2002), a linearly increasing undrained shear strength profile is adopted. The value of the reduction factor (α) shown in Equation (67) is taken as 0.40, which results in a unit shaft capacity that varies linearly from 19 kN/m^2 at the surface to 93 kN/m^2 at the base. The soil deformation modulus can be back-calculated with a value of 195×10^3 kPa, and the elastic modulus of the steel pile is taken as 210 GPa. Under the assumption of a constant value of α, the undrained shear strength can be back-calculated based on Equation (67), and effective unit weight can be computed based on Equation (68) once the value of undrained shear strength is known. A comparison of load-settlement curves between the experimental data and numerical results from Catelli and Maugeri (2002) and the proposed model without scour is shown in Figure 67(b). The curves track closely with an average percentage difference of 10% between experimental data and the proposed method. This comparison serves as a benchmark for further load-settlement analysis considering soil effects in the presence of scour events.

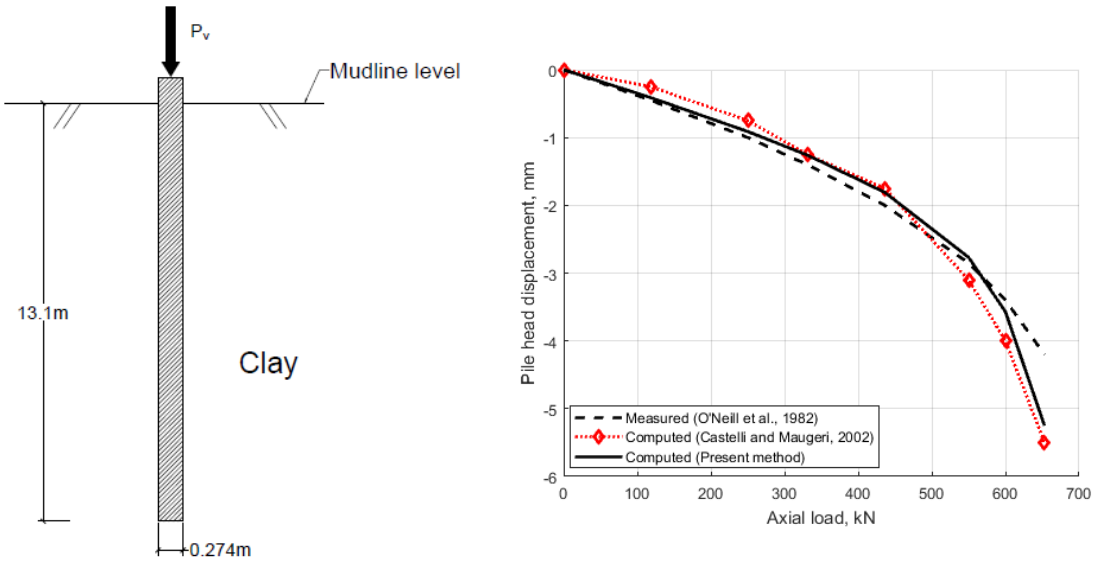

Figure 67. (a) Axially loaded pile in clay and (b) settlement at the pile head versus axially applied load for measured data and computed results without considering scour

The following investigates the impact of including soil effects in the assessment of pile displacement under varying scour scenarios. Figure 68 gives load-settlement curves of an axially loaded pile with two values of bottom scour width (0 and 15×D) and varying scour depths. The slope angle is taken as 40°. The observations from the results shown in Figure 68 are as follows. First, as scour depth increases, the estimated pile settlement in clay increases. The impact of scour depth is significant, as seen in the increase in pile head displacement as scour depth increases from 1m to 3m. Second, the scour width has a significant impact on the axial behavior of the pile in clay. Changing the scour width from 0 to 15×D, the load-settlement curves with soil effect significantly increase, especially for the curve for 3m scour depth, due to the reduced impact from scour-hole dimensions. As discussed previously, scour-hole dimensions provide additional vertical stress, which gives rise to the change in the value of $\boldsymbol{\psi}$ as shown in Equation (68c). As a result, the scour-hole dimensions affect the value of the reduction factor (α) due to the different stress state shown in Equation (68a) and (68b). The third observation from Figure 68 is that the impact

of including the soil effect in estimating the vertical response of the pile increases in significance as scour depth increases. As scour depth increases, there is an increasing difference between the solid lines (i.e., with soil effect) and dashed lines (i.e., without soil effect), indicating the importance of include soil effects in the analysis, particularly for more severe scour scenarios.

To further investigate the effect of scour width, Figure 69 provides load-settlement curves for varying scour widths ranging from 0 to ∞ under 2m scour depth. Note that an infinite scour width indicates the exclusion of the effect of scour-hole dimensions. Scour widths of 0 and ∞ provide upper and lower bounds for the load-settlement responses. Table 23 summarizes the settlement values, indicating the percentage increase in estimated settlement with and without considering the stress history effect in clay. Comparing the curve with $S_w = \infty$ and the curve without soil effect shows that the effect of stress history in clay increases settlement by as much as 61.1% for 2m scour depth and 600 kN axial load due to the reduction in undrained shear strength. The $S_w = \infty$ case is particularly applicable to the general scour scenario where the entire mudline is lowered, or local scour cases if the bottom width of the scour hole is large. In these cases, the stress history effect dominates, leading to the most vulnerable condition for scoured bridges. Neglecting to include the impact of stress history in clay leads to underestimated values of settlement under a given axial load, leading to potentially unconservative designs of axially loaded piles in clay.

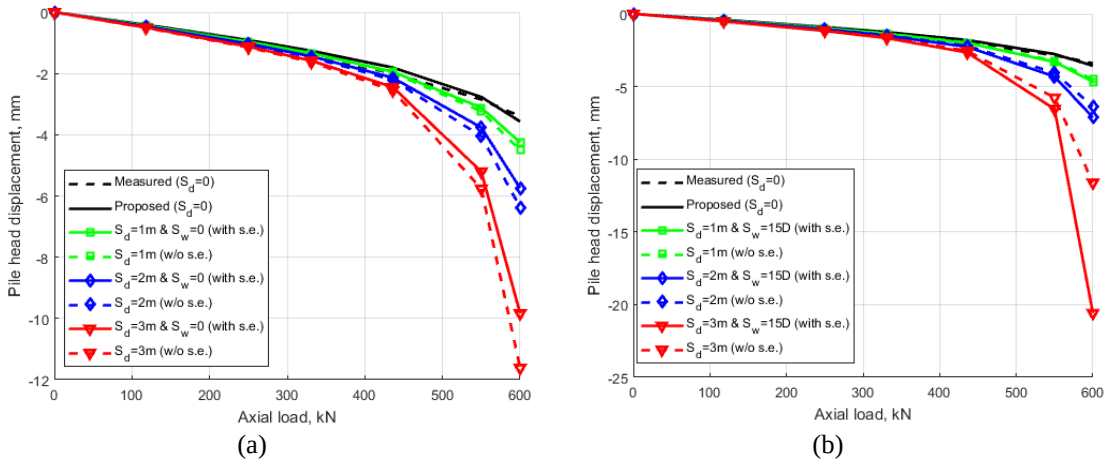

Figure 68. Load-settlement curves at the pile head with varying scour depths and values of (a) zero and (b) 15×D for bottom scour width in clay

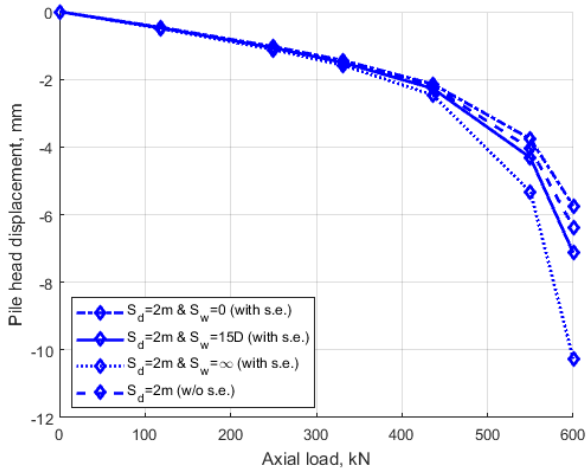

Figure 69. Load-settlement curves at the pile head with 2 m scour depth and varying bottom scour width in clay

Table 23. Summary of settlement values considering 2 m scour depth with and without including the effect of stress history in clay

Axial load (kN)	118	250	331	436	550	600
Settlement without soil effect (mm)	0.47	1.05	1.47	2.21	4.05	6.37
Settlement with $S_w = \infty$ (mm)	0.50	1.12	1.59	2.46	5.33	10.26
Percentage increase due to the effect of stress history	6.1%	6.7%	7.7%	11.4%	31.5%	61.1%

4.3.8 *Conclusions*

The study presents a framework that is able to capture the impacts from both soil stress history and scour-hole dimensions on the structural response of the pile for both cohesive and cohesionless soils in the presence of scour. Besides focusing on the lateral behavior of the pile as has been investigated in the past, the proposed framework also accounts for the combined soil effects on the vertical pile behavior. The proposed framework is validated with experimental data for no scour scenarios and verified with numerical data for scour scenarios, where available for lateral and axial loadings in sand and clay. The results from this study show that it is essential to include both stress history and scour-hole dimension effects in the modeling of soil-structure interaction in the presence of scour events. The following two bullet points summarize the main findings from the study.

- For a sand foundation, including either the effect of stress history or scour-hole dimensions could lead to a conservative design in the lateral direction. In comparison, in the vertical direction, including the effect of stress history results in an increase in estimated pile head deflection. For a $4\times D$ scour depth and 311.5 kN axial load, including soil effects lead to an increase in estimated settlement of 34.1%. The percentage could further increase with increasing applied axial load or increasing scour depth. These findings indicate that failing to consider soil effects under scour conditions could lead to an unconservative design, particularly in the axial direction.
- For a clay foundation, neglecting to include the effect of stress history could lead to an unconservative design in both lateral and vertical directions under scour conditions. In the lateral response of the pile in clay, the influence of stress history

is the dominating factor compared with the impact of scour-hole dimensions, with an increase of 13.5% in estimated lateral deflection under 3m scour depth, 5×D scour width, and 105 kN laterally applied load. The soil effect is greater in the axial direction. Under 2m scour depth and 600 kN axial load, the impact of including stress history effects in clay increases the estimated pile settlement by as much as 61.1% in the vertical direction in comparison with the outcome estimated without considering soil effects. An even larger percentage increase is expected if one considers higher axial load and scour depth scenarios.

This study provides a methodology to include soil stress history and scour-hole dimensions effects in the analysis of piles subject to scour. The potential underestimation of pile displacements under lateral and particularly axial loads if soil effects are not considered underscores the need to be able to quantitatively include soil effects in the estimation of pile responses and consider these effects for future design.

4.3.9 *Appendix: Calculating changes due to the effect of stress history and the effect of scour-hole dimensions*

Figures 70 and 71 show the equations and overall procedures used to obtain the updated properties of sandy and clayey soils, respectively, considering the effect of stress history. Figures 72 and 73 show the equations used to compute the equivalent depth of interest (z_e) considering scour-hole dimensions for sandy and clayey soils, respectively. Note that in Figure A.3 and A.4, D_1 = intermediate parameter, H_1 & H_2 = soil depth defining the locations of slope failure plane, F_{ue} = ultimate soil resistance of the equivalent

wedge, F_{u0} & F_{u1} & F_{u2} = ultimate soil resistance based on whether the slope failure plane intersects the slope of the scour hole. These procedures and equations are incorporated in the framework of the proposed model presented throughout this subtopic.

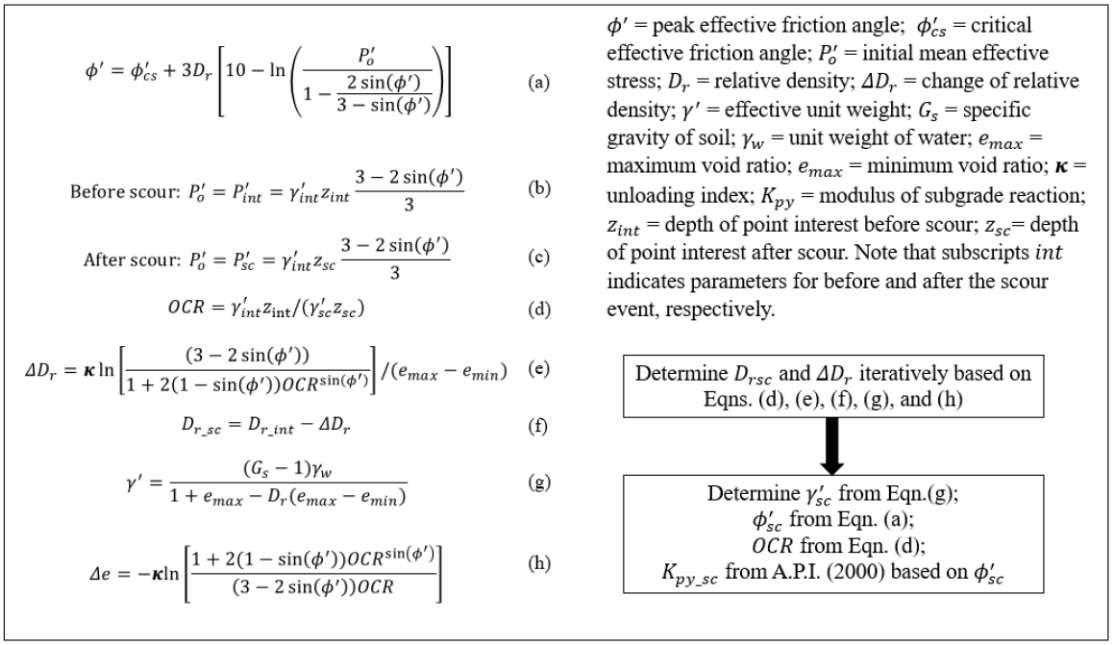

Figure 70. Procedures of computing soil properties considering the effect of stress history for sandy soil

$$\gamma'_{sc} = \frac{1+e_{int}}{1+e_{sc}}\gamma'_{int} \quad (a)$$

$$e_{int} = \frac{\gamma_w + \gamma'_{int}}{\gamma_w - \gamma'_{int} w_{int}} w_{int} \quad (b)$$

$$e_{sc} = e_{int} + C_{ur}\log\left(\frac{\sigma'_{v\_int}}{\sigma'_{v\_sc}}\right) \quad (c)$$

$$\sigma'_{v\_int} = \gamma'_{int}(z_{sc} + S_d) \quad (d)$$

$$\sigma'_{v\_sc} = (\gamma'_{sc}) z_{sc} \quad (e)$$

$$\gamma'_{sc} = \frac{1+e_{int}}{1+e_{int}+C_{ur}\log\left[\frac{\gamma'_{int}(z_{sc}+S_d)}{(\gamma'_{sc})z_{sc}}\right]}\gamma'_{int} \quad (f)$$

$$\frac{C_{u\_sc}/\sigma'_{v\_sc}}{C_{u\_int}/\sigma'_{v\_int}} = OCR^{\Lambda} \quad (g)$$

$$\Lambda = \frac{\lambda-\kappa}{\lambda} = 1 - \frac{C_{ur}}{C_c} \quad (h)$$

$$OCR = \frac{\gamma'_{int}(z_{sc}+S_d)}{\gamma'_{sc} z_{sc}} \quad (i)$$

γ' = effective unit weight; e = void ratio; γ_w = unit weight of water; w = soil moisture content; C_{ur} = swelling index; C_c = compression index; C_u = soil undrained shear strength; σ'_v = vertical effective stress; z_{sc} = depth of point interest after scour; λ and κ = compression and swelling indexes from isotropic consolidation tests. Note that subscripts int and sc indicate parameters for before and after the scour event, respectively.

Determine γ'_{sc} through solving Eqn. (f)

↓

Determine σ'_{v_int} & σ'_{v_sc} from Eqns. (d) and (e);
e_{sc} from Eqn. (c);
OCR from Eqn. (i);
C_{u_sc} from Eqns. (g) and (h)

Figure 71. Procedures of computing soil properties considering the effect of stress history for clayey soil

If $\theta < 90° - \beta$, then

$0 < z \le H_1$, $F_{ue} = F_{u0}$

$H_1 < z \le H_2$, $F_{ue} = F_{u1}$

$z > H_2$, $F_{ue} = F_{u2}$

If $\theta \ge 90° - \beta$, then

$0 < z \le H_1$, $F_{ue} = F_{u0}$

$z > H_1$, $F_{ue} = F_{u2}$

where

$$H_1 = \frac{S_w}{\tan\beta}$$

$$H_2 = \frac{S_w}{\tan\beta} + \frac{S_d}{D_1}$$

$$D_1 = \frac{\tan\beta\ \tan\theta}{1-\tan\beta\ \tan\theta}$$

F_{u0}, F_{u1}, F_{u2} and F_{ue} are given by,

$$F_{u0} = \frac{\gamma' K_o \tan\beta\, z^3}{3\cos\alpha}\left[\cos\alpha\sin\beta\tan\phi' - \sin\alpha + \frac{\tan\phi'\cos\beta}{\tan(\beta-\phi')}\right]$$

$$F_{u1} = \frac{\gamma' K_o \tan\beta}{3\cos\alpha}\left\{\left[z^3 + 3D_1\left(z^3 - \frac{z^2 S_w}{\tan\beta}\right) + 2D_1^2\left(z - \frac{S_w}{\tan\beta}\right)^3\right] \times \left[\cos\alpha\sin\beta\tan\phi' - \sin\alpha + \frac{\tan\phi'\cos\beta}{\tan(\beta-\phi')}\right]\right\}$$
$$+ \frac{1}{\tan(\beta-\phi')}\left(\frac{\gamma'(1-\tan\beta\ \tan\theta)\tan\beta}{6}\left\{3D\left[z(1+D_1) - \frac{S_w D_1}{\tan\beta}\right]^2 + 2\tan\beta\tan\alpha\left[z(1+D_1) - \frac{S_w D_1}{\tan\beta}\right]^3\right\}\right.$$
$$\left. + \frac{\gamma' S_w^2 \tan\theta}{6}(3D + 2S_w\tan\alpha)\right) - K_a\frac{\gamma' D z^2}{2}$$

$$F_{u2} = \frac{\gamma' K_o}{3\cos\alpha}\left\{\left[((z+S_d))^3\tan\beta - 3\left(S_w - \frac{S_d}{\tan\theta}\right)S_d^2 + 2\frac{S_d^3}{\tan\theta}\right] \times \left[\cos\alpha\sin\beta\tan\phi' - \sin\alpha + \frac{\tan\phi'\cos\beta}{\tan(\beta-\phi')}\right]\right\}$$
$$+ \frac{1}{\tan(\beta-\phi')}\left\{\frac{\gamma'(z+S_d)^2\tan\beta}{6}[3D + 2(z+S_d)\tan\beta\tan\alpha] - \gamma'\frac{(S_w\tan\theta + S_d)^2}{\tan\theta}\left[\frac{D}{2} + \frac{1}{3}\left(S_w - \frac{S_d}{\tan\theta}\right)\tan\alpha\right]\right.$$
$$\left. + \gamma' S_w^2\tan\theta\left(\frac{D}{2} + \frac{S_w\tan\alpha}{3}\right)\right\} - K_a\gamma' D\frac{(z+S_d)^2 - S_d^2}{2}$$

$$F_{ue} = \frac{\gamma' K_o \tan\beta\, z_e^3}{3\cos\alpha}\left[\cos\alpha\sin\beta\tan\phi' - \sin\alpha + \frac{\tan\phi'\cos\beta}{\tan(\beta-\phi')}\right] + \frac{\gamma' z_e^2}{\tan(\beta-\phi')}\left(\frac{D\tan\beta}{2} + \frac{z_e\tan^2\beta\tan\alpha}{3}\right) - K_a\frac{\gamma' D z_e^2}{2}$$

Figure 72. Equations used to compute the equivalent depth of interest considering the effect of scour-hole dimensions for sandy soil

If $\theta < 90° - \beta$, then
$0 < z \le H_1$, $F_{ue} = F_{u0}$
$H_1 < z \le H_2$, $F_{ue} = F_{u1}$
$z > H_2$, $F_{ue} = F_{u2}$
 	
If $\theta \ge 90° - \beta$, then
$0 < z \le H_1$, $F_{ue} = F_{u0}$
$z > H_1$, $F_{ue} = F_{u2}$
	F_{u0}, F_{u1}, F_{u2} and F_{ue} are given by,
	$F_{u0} = \frac{1}{2}\gamma' D z^2 + 2C_u D z + \sqrt{2} C_u z^2$
	$F_{u1} = \frac{1}{2}\gamma' D[(z - S_w)^2] + 2C_u D[z + (z - S_w)D_1] + \sqrt{2} C_u[z^2 + D_1(z - S_w)^2]$
	$F_{u2} = \frac{1}{2}\gamma' D[(z + S_d)^2 - (2S_w + S_d)] + 2C_u D[z + (z - S_w)D_1] + \sqrt{2} C_u[z^2 + D_1(z - S_w)^2]$
	$F_{ue} = \frac{1}{2}\gamma' D z_e^2 + 2C_u D z + \sqrt{2} C_u z_e^2$

where $H_1 = S_w$ $H_2 = S_w + \frac{S_d}{D_1}$ $D_1 = \frac{\tan\theta}{1 - \tan\theta}$	

Figure 73. Equations used to compute the equivalent depth of interest considering the effect of scour-hole dimensions for clayey soil

4.4 Subtopic No. 4

4.4.1 Background and introduction of non-uniform scour

Scoured bridges are subject to multiple hazards, which could be either correlated, such as flood and scour, or uncorrelated, such as earthquake and scour (Ghosn et al., 2003; Alampalli and Ettouney, 2008). Current design practice often neglects the importance of a multi-hazard design approach with only considering independent or single events. Thereby, the occurrence of multi-hazard events could lead to severe damage or even collapse of a bridge due to insufficient design. In prior studies of correlated multiple hazards (e.g., scour and flood), Hager and Unger (2010) investigate the effect of a single-peaked flood wave on pier scour through both theoretical and experimental approaches; Lin et al. (2010) study

the effect of including the stress-history of sand after scour events on the lateral response of bridges considering flood conditions; Klinga and Alipour (2014) provide a comprehensive procedure to account for the soil-pile-structure interaction to measure the susceptibility of the bridges under design flood and scour conditions. For the studies of uncorrelated multi-hazard events (e.g., earthquake and scour), Alipour and Shafei (2012) investigate the seismic response of multi-span continuous concrete bridges with varying number of spans considering scour conditions; Banerjee and Prasad (2013) focus on bridges in seismically active and flood-prone regions and assess the seismic performance of scoured bridges in those regions; Wang et al. (2014) evaluate seismic performance with emphasis on the failure mechanisms of bridge structural components in the presence of local scour across multiple RC bridge types; Zhang et al. (2019a) study seismic performance and risk assessment of corroded bridges with the emphasis on brittle failure modes (e.g., shear failure and pull-out failure) of bridge columns; Zhang et al. (2019b) investigate the seismic performance of bridges considering the combined effect of corrosion and scour, quantifying the combined effect through fragility assessment.

Among the studies described above, however, uniformity in scour depth at the foundation is assumed for simplicity. Yet, studies have shown that bridge failures do not exhibit uniform scour depth at the foundations (Khan and Amanat, 2015; Song et al., 2015; Tubaldi et al., 2018). In fact, multiple factors could lead to the non-uniformity in scour depth, including the composition of the soil profile, stream velocity, obstacles, geometry, configuration, position of bridge foundations, and so on. Any of these factors or combinations of them could result in a bridge experiencing varying levels of scour along its foundation. Despite its existence in scoured bridges, investigation of the impacts of this

non-uniformity on bridge performance has received only limited attention in the literature. A recent study by Fioklou and Alipour (2019) investigates the effect of non-uniformity in scour depth on the seismic performance of bridges for the upstream column and downstream column within a single column bent. However, non-uniformity in scour depth at foundations could also be observed at different foundations due to having a non-uniform bed profile in the longitudinal direction (i.e., along the direction parallel to the traffic of the bridge). Khan and Amanat (2014) study the riverbed scouring of the Meghna Bridge in Bangladesh. As an example, Figure 74 shows the as-built and existing non-uniform bed profile with severe local scour at piers 7, 8, and 9 of the Meghua Bridge. The study finds that by varying the riverbed scour depth, the moments in the piles increase by 137% and 87% under earthquake loading in the transverse and longitudinal directions (i.e., perpendicular and parallel to the direction of traffic), respectively, in comparison with the original no scour condition. However, the study uses response spectrum analysis to simulate earthquake loading, and all the materials in the study are assumed to remain in the elastic range. These assumptions cannot capture the structural damage induced by high seismic demand in the presence of non-uniform scour conditions.

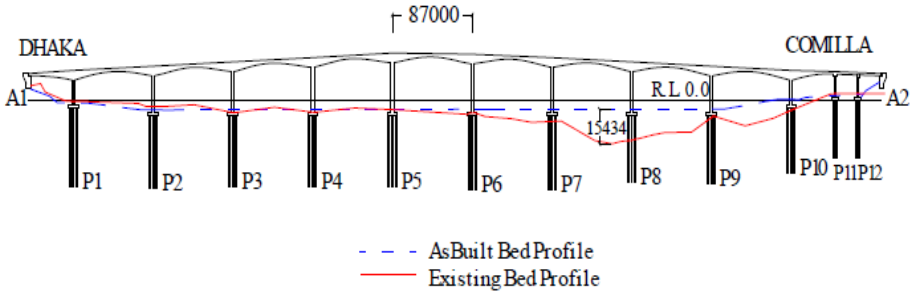

Figure 74. Bed Profile of Meghna Bridge (Khan and Amanat, 2014)

In addition, investigation of the effect of non-uniformity in scour depth on bridge risk under flood hazard is also lacking. Flood hazard analysis is particularly important as it can co-occur with scour events. This subtopic advances our knowledge of the performance of bridges under non-uniform scour conditions by investigating the impact of non-uniformity in scour depth in the longitudinal direction on bridge response under both seismic and flood hazards. Seismic hazard evaluation is conducted through nonlinear time history analysis; flood hazard evaluation is conducted through static load analysis with equivalent water pressure. Bridge performance is measured in terms of engineering demand parameters, including curvature demand of the columns and piles, and displacement of the deck.

The rest of this study is organized as follows. The sections 4.4.2 to 4.4.3 introduce the case study reinforced concrete (RC) bridge and the finite element modeling details of bridge components. Section 4.4.4 provides comprehensive procedures to investigate the performance of water-crossing RC bridges with non-uniformity in scour depth in the longitudinal direction considering seismic loads and flood loads. Sections 4.4.4 to 4.4.8 discuss the results quantifying the impact of non-uniform scour on RC bridges based on specific demand engineering parameters and failure mechanisms.

4.4.2 Case study RC bridge and modeling details

The selected RC bridge type is a typical multi-span continuous (MSC) concrete girder bridge. According to the inventory analysis done by Yilmaz and Banerjee (2018), the MSC concrete girder bridge is one of the three most common bridge types for water-crossing bridges in California. Figure 75 shows the layout of the bridge with the length of the center span (L_2) about 1.4 times the length of the approach span (L_1). Table 24 gives

the median values of the dimensional parameters based on bridges from the 1971-1990 design era (Ramanathan, 2012).

The superstructure of the bridge consists of a continuous concrete deck with a 190 mm thick slab and standard I-girder with a flange and depth of 480 mm and 915 mm, respectively, and weight per unit run of 670 kg/m. The concrete I-girders rest on elastomeric bearing pads with dimensions of 405 mm × 305 mm × 40 mm at the interior bents and the seat abutments. There is a gap of 20 mm between the bridge deck and the abutment backwall. The substructure of the bridge consists of single-column bents with a total of two columns. The bridge columns have a diameter of 1.8m with 72 #11 longitudinal rebars and #4 stirrups at 75 mm center-to-center spacing. The bridge foundation consists of a 5m × 5m pile cap with a group of nine 610-mm diameter piles with a length of 12m underneath the columns. The foundation soil is selected from Mustang Island, Texas (Cox et al., 1974), which is uniform-graded fine sand. The critical friction angle of the sand is estimated to be 28.5° with 90% relative density throughout the depth. Table 25 gives the properties of the selected sand profile.

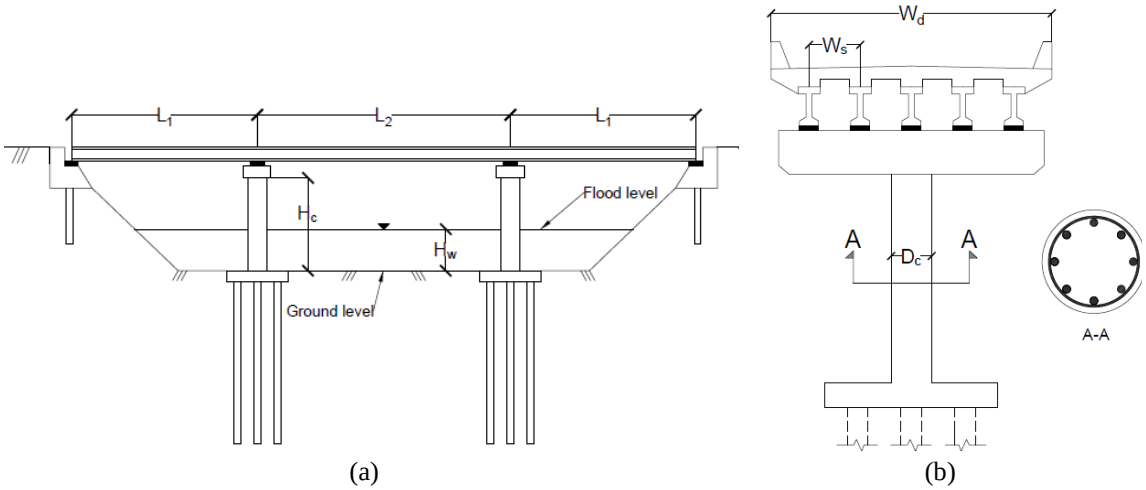

Figure 75. (a) Longitudinal and (b) transverse views of MSC concrete girder bridge

Table 24. Dimensions of the MSC concrete girder bridge

Parameters	L_1	L_2	H_c	H_w	D_c	W_d	W_s
Values (m)	13.4	18.3	6.7	3.0	1.8	8.5	1.7

Table 25. Modified dense sand properties (Cox et al., 1974)

Critical friction angle (°)	**Effective unit weight (kN/m^3)**	**Relative density (%)**	**Maximum void ratio**	**Minimum void ratio**	**Specific gravity**
28.5	10.4	90	1.0	0.598	2.65

4.4.3 *Finite element modeling details*

The finite element model of the selected MSC concrete girder bridge is built in the OpenSees software (Mazzoni et al., 2006). Figure 76 shows the 3-D view of the numerical model built in OpenSees with labels for specific locations and bridge components.

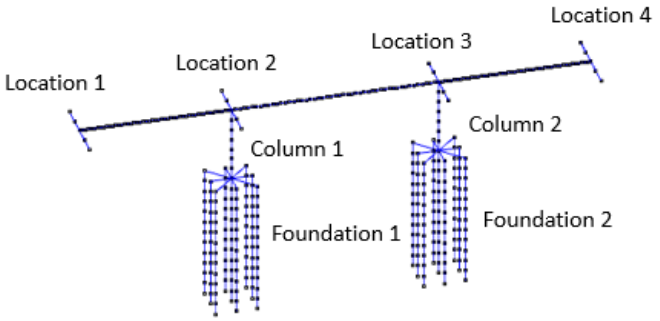

Figure 76. Finite element model of the MSC concrete girder bridge in OpenSees

For the superstructure of the bridge, the bridge deck is modeled using equivalent elastic beam-column elements, assuming that the deck remains elastic during seismic and flood events. The effective width of the deck is used and assigned to frame elements to account for the reduction of cross-sectional properties due to decreased torsional resistance for open soffit superstructures with I-girders (SDC, 2010). The computation of effective width is shown in Figure 77.

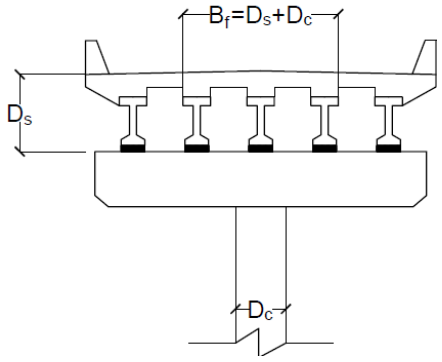

Figure 77. Effective width of the MSC concrete bridge deck

The column of the bridge has a height of 6.7m and is modeled using distributed plasticity elements with fiber discretization, allowing capture of material nonlinearity compared to prior linear elastic material assumptions (Khan and Amanat, 2014). Each column has been discretized into several displacement-based beam-column elements with about 0.96m spacing between nodes. Fiber discretization of the column consists of "Concrete02" and "Steel01" for modeling nonlinear uniaxial constitutive behavior for unconfined concrete and reinforcement in OpenSees, respectively. Unconfined concrete compressive strength is 33.5 Mpa, and the yield strength of longitudinal rebars is set to be 466 Mpa. For the confined concrete model, the maximum confined concrete stress and its corresponding strain are calculated based on Mander et al. (1988).

For the foundation system of the bridge, similar to the modeling of bridge columns, piles are modeled using several displacement-based beam-column elements with section discretization consisting of appropriate constitutive material. Pile elements are linked by rigid arms which are modeled as rigid elements in OpenSees (Han et al., 2010). To capture soil-structure interaction, a dynamic p-y method is adopted (Wang et al., 2014). Three types of nonlinear soil springs (i.e., p-y, t-z, and q-z springs) are utilized to model lateral, frictional, and bearings for the soil-structure interaction, as shown in Figure 78(a). Note that these nonlinear material springs have been implemented in the OpenSees framework with "PySimple1", "TzSimple1", and "QzSimple1", respectively. According to models proposed by Boulanger et al. (1999), p-y nonlinear springs can be conceptualized as consisting of elastic, plastic, and gap components in series. Figure 78(b) presents the detailed composition of the nonlinear p-y element. The group efficiency factor (Mokwa, 1999) has been adopted to modify the ultimate lateral resistance of the p-y element to account for piles with close spacing, and the study assumes the group efficiency factor has no impact on the vertical behavior of the piles.

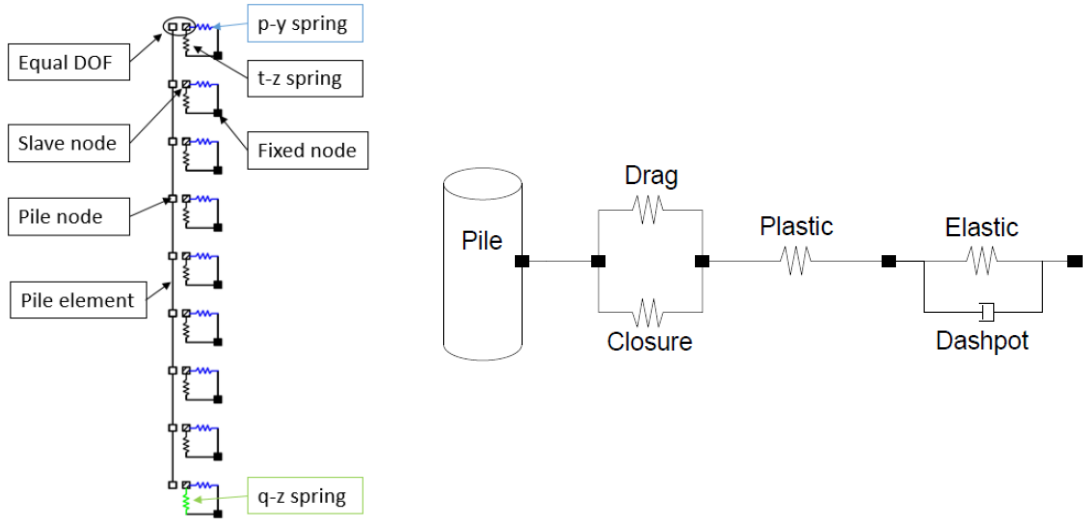

Figure 78. (a) Soil springs used to model soil-structure interaction and (b) details composition of p-y nonlinear spring

P_{ult} is the ultimate lateral capacity of the nonlinear p-y spring, and it is computed based on Equation (70a) for wedge failure near the ground surface (P_{st}) and Equation (70b) for flow failure well below the ground surface (P_{sd}) (Reese et al., 1974).

$$P_{st} = \gamma' z \left\{ \frac{K_o z \tan(\phi') \sin(\beta)}{\tan(\beta - \phi') \cos(\alpha)} + \frac{\tan(\beta)}{\tan(\beta - \phi')} [B + z \tan(\beta) \tan(\alpha)] + K_o z \tan(\beta) [\tan(\phi') \sin(\beta) - \tan(\alpha)] - K_a B \right\} \quad (70a)$$

$$P_{sd} = K_a B \gamma' z [\tan^8(\beta) - 1] + K_o B \gamma' z \tan(\phi') \tan^4(\beta) \quad (70b)$$

z is the distance between the ground level and point of interest, γ' is the effective unit weight of sand, β is passive failure angle, α is angle defining the shape of the failure wedge, K_a is the minimum coefficient of active earth pressure, K_o is the coefficient of lateral earth pressure at rest, B is the diameter of the pile, and ϕ' is friction angle. For the computation of ultimate frictional resistance (T_{ult}) of sand, Equation (71) is used (Tuma and Reese, 1974).

$$T_{ult} = K_o \tan(\phi')\sigma_v' \quad (71)$$

K_o is the coefficient of lateral earth pressure at rest (taken as 0.4), and σ_v' is effective total vertical stress. The computation of ultimate end bearing resistance (Q_{ult}) of sand is computed based on Meyerhof (1976) shown in Equation (72).

$$Q_{ult} = N_q \sigma_v' \quad (72)$$

N_q is a bearing capacity factor, which can be expressed as a function of friction angle, coefficient of lateral earth pressure, and shear modulus of soil at the pile tip.

A seat-type abutment with an initial gap of 20 mm between the bridge deck and the back wall is considered for this study. The numerical modeling of the abutment adopts the model proposed by Mackie and Stojadinovic (2006), which includes longitudinal, transverse, and vertical abutment responses. The longitudinal direction is assigned a gap element with an elastic-perfectly-plastic response. Ultimate strength (P_{abut}) and abutment stiffness (K_{abut}) for the longitudinal direction are computed based on the Caltrans SDC (2004) shown in Equation (73) and Equation (74), respectively, with units in meters for w the width of the back wall and h the height of the back wall.

$$P_{abut} = 239wh(\frac{h}{1.7}) \quad (73)$$

$$K_{abut} = 11500w(\frac{h}{1.7}) \quad (74)$$

w is the width of the back wall, and h is the height of the back wall. The wing wall is accounted for through considering the transverse abutment response computed by multiplying the longitudinal backbone by $C_L = 2/3$ and $C_W = 4/3$ with no gap included. The impact effect due to pounding between the deck slab and abutment back wall is captured through the contact element approach proposed by Muthukumar (2003), which

uses a bilinear model to simulate impact and energy dissipation with specified stiffness, yield displacement, and maximum deformation (Nielson, 2005).

Elastomeric bearing pads are placed at the bent and seat abutments. The modeling of bearings pads uses nonlinear springs with bilinear behavior assuming yield displacement to be 150% of the shear strain. The stiffness of the bearing pads in the horizontal (K_h) and vertical (K_h) directions are computed based on Equations (75) and (76), respectively, following ASSHTO (2012) recommendations.

$$K_h = \frac{GA}{H_t} \tag{75}$$

$$K_v = \frac{EA}{H_h} \tag{76}$$

G and E are the shear and elastic moduli of the bearing pad, A is the cross-section area, H_t is the thickness of the bearing pad, and H_h is the total height of the bearing.

4.4.4 Procedures of seismic and flood analyses considering non-uniform scour

The effect of non-uniformity in scour depth is evaluated through comparing the bridge response under particular scour scenarios shown in Tables 26 to 28 (for non-uniform scour) and Table 29 (for uniform scour). S_{d1} and S_{d2} represent the depth of general scour in bridge foundations 1 and 2, respectively, with locations as indicated in Figure 76. In the non-uniform scour scenarios, S_{d1} is assumed to be constant, while S_{d2} has a higher value and varies from 1m to 8m.

Table 26. Non-uniform scour scenarios with 1m S_{d1}

S_{d1}	1m	1m	1m	1m	1m
S_{d2}	1m	2m	4m	6m	8m
S_{d2}/S_{d1}	1.0	2.0	4.0	6.0	8.0

Table 27. Non-uniform scour scenarios with 2m S_{d1}

S_{d1}	2m	2m	2m	2m
S_{d2}	2m	4m	6m	8m
S_{d2}/S_{d1}	1.0	2.0	3.0	4.0

Table 28. Non-uniform scour scenarios with 3m S_{d1}

S_{d1}	3m	3m	3m
S_{d2}	4m	6m	8m
S_{d2}/S_{d1}	1.3	2.0	2.7

Table 29. Uniform scour scenarios

S_{d1}	1m	2m	4m	6m	8m
S_{d2}	1m	2m	4m	6m	8m

Figure 79 presents a general procedure of performing the bridge seismic or flood analysis. The procedure starts with inputting predefined flood-induced scour depths. If a

seismic analysis is desired, nonlinear time history analysis is performed by imposing recorded accelerations to the bridge structure. If a flood analysis is desired, static analysis is performed with equivalent water pressure applied to bridge vertical elements. The final results of bridge performance under varying scenarios are quantified in terms of engineering demand parameters at the component level.

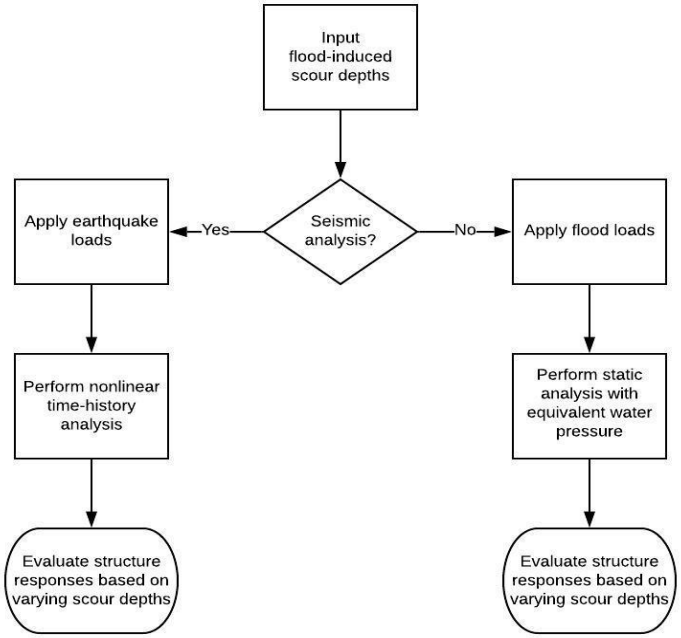

Figure 79. General flowchart of analysis procedures

4.4.5 *Seismic analysis*

The seismic analysis includes modal and nonlinear time history analyses considering varying scour depths. The purpose of the modal analysis is to evaluate the influence of non-uniform scour on the dynamic properties of the bridge, including natural

periods and mode shapes. Comparing modal information between intact, uniformly scoured, and non-uniformly scoured bridges facilitates a better understanding of the structural behavior of bridges, particularly under dynamic loadings. The nonlinear time-history analyses enable the comparison of bridge responses, and particularly values of engineering demand parameters, to quantify the impact of non-uniform scour on bridge performance.

For the nonlinear time history analysis of the bridge, 60 ground motions are randomly selected from a suite of 160 ground motions (Baker et al., 2011) for this study. The ground motions represent shallow crustal earthquakes with magnitudes ranging between 4.3 and 7.9. Figure 80 shows the response spectra for the full suite of ground motions. The ground motions are applied in the transverse and longitudinal directions of the bridge through a uniform input across the soil depth (Shang et al., 2018).

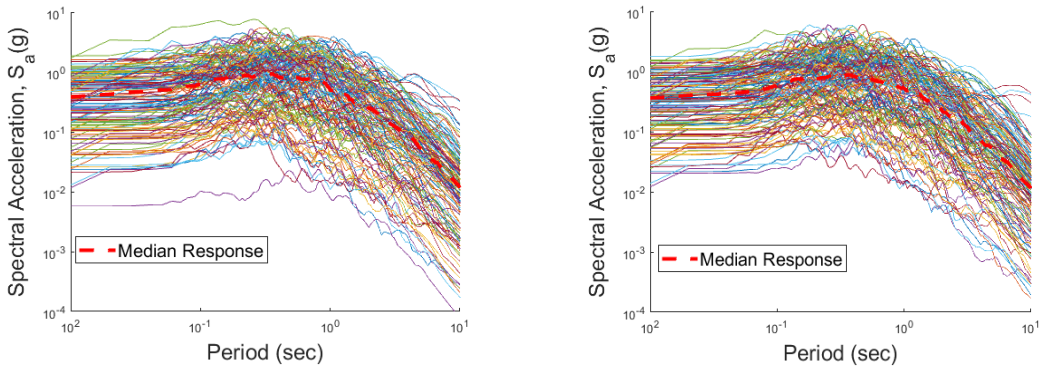

Figure 80. Response spectra for the selected ground motions in (a) horizontal component one and (b) horizontal component two

4.4.6 *Flood analysis*

The pressure of flowing water is commonly considered in bridge design. From AASHTO (2012), the water pressure should be applied to the bridge substructure along with floating debris loads that may further increase water pressure. This study assumes a deterministic parameter for flood level of 3m above the ground level as indicated in Figure 75, and the flow direction is assumed to be in the transverse direction as shown in Figure 81. Flow velocity is selected to be an intensity measure to quantify the intensity of the flood loading on the bridge (Lee et al., 2016).

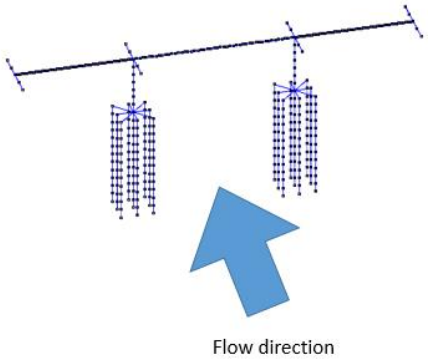

Figure 81. Flow direction on the bridges

To cover a broad range of flood levels, flow velocities from 4m/s to 12m/s are analyzed. Equation (77) is used to calculate water pressure (P_w) considering flood loading as well as debris force (AASHTO, 2012).

$$P_w = C_D \gamma V^2 \times 10^{-6}/2 \quad (77)$$

C_D is drag coefficient which is taken as 1.4, γ is the density of water (kg/m^3), and V is flow velocity (m/s). Note that the water pressure is modeled as a uniform pressure imposed along the appropriate portion of the bridge substructure. In addition, the debris force is obtained

based on Equation (77) and the area of debris accumulation (AASHTO, 2012). The area of debris accumulation is computed based on an inverted triangle with width taken as half the sum of adjacent span lengths but no greater than 13.5m, and depth is taken as half the water depth but no greater than 3m. As a result, the debris force is modeled as a concentrated load acting on the bridge column at the surface of the flood level.

4.4.7 *Seismic analysis results*

Figure 82 displays the results of the modal analysis, showing the first three mode shapes for the bridge with intact, uniform scour depth, and non-uniform scour depth. For clarity in the comparison in Figure 82, the uniform case is for an extreme scour condition with 8m sour depth for both columns. According to a probabilistic approach with a Latin hypercube sampling technique, Fioklou and Alipour (2019) estimate that 8m scour depth corresponds to a return period of 500 years. For the non-uniform case, the study selects the third case from Table 28 with 3m scour depth for column 1 and 8m scour depth for column 2. Table 30 summarizes the fundamental periods of the first three modes for the scour cases listed.

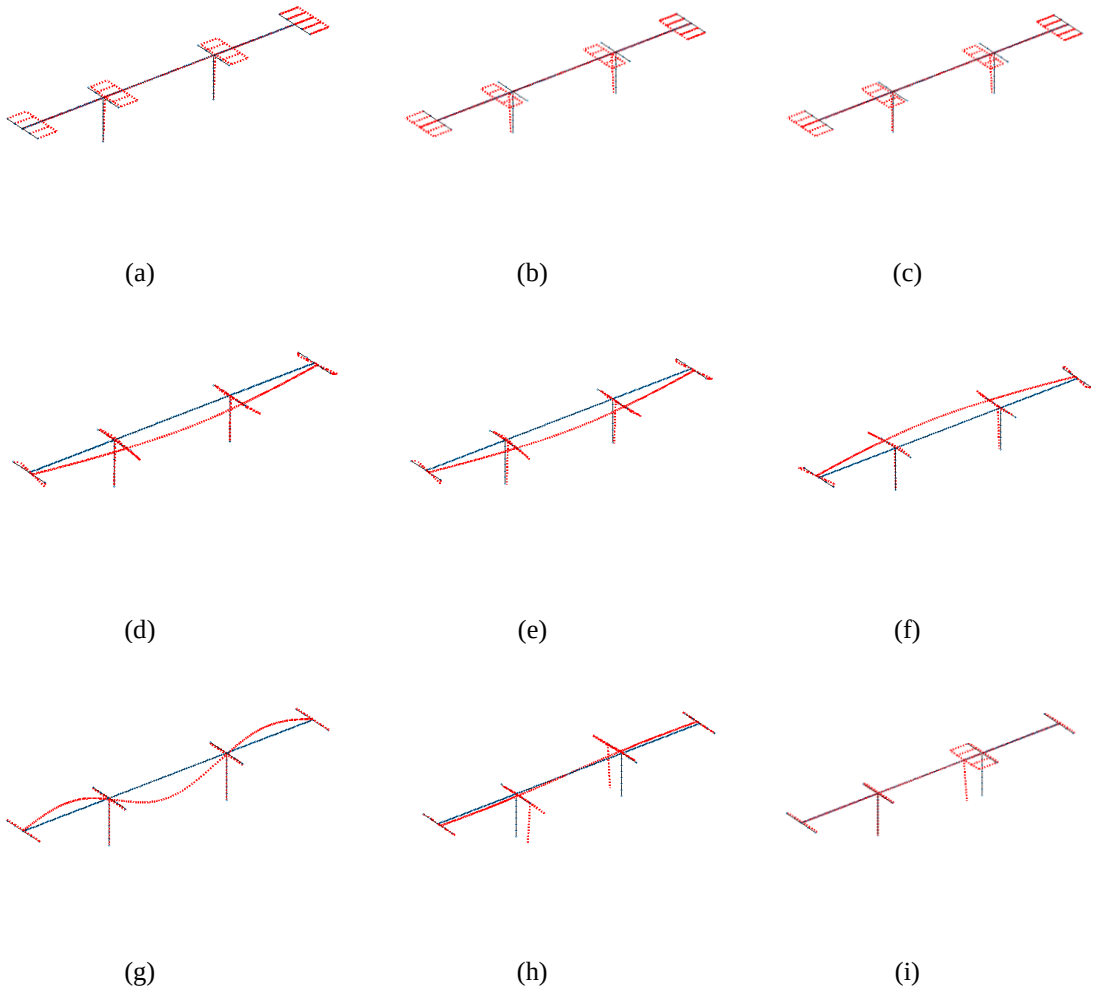

Figure 82. First three mode shapes for (a) & (d) & (g) intact, (b) & (e) & (h) uniformly scoured (8m & 8m), and (e) & (f) & (i) non-uniformly scoured (3m & 8m) bridges

Table 30. Fundamental periods of intact, uniformly scoured, and non-uniformly scoured bridges

Period (sec)	Intact	Uniform		Non-uniform	
		4m & 4m	8m & 8m	2m & 4m	3m & 8m
Mode 1	0.559	0.563	0.580	0.562	0.571
Mode 2	0.446	0.450	0.464	0.449	0.456
Mode 3	0.219	0.219	0.273	0.219	0.270

From the mode shapes shown in Figure 82, the first two modes of the bridges are identical for all three cases, with the first and second modes being longitudinal and transverse vibrations, respectively, regardless of scour conditions. The third mode shape, however, differs across the three cases, indicating the higher level of impact of scour on the dynamic behavior of the structural system. For the intact bridge, the third mode is the out-of-plane vibration of the bridge deck. In comparison, the third mode is a translational movement of both columns for the scour cases and localized translational movement of the column with the higher level of scour depth for the non-uniform scour case. From the modal analysis, scour has a larger influence on higher modes of the bridge, and a non-uniform scour depth causes localized movement due to the loss of stiffness in one of the bridge foundations. From the results shown in Table 30, the effect of scour lengthens the fundamental periods of the bridges, with a larger influence as scour depth increases. There is about a 25% increase in the structural period between the 8m & 8m scour case and the intact case in the third mode due to the significant loss of foundational stiffness, which also results in the change of mode shape. Comparing between uniform and non-uniform cases, the non-uniform scour cases exhibit slightly reduced fundamental periods by less than 5% due to the additional foundational stiffness contributed by one of the foundations with lower scour depth.

To assess the impact of non-uniform scour on bridge responses, 60 nonlinear time history analyses are performed for each scour scenario listed in Tables 26 to 29. Responses are evaluated based on the ratio (R_{EDP}) between the non-uniform scour case and uniform scour case in terms of an engineering demand parameter (EDP) as shown in Equation (78). The EDPs used in this study include curvature demand of the columns and piles, and

displacement of the deck. The curvature demand EDPs quantify the damage in the vertical members of the bridge, whereas the deck displacement EDP is associated with failure modes such as unseating of the bridge deck due to excessive translational movement in the longitudinal direction.

$$R_{EDP} = \frac{EDP_{non-uniform}}{EDP_{uniform}} \tag{78}$$

$EDP_{non-uniform}$ and $EDP_{uniform}$ are the EDPs obtained from analysis under non-uniform and uniform scour scenarios, respectively. For comparison and calculation of the ratio, for a given non-uniform scour case from Tables 26 to 28, the corresponding uniform case is selected from Table 29 with the same value of S_{d2}. If the value of R_{EDP} is greater than 1, the effect of non-uniform scour amplifies the value of the EDP compared to the uniform scour case, and vice versa.

To better categorize the seismic response of the bridges, this study carries out a grouping method to subdivide the ground motions based on intensity. Bridge responses and non-uniform scour impacts are found to differ by loading intensity, with analysis by group facilitating clarity in the evaluation. To characterize the duration of a ground motion, significant duration has been found to be a suitable metric for structural analysis (Chandramohan et al., 2016). Therefore, significant duration (SD) is combined with peak ground acceleration (PGA) to group the ground motions by the intensity in this study. SD is defined as the time interval between the time at which 5% of the seismic energy is obtained and the time at which 95% of the seismic energy is obtained (Papazafeiropoulos and Plevris, 2018). Figure 83 shows the grouping method taking into account both PGA and SD to subdivide the original ground motion set into four categories. PGA_i and SD_i are

the values of PGA and SD for the i^{th} ground motion, respectively, $i = 1, \ldots, 60$. $PGA_{threshold}$ and $SD_{threshold}$ are threshold values maximizing the corresponding mean value of R_{EDP} in category 4. Category 4 yields the strongest set of ground motions with the largest PGA and smallest SD, followed by categories 3, 2, and 1. The threshold values are determined based on detailed investigation of the relationships between R_{EDP}, $PGA_{threshold}$, and $SD_{threshold}$, with corresponding threshold values chosen based on maximized values of R_{EDP}.

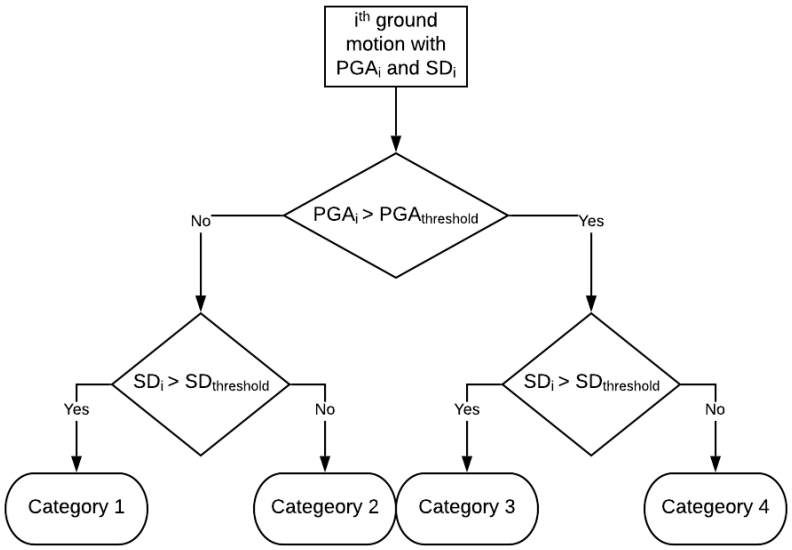

Figure 83. Flowchart of proposed grouping method

First, maximum column curvature is investigated with the impact of non-uniform scour quantified in terms of the ratio R_{cc} based on Equation (78), and the subscript indicating column curvature. Maximum column curvature is calculated as the geometric mean between the two orthogonal directions. To determine the $PGA_{threshold}$ and $SD_{threshold}$ values, Figure 86 shows the mean value of R_{cc}, i.e., the mean ratio $\overline{R_{cc}}$, as a function of PGA and SD. Each data point shown in Figure 86 represents a value of

$\overline{R_{cc}}$, which is the mean value of at least three or more values of R_{cc}. The peak values of $\overline{R_{cc}}$ for columns 1 and 2 are circled. The peak value occurs at 4m and 6m for S_{d2} in columns 1 and 2, respectively, and can be found in Figure 84(d) and Figure 85(d). From Figure 86, the values of $PGA_{threshold}$ and $SD_{threshold}$ are determined to be 1g and 7s for column 1 and 0.4g and 5s for column 2, respectively. The same procedures are used to determine $PGA_{threshold}$ and $SD_{threshold}$ for the foundation and bridge deck EDPs.

With these threshold values defined, Figure 84 shows $\overline{R_{cc}}$ for column 1 as S_{d2} changes for the four categories of ground motion intensity. Figure 85 gives the results for column 2. In both figures, each marker type represents a different S_{d1} scenario to evaluate responses under varying degrees of non-uniformity in scour depths. The vertical bars represent the standard deviation of the data set for R_{cc} given a value of S_{d2}.

From Figure 84, for bridge column 1, if one follows the order of category 1 through category 4, representing the increase of intensity of ground motion, it shows that the peak value of $\overline{R_{cc}}$ of around 1.1 occurs at 6m scour level (S_{d2}) at weak ground motion categories (e.g., categories 1 and 2). As the intensity of ground motion increases to categories 3 and 4, the peak value of $\overline{R_{cc}}$ starts to shift from 6m to 4m scour level (S_{d2}) with a maximum value of 1.43 for one of the curves with the highest degree of non-uniformity (e.g., 1m S_{d1}). In other words, as the intensity of the ground motion increases, the effect of non-uniformity in scour depth is amplified by as much as 43%. An additional interpretation of the peak value of $\overline{R_{cc}}$ is that its occurrence indicates a critical depth of scour, i.e., a non-uniform scour depth condition that results in a maximum increase in potential bridge response due to non-uniform scour effects. As ground motion intensity increases, the critical depth reduces.

For column 2, the results from Figure 85 indicate that even though foundation 2 experiences the same scour depth for the uniform and non-uniform cases, under high-intensity ground motions (e.g., categories 3 and 4) as well as differential scour depths at foundation 1, $\overline{R_{cc}}$ starts deviating from 1 and reaches up to 1.55, indicating a 55% increase in EDP for the non-uniform case at 6m S_{d2} scour level. Neglecting to include non-uniform scour effects in the analysis would significantly underestimate the estimated column response in this case. Compared to Figure 84, the three curves within each plot in Figure 86 are close. As such, the response at column 1 is found to be more sensitive to the degree of non-uniformity (e.g., with varying values of S_{d1}) than at column 2. The column 1 response is also found to be more sensitive to changes in PGA compared to SD as a measure of ground motion intensity. Table 31 summarizes the main findings from Figures 84 and 85 for column 1 and column 2.

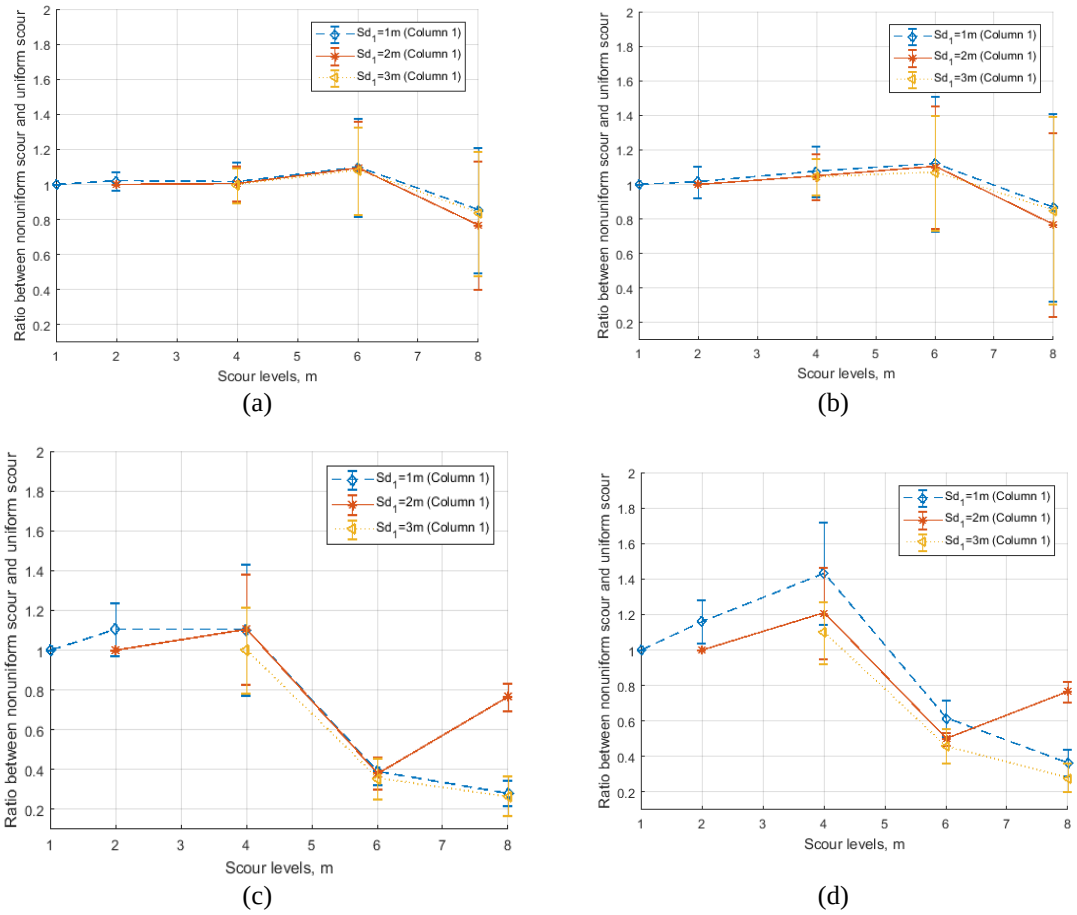

Figure 84. Ratio ($\overline{R_{cc}}$) versus scour levels (S_{d2}) for column 1 in (a) category 1, (b) category 2, (c) category 3, and (d) category 4

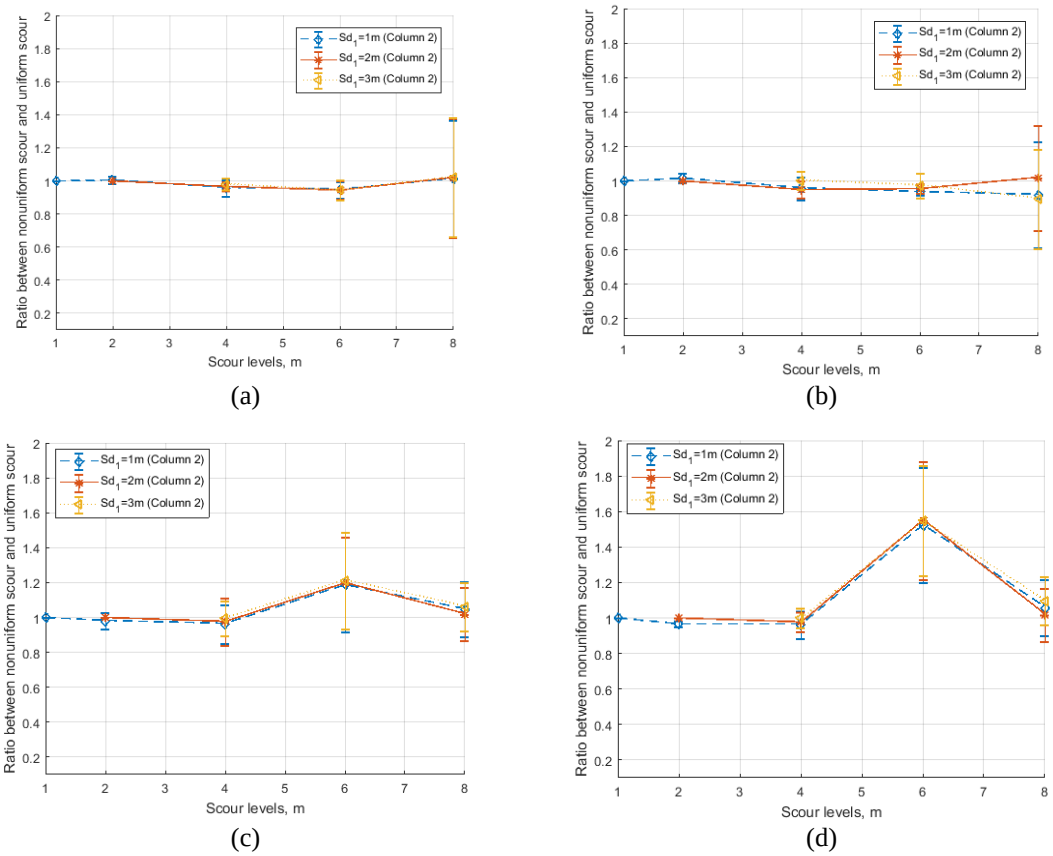

Figure 85. Ratio ($\overline{R_{cc}}$) versus scour levels (S_{d2}) for column 2 in (a) category 1, (b) category 2, (c) category 3, and (d) category 4

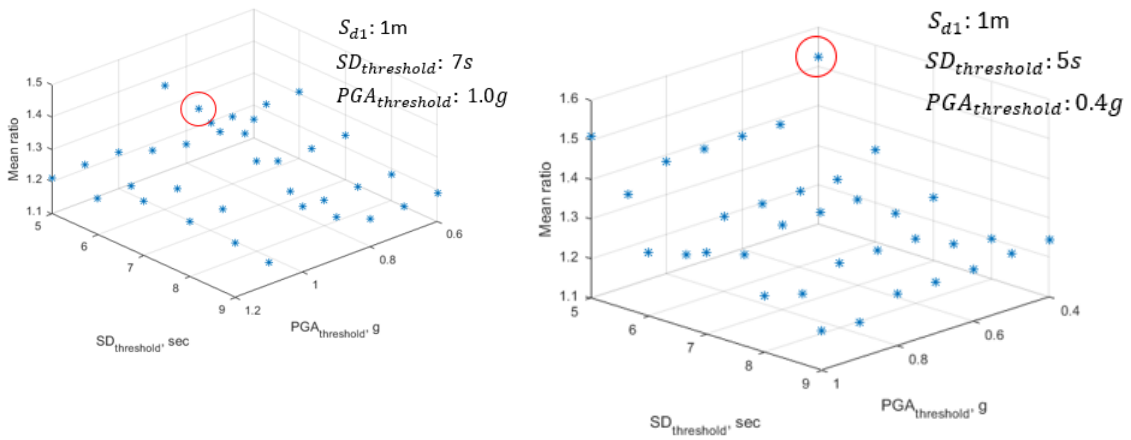

(a) (b)

Figure 86. Determination of $PGA_{threshold}$ and $SD_{threshold}$ for (a) column 1 and (b) column 2

Table 31. Summary of column curvature under earthquake loading with non-uniform scouring conditions

Column curvature	Degree of non-uniformity	Parameter sensitivity (PGA vs. SD)	Mean ratio ($\overline{R_{cc}}$)			Trend #1*	Trend #2**
			S_{d1}& S_{d2} (m)	Increase (%)	Interval		
Column 1	Larger impact	PGA	1 & 4	43	PGA > 1g SD ≤ 7s	Peak shifts from 6m to 4m S_{d2}	Ratio reduces well below 1
Column 2	Limited impact	SD	2 & 6	55	PGA > 0.4g SD ≤ 5s	From no peak to peak at 6m S_{d2}	Ratio reduces to 1

***Ground motions with low intensity to high intensity
**Post-peak behavior for ground motion with high intensity

To further visualize the impact of non-uniformity in scour depth on the seismic behavior of columns, envelopes of maximum curvature, maximum shear demand, and maximum moment demand are plotted in Figures 87, 88, and 89 based on a ground motion selected from the interval shown in Table 31 with corresponding values of S_{d1} and S_{d2} for columns 1 and 2, respectively. Four envelope curves are shown in each plot, with each one

representing bending in a specific direction with or without considering non-uniformity in scour depth. “L” stands for bending curvature along the longitudinal direction; “T” stands for bending curvature along the transverse direction.

From Figure 87, the results show that both columns 1 and 2 exhibit higher curvature demand at the base of the column for the non-uniform scour case in comparison with the uniform scour case due to the amplification of the response from non-uniform scour effects. An estimated yield curvature is computed based on the specific sectional properties of the bridge column, assuming the first yield of longitudinal reinforcement is plotted as a vertical dotted line. From Figure 87, due to the effect of non-uniform scour, the maximum longitudinal curvature exceeds the expected yield curvature for both columns, especially for column 2, with almost 80% of the column along the height yielded. Therefore, neglecting to include non-uniform scour effects in the analysis could underestimate curvature demand and the risk of structural damage in scoured bridges.

Figures 88 and 89 show the demand envelope in terms of column shear and moment in both transverse and longitudinal directions. From Figure 88, due to the effect of non-uniform scour, bridge columns experience larger shear demand, particularly at the base, except for column 2 in the transverse direction. With the higher shear demand, the risk of the column undergoing brittle failure is increased if both poor reinforcement details and non-uniform scour are present. Figure 89 is the corresponding moment envelope that the columns experience. Non-uniform scour amplifies the magnitude of the moment demand, especially at the base of the columns, which could lead to the formation of flexural hinges instead of remaining materially elastic.

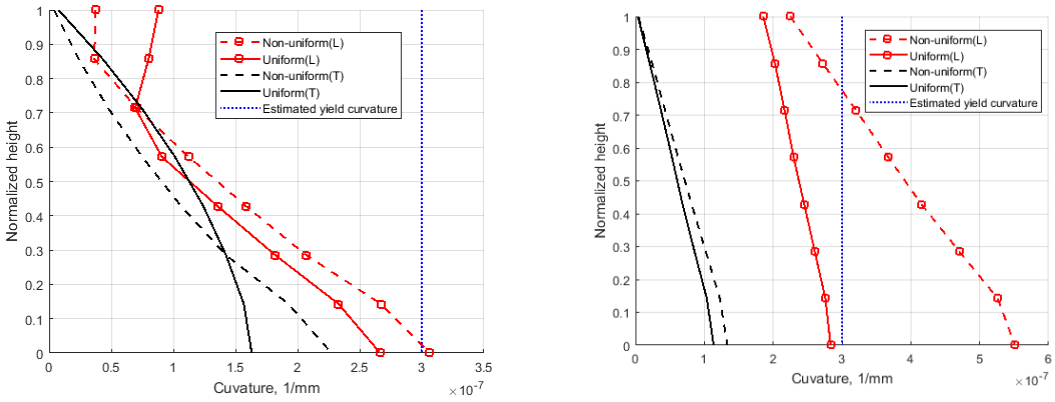

Figure 87. Envelope of maximum curvature distribution from seismic analysis for (a) column 1 and (b) column 2

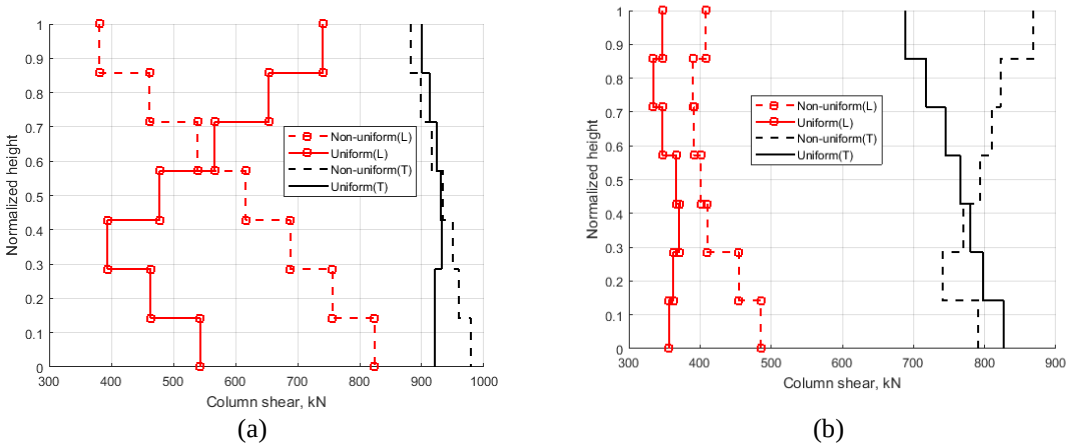

Figure 88. Envelope of maximum shear distribution from seismic analysis for (a) column 1 and (b) column 2

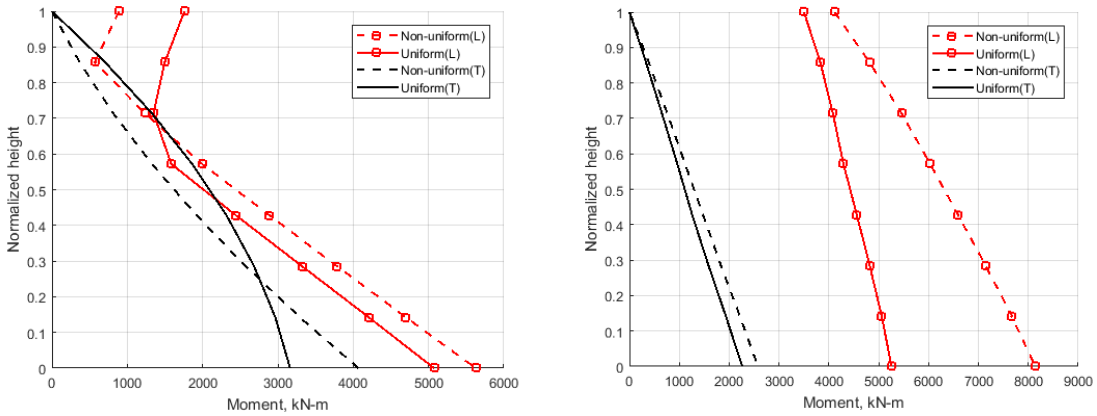

Figure 89. Envelope of maximum moment distribution from seismic analysis for (a) column 1 and (b) column 2

In addition to the ratio for column curvature (R_{cc}), ratios for pile curvature (R_{pc}) and longitudinal displacement of the bridge deck (R_{dd}) are investigated with seismic analysis. For brevity, Tables 32 and 33 display the main findings regarding the effect of non-uniformity in scour depth on pile curvature and longitudinal deck displacement responses, respectively. The plots showing values of $\overline{R_{pc}}$ and $\overline{R_{dd}}$ for varying scour depths are provided in the appendix. Based on the results for pile curvature, $\overline{R_{pc}}$ in foundation 1 shows a monotonic decrease as scour S_{d2} increases. In comparison, $\overline{R_{pc}}$ in foundation 2 displays a similar trend to that of $\overline{R_{cc}}$ in column 2 with a maximum increase of 57% in the response due to the effect of non-uniformity in scour depth. Comparatively, non-uniform scour conditions have a less insignificant impact on the response of the bridge deck, with a maximum increase of 16% and 11% in $\overline{R_{dd}}$ for locations 1 and 2, respectively.

Table 32. Summary of pile curvature under earthquake loading with non-uniform scouring conditions

Pile curvature	Degree of non-uniformity	Parameter sensitivity (PGA vs. SD)	Peak value of mean ratio ($\overline{R_{pc}}$)			Trend #1*	Trend #2**
			S_{d1}& S_{d2} (m)	Increase (%)	Intervals		
Foundation 1	Larger impact	PGA	1 & 6	13	PGA > 1.2g SD ≤ 10s	Entire curves start to shift upward	Ratio reduces monotonically well below 1
Foundation 2	Limited impact	SD	2 & 6	57	PGA > 0.5g, 0.6g, 0.7g, 0.8g SD ≤ 5s	From no peak to peak at 6m S_{d2}	Ratio reduces to 1

*****Ground motions with low intensity to high intensity
**Post-peak behavior of ground motion with high intensity

Table 33. Summary of longitudinal displacement of the deck under earthquake loading with non-uniform scouring conditions

Displacement of deck	Degree of non-uniformity	Parameter sensitivity (PGA vs. SD)	Peak value of mean ratio ($\overline{R_{dd}}$)			Trend #1*	Trend #2**
			S_{d1}& S_{d2} (m)	Increase (%)	Intervals		
Location 1	Limited impact	SD	3 & 6	16	PGA > 0.6g, 0.7g, 0.8g SD ≤ 5s	From no peak to peak at 6m S_{d2}	Ratio reduces to 1
Location 2	Limited impact	SD	3 & 6	11	PGA > 0.6g, 0.7g, 0.8g SD ≤ 5s	From no peak to peak at 6m S_{d2}	Ratio reduces to 1

*****Ground motions with low intensity to high intensity
**Post-peak behavior of ground motion with high intensity

4.4.8 *Flood analysis results*

The flood analysis is carried out assuming static water pressure applied between the flood level and ground level with loading intensity quantified by flow velocity. Figure 90

shows how the ratios for column curvature ($\overline{R_{cc}}$) change relative to flow velocity (V) and scour depth (S_{d2}) for both columns. From Figure 90, the flow velocity has a limited impact on $\overline{R_{cc}}$ for both columns. The value of $\overline{R_{cc}}$ is less sensitive to the degree of uniformity (e.g., the impact of the value of S_{d1}) for both columns, while the impact of the value of S_{d2} dictates the trend of the ratio. Due to the effect of non-uniform scour conditions, the value of $\overline{R_{cc}}$ monotonically increases as S_{d2} increases for column 1 with maximum increases of 40% at 8m S_{d2}. Column 2 exhibits the opposite trend with maximum decreases in $\overline{R_{cc}}$ of 10% at 8m S_{d2}, and the rate of change is relatively small due to the fact that column 2 experiences the same scouring conditions regardless of the uniform or non-uniform case. In sum, while effects on column 2 are limited, non-uniform scour greatly impacts the column curvature at column 1 with increasing effects as scour depth increases.

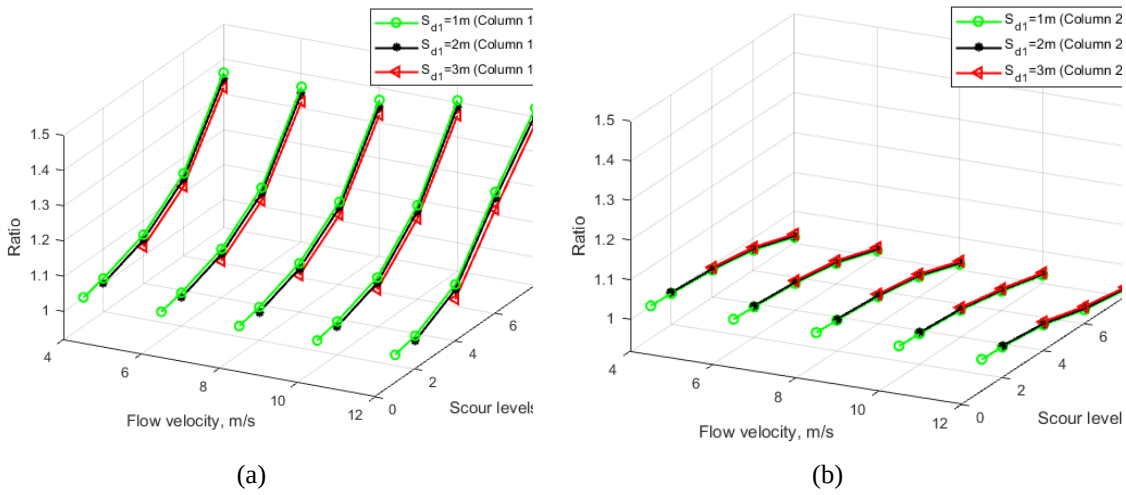

(a) (b)

Figure 90. Ratio ($\overline{R_{cc}}$) versus water velocity (V) and scour level (S_{d2}) for (a) column 1 and (b) column 2

Figures 91 and 92 further investigate the impact of non-uniform scour on structural responses under flood load by displaying the envelopes of maximum curvature and maximum shear along the columns with 6m/s flow velocity under uniform and non-

uniform scour conditions with specified values for S_{d1} and S_{d2}. From Figure 91, the maximum curvature starts to increase rapidly for both columns due to the water pressure and concentrated debris load. For column 2, the effect of non-uniformity has a limited impact on the maximum curvature distribution. For column 1, the increase in curvature due to non-uniform scour effects at 4m S_{d2} is relatively small; however, the increase is more than 30% at the base for 8m S_{d2}. Note that the maximum curvature shown in Figure 91 is far from the estimated yield curvature presented in Figure 87, and the columns remain materially elastic regardless of scouring conditions. For the shear envelope shown in Figure 92, there is an abrupt increase in shear force due to the concentrated debris load at the flood level. A slight increase in maximum shear due to non-uniform scour effects for column 1 is also observed.

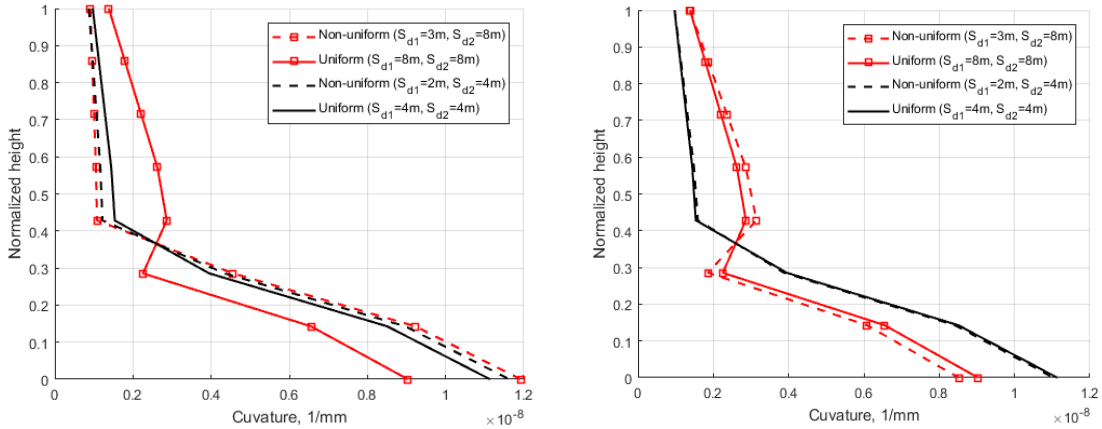

Figure 91. Envelope of maximum curvature distribution from flood analysis for (a) column 1 and (b) column 2

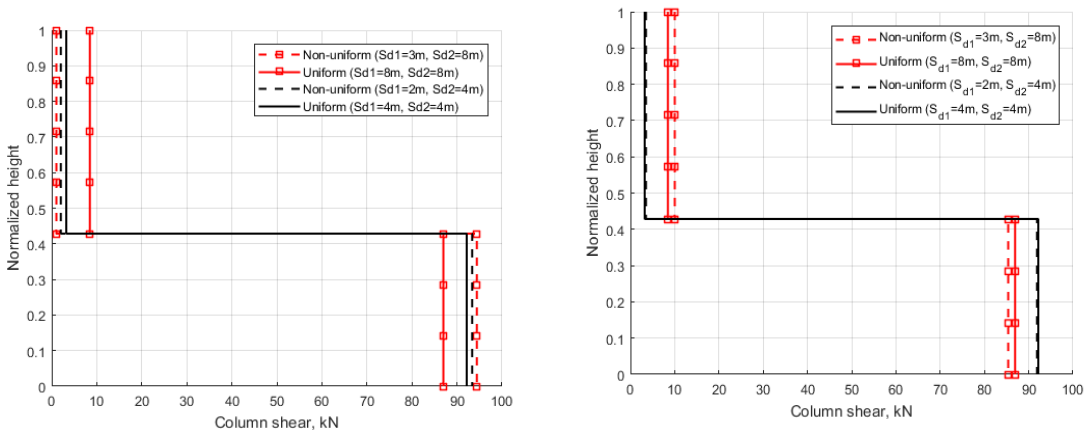

Figure 92. Envelope of maximum shear distribution from flood analysis for (a) column 1 and (b) column 2

In terms of pile curvature, $\overline{R_{pc}}$ as a function of flow velocity and scour level (S_{d2}) is shown in Figure 93. Compared to $\overline{R_{cc}}$, the value of $\overline{R_{pc}}$ for foundation 1 depends on both water velocity and S_{d2}. As flow velocity and S_{d2} increase, $\overline{R_{pc}}$ increases with a maximum increase of 15% due to the effect of non-uniformity in scour depth for 8m S_{d2} and 12m/s flow velocity. $\overline{R_{pc}}$ for foundation 2 shows no effect by flow velocity or S_{d2}. In sum, non-uniform scour depths lead to increases in pile curvature at foundation 1 with the effect increasing as flow velocity and scour depth increase.

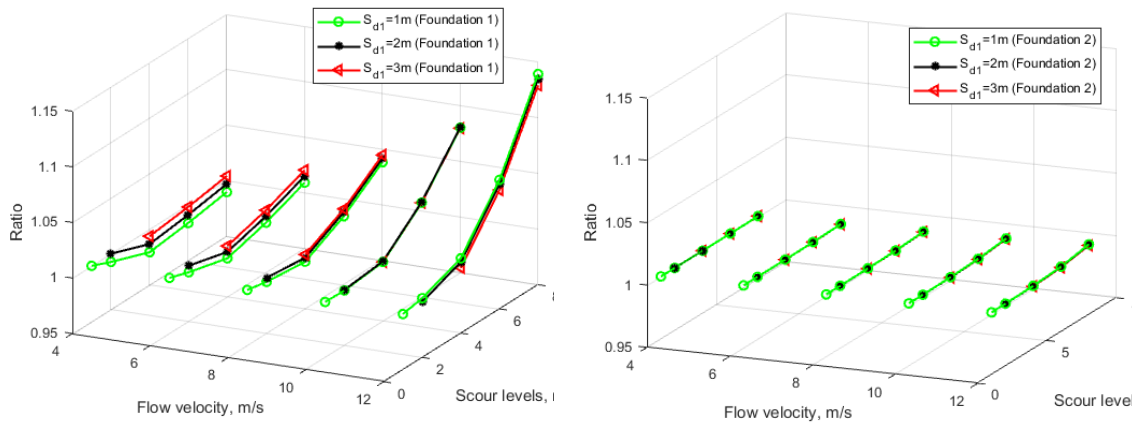

(a) (b)

Figure 93. Ratio ($\overline{R_{pc}}$) versus water velocity (V) and scour level (S_{d2}) for (a) foundation 1 and (b) foundation 2

4.4.9 Conclusions

While uniform scouring conditions are typically assumed in the design and analysis of bridges subject to scour, bridge foundations often experience non-uniform scour depths due to factors such as water flow velocity, obstacles, geometry and configuration of foundation, and so on. This study has investigated the impact of non-uniform scour conditions on the seismic and flood performance of scoured bridges. Under differential scouring conditions along the longitudinal direction of the bridge, analyses in terms of varying engineering demand parameters and failure mechanisms for different loadings are conducted. The following conclusions are drawn based on the results from the analysis of the MSC concrete girder bridge.

- Modal analysis of the bridge shows that both uniform and non-uniform scour conditions influence the mode shape of the higher mode of the scoured bridge in comparison with the intact bridge. In particular, non-uniform scour conditions

lead to localized translational movement of the column at the foundation with larger scour depth.

- Results based on nonlinear time history analyses of bridge performance under seismic loadings indicate that the estimated maximum curvature increases by up to 43% and 55% for bridge columns 1 and 2, respectively, under non-uniform scour conditions. More importantly, the bridge column could experience yielding of reinforcement due to non-uniform scour effects compared to remaining materially elastic in the uniform scour case.
- Estimated pile curvature under earthquake loading is found to increase by as much as 57% due to non-uniform scour effects. While the impact on longitudinal deck displacement is smaller, increases of up to 16% under non-uniform scour conditions are found.
- Results based on applying static water pressure for flood analyses show that due to the influence of non-uniform scouring conditions, there are increases of up to 40% and 15% in maximum curvature for column 1 and foundation 1, respectively, in comparison with uniform scour scenarios. The non-uniform scour effects on both column curvature and pile curvature increase as scour depth increases.

4.4.10 Appendix: Seismic analysis results of foundation piles and displacement of deck

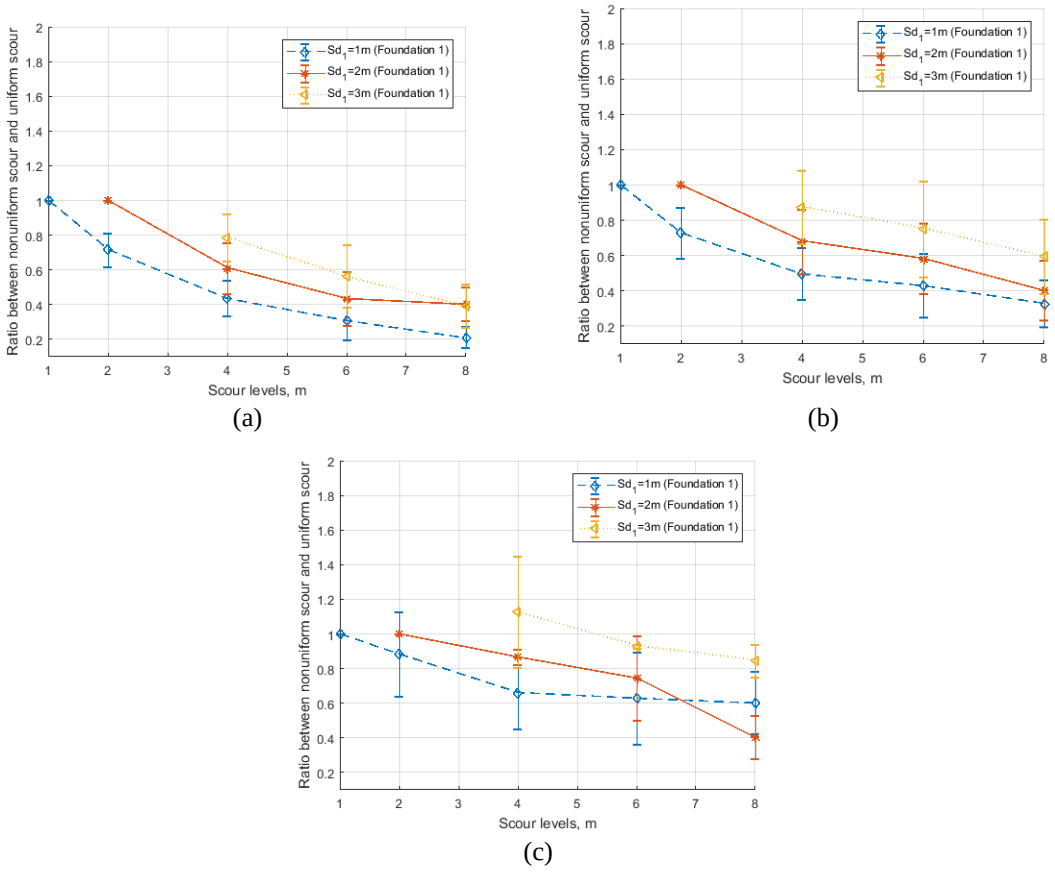

Figure 94. Ratio ($\overline{R_{pc}}$) versus scour levels (S_{d2}) for foundation 1 in (a) category 1, (b) category 2, and (c) category 4

*Note for pile curvature, there are mean ratio data points only for the categories 1, 2, and 4. The values of $PGA_{threshold}$ and $SD_{threshold}$ are 1.2g and 10.0 sec, respectively.

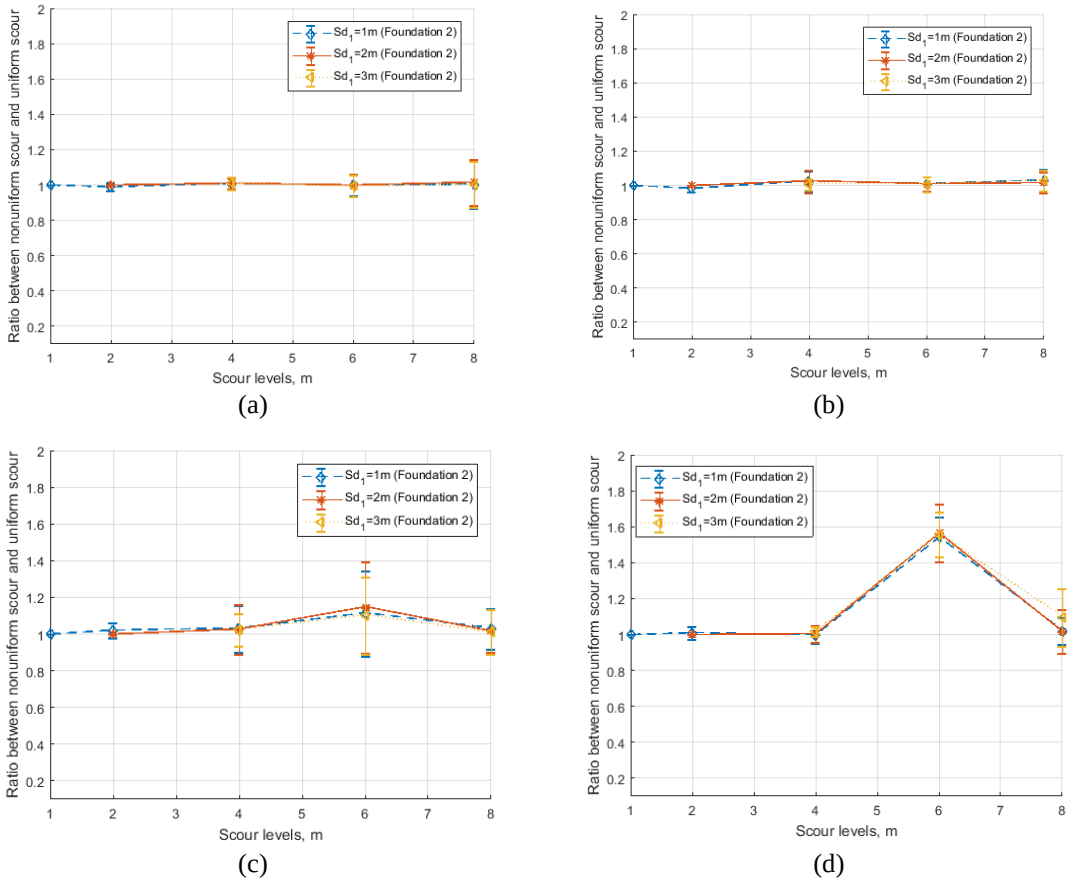

Figure 95. Ratio ($\overline{R_{pc}}$) versus scour levels (S_{d2}) for foundation 2 in (a) category 1, (b) category 2, (c) category 3, and (d) category 4

*Note the values of $PGA_{threshold}$ and $SD_{threshold}$ are 0.7g and 5.0 sec, respectively.

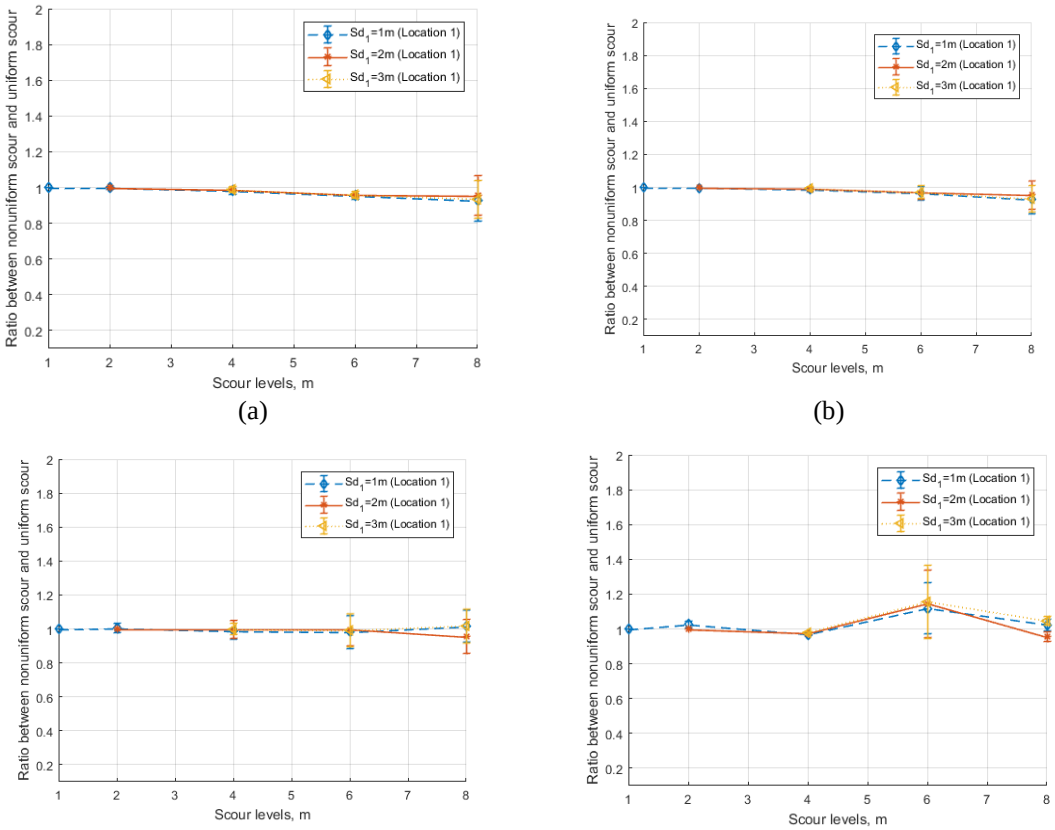

Figure 96. Ratio ($\overline{R_{dd}}$) versus scour levels (S_{d2}) for location 1 in (a) category 1, (b) category 2, (c) category 3, and (d) category 4

*Note the values of $PGA_{threshold}$ and $SD_{threshold}$ are 0.7g and 5.0 sec, respectively.

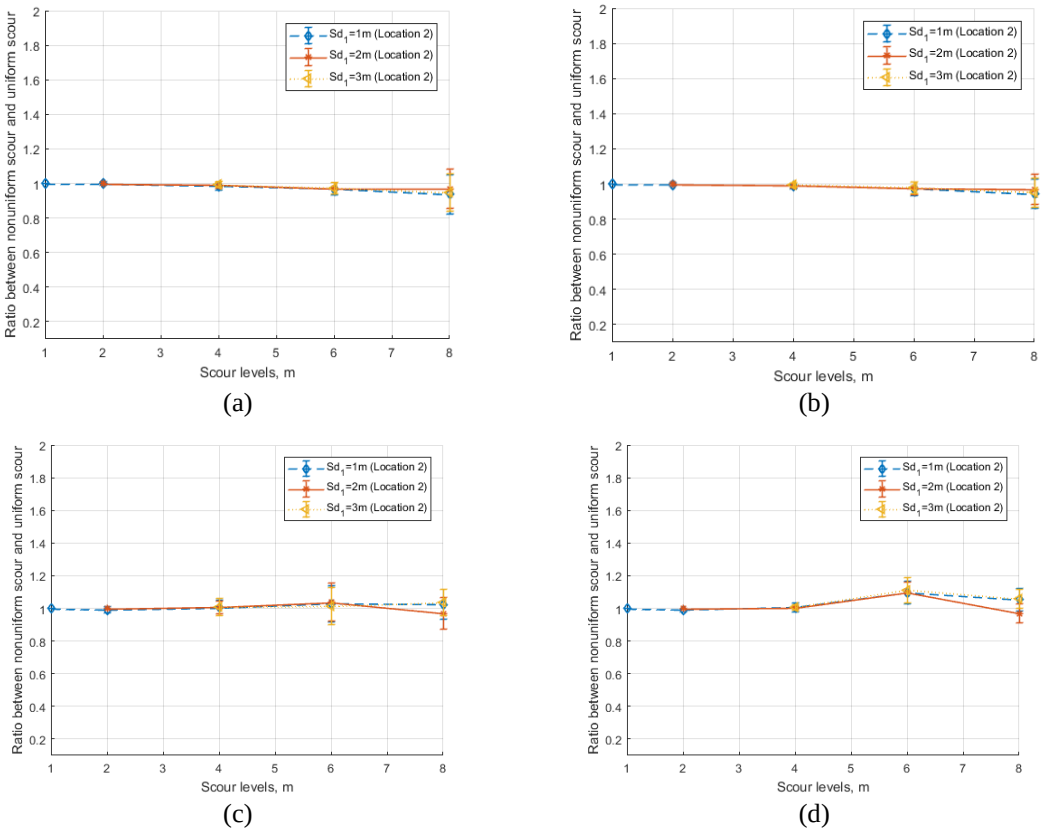

Figure 97. Ratio ($\overline{R_{dd}}$) versus scour levels (S_{d2}) for location 2 in (a) category 1, (b) category 2, (c) category 3, and (d) category 4

*Note the values of $PGA_{threshold}$ and $SD_{threshold}$ are 0.7g and 5.0 sec, respectively.

CHAPTER 5. OTHER DEGRADATION MECHANISMS ON BRIDGE STRUCTURES

5.1 Introduction

Two subtopics related to different forms of degradation mechanisms will be covered in this chapter. The first subtopic (Subtopic No. 5) discusses the combined effect of corrosion attack and scour on the seismic performance of bridges through fragility assessment based on publication Zhang et al. (2019b). On the other hand, the second subtopic (Subtopic No. 6) presents a study regarding the robust modeling of short lap splices on structural columns and investigates the impact of short lap splices on static and dynamic behaviors of the columns based on publication Zhang and Tien (2020a).

5.2 Subtopic No. 5

5.2.1 Introduction

During the life cycle of reinforced concrete (RC) highway bridges, multiple forms of aging and deterioration mechanisms may occur and impact the functionality of the bridge system. These mechanisms include the result of environmental stressors such as corrosion attack and water-induced erosion of the soil near the foundation system of bridge piles resulting in scour. Several previous studies focus on assessing the individual effects of these processes on the bridges' seismic performance. For example, Choe et al. (2009) investigate the reduction of RC bridge columns' capacity due to corrosion. Ghosh and

Padgett (2012) evaluate corrosion's impact on bridge fragility considering multiple components deterioration and exposure conditions. Wang et al. (2014) investigate the impact of local scour on seismic fragility of bridges considering various foundation system types. Corrosion and scour are prevalent across bridges and can act simultaneously to affect bridges' performance, particularly in marine environments. However, there is relatively limited previous research studying the combined effect of corrosion and bridge scour on bridge fragility.

This subtopic presents a framework that utilizes bridge inspection data for corrosion and scour to assess bridge safety through constructing bridge fragility curves. In particular, bridge inspection data includes mass loss of reinforcement in the bridge column due to corrosion attack and bridge scour depth due to sustained erosion and after flooding events.

5.2.2 Mechanism and modeling of deterioration

Corrosion's effect on the RC column is mainly manifested by degrading the mechanical properties of the reinforcement and cracking of the concrete cover due to the expansion of corrosion products. Particularly, corrosion attacks on reinforcement can be captured by modifying longitudinal reinforcement's geometric and constitutive behavior (Kashani et al., 2015). Cracking of the concrete cover can be modeled by modifying the constitutive behavior of unconfined concrete according to modified compression field theory (Vecchio and Collins, 1986). Details of the modeling of corrosion's effect on bridge performance can be found in Zhang et al. (2019a).

Material is carried away from the bed and banks due to flowing water's erosive action, leading to scour. The total depth of scour consists of three components: long-term

aggradation or degradation, contraction scour, and local scour. For bridges located in stream beds, due to the obstruction of the water flow by the bridge foundation system, local flow velocity, and turbulence levels increase, giving rise to vortices that can remove sediment and create a scour hole around the foundation system of the structure (May et al., 2002). This subtopic focuses on the effect of local scour on bridges as it has been reported to significantly increase the seismic fragility of bridges (Wang et al., 2014).

The modeling of the soil-structure interaction (SSI) in this study uses the dynamic p-y method. Details regarding this method can be found in Boulanger et al. (1999). The foundation pile is modeled as a beam on a nonlinear Winkler foundation where lateral SSI is captured by a p-y spring, and vertical axial friction and tip bearing capacity are captured by a t-z spring q-z spring, respectively. This study considers a bridge located in the sand and follows the recommendation provided by the American Petroleum Institute to calculate the ultimate bearing capacity for sand. The p-y relationship is shown in Equation (79) below.

$$P = AP_u \tanh\left[\frac{kH}{AP_u} y\right] \tag{79}$$

P is lateral soil resistance at any depth H, A is a modification factor that accounts for static or cyclic loading (0.9 in this case), P_u is ultimate bearing capacity at depth H, y is lateral deflection, and k is the initial modulus of sub-grade reaction. The dynamic p-y method can account for the dynamic effect of SSI while maintaining reasonable computational times for probabilistic analyses (Wang et al., 2014). In this study, local scour is modeled by including removing the nonlinear spring along the pile and modifying the remaining soil's properties due to the effects of stress history (Lin et al., 2010) and scour hole dimension (Lin et al., 2014).

5.2.3 Bridge description and site conditions

The bridge selected for this study is a single-bent concrete box-girder bridge with an integral pier, one of the most common bridge types in California (Mackie and Stojadinovic, 2003). A Type I pile shaft foundation is used in this bridge type, and the length of the embedded pile shaft is assumed to be 1.75 times the length of the column above grade (Wang et al., 2014). Figure 44 shows the layout of the single-frame box-girder concrete bridge investigated in this subtopic. To obtain results comparable with those from previous studies, dimensions are chosen consistent with those from previous work. Table 34 summarizes the main dimensions of the two bridges considered for this selected bridge type. Further details of this bridge can be found in Mackie and Stojadinovic (2003). Uniformly graded fine sand found at the Mustang Island site is used for this study. Properties of the sand are provided in Table 20.

Table 34. Dimensions of single-bent box-girder bridge

Single-bent box-girder bridge	***Span Length (L), ft.***	***Column Height (H), ft.***	***Column diameter (Dc), in.***
Short-span	60.0	24.6	63.0
Medium-span	120.0	32.8	79.0

5.2.4 Fragility assessment

In this section, bridge fragility considering the combined effect of corrosion and scour is assessed. First, the numerical model is built in the finite-element software OpenSees (McKenna et al., 1997). For the sub-structure, the column is modeled using a single force-based element. The pile foundation uses multiple distribution plasticity

elements with a fiber section consisting of a uniaxial constitutive model for concrete and steel. The super-structure is modeled using elastic beam-column elements. Figure 98 shows the 3D-view of the OpenSees bridge model, and Table 35 shows the dynamic properties of the short-span and medium-span bridges.

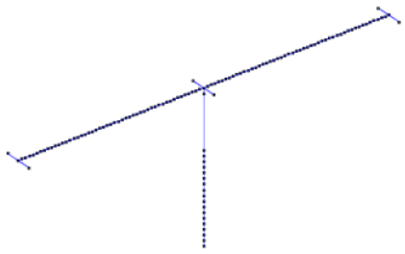

Figure 98. 3D-view of the bridge in OpenSees

Table 35. Dynamic properties of the single-bent concrete box-girder bridges

Unit: sec.	***1st period***	***2nd period***	***3rd period***
Short-span bridge	0.700	0.459	0.347
Medium-span bridge	0.916	0.527	0.499

Next, analytical fragility curves are computed by running a series of nonlinear time history analyses on deterministic bridges. Similar analyses can be conducted sampling from probabilistic bridge properties. Ground motions are selected from the assembled set in Baker et al. (2011). The level of corrosion is indicated by the percentage of measured mass loss of reinforcement. The amount of scour is indicated by the measured scour depth around the bridge pier. The engineering demand parameter selected to quantify the structural damage of the bridge column is the maximum curvature. The column fragility is expressed as the probability of exceeding some damage state for a specific intensity

measure. This can be defined as a function of parameters of the capacity and demand variables assuming both of them following a lognormal distribution.

This subtopic presents results for the most severe damage state, collapse, defined as a 20% reduction of column capacity. Figure 99 shows the resulting column fragility curves for the collapse damage state. Fragilities are calculated as a function of peak ground acceleration (PGA). Comparing across the cases considered, Figure 99 shows that the failure probability is higher for the short-span bridge at low corrosion levels and becomes similar to that of the medium-span bridge at higher corrosion levels, particularly at lower scour depths. Considering the combined effects of corrosion and scour, the impact of corrosion is more pronounced for bridges with less scour because higher levels of seismic force are experienced at bridge columns with less scour.

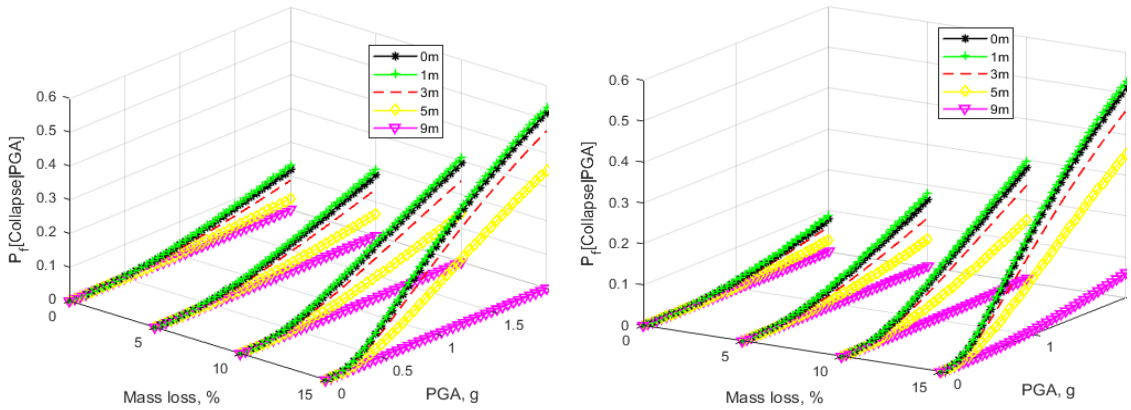

Figure 99. Column fragility curves varying corrosion and scour levels for (a) short-span and (b) medium-span bridge

Figure 100 shows the bridge system fragility for the collapse damage state moving from column fragility to system fragility. System fragility curves are constructed accounting for the structural responses of individual bridge components, e.g., column curvature and deck displacement, by comparing the joint probability density functions of

demand and capacity. The bridge system failure probability is computed assuming the bridge to be a series system composed of each bridge component as shown in Equation (80).

$$Pr[System\ Failure] = Pr[\cup_{m=1}^{M} m^{th}\ Component\ Failure] \quad (80)$$

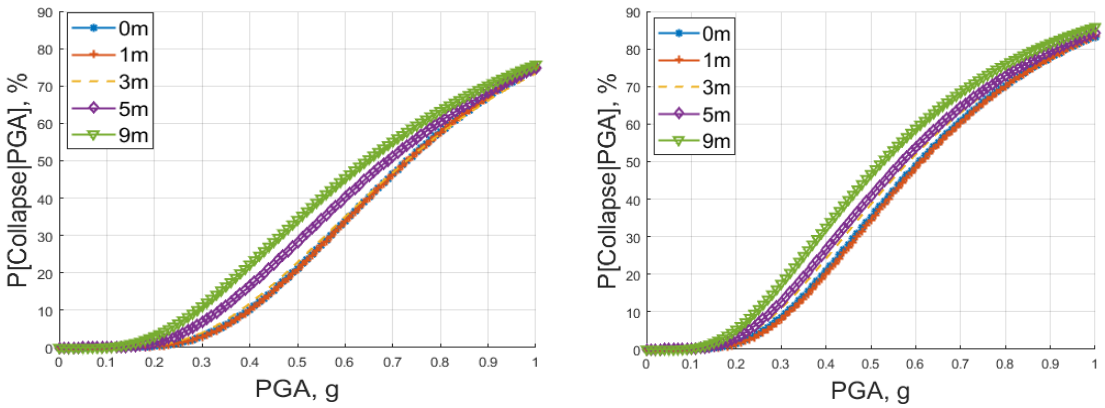

Figure 100. System fragility curves varying corrosion and scour levels for (a) short-span and (b) medium-span bridge

For this bridge type, the system fragility curves are governed by the failure mode of unseating of the bridge deck with an increase of approximately 15% in the failure probability for 9m compared to 0m scour depth. In terms of system failure probability, the medium-span bridge is more vulnerable than the short-span bridge with higher failure probabilities given a loading intensity. This is because the more slender column contributes to larger deck displacement from rigid body rotation at the foundation.

5.2.5 Conclusions

The subtopic presents a framework to assess bridges' safety conditions based on collected inspection data on corrosion and scour, including measurements of mass loss of

reinforcement and scour depth. Safety is evaluated as a probability of exceeding an undesired damage state under a future loading. The framework accounts for the degrading mechanical effects on reinforcement and concrete cover from corrosion and the loss of soil and effects of soil stress history and scour hole dimension under scour. To implement this framework, single-bent box-girder bridges with two geometric configurations are selected.

The results show that 15% mass loss due to corrosion increases the bridge column's failure probability by as much as 40% for both geometries. The medium-span bridge is more vulnerable at a system level at different scour hole depths due to the more slender column, with an increase in system failure probability of 15% for both geometries for a 9m compared to 0m scour hole. The effects of corrosion are more pronounced for bridges with less scour. The analysis framework presented in this study enables updating of bridge fragility assessment under varying levels of measured corrosion and scour. In assessing the safety of bridges across a transportation network, such assessments allow identifying the most vulnerable bridges and prioritizing resources for repair or retrofit. This will decrease the vulnerability of bridges across the network and increase resilience under future loading scenarios.

5.3 Subtopic No. 6

5.3.1 Introduction

In older structures, including both buildings (Melek and Wallace 2004; Cho and Pincheira 2006) and highway bridges (Chail et al. 1991; Sun et al. 1993) built pre-1970s, it was common for reinforced concrete columns to consist of widely spaced transverse

reinforcement and short lap splices at the base of the column with a lap length of 20–24 times the longitudinal bar diameter. Structures with short lap splices at the base have limited ductility and lateral strength. These structures are more likely to exhibit poor performance under lateral loadings and have an increased probability of suffering damage during seismic events. Damage includes potential pull-out failures and even structural collapse.

Nonlinear analysis is becoming common practice to predict and evaluate responses to assess the performance of these structures. Having accurate and consistent numerical models is essential to conduct these analyses and capture columns' failure mechanisms with short lap splices. However, existing approaches are not objective due to the softening characteristic of the force transferring mechanism between the concrete and lap-splice bars. In columns with short lap splices, the lap-splice region's behavior governs column response, which often governs overall structural response. Therefore, objective models, including the lap-spliced material for these analyses, are independent of the number of integration points and do not suffer from length scale issues, are needed.

In the numerical modeling of reinforced concrete columns presented in this study, two elements are used, with the bottom element covering the lap splice's length. Using two elements rather than a single element enables the distribution of plasticity along the lap-splice region to be captured. Previous studies have suggested using two integration points in the bottom element (Tariverdilo et al. 2009), leading to numerical results that correspond closely with experimental tests. However, as the length of a specimen increases, including lab-scale test specimens to full-scale columns, increasing the number of integration points may be desired to capture the behavior along the lap splice. Changing the number of

integration points leads to strain localization issues, resulting in inaccurate element response outcomes from the model. For example, the resulting element flexibility matrix and corresponding stiffness matrix, as well as element rotational and axial deformations, change based on the number of integration points used, leading to inaccuracies in the analysis results.

In addition, results even with two integration points may be inaccurate for some specimens, as shown subsequently in this study. Therefore, there is the need for an approach that is able to obtain accurate and consistent analysis results that are independent of the length of the element and independent of the number of integration points used. The proposed regularization approach results in objective numerical models. This study describes and evaluates the regularization approach that uses a constant post-peak energy criterion for reinforced concrete columns with short lap splices.

The rest of this study is organized as follows. The next section provides background and related studies motivating this work. The following section presents the formulation of the force-based numerical element. The proposed regularization procedure for the lap splice due to local softening behavior in tension is then presented. The modeling details for the columns analyzed using force-based beam-column elements are provided. The next section shows the results from using the proposed regularized compared to from the nonregularized model. Results include verifying the numerical model against experimental tests and convergence results for static and dynamic analyses considering varying numbers of integration points in the lap-splice region.

5.3.2 Background and related work

There have been several previous analytical studies of the nonlinear response of columns with short lap splices (Reyes and Pincheira 1999; Cho and Pincheira 2006; Tariverdilo et al. 2009). Cho and Pincheira (2006) proposed an analytical modeling approach using nonlinear rotational springs at the element end to model the degradation of stiffness and strength with increasing deformation amplitude. Even though the model is numerically efficient by taking advantage of a concentrated plasticity modeling approach, it requires the user to obtain the parameters to define the nonlinear rotational springs from other sources, e.g., through experimental tests. Tariverdilo et al. (2009) presented a model that can capture the degrading response due to bar slip in the lap splice based on the configuration and yield stress of the longitudinal reinforcement and the spacing and amount of transverse reinforcement. The model showed a good correlation with results from experimental tests. However, since the degrading mechanism in Tariverdilo et al.'s (2009) model due to bar slip is manifested through the softening stress-strain relation at the material level in the force-based beam-column element, loss of objectivity due to strain localization has become critical in the numerical modeling and analysis. Previous studies (e.g., Tariverdilo et al. 2009) suggested using two Gauss-Lobatto integration points within the lap-spliced element to model short lap splices' response regardless of the length of the splice. The selection of two integration points is ambiguous from a numerical standpoint because the integration length of the lap-splice region could change as the length of the element changes, for example, between a test specimen and a full-scale structural column. The assumption of using two integration points can thus impact the numerical model's accuracy in predicting the response of a real structural column subject to lap-splice failure.

The loss of objectivity has also been shown in other studies, where the number of integration points used in the force-based element dictates the response of the model at the location of softening constitutive behavior (Coleman and Spacone 2001; Addessi and Ciampi 2007; Scott and Hamutçuoğlu 2008). The variation in results with different numbers of integration points further leads to accuracy and convergence issues in the analysis. This subtopic presents a methodology to address strain localization for columns with short lap splices through regularization based on a constant post-peak energy criterion. Previous studies have used the concept of constant fracture energy to address mesh sensitivity issues in displacement-based continuum finite-element analyses due to the softening response for concrete in tension (Bažant and Oh 1983; Bazant and Planas 1997). The concept of a constant energy criterion has been extended to the softening response in compression (Jansen and Shah 1997; Lee and William 1997). Several studies have investigated strain localization specifically for force-based frame elements (Coleman and Spacone 2001; Addessi and Ciampi 2007; Scott and Hamutçuoğlu 2008). In particular, Coleman and Spacone (2001) showed that for modeling a reinforced column with a single force-based element, the force-displacement response loses objectivity and varies based on the number of integration points used. In the presence of the strain-softening behavior of crushing concrete, strain rapidly increases in the extreme fiber as the response proceeds in the post-peak region. Despite these studies investigating strain localization due to the nonlinear concrete response in compression, no study delves into the localized phenomenon in reinforced concrete columns with short lap splices due to the bond-slip mechanism. This study alleviates strain localization effects by regularizing the lap-splice material response. The numerical model utilizing the proposed approach shows objective

and accurate results compared with experimental values and consistent results that converge across varying numbers of integration points.

5.3.3 Formulation of force-based element

The structural engineering community has widely used force-based elements described by Spacone et al. (1996a, b) for nonlinear finite element analysis. Figure 101 shows the force and element deformation in the basic frame and global frame (Filippou and Fenves 2004), where **q, v** and $\bar{\mathbf{q}}$**,** $\bar{\mathbf{v}}$ represent force and element deformation in the natural frame and global frame, respectively.

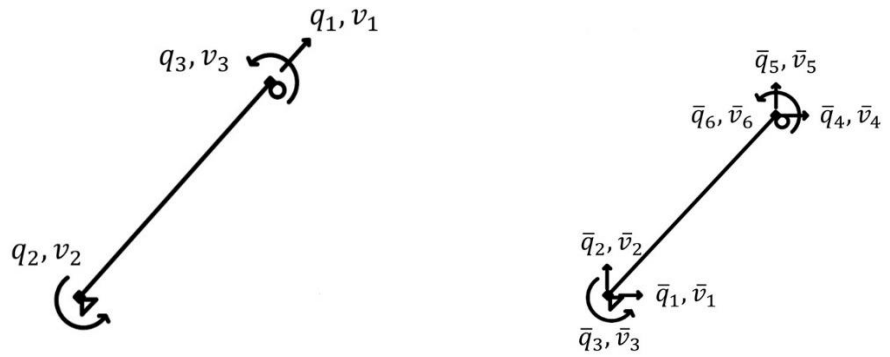

Figure 101. Degrees of freedom in (a) basic frame and (b) global frame

Compared with displacement-based elements with interpolation of the displacement field, force-based elements utilize the interpolation functions $\mathbf{b}(x)$ of basic forces **q** within the basic system. The product of interpolation functions and basic forces results in sectional forces sðxÞ consisting of axial force and moment located at distance x from one end of an element node. Under Euler-Bernoulli beam theory, sectional deformation **e** consists of only axial strain and curvature for the sectional response.

Equation (81a) shows the relation between basic and sectional forces in the absence of element loading.

$$\mathbf{s}(x) = \mathbf{b}(x)\mathbf{q} \tag{81a}$$

Equation (81a) can also be expressed explicitly as in Equation (81b)

$$\begin{bmatrix} N(x) \\ M(x) \end{bmatrix} = \begin{bmatrix} 1 & 0 & 0 \\ 0 & \frac{x}{L} - 1 & \frac{x}{L} \end{bmatrix} \begin{bmatrix} q_1 \\ q_2 \\ q_3 \end{bmatrix} \tag{81b}$$

where q_1, q_2 and q_3 represent axial force and end moments of the line element, L is the length of the element, and $N(x)$ and $M(x)$ are sectional forces at distance x from one end of the element node. According to the principle of virtual force, virtual sectional forces $\delta\mathbf{s}$ and sectional deformation $\mathbf{e}$ can be related to virtual element basic forces $\delta\mathbf{q}$ and element deformation $\boldsymbol{v}$ as shown in Equation (82).

$$\delta\mathbf{q}^T\mathbf{v} = \int_0^L \delta\mathbf{s}(x)^T\mathbf{e}(x)dx \tag{82}$$

By considering Equation (81a) in the virtual force system and Equation (82), Equation (83) establishes the relation between element deformation $\mathbf{v}$ and sectional deformation $\mathbf{e}$.

$$\mathbf{v} = \int_0^L \mathbf{b}(x)^T\mathbf{e}(x)dx \tag{83}$$

Element flexibility matrix $\mathbf{f_e}$ is obtained by taking the derivative of Equation (83) with respect to basic forces $\mathbf{q}$ as shown in Equation (84a) and Equation (84b).

$$\mathbf{f_e} = \frac{\partial}{\partial\mathbf{q}}\int_0^L \mathbf{b}(x)^T\mathbf{e}(x)dx \tag{84a}$$

$$\mathbf{f_e} = \int_0^L \mathbf{b}(x)^T\frac{\partial\mathbf{e}(x)}{\partial\mathbf{s}}\frac{\partial\mathbf{s}}{\partial\mathbf{q}}dx \tag{84b}$$

Element flexibility matrix $\mathbf{f_e}$ is derived in terms of sectional flexibility matrix $\mathbf{f_s}$ and interpolation function $\mathbf{b}(x)$ as shown in Equation (85).

$$\mathbf{f_e} = \int_0^L \mathbf{b}(x)^T \, \mathbf{f_s} \, \mathbf{b}(x) dx \tag{85}$$

Finally, the element stiffness matrix $\mathbf{k_e}$ is obtained by inversion of the element flexibility matrix. The force formulation enables equilibrium between sectional forces and element forces, while compatibility between sectional deformation and element deformation is satisfied in an integral sense.

Equation (83) and Equation (85) are evaluated through numerical integration according to Equation (86) and Equation (87), respectively. The authors adopt the Gauss-Lobatto integration scheme, which evaluates the structural element's endpoints where the maximum moment occurs in the absence of element loading.

$$\mathbf{v} \cong \sum_{IP=1}^{N} \mathbf{b}(x_{IP})^T \, \mathbf{e}(x_{IP}) \, L \, w_{IP} \tag{86}$$

$$\mathbf{f_e} \cong \sum_{\boldsymbol{IP=1}}^{\boldsymbol{N}} \mathbf{b}(x_{IP})^T \, \mathbf{f_s} \, \mathbf{b}(x_{IP}) \, L \, w_{IP} \tag{87}$$

In Equation (86) and Equation (87), w_{IP} and x_{IP} are the weight and position, respectively, for a particular integration point IP. Note that the domain for the integration weight w_{IP} is between 0 and 1; the domain for the position x_{IP} is between 0 and element length L. The product of L and w_{IP} is defined as L_{IP}, the length associated with an integration point. N is the total number of integration points along the element. The element response is dependent on L_{IP}, and the loss of objectivity that this study addresses arises when the number of integration points changes along each element in the presence of softening material response and when the length L_{IP} changes. This study proposes to regularize the lap-splice material response through a constant energy criterion. Specifically, the lap-spliced section's material model is modified based on a constant post-peak energy value obtained from

experimental tests and tied to the element response through Equation (86) and Equation (87) to regularize the element response.

5.3.4 *Regularization of the material constitutive model*

The following two sections detail the regularization of the material response for concrete in compression and the softening response of lap splice in tension. In a force-based beam-column model with fiber sections, regularization of the uniaxial material response deliberately increases the energy per length in the 1-D constitutive relation as the number of integration points increases along the element to achieve constant energy release. During the regularization process in this study, the regularized strain is modified to a larger value as the number of integration points increases in the lapped region. This artificial increase of strain produces additional energy per length enclosed by the modified stress-strain curve at the material level. However, the total energy release remains constant due to the reduction of the integration length. The regularization is implemented by adjusting the degrading slope after the peak stress. The increase of slope (i.e., having a less negative degrading slope) creates additional sectional stiffness $\widetilde{\mathbf{k}_s}$ as shown in Equation (88). As a result, the total sectional stiffness $\widehat{\mathbf{k}_s}$ increases, leading to a reduction of the sectional deformation $\mathbf{e}$ and sectional flexibility $\mathbf{f_s}$. Finally, the stabilization of the element response is achieved through stabilizing the element deformation $\mathbf{v}$ by adjusting the value of the sectional deformation $\mathbf{e}$ based on Equation (86).

$$\widehat{\mathbf{k}_s} = \int \mathbf{a_s}^T (\frac{\widehat{\partial\sigma}}{\partial\varepsilon}) \mathbf{a_s} dA = \int \mathbf{a_s}^T (\frac{\partial\sigma}{\partial\varepsilon}) \mathbf{a_s} dA + \int \mathbf{a_s}^T (\frac{\widetilde{\partial\sigma}}{\partial\varepsilon}) \mathbf{a_s} dA \quad (88a)$$

$$\widehat{\mathbf{k}_s} = \mathbf{k}_s + \widetilde{\mathbf{k}_s} \quad (88b)$$

In Equation (88), $\frac{\partial\sigma}{\partial\varepsilon}$ is the original tangent material stiffness of the softening portion, $\frac{\widehat{\partial\sigma}}{\partial\varepsilon}$ is the regularized tangent material stiffness of the softening portion, and $\frac{\widetilde{\partial\sigma}}{\partial\varepsilon}$ is the additional contribution of the tangent material stiffness of the softening portion due to regularization. $\widehat{\mathbf{k}_s}$ is the regularized sectional stiffness, and $\widetilde{\mathbf{k}_s}$ is the additional contribution to the sectional stiffness due to regularization. $\mathbf{a_s}$ is the sectional kinematic matrix that describes the strain distribution in the local coordinates.

5.3.5 *Regularization of concrete in compression*

The concept of constant fracture energy of concrete in compression is defined in Equation (89) based on Coleman and Spacone (2001).

$$G_f^c = \int \sigma \, du \quad (89)$$

G_f^c is the fracture energy of concrete with superscript c representing compression. σ and u are stress and inelastic displacement, respectively. The approach is adapted to a framework of stress and strain by expressing the fracture energy as

$$G_f^c = h \int \sigma \, d\varepsilon \quad (90)$$

$$G_f^c = L_{IP} \int \sigma \, d\varepsilon \quad (91)$$

Where h is a length scale representing the size of a single element. For a force-based element, h becomes the length associated with an individual integration point at the presence of a softening response (L_{IP}). Figure 102 shows the stress-strain relation and fracture energy in compression. The regularization is applied to the Kent and Park (1971) concrete model, and fracture energy of concrete is defined from the peak compressive stress until the end of the softening branch shown in the shaded area in Figure 102. f_c' denotes the compressive strength of unconfined concrete, E_C is the elastic modulus, ε_O is the strain corresponding to peak stress, and ε_{20u} is the strain corresponding to 20% f_c'.

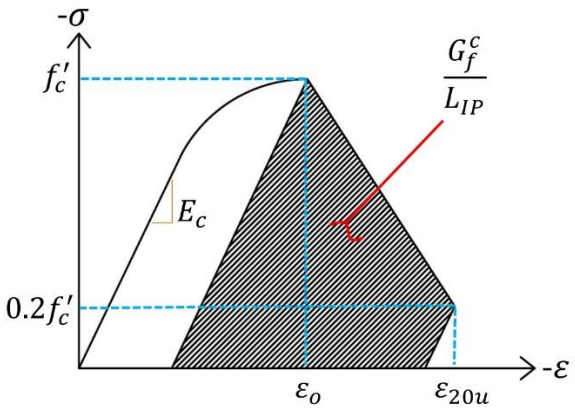

Figure 102. Regularized compressive concrete response

In order to implement the regularization process, the compressive fracture energy of concrete needs to be estimated. The authors refer to the few studies found in the literature to obtain this estimate. From Coleman and Spacone (2001), plain concrete's fracture energy obtained from cylinder tests gives values of 20~30 N/mm. Due to steel hoops' confining effect, the compressive fracture energy of well-confined concrete increases to about 180 N/mm, or six times that of unconfined concrete. Jansen and Shah (1997) recommend the use of a value of 25 N/mm for normal-weight concrete. Coleman and Spacone (2001) use

this same value for unconfined concrete and a value of $6G_f^c$ for a confined concrete material. Due to the lack of literature regarding the fracture energy for partially confined concrete, the current study assumes that concrete is either unconfined for the concrete cover with a fracture energy value of 25 N/mm or well-confined for the concrete core with a fracture energy value of 150 N/mm. Finally, modification of the concrete material is done by adjusting the strain ε_{20u} to ensure constant energy release, resulting in Equation (92).

$$\varepsilon_{20u} = \frac{G_f^c}{0.6f_c' L_{IP}} - \frac{0.8f_c'}{E_C} + \varepsilon_O \tag{92}$$

Note that the regularization of concrete in tension is neglected in this study as the concrete tensile response has minimal influence on the concrete section's softening behavior.

5.3.6 *Regularization of lap splice in tension*

To approach regularization of the material behavior in the lap splice region, it is essential to look at the constitutive material and failure mechanism of lap splices. This study combines findings from several previous studies to obtain the constitutive material model of the splice. The mechanism transferring the tensile stress in the splice relies on the concrete tensile stress capacity. The concrete acts as an intermediate material that transfers forces between two adjacent bars (Priestley et al., 1996). Splitting cracks along the bar in concrete can be formed due to the stress-transferring mechanism, which causes radially outward pressure on the concrete. The cracking of the concrete in tension causes initiation of softening due to the degrading behavior of the lap-spliced reinforcement (Wight and MacGregor, 2009). In addition to inadequate lap-splice length, widely spaced transverse

steel bars in the lap-splice region further reduces the ductility of the column response once cover concrete has spalled.

To assess the stress-strain relation for lap splices, this study uses the relation proposed in Priestley et al. (1996) to obtain the value of maximum force and stress developed in the lap-splice region, as shown in Equation (93) and Equation (94), respectively.

$$T_b = A_b f_s = F_t p L_s \tag{93}$$

$$f_s = \frac{F_t p L_s}{A_b} \tag{94}$$

T_b and f_s are force and stress developed in the lap-spliced bar, respectively; A_b is the cross-sectional area of longitudinal bar; F_t is the tensile strength of concrete; L_s is the length of lap splice; and p is the perimeter of the cylindrical block, determined through Equation (95) with an upper limit for widely spaced spliced bars.

$$p = \frac{s}{2} + 2(d_b + c) \leq 2\sqrt{2(c + d_b)} \tag{95}$$

s is the average distance between spliced bars, d_b is the diameter of the longitudinal steel bar, and c is the thickness of the concrete cover. Residual stress f_r is computed after the lap splice reaches its peak stress f_s as in Tariverdilo et al. (2009) and shown in Equation (96).

$$f_r = \frac{n_1 n_t \mu A_h f_s}{n A_b} \tag{96}$$

n_1 is the number of transverse reinforcement legs perpendicular to the crack plane; n_t is the number of transverse reinforcements in lap-splice length; μ is a frictional factor, which is taken as 1.4; A_h is the cross-sectional area of transverse reinforcement, and n is the number of spliced longitudinal bars developed by friction stress in the crack plane. Slip

corresponding to maximum stress is assumed to be 1 mm, and slip corresponding to reaching frictional stress is 10 mm, as in Tariverdio et al. (2009). As a result, residual strain ε_r is set to be 0.022, and peak strain ε_s can be obtained from Equation (97).

$$\varepsilon_s = \frac{f_s}{E_s} + \frac{\Delta_{BarSlip}}{l_{ss}} \tag{97}$$

E_s is the elastic modulus of steel bar, $\Delta_{BarSlip}$ at peak stress is taken as 1 mm, and l_{ss} is the length in which displacement due to slip occurs and is taken as section depth. The compression side of the reinforcement is assumed to follow perfectly plastic behavior. Based on Equation (93) to Equation (97), the stress-strain curve is illustrated in Figure 103.

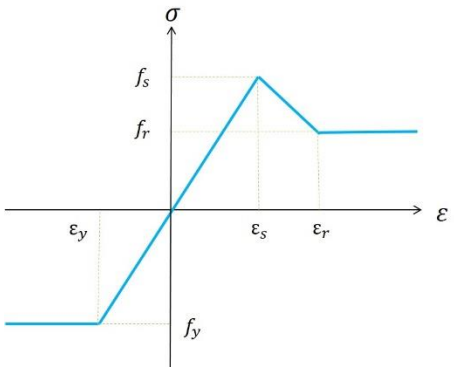

Figure 103. Constitutive material model of lap-spliced bar

This study considers six experimental specimens from Melek and Wallace (2004) and Aboutaha et al. (1996) to obtain the post-peak energy value. These column specimens consist of either square or rectangular cross-sections and lap-splice lengths of $20d_b$ or $24d_b$. Column geometries and material properties are listed in Table 36 and Table 37, respectively.

Table 36. Experimental column specimen geometries and axial load ratios

Specimens	Column Dimension			Shear Span Ratio	Axial Load Ratio
	Width (mm)	Depth (mm)	Height (mm)		
FC4	914	457	2743	3.00	0
FC14	686	457	2743	4.00	0
FC15	457	457	2743	6.00	0
S10MI	457	457	1829	4.00	0.10
S20MI	457	457	1829	4.00	0.20
S30MI	457	457	1829	4.00	0.30

.

Table 37. Experimental column specimen material properties

Specimens	Longitudinal reinforcement			Transverse reinforcement		Concrete
	No.	Lap-splice length (d_b)	Yield strength (MPa)	Spacing (mm)	Yield strength (MPa)	Compressive strength (MPa)
FC4	16#8	24	434	#3@406	400	19.7
FC14	12#8	24	434	#3@406	400	28.8
FC15	8#8	24	434	#3@406	400	28.8
S10MI	8#8	20	510	#3@305	476	36.3
S20MI	8#8	20	510	#3@305	476	36.3
S30MI	8#8	20	510	#3@305	476	36.3

Figure 104 shows the formulation for regularizing the tensile lap-splice response. From Figure 104, the constant post-peak energy of the lap-splice region in tension is computed based on the total shaded area as shown in Equation (98).

$$G_{LS}^{T} = L_{IP} \int_{\varepsilon_s}^{\varepsilon_{ult}} \sigma \, d\varepsilon \tag{98}$$

The superscript T indicates tension, and subscript LS indicates lap splice. G_{LS}^{T} consists of two portions, as indicated in Figure 104. The two portions are calculated according to Equation (99) and Equation (100).

$$G_{LS1}^{T} = \frac{1}{2}(\varepsilon_r - \varepsilon_s)(f_s + f_r)L_{IP} \tag{99}$$

$$G_{LS2}^{T} = (\varepsilon_{ult} - \varepsilon_r)\, f_r\, L_{IP} \tag{100}$$

ε_{ult} is the ultimate strain of the lap-splice section with the value taken to be 0.08. The other parameters needed to calculate the post-peak energy are computed based on the material stress-strain relations in Tariverdilo et al. (2009).

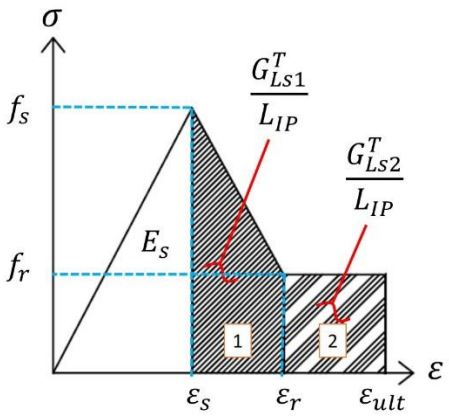

Figure 104. Regularized tensile lap-splice response

The resulting parameter values are shown in Table 38. In Tariverdilo et al. (2009), two Gauss-Labatto integration points at the lap section are taken to result in sufficient accuracy compared with experimental results. Therefore, the integration length L_{IP} is set equal to half of the lap-splice length. The resulting post-peak energies G_{LS1}^{T} and G_{LS2}^{T} calculated for each specimen based on the proposed Equation (99) and Equation (100) are shown in Table 38. The mean values for G_{LS1}^{T} and G_{LS2}^{T} are calculated over the six lap-splice column specimens as 1258 N/mm and 1886 N/mm, respectively. These values are used to obtain

the regularized residual strain ($\widetilde{\varepsilon_r}$) and regularized ultimate strain ($\widetilde{\varepsilon_{ult}}$) as shown in Equation (101) and Equation (102).

$$\widetilde{\varepsilon_r} = \frac{\overline{G_{LS1}^T}}{L_{IP}} \frac{2}{f_s + f_r} + \varepsilon_s \tag{101}$$

$$\widetilde{\varepsilon_{ult}} = \frac{\overline{G_{LS2}^T}}{L_{IP}\, f_r} + \widetilde{\varepsilon_r} \tag{102}$$

$\overline{G_{LS1}^T}$ and $\overline{G_{LS2}^T}$ are average values of post-peak energy for short lap splices. For Equation (101) and Equation (102), the regularized residual strain is determined first based on the average value of G_{LS1}^T. The regularized ultimate strain is then obtained by adding the strain contribution based on the average value of G_{LS2}^T. Figure 105 shows regularized stress-strain curves of lap splice in tension considering varying numbers of integration points with constant post-peak energy. $\widetilde{\varepsilon_{r\_2IP}}$, $\widetilde{\varepsilon_{r\_3IP}}$, and $\widetilde{\varepsilon_{r\_4IP}}$ represent regularized residual strains with two, three, and four integration points (IPs) along the element, respectively. Likewise, $\widetilde{\varepsilon_{ult\_2IP}}$, $\widetilde{\varepsilon_{ult\_3IP}}$, and $\widetilde{\varepsilon_{ult\_4IP}}$ represent regularized ultimate strains with two, three, and four integration points along the element, respectively.

Table 38. Material parameters and resulting post-peak energy

Specimens	f_s/f_y	f_r/f_y	ε_s	ε_r	G_{LS1}^T **(N/mm)**	G_{LS2}^T **(N/mm)**
FC4	0.79	0.25	0.0039	0.022	1246	1920
FC14	0.95	0.26	0.0043	0.022	1418	1997
FC15	0.95	0.20	0.0042	0.022	1348	1536
S10MI	0.78	0.26	0.0042	0.022	1195	1954
S20MI	0.78	0.26	0.0042	0.022	1195	1954
S30MI	0.78	0.26	0.0042	0.022	1195	1954
Mean post-peak energy (N/mm)					1258	1886

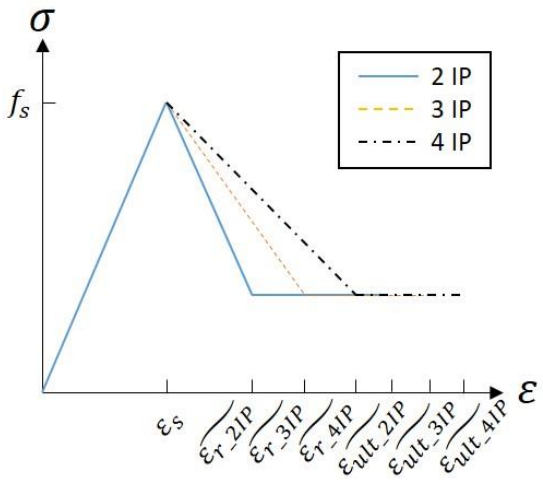

Figure 105. Regularized constitutive relation of lap-splice response with varying numbers of integration points

5.3.7 *Modeling details*

To evaluate the proposed regularization approach to model the lap-splice material response, the authors build a numerical column model simulating lap-splice failure. The finite element model of the reinforced concrete column with lap splice at the base consists of two force-based beam-column elements with fiber discretization connected in series. The deformation of the lapped region due to bar slip and column flexural behavior is captured by the bottom element with a length set equal to the actual length of splice; the top element captures the flexural behavior of the remaining portion of the column. The model is implemented in the finite element platform OPENSEES version 3.2.0 (Mckenna, 1997).

The uniaxial stress-strain relation of the longitudinal reinforcement in the lap-splice region adopts the stress-strain curve shown in Figure 103. It is implemented using the

material model *Hysteretic* in OPENSEES, capable of modeling the trilinear stress-strain relation depicted in Figure 103. The ultimate tensile strain of lap splices is implemented through the material model *MinMax* in OPENSEES. The longitudinal reinforcement in the top element uses a steel element with the material model Steel01 in OPENSEES, consisting of bilinear behavior with kinematic hardening. Yield strength and ultimate strength are based on the material properties of each specimen. The model from Yassin (1994) is adopted for the concrete material, which is implemented as *Concrete02* in OPENSEES. From Yassin (1994), the model from Hognestad (1951) is used for pre-peak behavior. The stress-strain curve between the concrete compressive strength and crushing strength is assumed to be linear, with the crushing strength assumed to be 20% of maximum compressive strength. The initial slope for the concrete model is $2f_c'/\varepsilon_o$, where f_c' and ε_o are concrete compressive strength and concrete strain at maximum strength, respectively. The unloading path from the compression envelope and tension envelope is bilinear and linear, respectively. The reloading path is assumed to be linear. Compressive strength is defined according to the material properties of each specimen, and the concrete modulus is computed based on American Concrete Institute (ACI, 2011). For the confined concrete model, the same uniaxial material model, *Concrete02,* is adopted. However, the maximum confined concrete stress and its corresponding strain are computed based on Mander et al. (1988). Figure 106 shows the 1-D constitutive models used for the steel and concrete materials.

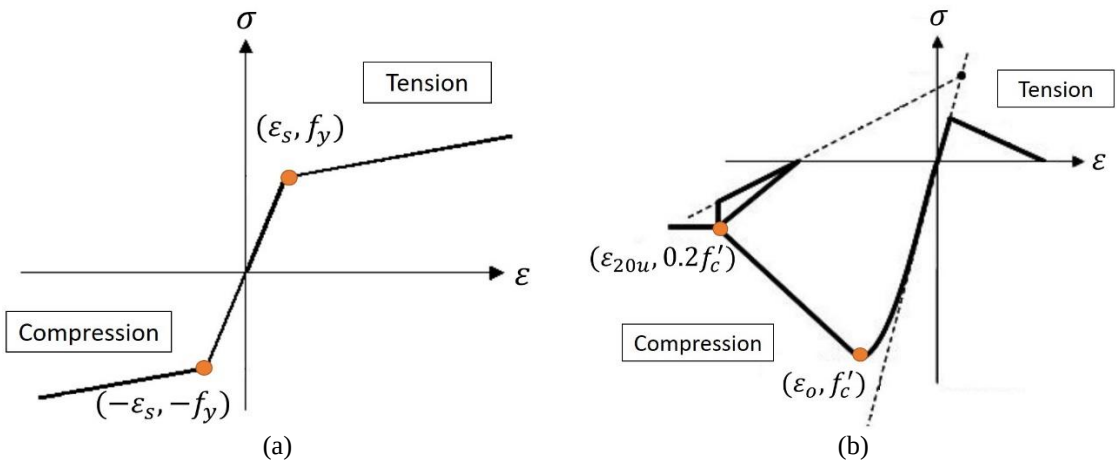

Figure 106. 1-D constitutive models used for (a) steel material and (b) concrete material

The proposed regularization process for the material response is implemented for the described numerical model. As shown in Figure 107, the column model's top element has three Gauss-Lobatto integration points; the bottom element has two integration points. Ls_{IP} indicates the integration length of the lapped region, and L_{upper} is the length of the upper element, excluding the lapped region. The number of integration points in the bottom element is varied in the next section to investigate the objectivity of the results with and without using the regularized concrete and lap-splice material models.

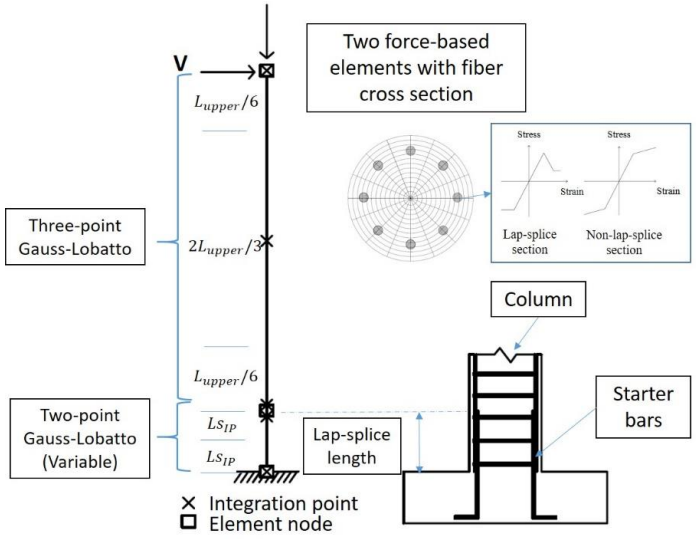

Figure 107. Modeling details of the numerical model

It is noted that theoretically, the proposed regularized strains should apply to each integration point. However, as the plastic hinge region is typically at the end of the element, the regularization is applied only to the extreme integration point in this study. Implementing the regularization at the other integration points does not significantly affect the results.

5.3.8 Evaluation of results with proposed regularization

In this section, the authors present results for five column specimens with short lap splices. Summary results in terms of estimating the displacement at 20% strength drop for the five specimens using a regularized compared to the nonregularized model and compared to experimental tests are presented to demonstrate the generalizability and utility of the proposed approach. Detailed results are then described for two out of the five specimens, with the figures for the remaining specimens provided in the Appendix for concision. In the analyses, the goal is to evaluate the objectivity of the proposed regularization approach across integration points and verify the regularized model's accuracy compared with experimental tests. Results for the pushover, static cyclic, and dynamic analyses are presented.

5.3.9 *Descriptions of test specimens*

Five test specimens are selected for evaluation of the proposed regularization approach, and these specimens are chosen due to the availability of experimental test data

for comparison. Table 39 and Table 40 show the geometries, axial load ratios, and each specimen's material properties. The test specimens consist of rectangular, square, and circular cross sections. Specimen 1 and Specimen 2 are from Sun et al. (1993) and Chail et al. (1991), respectively. Specimen 3 and Specimen 4 are from Jaradat et al. (1998), with Specimen 3 corresponding to specimen "T1" and Specimen 4 corresponding to "T2" in the study. Specimen 5 is from Melek and Wallace (2004), corresponding to specimen "2S20H." The specimens have a lap-splice length of 20 times the longitudinal bar diameter. Transverse reinforcement of the specimens is widely spaced with an average ratio of 0.2%. The shear span ratios of greater than 3.5 for all specimens ensure sufficient shear strength at the column's base such that lap-splice failures will result.

Table 39. Experimental column specimen geometries and axial load ratios

Specimens	Column Dimension			Shear Span Ratio	Axial Load Ratio
	Width (mm)	Depth (mm)	Height (mm)		
1 (Sun et al., 1993)	1830	1220	9140	4.99	0.15
2 (Chail et al., 1991)	610*	-	3660	6.00	0.18
3 (Jaradat et al., 1998, T1)	250*	-	1780	3.56	0.05
4 (Jaradat et al., 1998, T2)	250*	-	1780	3.56	0.05
5 (Melek and Wallace, 2004, 2S20H)	457	457	1676	3.67	0.20

* Circular cross section

Table 40. Experimental column specimen material properties

Specimens	Longitudinal reinforcement			Transverse reinforcement		Concrete Compressive strength (MPa)
	No.	Lap-splice length (d_b)	Yield strength (MPa)	Spacing (mm)	Yield strength (MPa)	
1	32#6	20	317	#2 @ 127	276	33.0
2	26#6	20	315	#2 @ 127	350	34.0
3	8#4	20	360	9 gage @ 98*	210	29.0
4	8#3	20	350	9 gage @ 98*	210	29.0
5	8#8	20	510	#3 @ 305	476	36.3

* 9-gage steel with a diameter of 3.8 mm

5.3.10 *Summary of results for test specimens*

Figure 108 summarizes the accuracy of the regularized model compared to the nonregularized model in terms of normalized displacement at 20% strength drop for different numbers of integration points used in the analysis. Figure 108(a) shows the results for all five test specimens. The normalization is computed as the ratio between the numerical and experimental results to assess the model's accuracy compared to experimental tests. Figure 108(b) provides the mean values over the five specimens. The results show that the nonregularized model's accuracy heavily depends on the number of integration points, with low accuracy when the number of integration points exceeds two. The nonregularized models show less than 50% accuracy once three or more integration points are used in the lapped region. This decrease in accuracy is typical when existing approaches are used. In comparison, the accuracy from using the regularized models remains constant regardless of the number of integration points. The mean accuracy of the response using the regularized model is 94% compared to the experimental tests.

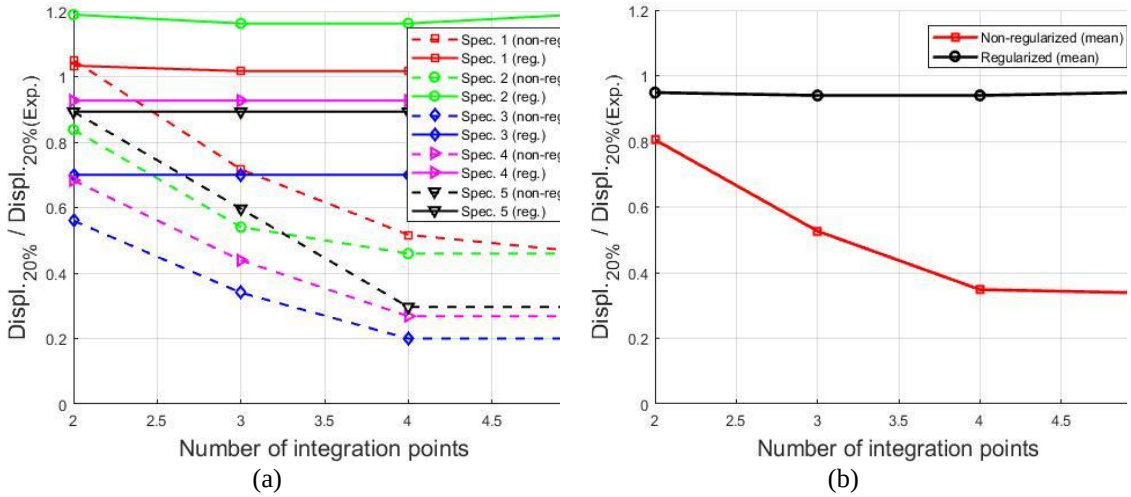

Figure 108. Normalized displacement at 20% strength drop versus the number of integration points between regularized and nonregularized models for (a) all five test specimens and (b) mean values

The following sections provide detailed results for two specimens, Specimen 1 and Specimen 2, from Table 39. Figures for the other specimens are provided in the Appendix. Specimen 1 is from Sun et al. (1993), designed based on a prototype rectangular column with dimensions of 1.83 m, 1.22 m, and 9.14 m for section depth, section width, and column height, respectively. The actual test specimen uses a scale factor of 40% of the prototype, which results in a 730 mm by 489 mm cross section and 3.66 m column height. The column consists of 32 M22 (#6) longitudinal bars and 6.4 mm (#2) transverse reinforcement with spacing at 127 mm. The cover concrete is 19 mm, and an axial load of 1780 kN is applied to the column at the top resulting in an axial load ratio of 15%. The concrete compressive strength is 33 MPa; the longitudinal steel's yield strength and ultimate strength are 317 MPa and 476 MPa. Lap splices at the base have a length of 381 mm, which is around 20 times the longitudinal bar diameter.

Specimen 2 is from Chail et al. (1991). The test specimen has a circular cross section with a diameter of 610 mm and a height of 3.66 m. The longitudinal reinforcement consists of 26 #6 steel bars, and the transverse reinforcement consists of #2 bars at 127 mm

spacing. The cover concrete is 20 mm, and an axial load of 2758 kN is applied to the column at the top resulting in an axial load ratio of 17.7%. The concrete compressive strength is 34 MPa; the longitudinal steel's yield strength and ultimate strength are 315 MPa and 498 MPa. Lap splices at the base have a length of 381 mm, which is around 20 times the longitudinal bar diameter.

5.3.11 Static pushover analysis (nonregularized vs. regularized model)

To assess the specimens' nonlinear behavior, pushover analyses with a displacement control strategy are performed in OPENSEES. The parameters considered for comparison include the number of Gauss integration points in the lap-splice region both with and without implementing the proposed regularized lap-splice material model. Pushover results for Specimen 1 and Specimen 2 are shown in Figures 110(a) and 110(b), and 110(c) and 110(d), respectively, with an applied maximum drift ratio of 2% in both cases.

Figures 110(a) and 110(c) show the pushover curves without implementing the proposed regularized material model. The analyses in the lap-splice region exhibit different levels of premature degrading behavior depending on the number of integration points (IPs) due to strain localization beginning at 0.8% and 0.6% drift ratio for Specimen 1 and Specimen 2, respectively. The analysis results thus highly depend on the number of integration points used by the analyst. However, if regularization is applied to both the concrete and lap-splice constitutive material models, convergent and objective structural responses are observed. Table 41 shows the drift ratios at a 20% drop of lateral strength between the two specimens' regularized and nonregularized models.

Table 41. Pushover values for test specimens using nonregularized vs. regularized models

Number of integration points	Drift ratio at 20% strength drop (%)			
	Specimen 1		Specimen 2	
	Nonregularized model	Regularized model	Nonregularized model	Regularized model
2	1.22	1.65	0.85	1.25
3	0.85	1.60	-	1.21
4	0.80	1.59	0.59	1.20
5	0.80	1.59	0.59	1.20
Mean	0.92	1.61	0.68	1.22
Standard deviation	0.18	0.02	0.12	0.02

Note: hyphen indicates analysis fails to converge

Table 41 quantifies the difference between the results obtained from using the nonregularized compared to regularized models in terms of drift ratio at 20% strength drop as the number of integration points varies. The nonregularized results show a considerable variation in drift ratio depending on the number of integration points used. In contrast, results indicate that the regularized model is able to eliminate the issue of premature degrading due to strain localization, reducing the standard deviation of drift ratio at 20% strength drop from 0.18% and 0.12% to 0.02% and 0.02% for the two specimens, respectively. The decrease in the standard deviation of the response combined with the results shown in Figure 109(b) and Figure 109(d) indicates that the regularization alleviates the convergence issue. The pushover curves become objective with results independent of the number of integration points used.

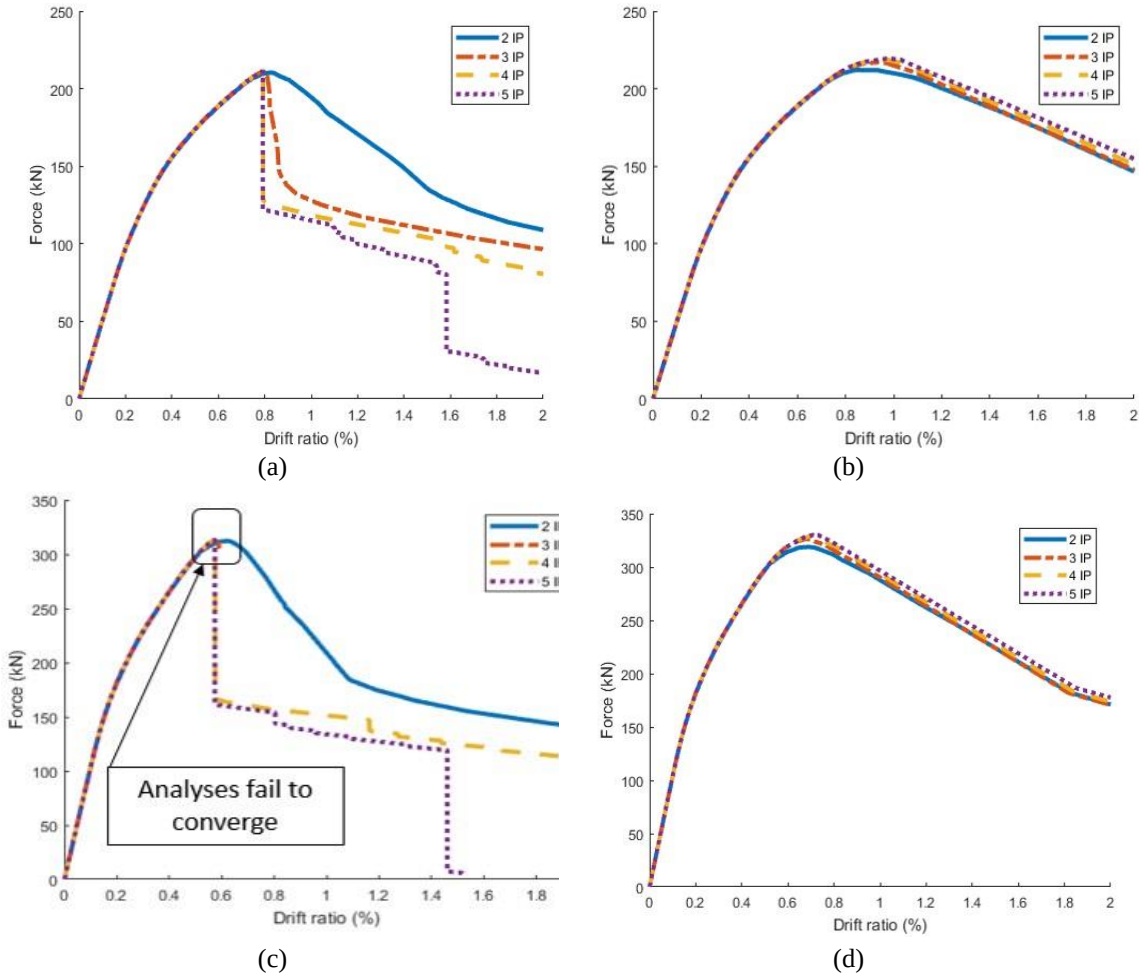

Figure 109. Static pushover curves of (a) & (c) non-regularized responses and (b) & (d) regularized responses for varying numbers of integration points in the lap-splice region

5.3.12 Static cyclic analysis (nonregularized vs. regularized model)

Cyclic loadings are also applied to assess the performance of the regularized compared to nonregularized models in this section. A lateral displacement cycle of prescribed magnitude is imposed at the top of the column node using the displacement control integrator in OPENSEES. The numerical models are subjected to the same displacement pattern of increasing magnitude in accordance with the experimental tests.

The study uses an adaptive strategy, which tries multiple solution algorithms, including Newton-Raphson, modified Newton-Raphson, Newton with linear search, and so on before it fails to converge. The resulting static cyclic curves are shown in Figure 110 for both specimens with and without considering regularization. The results from Specimen 1 and Specimen 2 are shown in Figures 111(a) and 111(b), and 111(c) and 111(d), respectively.

Figures 111(a) and 111(c) show the static cyclic curves for the two specimens when different numbers of integration points are used without regularization. Both cases show that the results vary based on the number of integration points in the model. The analyses using more integration points degrade faster, and the issue of convergence persists due to the decrease of integration weight as the number of integration points along the bottom of the element increases. The difference in integration weight leads to variations in the element deformation $\boldsymbol{v}$ during element-state determination. Without regularization, the results become non-objective as they depend on the number of integration points used by the analyst. In comparison, Figures 111(b) and 111(d) show that the static cyclic curves from using the regularized model for both specimens are free from the strain localization and convergence issues. The results are consistent across varying numbers of integration points and converge in all cases.

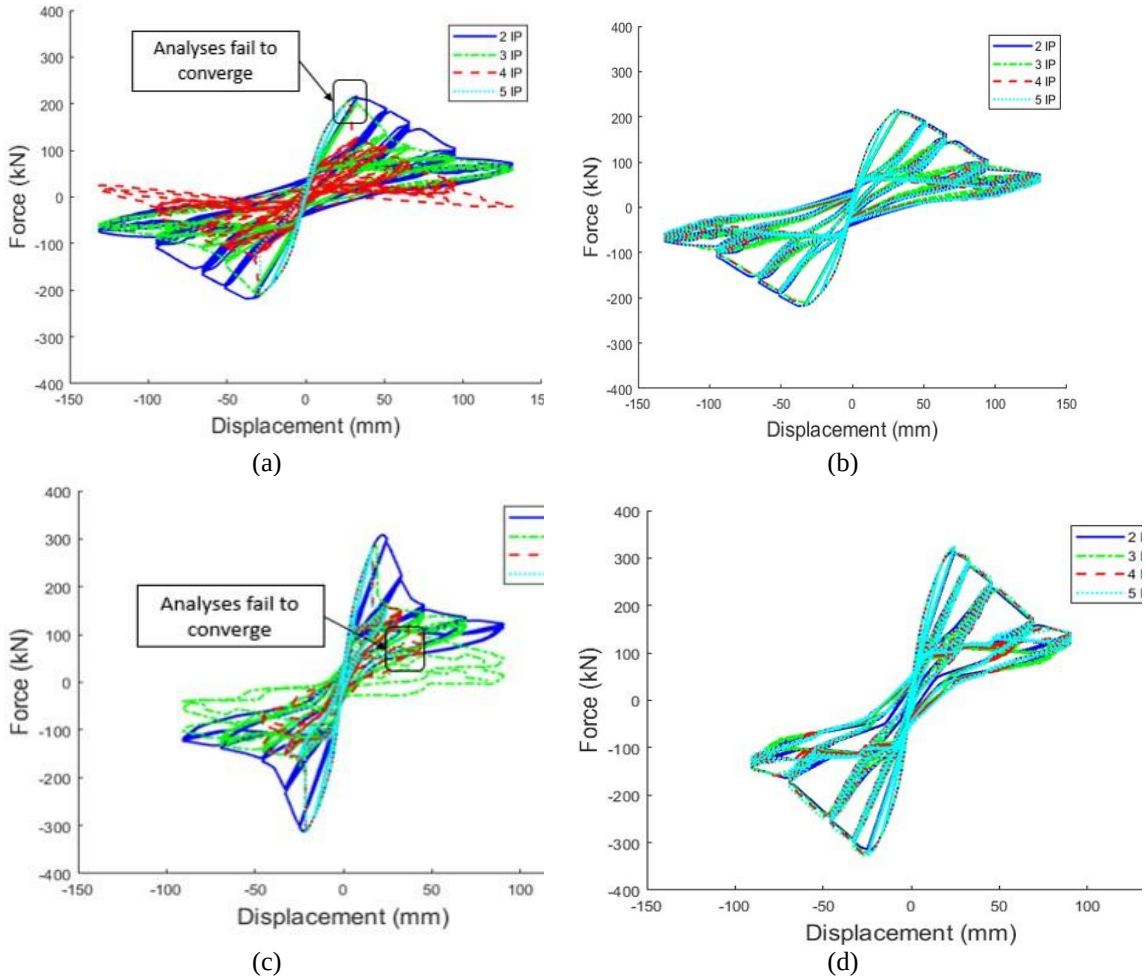

Figure 110. Static cyclic curves of (a) & (c) non-regularized responses and (b) & (d) regularized responses

Tables 42 and 43 quantify the differences between the regularized and nonregularized models across different integration points for Specimen 1 and Specimen 2, respectively. Results for the peak strength and displacement at 20% strength drop are shown. For both response parameters and both specimens, the nonregularized model leads to more significant variation as a function of the number of integration points. The variability is significantly reduced by using the regularized model. The standard deviations of displacements at 20% strength drop are reduced from 13.75 mm to 0.43 mm, and 5.76 mm to 0.50 mm. The reduction in variation of the response further demonstrates the

numerical consistency between the results from using different numbers of integration points for the regularized model.

Table 42. Static cyclic values for Specimen 1

Number of integration points	Nonregularized model		Regularized model	
	Peak strength (kN)	Displacement at 20% strength drop (mm)	Peak strength (kN)	Displacement at 20% strength drop (mm)
2	216	63	216	62
3	208	43	210	61
4	203	31	215	61
5	195	28	216	61
Mean	206	41	214	61
Standard deviation	7.63	13.75	2.49	0.43

Table 43. Static cyclic values for Specimen 2

Number of integration points	Nonregularized model		Regularized model	
	Peak strength (kN)	Displacement at 20% strength drop (mm)	Peak strength (kN)	Displacement at 20% strength drop (mm)
2	308	31	315	44
3	286	20	322	43
4	280	17	324	43
5	280	17	325	44
Mean	289	21	322	44
Standard deviation	11.52	5.76	3.91	0.50

5.3.13 Verification with experimental test results

The static pushover and cyclic analyses show that the model with regularization results in objective global force-displacement responses. In this section, the authors verify the accuracy of the proposed regularized model against experimental test results. Figures 112(a) and 112(b) show the comparison between the experimental tests' responses and the

regularized numerical model for Specimen 1 and Specimen 2, respectively. Both specimens have a bond-slip failure in the lap-splice region. From Figure 111, the regularized models are able to model the strength, softening slope, and degrading stiffness compared to experimental tests. Table 39 shows the percentage differences between the experimental tests and regularized model results in terms of peak force and displacement at a 20% strength drop. The percentage differences are below 10%, except for the displacement quantity for Specimen 2, with around 16% difference. This discrepancy could be caused by measurement error of the experimental test or modeling error in terms of accuracy of the fiber uniaxial behavior and damage parameters accounting for pinching behavior (Zhang et al., 2019a). In an overall sense, the regularized model can capture the force-displacement envelope of the lap-splice columns.

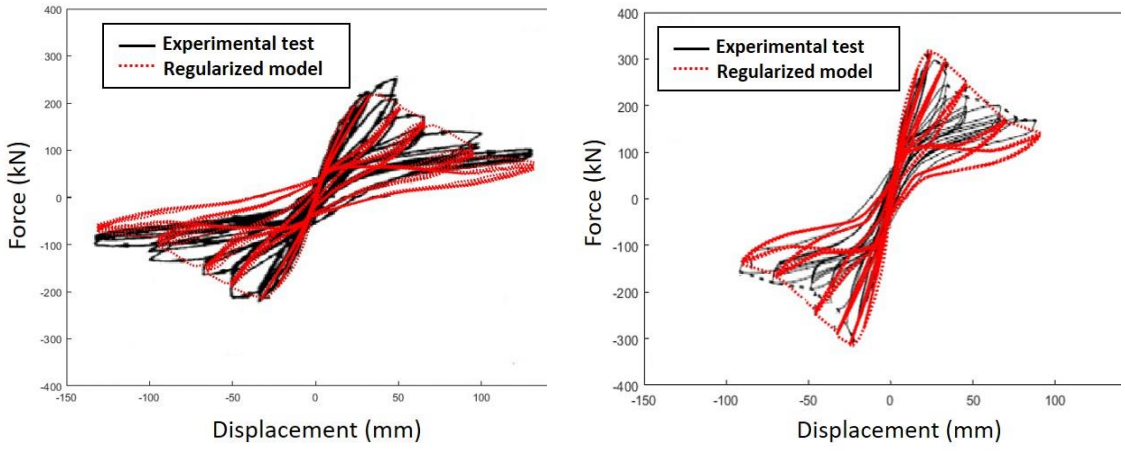

Figure 111. Experimental test results compared to regularized numerical model results for (a) Specimen 1 and (b) Specimen 2

Table 39 Comparison between experimental tests and regularized model results

Models and difference	Specimen 1		Specimen 2	
	Peak strength (kN)	Displacement at 20% strength drop (mm)	Peak strength (kN)	Displacement at 20% strength drop (mm)
Experimental test	218	60	300	37
Regularized model	214	61	322	43
Difference (%)	1.83%	1.67%	7.33%	16.22%

In addition to the summary of results for the five test specimens provided in Figure 108, the figures showing the detailed results from the static cyclic analyses comparing the regularized and nonregularized models as well as the verification between the experimental tests and regularized model results for the remaining three specimens are presented in the Appendix. The results for these three specimens are similar to those presented for Specimen 1 and 2 and serve to demonstrate the accuracy and objectivity of the results obtained from implementing the proposed methodology of regularization.

5.3.14 Dynamic analysis (nonregularized vs. regularized model)

This section evaluates the structural responses from the regularized compared to nonregularized models under dynamic loading. It investigates the convergence and objectivity of the displacement response with varying numbers of integration points in the lap-splice section. The first five ground motions from the SAC ground motion suite (Somerville, 1997) have been selected for this study (Note that SAC represents a joint venture of the following three organizations: Structural Engineers Association of California, Applied Technology Council, and California University for Research in

Earthquake Engineering) The response spectra of these ground motions are shown in Figure 112(a); as an example, the time history of the first ground motion (GM 1) is shown in Figure 112(b).

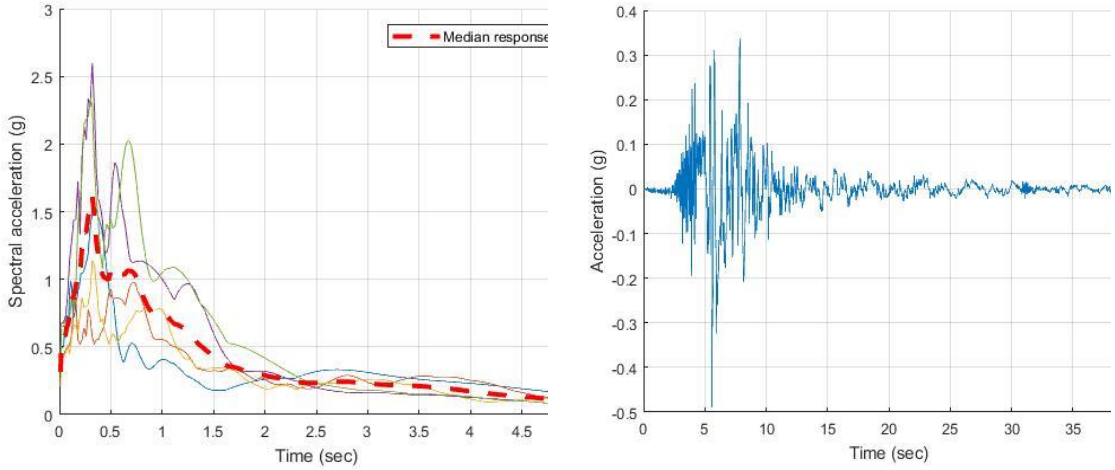

(a) (b)

Figure 112. (a) Response spectra of selected ground motions and (b) time history of GM 1

Figure 113 shows the physical system's details and the idealized system of the structural column with structural parameters based on those of Specimen 1. Ground excitations are applied at the base of the column.

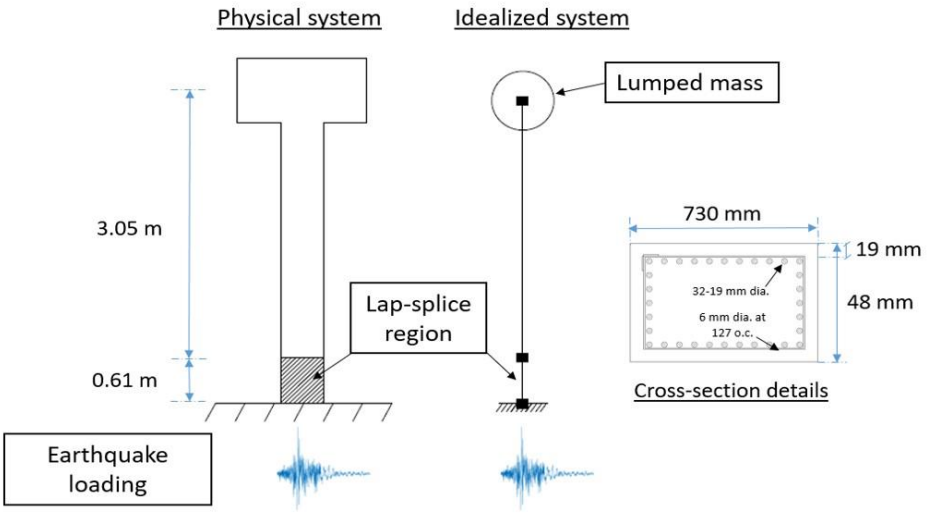

Figure 113. Details of dynamic simulation of the test specimen

The time history responses of the column tip displacement under GM 1 for the nonregularized and regularized models are shown in Figures 115(a) and 115(b), respectively. From Figure 114, except for the case with two integration points in the lap-splice region, the model without considering regularization fails to converge when more than two integration points are used, and analyses halt at around 6 seconds due to convergence issues. In comparison, the numerical model with the proposed regularization implemented has improved performance regarding convergence, and the displacement response histories are similar regardless of the number of integration points used.

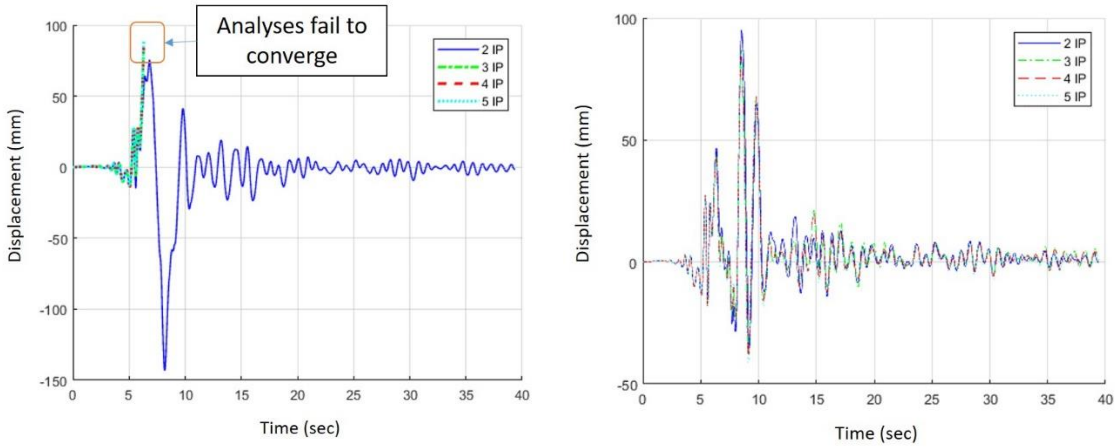

Figure 114. Time history of column displacement from (a) nonregularized model and (b) regularized model under GM 1

Table 40 and Table 41 show the maximum drift ratios of the nonregularized and regularized models with varying numbers of integration points in the lap-splice region under each of the five ground motions. In Table 40, it is clear that the model without considering regularization exhibits poor convergence performance when the number of integration points exceeds two in the lap-splice region. In comparison, Table 41 shows the issue of convergence is alleviated through the use of the regularized models. Although there are still cases when the analysis does not converge, most cases run successfully. Moreover, the resulting maximum drift ratios calculated from the analyses are consistent as the numbers of integration points change. The average coefficient of variation of maximum drift ratio under varying numbers of integration points for these five ground motions is 5.58%.

Table 40 Maximum drift ratios from non-regularized models

Non-regularized model	2 IP	3 IP	4 IP	5 IP	Mean
GM1	3.97%	-	-	-	3.97%
GM2	4.24%	-	-	-	4.24%
GM3	-	-	-	-	-
GM4	6.50%	-	-	-	6.50%
GM5	8.93%	-	-	-	8.93%

Note: hyphen indicates analysis fails to converge

Table 41 Maximum drift ratios from regularized models

Regularized model	2 IP	3 IP	4 IP	5 IP	Mean	Standard deviation
GM1	2.60%	2.37%	2.30%	2.24%	2.38%	0.16%
GM2	4.74%	-	4.28%	3.87%	4.30%	0.44%
GM3	-	4.95%	4.59%	4.91%	4.82%	0.20%
GM4	6.61%	6.64%	6.70%	-	6.65%	0.05%
GM5	7.86%	7.07%	6.97%	6.85%	7.19%	0.46%

5.3.15 Conclusions

This subtopic proposes a methodology to regularize force-based beam-column elements for reinforced concrete columns with short lap splices at the column base. The regularization process uses a constant energy criterion to impose an extra constraint in the material uniaxial behavior, stabilizing element end deformation and element stiffness and tying material response directly to element response. Regularizing the material behavior based on a constant energy release criterion provides additional sectional stiffness, reducing sectional deformation and section flexibility. The proposed post-peak energy of the lap-splice region is determined according to six experimental tests resulting in average values of 1258 N/mm and 1886 N/mm for $\overline{G_{LS1}^{T}}$ and $\overline{G_{LS2}^{T}}$, respectively. The regularized

residual strain is then computed based on $\overline{G_{LS1}^{T}}$ and the regularized ultimate strain determined based on the value of regularized residual strain and $\overline{G_{LS2}^{T}}$.

The authors apply the proposed regularized constitutive material model in numerical models to evaluate performance compared to nonregularized models. Results using the nonregularized model heavily depend on the number of integration points used by the analyst. In contrast, the regularized model is able to obtain objective force-displacement results across varying numbers of integration points used, with an order of magnitude decrease in the standard deviation of the response compared to the nonregularized model. In estimating the displacements at 20% strength drop, the nonregularized models show decreased accuracy compared with experimental results as the number of integration points changes, with less than 50% accuracy once three or more integration points are used in the lapped region. This decrease in accuracy is characteristic when existing nonregularized models are used. In comparison, the use of the proposed regularized model results in constant response estimates regardless of the number of integration points used with a mean accuracy of 94% for the five test specimens. The regularized model provides more accurate results against experimental data and more stable and reliable results for both static and dynamic analyses compared to a nonregularized model. As specimen lengths change, such as from lab-scale test specimens to the analysis of full-scale columns, the proposed regularization approach alleviates convergence issues and produces consistent results across integration points and length scales in numerical modeling and analysis.

5.3.16 Appendix: additional analysis results

Figure 115 shows the static cyclic analysis results for Specimens 3, 4, and 5, as described in Table 39. Comparison between the experimental tests and regularized model results for the three specimens is provided in Figure 116.

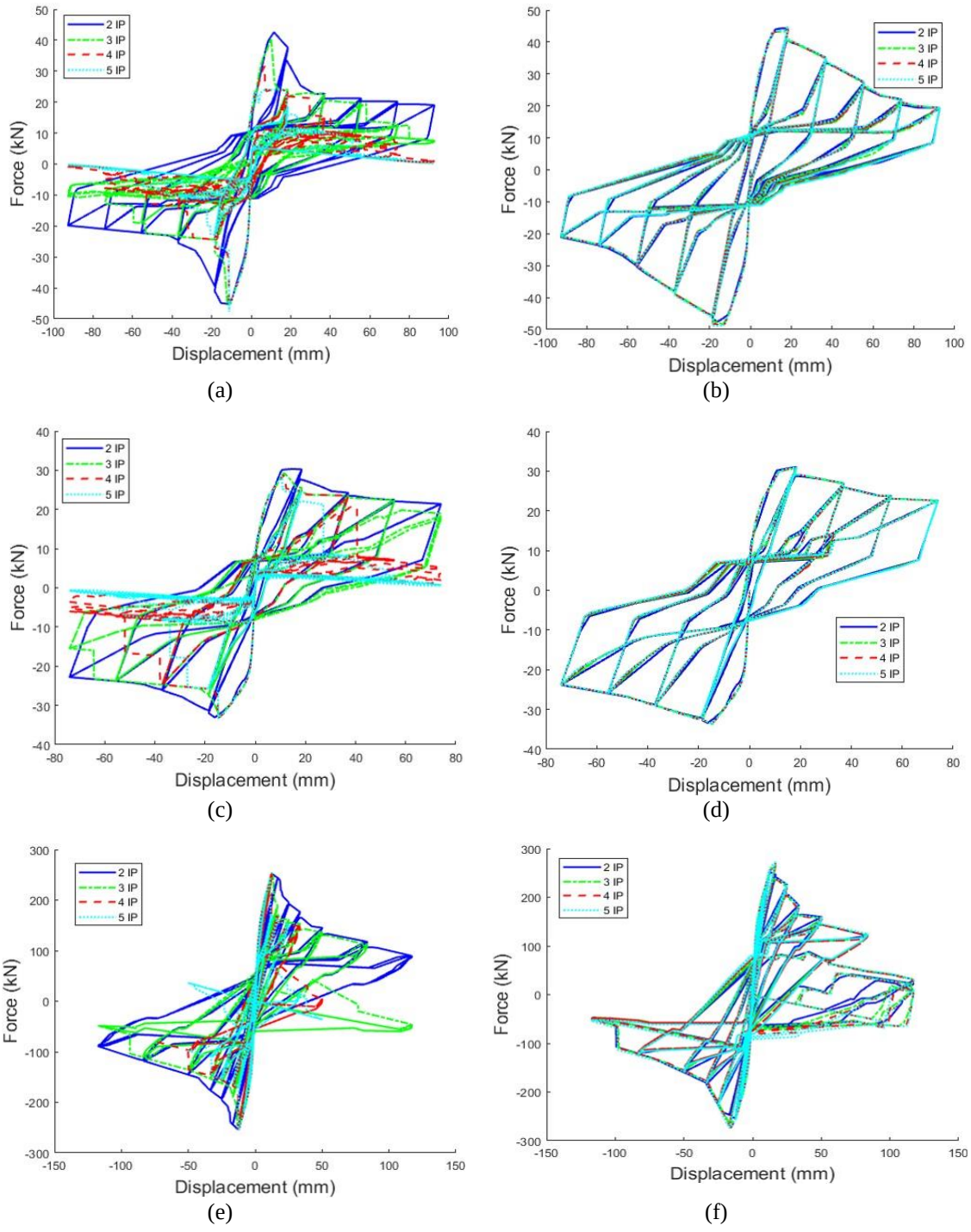

Figure 115. (a) & (c) & (e) non-regularized responses and (b) & (d) & (f) regularized responses of Specimens 3, 4, and 5, respectively

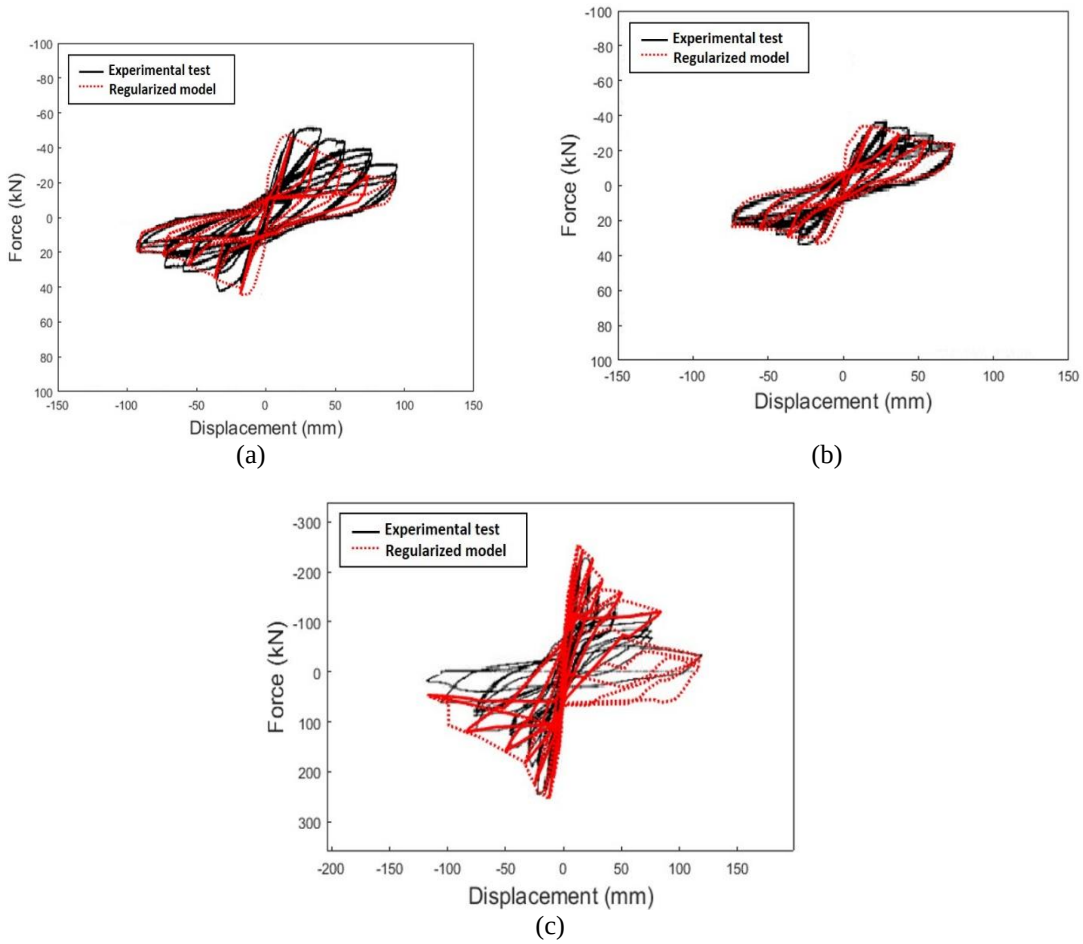

Figure 116. Experimental test results compared to regularized numerical model results for (a) Specimen 3, (b) Specimen 4, and (c) Specimen 5

CHAPTER 6. CONCLUSIONS AND FUTURE WORK

6.1 Introduction

This chapter consists of two sections. The first section presents a summary and conclusions of the study, and the second section provides a brief introduction to the ongoing and future work.

6.2 Summary and Conclusions

This section provides a summary of the contributions for each subtopic presented in the study.

6.2.1 Subtopic No. 1

Subtopic No. 1 presents a procedure for low-ductility columns to account for corrosion's impact on structural performance. For shear-critical columns, the corrosion effect decreases the magnitude of the shear capacity limit due to corroded transverse reinforcement. Increased likelihood of the brittle shear failure mode results due to early shear degradation. For columns with short lap splice, bond deterioration between the concrete and reinforcement in the lapped region leads to possible lap-splice failure. The cracking of column cover causes bond deterioration due to the expansion of corrosion products.

Fragility assessment of the corroded bridges shows that corrosion has a larger effect on the more severe damage states and intermediate loading intensities. Failure probabilities increase by 49% and 34% for the shear-critical and short lap-spliced columns under 20% mass loss of column reinforcement. The results also indicate that columns with short lap splice are more vulnerable to collapse damage state than shear-critical columns are under the same corrosion level.

6.2.2 Subtopic No. 2

Subtopic No. 2 demonstrates the need for increasing the efficiency of dynamic analysis used in fragility assessment. The proposed methodology is used to efficiently update analytical fragility curves through a Bayesian approach considering the corrosion effect.

Two types of observational data types are investigated in this subtopic. The first observational data type combines bridge-level response with conjugate Bayesian inference to obtain stable fragility functions. The proposed methodology shows faster convergence and results in more stable estimates through reducing the number of nonlinear time history analyses required. The second observational data type further decreases computational time by applying the proposed methodology based on bridge component-level response rather than the full bridge response. Results show the proposed method to achieve accurate, stable, and more quickly converging fragility calculations with a significantly reduced computational cost. It enables updated fragilities to be efficiently obtained based on new information across loading intensities and damage states.

6.2.3 Subtopic No. 3 (part 1)

Scour has been recognized as one of the leading causes of the bridge collapse in the U.S. Therefore, it is essential to be able to build models that accurately capture the response of bridges vulnerable to scour, including those located in layered rather than homogeneous soil deposits. A simple removal of soil springs due to scour ignores the effect of stress history for layered soils, leading to unconservative designs of foundations.

This subtopic proposes a methodology called the equivalent stress history and layered effects (ESHaLE) approach to capture the impact of the soil stress history of layered soils on vulnerability assessment of scoured bridges. It utilizes conservation of strength and mass to derive corresponding soil and depth parameters. Results show that neglecting to include stress history impacts in layered soils can lead to underestimating the single pile axial displacements by up to 35% in static analysis and underestimating the probability of exceeding the bridge deck deflection thresholds by up to 25% in seismic fragility assessment. The study presents a method to include soil stress history and layered effects in soil modeling and shows the importance of considering these soil effects in assessing bridges vulnerable to scour.

6.2.4 Subtopic No. 3 (part 2)

Removal of soil around the bridge foundation due to scour results in a reduction of the lateral and vertical foundation capacity due to the loss of soil support. The common approach in modeling the scour phenomenon of removal of soil springs without modifying the parameters of the remaining soil fails to consider the change of stress state of the

remaining soil and the formation of scour-hole geometry around the pile foundation. In practice, both of these factors impact the mechanical properties of the remaining soil and the resulting expected structural response of the pile under loadings. This subtopic proposes a methodology to comprehensively evaluate the combined effects of stress history and scour-hole dimensions on piles under scour conditions. It enables the examination of the lateral and axial behaviors of a loaded pile subject to scour and is applicable for both cohesive and cohesionless soils. The methodology is validated with results from field tests for no scour scenarios and verified with existing numerical models for scour scenarios.

The proposed methodology enables us to evaluate the combined effect of stress history and scour-hole dimensions for cohesive and cohesionless soils. Quantification of the soil effects is investigated through lateral pile deflection and load-settlement curves for lateral and axial behaviors, respectively. Load-settlement curves demonstrate that including the effect of stress history results in increases of up to 34.1% and 61.1% in estimated pile settlement for sand and clay, respectively, leading to potential unconservative designs if soil effects are not properly included in the analysis.

6.2.5 Subtopic No. 4

Scour leading to the removal of soil around water-crossing bridge foundations can result in loss of load-carrying capacity and increase the risk of bridge collapse due to the loss of soil support. Bridges may experience non-uniformity in scour depths for bridge columns located under different column bents due to varying water steam velocities and environmental conditions. The common practice in modeling of scour is to assume uniform scour depths for the bridge foundation regardless of the location of bridge columns.

However, such assumptions neglect the amplification of engineering demand due to the impact of non-uniform scour, leading to inaccurate and potentially unconservative evaluation of the seismic and flood resistance of the bridge.

This study investigates the impact of non-uniform scour on the performance of reinforced concrete bridges under seismic and flood hazards. It finds that non-uniformity in scour depths for bridge columns under different column bents results in increases of estimated column curvature demand by as much as 55% and 40% in seismic and flood analyses, respectively, through tracking the maximum curvature demand along the columns under varying loading scenarios and scour depths. The study shows that non-uniform scour conditions can further escalate the level of structural damage, including yielding of reinforcement, highlighting the importance of considering non-uniform scour in the assessment of bridge risk.

6.2.6 Subtopic No. 5

Aging and degrading structural bridge components due to corrosion and scour can create severe safety issues in the structural system and lead to possible bridge failures. Collecting and analyzing inspection data provide a way to monitor and assess the safety condition of bridges.

Subtopic No. 5 proposes a framework to utilize collected inspection data to assess a bridge's condition by updating both component- and system-level fragility curves of the bridge. Particularly, collected data such as mass loss of reinforcement and depth of scour hole are utilized to update the mechanical properties of structural members in the finite element model. Fragility curves are then updated by performing a series of nonlinear time

analyses based on the inspection data. As bridges age, they are susceptible to increasing corrosion and scour. This study investigates bridges' performance considering the combined effect of reinforcement corrosion and foundation scour under extreme loadings such as seismic events to assess bridge resilience. Fragility results quantify increases in the probabilities of damage and collapse of the structural system as measured mass loss and scour depth increase. The results show that an increase of 40% of failure probability can be triggered by 15% mass loss due to the corrosion effect. The medium-span bridge is more vulnerable than the short-span bridge at the system level with different scour levels. The impact of corrosion is more pronounced for bridges with less scour.

6.2.7 Subtopic No. 6

In reinforced concrete structures built before the 1970s, it was common for columns to be constructed with short lap splices and widely spaced transverse bars at the column base, leading to increased likelihoods of pull-out failures and structural collapse during seismic events. Several challenges arise in the modeling and analyzing reinforced concrete columns with short lap splices, particularly with softening behavior that leads to strain localization and scaling and convergence issues in analyses.

Subtopic No. 6 presents a methodology to regularize force-based beam-column elements with softening lap-splice material response. A constant energy release criterion is imposed with the constant post-peak energy of the lap-splice region determined from relevant experimental data. With the proposed regularization, the numerical model shows objective results independent of the length of the element and the number of integration points used. Whereas the accuracy in estimating, for example, the displacement at 20%

strength drop using existing non-regularized models changes with the number of integration points, the accuracy using the proposed model remains constant across numbers of integration points used with a mean accuracy of 94% compared with experimental tests. Results from static pushover and cyclic analyses show an order of magnitude decrease in the standard deviation of the response using the regularized model. Increased accuracy and improved convergence for the method across the number of integration points used are shown in static and dynamic analyses. The proposed regularization approach has demonstrated the ability to alleviate strain localization issues and facilitates the scaling of analyses from small-scale to full-scale structures.

6.3 Ongoing Work

Bridge failure due to buckling of the pile under scour conditions has been reported in the past (Hughes et al., 2007). One of the recent studies has also shown that ignoring the stress history of the soft clay will overestimate the pile's static buckling capacity in the presence of scour (Liang et al., 2015). At the same time, it is critical to consider time-dependent loadings on bridges when designing and analyzing these structures. For example, heavy truckloads, wind effects, and earthquakes can introduce dynamic loadings on the bridge pile. Excessive simplifications on time-dependent loadings in both structural analysis and design could result in a compromise in structural safety. Hence, this ongoing study aims to address the impact of stress history in soft clay and scour level (i.e., scour depth) based on the pile's dynamic buckling behavior under scour conditions.

A unified dynamic buckling analysis (Motamarri and Suryanarayan, 2012; Kuzkin and Dannert, 2016; Gao et al., 2017) for an embedded pile with initial imperfection under

scour conditions will be investigated in this study. Figure 117 presents a proposed flowchart for the dynamic buckling analysis. The procedure starts with a derivation of the governing partial differential equation (PDE) of the embedded pile based on Hamilton's Principle. Among various computational approaches, the Galerkin method is adopted in this study, assuming the first buckling mode as a trial function. After applying the Galerkin method to the PDE and simplify the equations, the unified nonlinear ODE can then be obtained and numerically solved by the Runge-Kutta method. Finally, the result obtained from the proposed method is verified against the numerical results from another computational scheme (i.e., Finite-element method) using the commercial software Abaqus. Several assumptions need to be addressed for the analysis. First of all, initial imperfection is assumed to be identical to the embedded pile's first buckling mode. Second, the effects of axial inertia, rotatory inertial, transverse shear, and skin friction are neglected for simplicity. Third, only geometric nonlinearity is considered, and material remains linear elastic. The following bullet points are the ongoing and future investigations.

- Study the impact of scour levels on the dynamic buckling load
- Compare dynamic buckling of the embedded pile with and without considering the soil stress history
- Compute the ratio between dynamic buckling load and static buckling load in the presence of scour and soil stress history
- Investigate the impact of various boundary conditions, such as a pinned top-free end and fixed top-free end.

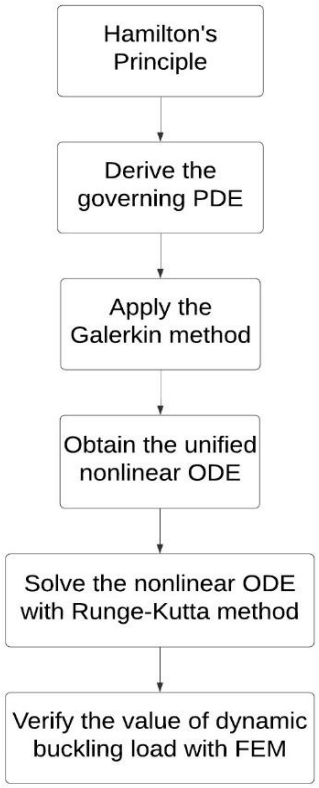

Figure 117. Flowchart of the proposed procedures for dynamic buckling of an embedded pile under scour conditions

6.4 Recommendation for Future Work

Several potential research topics can be extended for future study from the work presented in this dissertation. The following bullet points present some of these topics:

- A sudden drop in shear resistance in saturated cohesionless soil (i.e., sand) due to the liquefaction effect can create a tremendous hazard in bridge safety. At the same time, bridge foundation piles embedded into saturated sand can also be susceptible to scour hazards. Therefore, one potential topic for future study is to investigate the combined effect of the liquefaction and scour phenomena on bridges' seismic

performance. Moreover, proposing a physics-based model that has the ability to capture and simulate the physical phenomena, such as the interaction between scour and liquefaction, is particularly essential because the interaction between these two phenomena could potentially post a high risk of bridge collapse, and only a few studies have explored this topic.

- This study has looked at the seismic performance of straight bridges subjected to the non-uniform scour phenomenon. Another area that one can extend this work to is the vulnerability assessment of non-uniformity in scour on skewed bridges and curved bridges. How does non-uniformity in scour depths impact the bridges with skew and curve effects under external loadings? Will the combination of these effects increase the torsional demand in bridge response?
- The investigation of vulnerability assessment of bridges subjected to corrosion and scour at the bridge level has been explored in this study. Meanwhile, it is also essential to look at the vulnerability assessment of bridges at the network level, considering the effect of corrosion and scour. The study of the vulnerability of bridges at the network level facilitates decision-makers to prioritize bridges across a network for repair after hazard events. The framework can also be used to minimize downtime and repair costs associated with the hazards.

REFERENCES

AASHTO, L. (2012). AASHTO LRFD bridge design specifications. *American Association of State Highway and Transportation Officials, Washington, DC*.

Aboutaha, R. S., Engelhardt, M. D., Jirsa, J. O., & Kreger, M. E. (1996). Retrofit of concrete columns with inadequate lap splices by the use of rectangular steel jackets. *Earthquake Spectra*, *12*(4), 693-714.

ACI (American Concrete Institute). (2011). Building code requirements for structural concrete and commentary.

Addessi, D., & Ciampi, V. (2007). A regularized force-based beam element with a damage–plastic section constitutive law. *International Journal for Numerical Methods in Engineering*, *70*(5), 610-629.

Alampalli, S., & Ettouney, M. (2008). Multihazard applications in bridge management. *International Bridge and Structure Management*, 356.

Alipour, A., Shafei, B., & Shinozuka, M. (2012). Reliability-based calibration of load and resistance factors for design of RC bridges under multiple extreme events: Scour and earthquake. *Journal of Bridge Engineering*, *18*(5), 362-371.

Almusallam, A. A. (2001). Effect of degree of corrosion on the properties of reinforcing steel bars. *Construction and Building Materials*, *15*(8), 361-368.

American Concrete Institute (ACI) Committee 318. (2011). *Building code requirements for structural concrete (ACI 318-11) and commentary*. Farmington Hills, MI: American Concrete Institute.

American Society of Civil Engineers (ASCE). (2007). *Seismic rehabilitation of existing buildings*, ASCE/SEI 41-06. Reston, VA: American Society of Civil Engineers.

Ang, A. H., and Tang, W. H. (1975). Probability concepts in engineering planning and design: Basic principles, Vol. I, Wiley, New York.

Ang, B. G. (1985). Seismic shear strength of circular bridge piers.

A. P. I. (2000). Recommended practice for planning, designing and constructing fixed offshore platforms–working stress design–. In *Twenty*-.

Apostolopoulos, C. A., Papadopoulos, M. P., & Pantelakis, S. G. (2006). Tensile behavior of corroded reinforcing steel bars BSt 500s. *Construction and building materials*, *20*(9), 782-789.

Aygun, B. (2009). *Efficient seismic fragility assessment of highway bridges on liquefiable soils* (Master thesis, Rice University).

Baker, J. W., Lin, T., Shahi, S. K., & Jayaram, N. (2011). New ground motion selection procedures and selected motions for the PEER transportation research program, *PEER Report*, (2011/3).

Baker, J. W. (2015). Efficient analytical fragility function fitting using dynamic structural analysis. *Earthquake Spectra*, *31*(1), 579-599.

Banerjee, S., & Ganesh Prasad, G. (2013). Seismic risk assessment of reinforced concrete bridges in flood-prone regions. *Structure and Infrastructure Engineering*, *9*(9), 952-968.

Bažant, Z. P., & Oh, B. H. (1983). Crack band theory for fracture of concrete. *Matériaux et construction*, *16*(3), 155-177.

Bažant, Z. P., & Planas, J. (1997). *Fracture and size effect in concrete and other quasibrittle materials* (Vol. 16). CRC press.

Bhargava K, Ghosh A K, Mori Y, Ramanujam S. (2007). Corrosion-induced bond strength degradation in reinforced concrete-Analytical and empirical models. *Nuclear Engineering and Design Journal*. 1140-1157.

Billah, A. H. M., & Alam, M. (2015). Seismic fragility assessment of highway bridges: a state-of-the-art review. *Structure and Infrastructure Engineering*, *11*(6), 804-832.

Boulanger, R. W., Curras, C. J., Kutter, B. L., Wilson, D. W., & Abghari, A. (1999). Seismic soil-pilestructure interaction experiments and analyses. *Journal of Geotechnical and Geoenvironmental Engineering*, *125*(9), 750-759.

Brown, D. A., and Castelli, R. J. (2010). "Construction procedures and LRFD design methods." Rep. FHWA-NHI-10-016, Federal Highway Administration, Washington, DC.

Cairo, R., & Conte, E. (2006). Settlement analysis of pile groups in layered soils. *Canadian Geotechnical Journal*, *43*(8), 788-801.

Capé, M. (1999). Residual service-life assessment of existing R/C structures. In *Chalmers University of Technology, Goteborg (Sweden) and Milan University of Technology, Italy Erasmus Program*.

Chail, Y. H., Priestley, M. N., & Seible, F. (1991). Seismic retrofit of circular bridge columns for enhanced flexural performance. Structural Journal, 88(5), 572-584.

Chandramohan, R., Baker, J. W., & Deierlein, G. G. (2016). Impact of hazard-consistent ground motion duration in structural collapse risk assessment. *Earthquake Engineering & Structural Dynamics*, *45*(8), 1357-1379.

Chiou, B., Darragh, R., Gregor, N., & Silva, W. (2008). NGA project strong-motion database. *Earthquake Spectra*, *24*(1), 23-44.

Cho, J. Y., & Pincheira, J. A. (2006). Inelastic analysis of reinforced concrete columns with short lap splices subjected to reversed cyclic loads. *ACI Materials Journal*, *103*(2), 280.

Choe, D., Gardoni, P., Rosowsky, D., & Haukaas, T. (2009). Seismic fragility estimates for reinforced concrete bridges subject to corrosion. Structural Safety, 31, 275–283.

Choi, E. (2002). *Seismic analysis and retrofit of Mid-America bridges*, Ph.D. thesis, School of Civil and Environmental Engineering, Georgia Institute of Technology, Georgia.

Choi, E., DesRoches, R., & Nielson, B.G. (2004). Seismic fragility of typical bridges in moderate seismic zones. Engineering Structures, 26, 187–199.

Coleman, J., & Spacone, E. (2001). Localization issues in force-based frame elements. *Journal of Structural Engineering*, *127*(11), 1257-1265.

Cornell, A. C., Jayaler, F., Hamburger, R. O., Foutch, A. D. (2002). *Probabilistic Basis for 2000 SAC Federal Emergency Management Agency Steel Moment Frame Guidelines*, Journal of Structural Engineering, 128(4), pp: 526-533.

Coronelli, D., & Gambarova, P. (2004). Structural assessment of corroded reinforced concrete beams: modeling guidelines. *Journal of structural engineering*, *130*(8), 1214-1224.

Cox, W. R., Reese, L. C., & Grubbs, B. R. (1974). Field testing of laterally loaded piles in sand. In *Offshore Technology Conference*. Offshore Technology Conference.

Davisson, M. T., & Gill, H. L. (1963). Laterally loaded piles in a layered soil system. *Journal of the Soil Mechanics and Foundations Division*, *89*(3), 63-94.

Deng, L., Wang, W., & Yu, Y. (2016). State-of-the-art review on the causes and mechanisms of bridge collapse. *Journal of Performance of Constructed Facilities*, *30*(2), 04015005.

Der Kiureghian, A. (2002). Bayesian methods for seismic fragility assessment of lifeline components. In A.D. Kiureghian (Ed.), Acceptable risk processes: Lifelines and natural hazards, Monograph No. 21. Reston, VA: Technical Council for Lifeline Earthquake Engineering, ASCE.

Du, Y. G., Clark, L. A., & Chan, A. H. C. (2005). Residual capacity of corroded reinforcing bars. *Magazine of Concrete Research*, *57*(3), 135-147.

Du, Y. G., Clark, L. A., & Chan, A. H. C. (2005). Effect of corrosion on ductility of reinforcing bars. *Magazine of Concrete Research*, *57*(7), 407-419.

Ellingwood, B. R., Hwang, H. (1985). *Probabilistic Descriptions of Resistance of Safety-Related Structures in Nuclear Plants*, Nuclear Engineering and Design, 88(2), 169-178.

Ellingwood, B. R. (2001). Earthquake risk assessment of building structures. *Reliability Engineering & System Safety*, *74*(3), 251-262.

Elwood, K. J. (2004). Modelling failures in existing reinforced concrete columns. *Canadian Journal of Civil Engineering*, *31*(5), 846-859.

FHWA, U. (2013). National bridge inventory. *US FHWA*.

Filippou, F. C., & Fenves, G. L. (2004). Methods of analysis for earthquake-resistant structures. *Earthquake engineering: From engineering seismology to performance-based engineering*, *6*, 6-1.

Fioklou, A., & Alipour, A. (2019). Significance of non-uniform scour on the seismic performance of bridges. *Structure and Infrastructure Engineering*, *15*(6), 822-836.

Gao, K., Gao, W., Wu, D., & Song, C. (2017). Nonlinear dynamic stability analysis of Euler–Bernoulli beam–columns with damping effects under thermal environment. *Nonlinear Dynamics*, *90*(4), 2423-2444.

Gardoni, P., Der Kiureghian, A., & Mosalam, K.M. (2002). Probabilistic capacity models and fragility estimates for reinforced concrete columns based on experimental observations. ASCE Journal of Engineering Mechanics, 128, 1024–1038.

Gazetas, G., & Dobry, R. (1984). Horizontal response of piles in layered soils. *Journal of Geotechnical engineering*, *110*(1), 20-40.

Georgiadis, M. (1983, April). Development of py curves for layered soils. In *Geotechnical practice in offshore engineering* (pp. 536-545). ASCE.

Georgiadis, M., Anagnostopoulos, C., & Naskos, N. (1999). Effect of pile-head enlargement on lateral and axial responses of a bored pile. In *International Conference on Soil Mechanics and Foundation Engineering* (pp. 809-812).

Ghosh, J., & Padgett, J. E. (2010). Aging considerations in the development of time-

dependent seismic fragility curves. *Journal of Structural Engineering*, *136*(12), 1497-1511.

Ghosn, M., Moses, F., & Wang, J. (2003). *Design of highway bridges for extreme events* (Vol. 489). Transportation Research Board.

Hager, W. H., & Unger, J. (2010). Bridge pier scour under flood waves. *Journal of Hydraulic Engineering*, *136*(10), 842-847.

Han, Z., Ye, A., & Fan, L. (2010). Effects of riverbed scour on seismic performance of high-rise pile cap foundation. *Earthquake Engineering and Engineering Vibration*, *9*(4), 533-543.

He, Z., Liu, W., Wang, X., & Ye, A. (2016). Optimal force-based beam-column element size for reinforced-concrete piles in bridges. *Journal of Bridge Engineering*, *21*(11), 06016006.

Hognestad, E. (1951). *Study of combined bending and axial load in reinforced concrete members*. University of Illinois at Urbana Champaign, College of Engineering. Engineering Experiment Station.

Huang, M., Liang, F., & Jiang, J. (2011). A simplified nonlinear analysis method for piled raft foundation in layered soils under vertical loading. *Computers and Geotechnics*, *38*(7), 875-882.

Hughes D, Ramey GE, Hughes ML (2007) Effects of extreme scour and soil subgrade modulus on bridge pile bent buckling. Pract Period Struct Des Constr 12(2):96–108

Hwang, H., Liu, J. B., & Chiu, Y. H. (2001). Seismic fragility analysis of highway bridges. *Mid-America Earthquake Center CD Release 01-06*.

p

Jansen, D. C., & Shah, S. P. (1997). Effect of length on compressive strain softening of concrete. *Journal of Engineering Mechanics*, *123*(1), 25-35.

Jaradat, O. A., McLean, D. I., & Marsh, M. L. (1998). Performance of existing bridge columns under cyclic loading—part 1: experimental results and observed behavior. *Structural Journal*, *95*(6), 695-704.

Kashani, M. M., Crewe, A. J., & Alexander, N. A. (2013). Use of a 3D optical measurement technique for stochastic corrosion pattern analysis of reinforcing bars subjected to accelerated corrosion. *Corrosion Science*, *73*, 208-221.

Kashani, M. M., Lowes, L. N., Crewe, A. J., & Alexander, N. A. (2015). Phenomenological

hysteretic model for corroded reinforcing bars including inelastic buckling and low-cycle fatigue degradation. *Computers & Structures*, *156*, 58-71.

Kashani, M. M., Lowes, L. N., Crewe, A. J., & Alexander, N. A. (2016). Computational modelling strategies for nonlinear response prediction of corroded circular RC bridge piers. *Advances in Materials Science and Engineering*, *2016*.

Kent, D. C., & Park, R. (1971). Flexural members with confined concrete. *Journal of the Structural Division*.

Khan, Z., & Amanat, K. M. (2015). Riverbed scouring effect in bridge pile foundation during earthquake. American Society of Civil Engineers. doi:10.1061/9780784413425.035

Klinga, J. V., & Alipour, A. (2015). Assessment of structural integrity of bridges under extreme scour conditions. *Engineering Structures*, *82*, 55-71.

Kulhawy, F. H., & Mayne, P. W. (1990). *Manual on estimating soil properties for foundation design* (No. EPRI-EL-6800). Electric Power Research Inst., Palo Alto, CA (USA); Cornell Univ., Ithaca, NY (USA). Geotechnical Engineering Group.

Kuzkin, V. A., & Dannert, M. M. (2016). Buckling of a column under a constant speed compression: a dynamic correction to the Euler formula. *Acta Mechanica*, *227*(6), 1645-1652.

Koutsourelakis, P.S. (2010). Assessing structural vulnerability against earthquakes using multi-dimensional fragility surfaces: A Bayesian framework. Probabilistic Engineering Mechanics, 25, 49–60.

Lagasse, P. F., Clopper, P. E., Zevenbergen, L.W., and Girard, L.W. (2007). "Countermeasures to protect bridge piers from scour." NCHRP Rep. 593, National Cooperative Highway Research Program, Transportation Research Board, National Academies, Washington, DC.

LeBorgne, M. R. (2012). *Modeling the post shear failure behavior of reinforced concrete columns* (Doctoral dissertation).

LeBorgne, M. R., & Ghannoum, W. M. (2013). Analytical element for simulating lateral-strength degradation in reinforced concrete columns and other frame members. *Journal of Structural Engineering*, *140*(7), 04014038.

Lee, J., Lee, Y. J., Kim, H., Sim, S., & Kim, J. (2016). A new methodology development for flood fragility curve derivation considering structural deterioration for bridges. *Smart Structures and Systems*, *17*(1), 149-165.

Lee, Y. H., & William, K. (1997). Mechanical properties of concrete in uniaxial compression. *Materials Journal*, *94*(6), 457-471

Li, J., Spencer, B.F., & Elnashai, A.S. (2012). Bayesian updating of fragility functions using hybrid simulation. ASCE Journalof Structural Engineering, 139, 1160–1171.

Liang, F., Zhang, H., & Huang, M. (2015). Extreme scour effects on the buckling of bridge piles considering the stress history of soft clay. *Natural Hazards*, *77*(2), 1143-1159.

Lin, C., Bennett, C., Han, J., & Parsons, R. L. (2010). Scour effects on the response of laterally loaded piles considering stress history of sand. *Computers and Geotechnics*, *37*(7-8), 1008-1014.

Lin, C., Bennett, C., Han, J., & Parsons, R. L. (2010). Scour effects on the response of laterally loaded piles considering stress history of sand. *Computers and Geotechnics*, *37*(7-8), 1008-1014.

Lin, C. (2012). *Evaluation of lateral behavior of pile-supported bridges under scour conditions* (Doctoral dissertation, University of Kansas).

Lin, C., Han, J., Bennett, C., & Parsons, R. L. (2014a). Behavior of laterally loaded piles under scour conditions considering the stress history of undrained soft clay. *Journal of Geotechnical and Geoenvironmental Engineering*, *140*(6), 06014005.

Lin, C., Han, J., Bennett, C., & Parsons, R. L. (2014b). Analysis of laterally loaded piles in sand considering scour hole dimensions. *Journal of Geotechnical and Geoenvironmental Engineering*, *140*(6), 04014024.

Lin, C., Han, J., Bennett, C., & Parsons, R. L. (2014c). Case history analysis of bridge failures due to scour. In *Climatic effects on pavement and geotechnical infrastructure* (pp. 204-216).

Lin, C., Bennett, C., Han, J., & Parsons, R. (2015). Effect of soil stress history on scour evaluation of pile-supported bridges. *Journal of Performance of Constructed Facilities*, *29*(6), 04014178.

Lin, C., Han, J., Bennett, C., & Parsons, R. L. (2016). Analysis of laterally loaded piles in soft clay considering scour-hole dimensions. *Ocean Engineering*, *111*, 461-470.

Lin, C. (2017). The loss of pile axial capacities due to scour: vertical stress distribution. *DEStech Transactions on Materials Science and Engineering*, (ictim).

Liu, K. Y., Witarto, W., & Chang, K. C. (2015). Composed analytical models for seismic assessment of reinforced concrete bridge columns. *Earthquake Engineering & Structural Dynamics*, *44*(2), 265-281.

Luco, N., & Cornell, C.A. (1998). Effects of random connection fractures on the demands and reliability for a three-story pre-Northridge (SMRP) structure. In Proceedings of the 6th U.S. National Conference on Earthquake Engineering. Oakland, California: Earthquake Engineering Research Institute.

Lunn, D., Jackson, C., Best, N., Spiegelhalter, D., & Thomas, A. (2012). *The BUGS book: A practical introduction to Bayesian analysis*. Chapman and Hall/CRC.

Mackie, K., & Stojadinović, B. (2003). *Seismic demands for performance-based design of bridges*. Berkeley: Pacific Earthquake Engineering Research Center.

Mackie, K., & Stojadinovic, B. (2005). Fragility basis for california highway overpass bridge seismic decision making, (PEER Report 2005/02). Pacific Earthquake Engineering Research Center. Berkeley, CA: University of California.

Mackie, K. and Stojadinovic, B. (2006). Seismic Vulnerability of Typical Multi-span California Highway Bridges, Proceedings of the Fifth National Seismic Conference on Bridges and highways, September 18-20, San Francisco.

Mander, J. B., Priestley, M. J., & Park, R. (1988). Theoretical stress-strain model for confined concrete. *Journal of structural engineering*, *114*(8), 1804-1826.

Mangalathu Sivasubramanian Pillai, S. (2017). *Performance based grouping and fragility analysis of box-girder bridges in California* (Doctoral dissertation, Georgia Institute of Technology).

Matlock, H. (1970). "Correlation for design of laterally-loaded piles in soft clay." Proc., 2nd Annual Offshore Technology Conf., American Institute of Mining, Metallurgical, and Petroleum Engineers, Houston, 277–594.

May, R. W. P., Ackers, J. C., & Kirby, A. M. (2002). *Manual on scour at bridges and other hydraulic structures* (Vol. 551). London: Ciria.

Mayerhof, G. G. (1976). Bearing capacity and settlement of pile foundations. *Journal of Geotechnical and Geoenvironmental Engineering*, *102*(ASCE# 11962).

Mazzoni, S., McKenna, F., Scott, M. H., & Fenves, G. L. (2006). OpenSees command language manual. *Pacific Earthquake Engineering Research (PEER) Center*, *264*.

McKay, M. D., Conover, W. J., Beckman, R. J. (1979). *A comparison of three methods for selecting values of input variables in the analysis of output from a computer code*, Technometrics, 21, pp: 239-245.

McKenna, F. T. (1997). Object-oriented finite element programming: frameworks for analysis, algorithms and parallel computing. (Doctoral dissertation). Berkeley, CA: University of California at Berkeley.

Melchers, R. E. (2001). *Structural Reliability Analysis and Prediction*. JohnWiley & Sons Ltd., West Sussex, England, second edition.

Melek, M., & Wallace, J. W. (2004). Cyclic behavior of columns with short lap splices. *Structural Journal*, *101*(6), 802-811.

Molina, F. J., Alonso, C., & Andrade, C. (1993). Cover cracking as a function of rebar corrosion: part 2—numerical model. *Materials and structures*, *26*(9), 532-548.

Mokwa, R. L. (1999). *Investigation of the resistance of pile caps to lateral loading* (Doctoral dissertation, Virginia Tech).

Mosher, R. L. (1984). Load-Transfer Criteria for Numerical Analysis of Axially Loaded Piles in Sand. Part 1. Load-Transfer Criteria (No. WES-TR-K-84-1). ARMY ENGINEER WATERWAYS EXPERIMENT STATION VICKSBURG MS.

Motamarri, P., & Suryanarayan, S. (2012). Unified analytical solution for dynamic elastic buckling of beams for various boundary conditions and loading rates. *International Journal of Mechanical Sciences*, *56*(1), 60-69.

Muthukumar, S. (2003). *A contact element approach with hysteresis damping for the analysis and design of pounding in bridges* (Doctoral dissertation, Georgia Institute of Technology).

Nielson, B. G. (2005). *Analytical Fragility Curves for Highway Bridges in Moderate Seismic Zones*, Ph.D. Dissertation, Georgia Institute of Technology, Atlanta, GA.

Nielson, B.G., & DesRoches, R. (2007a). Seismic fragility curves for typical highway bridge classes in the Central and Southeastern United States. Earthquake Spectra, 23, 615–633.

Nielson, B.G., & DesRoches, R. (2007b). Seismic fragility methodology for highway bridges using a component level approach. Earthquake Engineering and Structural Dynamics, 36, 823–839.

Noh, H. Y., Kiremidjian, A., Ceferino, L., & So, E. (2017). Bayesian updating of earthquake vulnerability functions with application to mortality rates. *Earthquake spectra*, *33*(3), 1173-1189.

O'Neill, M. W., Hawkins, R. A., and Mahar, L. J. (1982). ''Load-transfer mechanisms in piles and pile groups.'' *J. Geotech. Eng.*, 108~12!, 1605–1623.

Padgett, J.E. (2007). Seismic vulnerability assessment of retrofitted bridges using probabilistic methods, Ph.D. Dissertation. Georgia Institute of Technology, Atlanta, GA.

Pan, Y., Agrawal, A.K., Ghosn, M., & Alampalli, S. (2010). Seismic fragility of multi-span simply supported steel highway bridges in New York State. I: Bridge modeling, parametric analysis, and retrofit design. ASCE Journal of Bridge Engineering, 15, 448–461.

Papazafeiropoulos, G., & Plevris, V. (2018). OpenSeismoMatlab: A new open-source software for strong ground motion data processing. *Heliyon*, *4*(9), e00784.

Priestley, M. N., Seible, F., Calvi, G. M., & Calvi, G. M. (1996). *Seismic design and retrofit of bridges*. John Wiley & Sons.

Ramanathan, K., DesRoches, R., & Padgett, J.E. (2012). A comparison of pre- and post-seismic design considerations in moderate seismic zones through the fragility assessment of multi-span bridge classes. Engineering Structures, 45, 559–573.

Ramanathan, K. N. (2012). *Next generation seismic fragility curves for California bridges incorporating the evolution in seismic design philosophy* (Doctoral dissertation, Georgia Institute of Technology).

Reese, L. C., Cox, W. R., & Koop, F. D. (1974). Analysis of laterally loaded piles in sand. *Offshore Technology in Civil Engineering Hall of Fame Papers from the Early Years*, 95-105.

Reese, L. C. and O'Neill, M. W. (1987). Drilled shafts: Construction procedures and design methods, Report No. FHWA-HI-88-042, US Department of Transportation, Federal Highway Administration, Virginia.

Reese, L. C., & Van Impe, W. F. (2001). Single pile and pile group under lateral loading I-M. *Rotterdam. Balkema AA*.

Reese, L. C., & Welch, R. C. (1975). Lateral loading of deep foundations in stiff clay. *Journal of Geotechnical and Geoenvironmental Engineering*, *101*(ASCE# 11456 Proceeding).

Reyes, O., & Pincheira, J. A. (1999, April). R/C columns with lap splices subjected to earthquake. In *ASCE structures congress* (pp. 369-372).

Rudriguez J, Ortega L, Izquierdo D, Andrade C. (2006). Calculation of Structural Degradation Due to Corrosion of Reinforcements. *Measuring, Monitoring and Modeling Concrete Properties.* Springer, 527-536.

Scott, M. H., & Hamutçuoğlu, O. M. (2008). Numerically consistent regularization of force-based frame elements. *International journal for numerical methods in engineering*, *76*(10), 1612-1631.

SDC (2004). *Seismic Design Criteria*, Version 1.3, California Department of Transportation, Sacramento, CA.

SDC (2010). *Seismic Design Criteria*, Version 1.6, California Department of Transportation, Sacramento, CA.

Sezen, H., & Moehle J. P. (2004). Shear strength model for lightly reinforced concrete columns. *Journal of Structural Engineering*, *130*(11), 1692-1703.

Shang, F., An, X., Mishima, T., & Maekawa, K. (2011). Three-dimensional nonlinear bond model incorporating transverse action in corroded RC members. *Journal of Advanced Concrete Technology*, *9*(1), 89-102.

Shinozuka, M., Feng, M.Q., Kim, H.-K., & Kim, S.-H. (2000). Nonlinear static procedure for fragility curve development. ASCE Journal of Engineering Mechanics, 126, 1287–1296.

Singhal, A., & Kiremidjian, A. S. (1998). Bayesian updating of fragilities with application to RC frames. *Journal of structural Engineering*, *124*(8), 922-929.

Soleimani, F. (2017). *Fragility of California bridges-development of modification factors* (Doctoral dissertation, Georgia Institute of Technology).

Somerville, P., Smith, N., Punyamurthula, S., and Sun, J., 1997. Development of ground motion time histories for phase 2 of the FEMA/SAC steel project, SAC Background Document Report No. SAC/BD-9/04, SAC Joint Venture, 555 University Ave., Sacramento, CA.

Soneji, B. B., & Jangid, R. S. (2008). Influence of soil–structure interaction on the response of seismically isolated cable-stayed bridge. *Soil Dynamics and Earthquake Engineering*, *28*(4), 245-257.

Song, S.-T., Wang, C. Y., & Huang, W.-H. (2015). Earthquake damage potential and critical scour depth of bridges exposed to flood and seismic hazards under lateral seismic loads. Earthquake Engineering and Engineering Vibration, 14(4), 579–594. doi:10.1007/s11803-015-0047-9

Sotoud, S., & Aboutaha, R. S. (2014). Flexural Strength of Corroded Lap Spliced RC Bridge Column Section. In *Structures Congress 2014* (pp. 303-312).

Spacone, E., Filippou, F. C., and Taucer, F. F. (1996a). ‘‘Fibre beamcolumn model for nonlinear analysis of R/C frames. I: Formulation.’’ *Earthquake Engrg. and Struct. Dyn.*, 25(7), 711–725.

Spacone, E., Filippou, F. C., and Taucer, F. F. (1996b). ‘‘Fibre beamcolumn model for nonlinear analysis of R/C frames. II: Applications.’’ *Earthquake Engrg. and Struct. Dyn.*, 25(7), 727–742.

Sun, Z., Priestley, M. J. N., & Seible, F. (1993). *Diagnostics and retrofit of rectangular bridge columns for seismic loads*. Department of Applied Mechanics & Engineering Sciences, University of California, San Diego.

Takemiya, H., & Yamada, Y. (1981). Layered soil-pile-structure dynamic interaction. *Earthquake Engineering & Structural Dynamics*, *9*(5), 437-457.

Tariverdilo, S., A. Farjadi, and M. Barkhordary. (2009). "Fragility Curves for Reinforced Concrete Frames With Lap-Spliced Columns." *International Journal of Engineering - Transactions A: Basics* 22 (3): 213.

Terzaghi, K. (1943). Theoretical Soil Mechanics. JohnWiley & Sons. *New York*, 11-15.

Tomlinson, M. J., & Boorman, R. (2001). *Foundation design and construction*. Pearson education.

Touma, F. T., & Reese, L. C. (1974). Behavior of bored piles in sand. *Journal of Geotechnical and Geoenvironmental Engineering*, *100*(Proc Paper 10064).

Tubaldi, E., Lorenzo, M., & Bassam, A. I. (2018). Three-dimensional mesoscale modelling of multi-span masonry arch bridges subjected to scour. Engineering Structures, 165, 486–500. doi:10.1016/j.engstruct.2018.03.031

Vamvatsikos, D., & Cornell, A.C. (2002). Incremental dynamic analysis. Earthquake Engineering & Structural Dynamics, 31, 491–514.

Vecchio, F. J., & Collins, M. P. (1986). The modified compression-field theory for reinforced concrete elements subjected to shear. *ACI J.*, *83*(2), 219-231.

Veletzos, M., Restrepo, J. I., & Sahs, S. (2006). Post Seismic Inspection and Capacity Assessment of Reinforced Concrete Bridge Columns. In *Fifth National Seismic Conference on Bridges & HighwaysMultidisciplinary Center for Earthquake Engineering Research California Department of Transportation Federal Highway Administration Transportation Research Board* (No. A25).

Vijayvergiya, V. N. (1977). Load-movement characteristics of piles. In *Ports'77. 4 th annual symposium of the American Society of Civil Engineers, Waterway, Port, Coastal and Ocean Division, Long Beach, California, v. 2* (pp. 269-284).

Wang, Z., Dueñas-Osorio, L., & Padgett, J. E. (2014). Influence of scour effects on the seismic response of reinforced concrete bridges. *Engineering structures*, *76*, 202-214.

Wardhana, K., & Hadipriono, F. C. (2003). Analysis of recent bridge failures in the United States. *Journal of performance of constructed facilities*, *17*(3), 144-150.

Wang, Z., Xie, X., & Wang, J. (2012). A new nonlinear method for vertical settlement prediction of a single pile and pile groups in layered soils. *Computers and geotechnics*, *45*, 118-126.

Welch, R. C., & Reese, L. C. (1972). *Lateral load behavior of drilled shafts* (No. Interim). University of Texas at Austin.

Wight, J. K., & MacGregor, J. G., (2009). Reinforced concrete: mechanics and design (Fifth ed.). New Jersey: Prentice Hall Upper Saddle River, NJ.

Yang, Z., Lu, J., & Elgamal, A. (2008). OpenSees soil models and solid-fluid fully coupled elements. *User's Manual. Ver*, *1*, 27.

Yassin, M. H. M. (1994). *Nonlinear analysis of prestressed concrete structures under monotonic and cyclic loads*. University of California, Berkeley.

Yilmaz, T., Banerjee, S., & Johnson, P. A. (2018). Uncertainty in risk of highway bridges assessed for integrated seismic and flood hazards. *Structure and Infrastructure Engineering*, *14*(9), 1182-1196.

Zhang, H., Chen, S., & Liang, F. (2016). Effects of scour-hole dimensions and soil stress history on the behavior of laterally loaded piles in soft clay under scour conditions. *Computers and Geotechnics*, *84*, 198-209.

Zhang, J., & Huo, Y. (2009). Evaluating effectiveness and optimum design of isolation devices for highway bridges using the fragility function method. Engineering Structures, 31, 1648–1660.

Zhang Y, DesRoches R., & Tien I. (2018). Updating bridge resilience assessment considering corrosion inspection data. In: ASCE Engineering Mechanics Institute Conference (EMI), Cambridge, MA, May 29–June 1; 2018.

Zhang, Y., DesRoches, R., & Tien, I. (2019a). Impact of corrosion on risk assessment of shear-critical and short lap-spliced bridges. *Engineering Structures*, *189*, 260-271.

Zhang, Y., DesRoches, R., & Tien, I. (2019b). Updating Bridge Resilience Assessment Based on Corrosion and Foundation Scour Inspection Data. *9th International Conference on Structural Health Monitoring of Intelligent Infrastructure (SHMII)*, St. Louis, MO.

Zhang, Y., & Tien, I. (2020a). Methodology for Regularization of Force-Based Elements to Model Reinforced Concrete Columns with Short Lap Splices. *Journal of Engineering Mechanics*, *146*(7), 04020073.

Zhang, Y., & Tien, I. (2020b). Methodology to account for the impact of stress history in

layered soils for seismic vulnerability assessment of scoured bridges. *Structure and Infrastructure Engineering.* 10.1080/15732479.2020.1860096.

Zhao, J., & Sritharan, S. (2007). Modeling of strain penetration effects in fiber-based analysis of reinforced concrete structures. *ACI structural journal*, *104*(2), 133.

Zhong, J., Gardoni, P., Rosowsky, D., and Haukaas, T. (2008). "Probabilistic seismic demand models and fragility estimates for reinforced concrete bridges with two-column bents." J. Eng. Mech., 134(6), 495–504.